Spectroscopic Studies on Photoreactivity of Inorganic Nanocrystals and Medicinally Important Organic Dyes

THESIS

SUBMITTED FOR THE DEGREE OF

DOCTOR OF PHILOSOPHY (SCIENCE)

OF

JADAVPUR UNIVERSITY

2013

BY

SOUMIK SARKAR

DEPARTMENT OF CHEMICAL, BIOLOGICAL AND MACROMOLECULAR SCIENCES,

S. N. BOSE NATIONAL CENTRE FOR BASIC SCIENCES,

BLOCK JD, SECTOR III, SALT LAKE,

KOLKATA 700 098, INDIA

CERTIFICATE FROM THE SUPERVISOR

This is to certify that the thesis entitled "SPECTROSCOPIC STUDIES ON PHOTOREACTIVITY OF INORGANIC NANOCRYSTALS AND MEDICINALLY IMPORTANT ORGANIC DYES" submitted by Mr. Soumik Sarkar, who got his name registered on June 24, 2010 for the award of **Ph.D. (Science) degree** of **Jadavpur University**, is absolutely based upon his own work under the supervision of Dr. Samir Kumar Pal and that neither this thesis nor any part of it has been submitted for any degree/diploma or any other academic award anywhere before.

(Signature of Supervisor/date with official seal)

To My Parents
and Sister

Acknowledgements

First of all I would like to express my gratitude to Dr. Samir Kumar Pal for giving me the opportunity to work on this fascinating subject, for his great interest in my work, for his constant availability and innumerous helpful discussions. I was fortunate enough to write him an email a little more than three years ago and get the opportunity to conduct my research here.

I have enjoyed fruitful collaborations of Prof. Joydeep Dutta, Prof. Peter Lemmens, Prof. A. K. Raychaudhuri and Dr. Achintya Singha. Special recognition is given to Prof. Dutta for his valuable advices and for reviewing my works. Special thanks are also due to a great help from his research group, especially to Tanujjal and Karthik, for introducing me to the fabrication and measurement of the dye-sensitized solar cells and for their constant help on technical points. I am also very thankful to them for their hospitality and the great efforts they made during my visit in Bangkok. I'm very much indebted to Dr. Sunandan Baruah for promptly supplying me with excellent quality ZnO samples in earlier days of PhD. Great appreciation is extended to SNBNCBS staffs for their remarkable technical assistances in my research career. I owe a special thank to the University Grants Commission (UGC), India for my research fellowship, and Department of Science and Technology (DST), India for projects.

I would like to acknowledge my colleagues (Dr. Pramod Kumar Verma, Dr. Abhinandan Makhal, Ranajay, Tanumoy, Soma, Subrata, Anupam, Surajit, Nirmal, Samim, Nabarun and Sushovan) for providing a homely and cheerful environment, and also for assisting me in research. Specially, I have to thank Abhinandan'da for introducing me to the experimental techniques and Samim for thesis proof-reading. A special thank to Ranajay and Tanumoy who shared the same cubicle for a long period of time, supported my work annoyances, and also for the good moments of fun! I also want to thank all my friends for the good times I shared with them.

Finally, I would like to express my gratitude to my family who supports me through thick and thin, with loves and affections. I want them to know that I love them cordially. Without their sacrifices, moral supports and blessings the thesis would not have taken its shape.

Dated:
Department of Chemical, Biological
and Macromolecular Sciences,
S. N. Bose National Centre for Basic Sciences,
Salt Lake, Kolkata 700098, India *(Soumik Sarkar)*

CONTENTS

Page

Page

Chapter 1

Introduction

1.1. Scope of the Spectroscopic Studies on Photoreactivity of Inorganic Nanocrystals and Medicinally Important Organic Dyes:

'Photoreactivity' is a general name for a group of rather different types of reactions occurring in most redox-active systems, including inorganic nanostructures associated with some organic dyes having some medicinal significance. It is well-recognized that optical radiation can change the properties in those inorganic−organic nanohybrid materials and the great majority of those materials absorb UV and an appreciable amount of visible radiation. Therefore, absorption is a first indication that a compound may participate in a photochemical process, thereby having the potential of being photoreactive. The importance of photoreactivity of some organic dyes lies in various fields of science like photodynamic therapy, bioremediation in biomedical applications. Some of the medicinally important organic dyes are also well-known as photosensitizers. All of these photoreactivities of a photosensitizer are associated with ultrafast electron or electronic energy transfer processes from a donor to an acceptor molecule, but the degree and character of excited-state deactivation varies strongly from case to case. Therefore, ultrafast spectroscopic technique is an ideal tool for probing such charge carrier dynamics in nanohybrid materials.

In many fields of research, nanomaterials have played a key role due to their unique optical and electronic properties, which strongly depend on their size, shape and surface properties. In the size regime of 2 to ~20 nm, the electronic structure and optical properties of materials can be tuned by varying the physical size of the crystal, leading to new phenomena, such as surface plasmon resonance in Au and Ag nanoparticles (NPs) [1], size-dependent band-gap of semiconductor nanomaterials [2], and the defect-mediated room-temperature photoluminescence from ZnO NPs [3-4]. These phenomena open interesting opportunities to utilize the nanomaterials as building blocks of light-harvesting

systems. Areas of particular interest are their role in capturing incident photons to induce charge separation in dye/quantum dot (QD)-sensitized solar cells [5-15] and photocatalyst systems [16-18]. Efficient transfer of electrons or electronic energy across the semiconductor interface is the key for the efficiency of converting light energy into electricity or photoinduced catalytic activity. Therefore, a fundamental understanding of the mechanisms and dynamics of these ultrafast charge transfer processes is crucial from the viewpoint of developing efficient light-harvesting systems and for their large-scale industrialization. At present, however, the drawbacks include the toxicity, cost hike and low abundance of the raw materials, which are the major barriers that are holding back progress and this thesis attempts to identify some of the factors that determine solar cell performance. Another setting that requires attention is the potential to combat jaundice when excess bilirubin (BR) bind and deposit to various tissues, giving rise to severe hyperbilirubinemia and neurotoxicity. Within the scope of the thesis, we investigated the utilization of nanomaterials in medical science, which has been a promising direction over a past few years in nanotechnology [19], particularly in drug delivery [20], cancer cell diagnostics [21], and therapeutics [22].

The key focus of this thesis is to investigate the excited-state dynamics of nanomaterials when they are in a close proximity of other organic, inorganic and biological macromolecules, which is important from both fundamental and application perspectives, such as, light-harvesting devices, efficient photocatalysts and phototherapeutic agents. For example, we have explored a novel mechanism for ZnO NP-sensitized BR degradation *via* defect-mediated nonradiative energy transfer pathway, and rigorous medical trials are likely to offer phototherapeutic improvements in the treatment of hyperbilirubinemia. By using a picosecond-resolved Förster resonance energy transfer (FRET) technique, we have demonstrated the role of the gold layer in promoting photoinduced charge transfer from ZnO−Au nanocomposite (NC) to a model contaminant methylene blue (MB). Due to the formation of the Schottky barrier at the ZnO−Au interface and the higher optical absorptions of the ZnO−Au photoelectrodes arising from the surface plasmon absorption of the Au NPs, enhanced power-conversion efficiency was achieved compared to bare ZnO-based dye-sensitized solar cells (DSSCs). In another study, potential cosensitization of extrinsic sensitizer CdTe QDs in ZnO nanorod (NR)-based DSSCs has been established,

and the multipath enhancement offered in this device architecture results in an increased and extended photoresponse with respect to the individual materials employed. We have also revealed that biomolecules and NPs can be linked to prepare a novel multifunctional bio-nanocomposite (BNC) that is able to recognize and efficiently reduce target organic molecules. Another study provides a mechanistic explanation for the ultrafast excited-state deactivation by considering every single aspect of the quenching mechanisms, namely photoinduced electron transfer (PET), FRET and nanosurface energy transfer (NSET) from the host porous alumina membrane to different guest molecules, which may find its importance in the use of porous alumina in light-harvesting devices. Finally, we have demonstrated the exciting potential of porphyrins as light-harvesting green dyes that can simultaneously be used in visible-light photocatalysis (VLP) and photovoltaics.

The experimental tools used for studying the dynamical processes involve picosecond and femtosecond-resolved carrier relaxation dynamics, such as, PET, FRET or NSET, irradiation induced luminescence enhancement (IILE) effect, Langmuir−Hinshelwood (L−H) model for surface catalysis and various characterization tools of photovoltaic solar cells. The different experimental techniques employed for the structural and functional characterization of the nanomaterials and their conjugates include steady-state UV-vis absorption and fluorescence, enzyme kinetics, thermogravimetric analysis (TGA), picosecond and femtosecond-resolved fluorescence spectroscopy, Fourier transform infrared spectroscopy (FTIR), Raman scattering, X-ray diffraction (XRD), circular dichroism (CD), scanning electron microscopy (SEM) and high-resolution transmission electron microscopy (HRTEM), water contact angle (WCA) measurement, photoconductivity, incident photon-to-current conversion efficiency (IPCE) and photocurrent−voltage ($J-V$) measurements.

1.2. Objective:

Photon can be considered as an ultimate reagent to initiate reactivity in certain materials; unlike many conventional reagents, light is environmentally friendly, generates no ravage, and can be obtained from renewable sources. Beneficial as well as adverse reactions of solar light have been known for many centuries, and visible-light has always been used for many therapeutic purposes also. However, the basic insights into mechanism and dynamics

would be imperative for the practical utilization of light reactions, which will be the key objective of this thesis.

Nowadays, use of NPs in medical science is a promising direction in nanotechnology [19]. Their applications in drug delivery [20], cancer cell diagnostics [21], and therapeutics [22] have been active fields of research. In one of our studies, we have demonstrated the potential use of ZnO NPs as phototherapeutic agents, where defect-mediated emission from NP surface introduces a pathway to degrade BR [23]. Although the photoexcited charge transfer is widely used in the remediation of chemical contaminants, to the best of our knowledge, no effort has been made to utilize the visible emission of ZnO in order to degrade any organic contaminants. To investigate the most effective phototherapeutic ZnO nanostructure, their physicochemical properties, which include size, shape, morphology and surface chemistry, have also been investigated.

Improving the performance of photoactive solid-state devices begins with systematic studies of the metal–semiconductor NCs upon which such devices are based. In the structure of composite nanocluster-based DSSCs, Au NPs are employed to facilitate efficient charge separation, thus serving as a Schottky barrier for reducing the rate of electron–hole recombination [24]. Earlier research indicates improved device performance by using Au Schottky contacts in photovoltaic cells [25]. In another investigation [26], it was shown that the photoelectrochemical performance of nanostructured TiO_2 films could be improved by coupling to noble metal NPs. Using the hypothesis of Fermi level equilibration, it has been possible to understand the increase in the photovoltage of TiO_2–Au films [26-27], as well as the charging effects in metal–semiconductor colloids [28-31]. Although there have been many attempts to obtain improved device performance with metal–semiconductor NCs, the mechanism of charge separation as well as the excitation-dependent interfacial charge transfer kinetics in the nanoscale regime are yet to be fully understood. One of our studies in this direction is aimed at elucidating the mechanism of pronounced intrinsic emission from colloidal ZnO and ZnO–Au NCs upon above band-edge and below band-gap excitation [32]. To probe the correlation between dynamics of photogenerated carrier trapping at the defect sites and kinetics of charge migration from ZnO and ZnO–Au semiconductors, MB degradation was examined using UV-light and optical filters. Finally, we have designed a model DSSC based on ZnO NPs which leads to

an increase in short-circuit photocurrent (J_{sc}) and improved overall efficiency (η) in the presence of Au NPs.

The sensitizing dye (SD) is an essential constituent in nanocrystalline DSSCs that has a potential for future photovoltaic applications owing to the lower fabrication costs of solar cells with acceptable conversion efficiencies [33-34]. However, dyes with strong absorptivity do not typically exhibit broad absorption overlapping the solar spectra, which is one of the major pitfalls of using dyes as photosensitizers in solar cells. Therefore, the utilization of two sensitizers (one acting as energy donor while the other as an acceptor) can be very useful in order to achieve both broadening of optical absorption region in DSSCs, as well as increasing the absolute loading of absorbing media on the semiconductor. This novel approach is based on FRET, which has recently experienced a significant interest of several groups [9, 35-39] including ours [32, 40]. By using spectroscopic techniques, we have demonstrated the utilization of dual-sensitization in a CdTe QD-assembled N719-based DSSCs [41]. The cosensitization in the presence of CdTe QDs leads to a significant increment in photocurrent throughout the visible spectral region and also enhances the short-circuit current density as additional photogenerated charge carriers from N719 dyes (*via* FRET) adds up to the net photocurrent.

The use of proteins and peptides to direct the *in vitro* synthesis of inorganic NPs is attractive for a number of reasons [42]. Due to their extremely high surface-to-volume ratio, NPs have a very active surface chemistry in comparison to bulk materials; hence, in biological applications they tend to reduce their large surface energy by interaction with the medium components in which they are dispersed [43-44]. Thus, the dispersion of NPs in a biological medium results in their surfaces (as with bulk materials) being covered by a complex layer of biomolecules, which may induce interesting multifunctional properties in the BNCs. In this respect, we have shown that biomolecules and NPs can be linked to prepare a novel BNC that is able to recognize and efficiently reduce target organic molecules [45]. A simple, fast, water-soluble, and green phosphine free colloidal synthesis strategy has been developed for the preparation of multifunctional protein (enzyme)-capped ZnS NPs with/without transitional metal-ion doping. A detailed study on the photoselective excited state dynamics and electron migration in such NPs in a biological macromolecular environment is sparse in literature and is one of the motives of the present

work. The studies are important in the context that the interaction of NPs with proteins [46] has emerged as a key parameter in nanomedicine and nanotoxicology [47].

At present time, anodic aluminum oxide (AAO) is an important material for a variety of nanotechnological applications because its unique nanoporous honeycomb structure can act as a template for the fabrication of other nanostructured materials [48-54]. To enable studies of the interesting properties appearing for NCs or nanodevices related to AAO films, a complete understanding of the self-properties of the AAO membranes is essential and necessary. Based on this idea, we aimed to establish the electrochemically grown (AAO) membrane as an advantageous light-harvesting material depicting both energy and electron transport ability in the presence of organic molecules and inorganic nanostructures [55]. The study will provide a mechanistic explanation for the ultrafast excited state deactivation by considering every single aspect of the quenching mechanisms, namely PET, FRET and NSET from the host AAO membrane to different guest molecules. Based on these techniques, the location of the oxygen defect center was assigned and their distances from the surface adsorbed acceptor molecules were reported. The present work may find its applications in the use of porous alumina in light-harvesting devices.

Light-harvesting nanohybrids (LHNs) are of another current interest, as the simple search for individual nanomaterials no longer incites broad scientific interests for specific high-end applications. Most of these LHNs are composed of an inorganic nanostructure associated with an organic pigment. For example, association of a ruthenium-based sensitizer N719 with TiO_2 or ZnO nanomaterials leads to very efficient LHNs for DSSC applications [56-59]. Although various organic−inorganic LHNs are found to be active for energy conversion, we come up with an approach to achieve both the eco-friendly VLP process and cost-effective DSSC with a model LHN [60]. In this work, hematoporphyrin (HP) has been conjugated onto covalently functionalized ZnO NRs, forming electron donor−acceptor HP−ZnO nanohybrids, which were being established as potential light-harvesting materials. We believe these promising LHNs to find their dual applications in organic electronics and for the treatment of contaminants in wastewater.

1.3. Summary of the Work Done:

I. Photoreactivity of Inorganic Nanoparticles in the Proximity of Bilirubin, a Potential Jaundice Marker:

A. Nanoparticle-Sensitized Photodegradation of Bilirubin and Potential Therapeutic Application [23]:

Bilirubin (BR) is a protective antioxidant; however, when its conjugation and excretion are impaired, as in neonatal and hereditary jaundice, BR accumulates and may cause severe neurotoxicity. In the present study, we report a novel mechanism for ZnO NP-sensitized BR degradation *via* defect-mediated nonradiative energy transfer pathway. Among different sizes and shapes, ZnO particles with diameter of 5 nm having very high concentration of defect states were found to be the most effective catalyst, which particularly follows a pseudo first-order kinetics validating the Langmuir−Hinshelwood (L−H) model of surface catalysis. The nontoxic wide band-gap ZnO NPs essentially transmit defect-mediated visible optical radiation, which is not supposed to interfere with the conventional phototherapy process. Therefore, the recyclable ZnO nanocatalysts essentially invite an added advantage in potential therapeutic applications, which has been explored in a flow-device in the present study.

II. Excited State Dynamics of Electron/Energy Transfer in Metal−Semiconductor Nanocomposites and their Implications in the Proximity of Organic Dyes:

A. Photoselective Excited State Dynamics in ZnO−Au Nanocomposites and their Implications in Photocatalysis and Dye-Sensitized Solar Cells [32]:

Improving the performance of photoactive solid-state devices begins with systematic studies of the metal–semiconductor NCs upon which such devices are based. In the present contribution, we have explored the photodependent excitonic mechanism and the charge migration kinetics in a colloidal ZnO–Au NC system. By using a picosecond-resolved FRET technique, we have demonstrated that excited ZnO NPs resonantly transfer visible

optical radiation to the Au NPs, and the quenching of defect-mediated visible emission depends solely on the excitation level of the semiconductor. The role of the gold layer in promoting photolytic charge transfer, the activity of which is dependent upon the degree of excitation, was probed using MB reduction at the metal−semiconductor interface. The IPCE measurements show improved charge injection from a SD to a semiconductor electrode in the presence of gold at visible region. Furthermore, the short-circuit current density and the energy conversion efficiency of the ZnO–Au NCs-based DSSC are much higher than those of a DSSC comprised of only ZnO NPs. Our results represent a new paradigm for understanding the mechanism of defect-state passivation and photolytic activity of the metal component in metal–semiconductor NC systems.

B. Highly Efficient ZnO−Au Schottky Barrier Dye-Sensitized Solar Cells: Role of Gold Nanoparticles on the Charge Transfer Process [61]:

As a complementary of the previous study, the role of Au NPs on the charge transfer process has also been investigated in ZnO NR-based devices. For this purpose, ZnO NRs decorated with gold NPs were synthesized and used to fabricate DSSCs. The time-correlated single photon count (TCSPC) spectroscopy technique was used to explore the charge transfer mechanism in the ZnO−Au NC-based DSSCs. Due to the formation of the Schottky barrier at ZnO−Au interface and the higher optical absorptions of ZnO−Au photoelectrodes arising from the surface plasmon absorption of the Au NPs, enhanced power-conversion efficiency (PCE) of 6.49% for small-area (0.1 cm^2) ZnO−Au NC DSSC was achieved compared to 5.34% efficiency of the bare ZnO NR-based DSSCs. The picosecond-resolved fluorescence studies revealed similar dynamics for the charge transfer from dye molecules to ZnO both in the presence and absence of Au NPs. For large area DSSCs (1 cm^2), ~130% enhancement in PCE (from 0.50% to 1.16%) was achieved after incorporation of the Au NPs into the ZnO NRs.

III. Metal Oxide Semiconductors in the Simultaneous Proximity of Organic Dyes and Quantum Dots:

A. "Dual-Sensitization" *via* Electron and Energy Harvesting in CdTe Quantum Dots Decorated ZnO Nanorod-based Dye-Sensitized Solar Cells [41]:

In this study, different-sized, 3-mercaptopropionic acid (MPA)-stabilized CdTe QDs have been prepared in aqueous solution, and potential cosensitization of such QDs in ZnO NR-based DSSCs has been established. The results presented in this study highlight two major pathways by which CdTe QDs may contribute to the net photocurrent in a DSSC: (1) a direct injection of charge carriers from QDs to ZnO semiconductor *via* PET and (2) an indirect excitation of the sensitizer N719 molecules by funneling harvested light *via* FRET. The steady-state and picosecond-resolved luminescence measurements were combined to clarify the process of PET and FRET from the excited QDs to ZnO NR and SD N719, respectively. On the basis of these advantages, the short-circuit current density and the photoconductivity of the QD-assembled DSSCs with distinct architectures are found to be much higher than DSSCs fabricated with N719 sensitizer only.

IV. Photoinduced Dynamical Processes and Promising Applications of a Potential Bio-Nanocomposite:

A. Protein-Mediated Synthesis of Nanosized Mn-Doped ZnS: A Multifunctional, UV-Durable Bio-Nanocomposite (BNC) [45]:

The design of synthetic NPs capable of recognizing given chemical entities in a specific and predictable manner is of great fundamental and practical importance. In this study, we addressed a simple, fast, water-soluble, and green phosphine free colloidal synthesis route for the preparation of multifunctional enzyme-capped ZnS BNCs with/without transitional metal-ion doping. The enzymes α-Chymotrypsin (CHT), associated with the NPs, are demonstrated as an effectual host for organic dye MB revealing the molecular recognition of such dye molecules by the BNCs. An effective hosting of MB in the close proximity of ZnS NPs (with ~3 nm size) leads to photocatalysis of the dyes which has further been investigated with doped-semiconductors. The NP-associated enzyme CHT is found to be

active toward a substrate (Ala-Ala-Phe-7-amido-4-methyl coumarin), hence leads to significant enzyme catalysis. The IILE measurements on the BNCs clearly interpret the role of surface capping agents which protect against deep UV damaging of ZnS NPs.

V. Ultrafast Photoinduced Energy/Electron Transfer from a Technologically Important Nanoporous Host Membrane to Various Inorganic/Organic Guests:

A. Ultrafast Excited State Deactivation of Doped Porous Anodic Aluminum Oxide (AAO) Membranes [55]:

Free-standing, bi-directionally permeable and ultra-thin AAO membranes establish attractive templates (host) for the synthesis of nanodots and rods of various materials (guest). This is due to their chemical and structural integrity and high periodicity on length scales of 5–150 nm, which are often used to host photoactive nanomaterials for various device applications including DSSCs. In the present study, AAO membranes are synthesized by using electrochemical methods and a detailed structural characterization using FEG (Field Emission Gun)-SEM, XRD and TGA confirms the porosity and purity of the material. Defect-mediated photoluminescence quenching of the porous AAO membrane in the presence of an electron accepting guest organic molecule (*p*-benzoquinone) is studied by means of steady-state and picosecond/femtosecond-resolved luminescence measurements. Using time-resolved luminescence transients, we have also revealed light harvesting of complexes of porous alumina impregnated with inorganic QDs (Maple Red) or Au nanowires. Both the FRET and NSET techniques are employed to examine the observed quenching behavior as a function of the characteristic donor–acceptor distances. The experimental results will find their relevance in light-harvesting devices based on AAOs combined with other materials involving a decisive energy/charge transfer dynamics.

VI. Photosensitization Dynamics of Metal Oxide Semiconductors by Medicinally Important Porphyrins: Towards '*Two-in-One'* Applications:

A. Hematoporphyrin−ZnO Nanohybrids: Twin Applications in Efficient Visible-Light Photocatalysis and Dye-Sensitized Solar Cells [60]:

Light-harvesting nanohybrids (LHNs) are systems composed of an inorganic nanostructure associated with an organic pigment that have been exploited to improve the light-harvesting performance over individual components. The present study is focused on developing a potential LHN, attained by the functionalization of dense arrays of ZnO NRs with a biologically important organic pigment hematoporphyrin (HP), which is an integral part of red blood cells (hemoglobin). Application of spectroscopic techniques, namely, FTIR and Raman scattering, confirm monodentate binding of HP carboxylic groups to Zn^{2+} located at the surface of ZnO NRs. Picosecond-resolved fluorescence studies on the resulting HP−ZnO nanohybrid show efficient electron migration from photoexcited HP to the host ZnO NRs. This essential photoinduced event activates the LHN under sunlight, which ultimately leads to the realization of visible-light photocatalysis (VLP) of a model contaminant MB in aqueous solution. A control experiment in an inert gas atmosphere clearly reveals that the photocatalytic activity is influenced by the formation of reactive oxygen species (ROS) in the media. Furthermore, the stable LHNs prepared by optimized dye loading have also been used as an active layer in DSSCs. We believe these promising LHNs to find their dual applications in organic electronics and for the treatment of contaminants in wastewater.

1.4. Plan of Thesis:

The plan of the thesis is as follows:

Chapter 1: This chapter gives a brief introduction to the scope and motivation behind the thesis work. A brief summary of the work done is also included in this chapter.

Chapter 2: This chapter provides an overview of the dynamical and steady-state tools, the structural aspects of biologically important systems (proteins) and probes used in the research.

Chapter 3: Details of instrumentation, data analysis and experimental procedures have been discussed in this chapter.

Chapter 4: In this chapter, a novel mechanism for ZnO NP-sensitized BR degradation *via* FRET process has been reported, which makes this recyclable ZnO NP photocatalyst promising to be useful in the future technology of BR phototherapy. A FRET-based phototherapeutical device involving ZnO NP thin film has also been demonstrated in order to degrade BR when attached to albumin.

Chapter 5: The photodependent excitonic mechanism and the charge migration kinetics in a colloidal ZnO–Au NC system have been explored. By fabricating ZnO and ZnO−Au-based DSSCs, we have also demonstrated that the incident photon-to-current conversion efficiency and short-circuit current are significantly improved in the presence of Au NPs, which is attributed to the formation of the Schottky barrier at the ZnO−Au interface and higher optical absorptions of the ZnO−Au photoelectrodes arising from the surface plasmon absorption of Au NPs.

Chapter 6: In this chapter, different-sized, 3-mercaptopropionic acid (MPA)-stabilized CdTe QDs have been prepared in aqueous solution, and potential cosensitization of such QDs in ZnO NR-based DSSCs has been established.

Chapter 7: In this chapter, we report a simple, fast, water-soluble, and green phosphine free colloidal synthesis route for the preparation of multifunctional enzyme-capped ZnS bio-nanocomposites (BNCs) with/without transitional metal-ion doping.

Chapter 8: This chapter deals with a mechanistic explanation for the ultrafast excited state deactivation of anodic aluminium oxide (AAO) membrane by considering every single

aspect of quenching mechanisms, namely PET, FRET and NSET from the host AAO membrane to different guest molecules.

Chapter 9: This chapter demonstrates the exciting potential of porphyrins as light-harvesting green dyes that can be used in the '*two-in-one'* applications of visible-light photocatalysis and photovoltaics.

References

[1] S. Link, M.A. El-Sayed, Spectral Properties and Relaxation Dynamics of Surface Plasmon Electronic Oscillations in Gold and Silver Nanodots and Nanorods, *J. Phys. Chem. B* 103 (1999) 8410.

[2] L. Brus, Electronic Wavefunctions in Semiconductor Clusters: Experiment and Theory, *J. Phys. Chem.* 90 (1986) 2555.

[3] A.V. Dijken, E.A. Meulenkamp, D. Vanmaekelbergh, A. Meijerink, The Luminescence of Nanocrystalline ZnO Particles: The Mechanism of the Ultraviolet and Visible Emission, *J. Lumin.* 87-89 (2000) 454.

[4] K. Vanheusden, W.L. Warren, C.H. Seager, D.R. Tallant, J.A. Voigt, Mechanisms Behind Green Photoluminescence in ZnO Phosphor Powders, *J. Appl. Phys.* 79 (1996) 7983.

[5] P.V. Kamat, K. Tvrdy, D.R. Baker, J.G. Radich, Beyond Photovoltaics: Semiconductor Nanoarchitectures for Liquid-Junction Solar Cells, *Chem. Rev.* 110 (2010) 6664.

[6] I. Mora-Sero, J. Bisquert, Breakthroughs in the Development of Semiconductor Sensitized Solar Cells, *J. Phys. Chem. Lett.* 1 (2010) 3046.

[7] A.J. Nozik, M.C. Beard, J.M. Luther, M. Law, R.J. Ellingson, J.C. Johnson, Semiconductor Quantum Dots and Quantum Dot Arrays and Applications of Multiple Exciton Generation to Third-Generation Photovoltaic Solar Cells, *Chem. Rev.* 110 (2010) 6873.

[8] J. Gao, C.L. Perkins, J.M. Luther, M.C. Hanna, H.Y. Chen, O.E. Semonin, A.J. Nozik, R.J. Ellingson, M.C. Beard, n-Type Transition Metal Oxide as a Hole Extraction Layer in PbS Quantum Dot Solar Cells, *Nano Lett.* 11 (2011) 3263.

[9] S. Buhbut, S. Itzhakov, E. Tauber, M. Shalom, I. Hod, T. Geiger, Y. Garini, D. Oron, A. Zaban, Built-in Quantum Dot Antennas in Dye-Sensitized Solar Cells, *ACS Nano* 4 (2010) 1293.

[10] Y. Chiba, A. Islam, Y. Watanabe, R. Komiya, N. Koide, L. Han, R. Komiya, N. Koide, L.Y. Han, Dye-Sensitized Solar Cells with Conversion Efficiency of 11.1%, *Jpn. J. Appl. Phys.* 45 (2006) L638.

[11] A. Yella, H.W. Lee, H.N. Tsao, C. Yi, A.K. Chandiran, M.K. Nazeeruddin, W.G.E. Diau, C.Y. Yeh, S.M. Zakeeruddin, M. Grätzel, Porphyrin-Sensitized Solar Cells with Cobalt (II/III)–Based Redox Electrolyte Exceed 12 Percent Efficiency, *Science* 334 (2011) 629.

[12] Q.J. Yu, Y.H. Wang, Z.H. Yi, N.N. Zu, J. Zhang, M. Zhang, P. Wang, High-Efficiency Dye-Sensitized Solar Cells: The Influence of Lithium Ions on Exciton Dissociation, Charge Recombination, and Surface States, *ACS Nano* 4 (2010) 6032.

[13] T. Horiuchi, H. Miura, S. Uchida, Highly-Efficient Metal-Free Organic Dyes for Dye-Sensitized Solar Cells, *Chem. Commun.* (2003) 3036.

[14] T. Daeneke, T.H. Kwon, A.B. Holmes, N.W. Duffy, U. Bach, L. Spiccia, High-Efficiency Dye-Sensitized Solar Cells with Ferrocene-Based Electrolytes, *Nat. Chem.* 3 (2011) 211.

[15] J.H. Yum, E. Baranoff, S. Wenger, M.K. Nazeeruddin, M. Grätzel, Panchromatic Engineering for Dye-Sensitized Solar Cells, *Energy Environ. Sci.* 4 (2011) 842.

[16] M.R. Hoffmann, S.T. Martin, W.Y. Choi, D.W. Bahnemann, Environmental Applications of Semiconductor Photocatalysis, *Chem. Rev.* 95 (1995) 69.

[17] H. Chen, C.E. Nanayakkara, V.H. Grassian, Titanium Dioxide Photocatalysis in Atmospheric Chemistry, *Chem. Rev.* 112 (2012) 5919.

[18] D. Ravelli, D. Dondi, M. Fagnoni, A. Albini, Photocatalysis. A Multi-faceted Concept for Green Chemistry, *Chem. Soc. Rev.* 38 (2009) 1999.

[19] J.Z. Zhang, Biomedical Applications of Shape-Controlled Plasmonic Nanostructures: A Case Study of Hollow Gold Nanospheres for Photothermal Ablation Therapy of Cancer, *J. Phys. Chem. Lett.* 1 (2010) 686.

[20] G.F. Paciotti, L. Myer, D. Weinreich, D. Goia, N. Pavel, R.E. McLaughlin, L. Tamarkin, Colloidal Gold: A Novel Nanoparticle Vector for Tumor Directed Drug Delivery, *Drug Delivery* 11 (2004) 169.

[21] X. Wu, H. Liu, J. Liu, K.N. Haley, J.A. Treadway, J.P. Larson, N. Ge, F. Peale, M.P. Bruchez, Immunofluorescent Labeling of Cancer Marker Her2 and Other Cellular Targets with Semiconductor Quantum Dots, *Nat. Biotechnol.* 21 (2002) 41.

[22] L.R. Hirsch, R.J. Stafford, J.A. Bankson, S.R. Sershen, B. Rivera, R.E. Rrice, J.D. Hazle, N.J. Halas, J.L. West, Nanoshell-Mediated Near-Infrared Thermal Therapy of Tumors under Magnetic Resonance Guidance, *Proc. Natl. Acad. Sci. U.S.A.* 100 (2003) 13549.

[23] S. Sarkar, A. Makhal, S. Baruah, M.A. Mahmood, J. Dutta, S.K. Pal, Nanoparticle-Sensitized Photodegradation of Bilirubin and Potential Therapeutic Application, *J. Phys. Chem. C* 116 (2012) 9608.

[24] Z.H. Chen, Y.B. Tang, C.P. Liu, Y.H. Leung, G.D. Yuan, L.M. Chen, Y.Q. Wang, I. Bello, J.A. Zapien, W.J. Zhang, C.S. Lee, S.T. Lee, Vertically Aligned ZnO Nanorod Arrays Sentisized with Gold Nanoparticles for Schottky Barrier Photovoltaic Cells, *J. Phys. Chem. C* 113 (2009) 13433.

[25] Y. Tian, T. Tatsuma, Mechanisms and Applications of Plasmon-Induced Charge Separation at TiO_2 Films Loaded with Gold Nanoparticles, *J. Am. Chem. Soc.* 127 (2005) 7632.

[26] V. Subramanian, E.E. Wolf, P.V. Kamat, Semiconductor−Metal Composite Nanostructures. To What Extent Do Metal Nanoparticles Improve the Photocatalytic Activity of TiO_2 Films?, *J. Phys. Chem. B* 105 (2001) 11439.

[27] N. Chandrasekharan, P.V. Kamat, Improving the Photoelectrochemical Performance of Nanostructured TiO_2 Films by Adsorption of Gold Nanoparticles, *J. Phys. Chem. B* 104 (2000) 10851.

[28] A. Wood, M. Giersig, P. Mulvaney, Fermi Level Equilibration in Quantum Dot−Metal Nanojunctions, *J. Phys. Chem. B* 105 (2001) 8810.

[29] V. Subramanian, E.E. Wolf, P.V. Kamat, Green Emission to Probe Photoinduced Charging Events in ZnO-Au Nanoparticles.Charge Distribution and Fermi-Level Equilibration, *J. Phys. Chem. B* 107 (2003) 7479.

[30] M. Jakob, H. Levanon, Charge Distribution between UV-Irradiated TiO_2 and Gold Nanoparticles: Determination of Shift in the Fermi Level, *Nano Lett.* 3 (2003) 353.

[31] C. Li, L. Li, Z. Du, H. Yu, Y. Xiang, Y. Li, Y. Cai, T. Wang, Rapid and Ultrahigh Ethanol Sensing Based on Au-Coated ZnO Nanorods, *Nanotechnology* 19 (2008) 035501.

[32] S. Sarkar, A. Makhal, T. Bora, S. Baruah, J. Dutta, S.K. Pal, Photoselective Excited State Dynamics in ZnO-Au Nanocomposites and their Implications in Photocatalysis and Dye-Sensitized Solar Cells, *Phys. Chem. Chem. Phys.* 13 (2011) 12488.

[33] B. O'Regan, M. Grätzel, A Low-Cost, High-Efficiency Solar Cell Based on Dye-Sensitized Colloidal TiO_2 Films, *Nature* 353 (1991) 737.

[34] M. Grätzel, Photoelectrochemical Cells, *Nature* 414 (2001) 338.

[35] L. Etgar, J. Park, C. Barolo, V. Lesnyak, S.K. Panda, P. Quagliotto, S.G. Hickey, M.K. Nazeeruddin, A. Eychmuller, G. Viscardi, M. Grätzel, Enhancing the Efficiency of a Dye Sensitized Solar Cell due to the Energy Transfer between CdSe Quantum Dots and a Designed Squaraine Dye, *RSC Adv.* 2 (2012) 2748.

[36] S. Giménez, A.L. Rogach, A.A. Lutich, D. Gross, A. Poeschl, A.S. Susha, I. Mora-Seró, T. Lana-Villarreal, J. Bisquert, Energy Transfer versus Charge Separation in Hybrid Systems of Semiconductor Quantum Dots and Ru-Dyes as Potential Co-Sensitizers of TiO_2-based Solar Cells, *J. Appl. Phys.* 110 (2011) 014314.

[37] A. Ruland, C. Schulz-Drost, V. Sgobba, D.M. Guldi, Enhancing Photocurrent Efficiencies by Resonance Energy Transfer in CdTe Quantum Dot Multilayers: Towards Rainbow Solar Cells, *Adv. Mater.* 23 (2011) 4573.

[38] K. Shankar, X. Feng, C.A. Grimes, Enhanced Harvesting of Red Photons in Nanowire Solar Cells: Evidence of Resonance Energy Transfer, *ACS Nano* 3 (2009) 788.

[39] S. Buhbut, S. Itzhakov, D. Oron, A. Zaban, Quantum Dot Antennas for Photoelectrochemical Solar Cells, *J. Phys. Chem. Lett.* 2 (2011) 1917.

[40] A. Makhal, S. Sarkar, T. Bora, S. Baruah, J. Dutta, A.K. Raychaudhuri, S.K. Pal, Role of Resonance Energy Transfer in Light Harvesting of Zinc Oxide-Based Dye-Sensitized Solar Cells, *J. Phys. Chem. C* 114 (2010) 10390.

[41] S. Sarkar, A. Makhal, K. Lakshman, T. Bora, J. Dutta, S.K. Pal, "Dual-Sensitization" via Electron and Energy Harvesting in CdTe Quantum Dots Decorated ZnO Nanorod-based Dye-Sensitized Solar Cells, *J. Phys. Chem. C* 116 (2012) 14248.

[42] M.B. Dickerson, K.H. Sandhage, R.R. Naik, Protein- and Peptide-Directed Syntheses of Inorganic Materials, *Chem. Rev.* 108 (2008) 4935.

[43] J. Klein, Probing the Interactions of Proteins and Nanoparticles, *Proc. Natl. Acad. Sci. U.S.A.* 104 (2007) 2029.

[44] M.P. Monopoli, D. Walczyk, A. Campbell, G. Elia, I. Lynch, F.B. Bombelli, K.A. Dawson, Physical-Chemical Aspects of Protein Corona: Relevance to in Vitro and in Vivo Biological Impacts of Nanoparticles, *J. Am. Chem. Soc.* 133 (2011) 2525.

[45] A. Makhal, S. Sarkar, S.K. Pal, Protein-Mediated Synthesis of Nanosized Mn-Doped ZnS: A Multifunctional, UV-Durable Bio-Nanocomposite, *Inorg. Chem.* 51 (2012) 10203.

[46] M. Mahmoudi, I. Lynch, M.R. Ejtehadi, M.P. Monopoli, F.B. Bombelli, S. Laurent, Protein-Nanoparticle Interactions: Opportunities and Challenges, *Chem. Rev.* 111 (2011) 5610.

[47] M. Lundqvist, J. Stigler, T. Cedervall, G. Elia, I. Lynch, K.A. Dawson, Nanoparticle Size and Surface Properties Determine the Protein Corona with Possible Implications for Biological Impacts, *Proc. Natl. Acad. Sci. U.S.A.* 105 (2008) 14265.

[48] Y. Zhang, G.H. Li, Y.C. Wu, B. Zhang, W.H. Song, L. Zhang, Antimony Nanowire Arrays Fabricated by Pulsed Electrodeposition in Anodic Alumina Membranes, *Adv. Mater.* 14 (2002) 1227.

[49] D. Chen, W. Zhao, T.P. Russell, P3HT Nanopillars for Organic Photovoltaic Devices Nanoimprinted by AAO Templates, *ACS Nano* 6 (2012) 1479.

[50] X. Mei, D. Kim, H.E. Ruda, Q.X. Guo, Molecular-Beam Epitaxial Growth of GaAs and InGaAs/GaAs Nanodot Arrays using Anodic Al_2O_3 Nanohole Array Template Masks, *Appl. Phys. Lett.* 81 (2002) 361.

[51] W.C. Hu, D.W. Gong, Z. Chen, L.M. Yuan, K. Saito, C.A. Grimes, P. Kichambare, Growth of Well-Aligned Carbon Nanotube Arrays on Silicon Substrates using Porous Alumina Film as a Nanotemplate, *Appl. Phys. Lett.* 79 (2001) 3083.

[52] M.S. Sander, A.L. Prieto, R. Gronsky, T. Sands, A.M. Stacy, Fabrication of High-Density, High Aspect Ratio, Large-Area Bismuth Telluride Nanowire Arrays by

Electrodeposition into Porous Anodic Alumina Templates, *Adv. Mater.* 14 (2002) 665.

[53] M.S. Sander, R. Gronsky, T. Sands, A.M. Stacy, Structure of Bismuth Telluride Nanowire Arrays Fabricated by Electrodeposition into Porous Anodic Alumina Templates, *Chem. Mater.* 15 (2003) 335.

[54] L. Liu, W. Lee, Z. Huang, R. Scholz, U. Gösele, Fabrication and Characterization of a Flow-through Nanoporous Gold Nanowire/AAO Composite Membrane, *Nanotechnology* 19 (2008) 335604.

[55] A. Makhal, S. Sarkar, S.K. Pal, H. Yan, D. Wulferding, F. Cetin, P. Lemmens, Ultrafast Excited State Deactivation of Doped Porous Anodic Alumina Membranes, *Nanotechnology* 23 (2012) 305705.

[56] C.Y. Chen, M. Wang, J.Y. Li, N. Pootrakulchote, L. Alibabaei, C. Ngoc-le, J.D. Decoppet, J.H. Tsai, C. Grätzel, C.G. Wu, S.M. Zakeeruddin, M. Grätzel, Highly Efficient Light-Harvesting Ruthenium Sensitizer for Thin-Film Dye-Sensitized Solar Cells, *ACS Nano* 3 (2009) 3103.

[57] M.K. Nazeeruddin, C. Klein, P. Liska, M. Grätzel, Synthesis of Novel Ruthenium Sensitizers and Their Application in Dye-Sensitized Solar Cells, *Coord. Chem. Rev.* 249 (2005) 1460.

[58] C. Ku, J. Wu, Electron Transport Properties in ZnO Nanowire Array/Nanoparticle Composite Dye-Sensitized Solar Cells, *Appl. Phys. Lett.* 91 (2007) 093117.

[59] Z. Wanga, H. Kawauchib, T. Kashimab, H. Arakawa, Significant Influence of TiO_2 Photoelectrode Morphology on the Energy Conversion Efficiency of N719 Dye-Sensitized Solar Cell, *Coord. Chem. Rev.* 248 (2004) 1381.

[60] S. Sarkar, A. Makhal, T. Bora, K. Lakshman, A. Singha, J. Dutta, S.K. Pal, Hematoporphyrin−ZnO Nanohybrids: Twin Applications in Efficient Visible-Light Photocatalysis and Dye-Sensitized Solar Cells, *ACS Appl. Mater. Interfaces* 4 (2012) 7027.

[61] T. Bora, H.H. Kyaw, S. Sarkar, S.K. Pal, J. Dutta, Highly Efficient ZnO/Au Schottky Barrier Dye-Sensitized Solar Cells: Role of Gold Nanoparticles on the Charge Transfer Process, *Beilstein J. Nanotechnol.* 2 (2011) 681.

Chapter 2

An Overview of Steady-State and Dynamical Tools and Systems

In order to investigate the ultrafast processes involved in the studies on chemically and biologically relevant aqueous/non-aqueous environments, different steady-state and dynamical tools have been employed. These include photoinduced electron transfer (PET), Förster resonance energy transfer (FRET), nanosurface energy transfer (NSET), irradiation induced luminescence enhancement (IILE) effect, Langmuir−Hinshelwood (L−H) model for surface catalysis and photocurrent−voltage ($I-V$) characterization of photovoltaic solar cells. In this chapter, we have included a brief discussion about the above mentioned tools. Overviews of the various systems and the fluorescent probes used in the studies have also been provided.

2.1. Steady-State and Dynamical Tools:

2.1.1. Photoinduced Electron Transfer (PET): PET can be described most simply as the movement of an electron, caused by the absorption of light, from an electron-rich species (a donor D) to an electron deficient species (an acceptor A), as shown in equation 2.1.

$$D + A \rightarrow D^{+} + A^{-} \tag{2.1}$$

The first law of photochemistry tells us that a photoinduced process must be initiated by the absorption of light. In PET, the absorbing species can either be a donor, the acceptor, or a ground-state complex between the donor and acceptor, often referred to as a charge transfer complex. These possibilities are shown in equations 2.2−2.4.

$$D \xrightarrow{h\upsilon} D^{*} + A \longrightarrow D^{+} + A^{-} \tag{2.2}$$

$$A \xrightarrow{h\upsilon} A^{*} + D \longrightarrow D^{+} + A^{-} \tag{2.3}$$

$$(D\cdots A) \xrightarrow{h\upsilon} (D\cdots A)^{*} \longrightarrow D^{+} + A^{-} \tag{2.4}$$

Transports of charges or excitons are commonly seen fundamental processes in many optoelectronic devices as well as biological systems. The creation, diffusion, and annihilation for excitons and the mobility of charges are some of the key processes in many devices that interconvert electric and light energies [1-2]. PET is an important process in many biochemical systems, such as those in respiration and photosynthesis [3-4]. To gain a deep understanding for these systems, it is important to describe the rates of these processes with a few empirically derived parameters [5-6]. Therefore, it has become increasingly important to develop computational techniques that allow us to calculate the rate of charge or energy transport. In our systems the apparent rate constants, k_{nr}, were determined for the nonradiative processes by comparing the lifetimes of donor in the absence (τ_0) and in the presence (τ) of an acceptor, using equation 2.5 [7].

$$k_{nr} = 1/\langle\tau\rangle - 1/\langle\tau_0\rangle \qquad (2.5)$$

This Thesis demonstrates several PET processes, particularly in light-harvesting devices and in visible-light photocatalysis, and discusses strategies to overcome the limitations of various interfacial electron transfer processes. In a dye/quantum dot-sensitized solar cells (DSSC/QDSCs), a series of charge transfer processes had to occur cooperatively so that the electrical output can be harnessed efficiently. These include (i) electron injection from excited dye/QD into metal oxides, (ii) electron transport to the collecting electrode surface, (iii) hole transfer to the redox couple, and (iv) regeneration of the redox couple at the counter electrode. A major force that counteracts these favourable processes (i−iv) is the charge recombination of electrons at the electrolyte interface. The matching of the band energies of the two semiconductors facilitates desired functionality either to induce electron−hole recombination (e.g., light-emitting diodes) or to improve charge separation by driving electrons and holes in two different nanoparticles (e.g., QDSCs). In each instance where semiconductor nanocrystals are implemented into a practical device, PET reactions are intimately involved, and they dictate overall functionality. This Thesis focuses on the recent progress made in understanding the kinetics and mechanistic aspects of various PET processes at the semiconductor interface and their role in optimization of solar cell performance.

2.1.2. Förster Resonance Energy Transfer (FRET): FRET is an electrodynamic phenomenon involving the nonradiative transfer of the excited state energy from the donor dipole (D) to an acceptor dipole (A) in the ground-state (Figure 2.1a). FRET has been widely used in fluorescence applications including medical diagnostics, DNA analysis and optical imaging. Since, FRET can measure the size of a protein molecule or the thickness of a membrane, it is also known as "spectroscopic ruler" [8]. FRET is very often used to measure the distance between two sites on a macromolecule. Basically, FRET is of two types: (a) homomolecular FRET and (b) heteromolecular FRET. In the former case, the same fluorophore acts both as energy donor and acceptor, while in the latter case two different molecules act as donor and acceptor.

Each donor−acceptor (D−A) pair participating in FRET is characterized by a distance known as Förster distance (R_0) i.e., the D−A separation at which energy transfer is 50% efficient. The R_0 value ranges from 20 to 60 Å. The rate of resonance energy transfer (k_T) from donor to an acceptor is given by [9],

$$k_T = \frac{1}{\tau_D}\left(\frac{R_0}{r}\right)^6 \tag{2.6}$$

where, τ_D is the lifetime of the donor in the absence of the acceptor and r is the donor to acceptor (D−A) distance. The rate of transfer of donor energy depends upon the extent of overlap of the emission spectrum of the donor with the absorption spectrum of the acceptor ($J(\lambda)$), the quantum yield of the donor (Q_D), the relative orientation of the donor and acceptor transition dipoles (κ^2) and the distance between the donor and acceptor molecules (r) (Figure 2.1b). In order to estimate FRET efficiency of the donor and hence to determine distances between D−A pairs, the methodology described below is followed [9]. R_0 is given by,

$$R_0 = 0.211\left[\kappa^2 n^{-4} Q_D J(\lambda)\right]^{1/6} \text{ (in Å)} \tag{2.7}$$

where, n is the refractive index of the medium, Q_D is the quantum yield of the donor and $J(\lambda)$ is the overlap integral. κ^2 is defined as,

$$\kappa^2 = \left(\cos\theta_T - 3\cos\theta_D \cos\theta_A\right)^2 = \left(\sin\theta_D \sin\theta_A \cos\varphi - 2\cos\theta_D \cos\theta_A\right)^2 \tag{2.8}$$

where, θ_T is the angle between the emission transition dipole of the donor and the

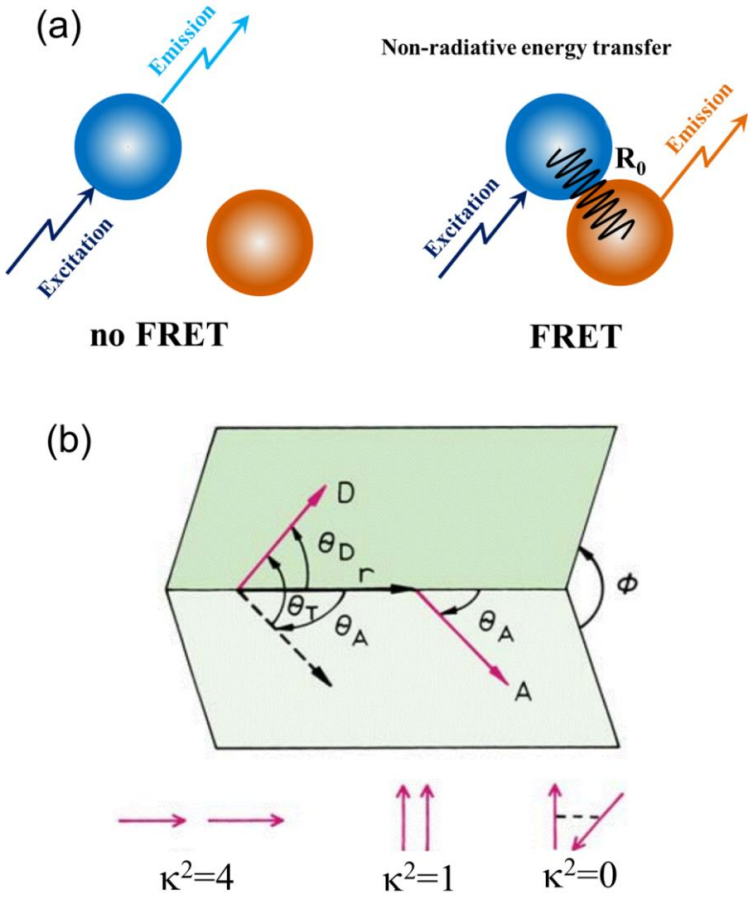

Figure 2.1. *a) Schematic illustration of the Förster resonance energy transfer (FRET) process. b) Dependence of the orientation factor κ^2 on the directions of the emission and absorption dipoles of the donor and acceptor, respectively.*

absorption transition dipole of the acceptor, θ_D and θ_A are the angles between these dipoles and the vector joining the donor and acceptor and φ is angle between the planes of the donor and acceptor (Figure 2.1b). κ^2 value can vary from 0 to 4. For collinear and parallel transition dipoles, $\kappa^2 = 4$; for parallel dipoles, $\kappa^2 = 1$; and for perpendicularly oriented dipoles, $\kappa^2 = 0$. For donor and acceptors that randomize by rotational diffusion prior to energy transfer, the magnitude of κ^2 is assumed to be 2/3. $J(\lambda)$, the overlap integral, which expresses the degree of spectral overlap between the donor emission and the acceptor absorption, is given by,

$$J(\lambda) = \frac{\int_0^\infty F_D(\lambda)\varepsilon_A(\lambda)\lambda^4 d\lambda}{\int_0^\infty F_D(\lambda)d\lambda} \tag{2.9}$$

where, $F_D(\lambda)$ is the fluorescence intensity of the donor in the wavelength range of λ to λ+dλ and is dimensionless. $\varepsilon_A(\lambda)$ is the extinction coefficient (in M^{-1} cm^{-1}) of the acceptor at λ. If λ is in nm, then $J(\lambda)$ is in units of M^{-1} cm^{-1} nm^4.

Once the value of R_0 is known, the efficiency of energy transfer can be calculated. The efficiency of energy transfer (E) is the fraction of photons absorbed by the donor which are transferred to the acceptor and is defined as,

$$E = \frac{k_T(r)}{\tau_D^{-1} + k_T(r)} \tag{2.10}$$

or,
$$E = \frac{R_0^6}{r^6 + R_0^6} \tag{2.11}$$

The transfer efficiency is measured by using the relative fluorescence intensity of donor, in the absence (F_D) and presence (F_{DA}) of the acceptor as,

$$E = 1 - \frac{F_{DA}}{F_D} \tag{2.12a}$$

For D−A systems decaying with multiexponential lifetimes, E is calculated from the amplitude weighted lifetimes $\langle\tau\rangle = \sum_i \alpha_i \tau_i$ of the donor in absence (τ_D) and presence (τ_{DA}) of the acceptor as,

$$E = 1 - \frac{\tau_{DA}}{\tau_D} \tag{2.12b}$$

The D−A distance can be measured using equations 2.11, 2.12a−b. The distances measured using equations 2.12a−b are revealed as R^S (steady-state measurement) and R^{TR} (time-resolved measurement), respectively.

2.1.3. Nanosurface Energy Transfer (NSET): The D−A separations can also be calculated using another prevailing technique, NSET [10-11], in which the energy transfer efficiency depends on the inverse of the fourth power of the D−A separation [12]. The

NSET technique is based on the model of Persson and Lang [11], which is concerned with the momentum and energy conservation in the dipole-induced formation of electron−hole pairs. Here the rate of energy transfer is calculated by performing a Fermi golden rule calculation for an excited-state material depopulating with the simultaneous scattering of an electron in the nearby metal to above the Fermi level. The Persson model states that the damping rate to a surface of a noble metal may be calculated by,

$$k_{NSET} = 0.3 \times \left(\frac{\mu^2 \omega}{\hbar \omega_F k_F d^4} \right) \tag{2.13}$$

which can be expressed in more measurable parameters through the use of the Einstein A_{21} coefficient [13],

$$A_{21} = \frac{\omega^3}{3\varepsilon_0 \hbar \pi c^3} |\mu|^2 \tag{2.14}$$

To give the following rate of energy transfer in accordance with Coulomb's law ($1/4\pi\varepsilon_0$):

$$k_{NSET} = 0.225 \frac{c^3 \Phi_D}{\omega^2 \omega_F k_F d^4 \tau_D} \tag{2.15}$$

where, c is the speed of light, Φ_D is the quantum yield of the donor, ω is the angular frequency for the donor, ω_F is the angular frequency for acceptor, d is the D−A separation, μ is the dipole moment, τ_D is the average lifetime of the donor, and k_F is the Fermi wave-vector [14-15]. In our studies, we used k_{NSET} as,

$$k_{NSET} = \frac{1}{\tau_{donor-acceptor}} - \frac{1}{\tau_{donor}} \tag{2.16}$$

where, $\tau_{donor-acceptor}$ is the average lifetime of the D−A system [16].

2.1.4. Data Analysis of Time-Resolved Fluorescence Transients: Curve fitting of the time-resolved fluorescence transients were carried out using a nonlinear least square fitting procedure to a function $(X(t) = \int_0^t E(t')R(t-t')dt')$ comprised of convolution of the IRF (E(t)) with a sum of exponentials $(R(t) = A + \sum_{i=1}^{N} B_i e^{-t/\tau_i})$ with pre-exponential factors (B_i), characteristic lifetimes (τ_i) and a background (A). Relative concentration in a

multiexponential decay is expressed as, $c_n = \frac{B_n}{\sum_{i=1}^{N} B_i} \times 100$. The average lifetime (amplitude-weighted) of a multiexponential decay [9] is expressed as,

$$\tau_{av} = \sum_{i=1}^{N} c_i \tau_i \tag{2.17}$$

2.1.5. Irradiation Induced Luminescence Enhancement (IILE) Effect: The optical properties of transition metal-ion doped semiconductor NPs have been studied extensively in recent years [17-18]. Bhargava *et al.* reported high luminescent efficiencies of nanocrystals of ZnS:Mn^{2+}, and claimed that doped nanocrystals are a new class of material [19]. Yu and Sun *et al.* reported the effects of IILE by ZnS:Mn^{2+} NPs in poly(vinyl butyral) films [20]. The luminescence intensity increases several times when fresh samples are irradiated by a 248 nm excimer laser. The decay time also increases with exposure time. The increase in the initial intensity of the slow component of luminescence makes the main contribution to the enhancement effect. A tentative model is proposed in which the efficiency of the energy transfer to Mn^{2+} ions increases with exposure. States at interfaces are expected to play an important role in this process.

Several mechanisms have been considered as the cause of the IILE effect. The first is the laser annealing effect. However, even weak light from a Xe-lamp at an appropriate wavelength can produce the IILE effect. So the laser annealing effect is ruled out as a cause of IILE. There are three possible ways to increase luminescence intensity under weak excitation: (1) increasing the radiative transition probability of Mn^{2+} ions, (2) decreasing the nonradiative transition probability or even blocking the nonradiative path, and (3) increasing the efficiency of the energy transfer to Mn^{2+} ion. Since the main cause of the IILE effect is the increase in initial intensity of the slow component of luminescence, the first of these possibilities can be ruled out. Also the experimental data could not be fitted theoretically by decreasing the nonradiative transition or blocking the nonradiative path but was fitted by using a tentative model, in which the increase in efficiency of the energy transfer to Mn^{2+} ions with irradiation is considered [20]. The electron states at the interface are expected to play an important role in this process. From the applied point of view, the IILE effect may provide a means to raise the luminescence efficiency of NPs. Furthermore, we have performed IILE studies under different irradiance doses on enzyme-

capped bio-nanocoposites (BNCs) to investigate the efficacy of the protein-shell around the BNCs against the UV damage of the encapsulated NPs [21].

2.1.6. Langmuir−Hinshelwood (L−H) Model: In the Langmuir−Hinshelwood (L−H) treatment of heterogeneous surface reactions, the rate of the photochemical degradation can be expressed in general terms for both the oxidant (e.g., O_2) and the reductant (e.g., $CHCl_3$) as follows:

$$-\frac{d[\mathrm{Re}\,d]}{dt} = -\frac{d[Ox]}{dt} = k_d \theta_{\mathrm{Re}d} \theta_{Ox} \tag{2.18}$$

where, k_d is the photodegradation rate constant, θ_{Red} represents the fraction of the electron-donating reductant (e.g., chloroform) sorbed to the surface, and θ_{Ox} represents the corresponding fraction of the electron-accepting oxidant (e.g., oxygen) sorbed to the surface. This treatment is subjected to the assumptions that sorption of both the oxidant and the reductant is a rapid equilibrium process in both the forward and reverse directions and that the rate-determining step of the reaction involves both species present in a monolayer at the solid-liquid interface. The Langmuir adsorption coefficient, *K*, for sorption of each reactant is assumed to be readily determined from a classical Langmuir sorption isotherm. In this case, the surface concentration of the reactants is related to their corresponding activities or concentrations in the bulk aqueous phase as follows:

$$R_0 = \frac{dC_0}{dt} = \frac{k_{L-H} K C_0}{1 + K C_0} \tag{2.19}$$

where, C_0 is the initial concentration of substrate, k_{L-H} is the Langmuir–Hinshelwood (L–H) rate constant, and R_0 is the rate of reaction. If the initial concentration of the BR solution is sufficiently low ($KC_0 << 1$), the equation 2.19 can be simplified to an apparent first-order equation:

$$R_0 = k_{L-H} K C_0 = k_{app} C_0 \tag{2.20}$$

where, k_{app} is the apparent first-order rate constant. If the initial concentration of the BR solution is sufficiently high ($KC_0 >> 1$), the equation 2.19 can be simplified to a zero-order rate equation:

$$R_0 = k_{L-H} \tag{2.21}$$

The L−H model appears to be a promising tool that has a number of applications in semiconductor photocatalysis such as dye degradation, air purification, water disinfection,

hazardous waste remediation, and water purification. In addition, the basic research that underlies the application of this potential tool is forging a better understanding of the complex heterogeneous photochemistry of metal oxide systems in multiphasic environments.

2.1.7. Dye-Sensitized Solar Cells (DSSCs): DSSCs [22-24] are potentially inexpensive alternatives to traditional semiconductor solar cells. The essential components of a DSSC are semiconductor metal oxides attached to sensitizing dyes (mostly, ruthenium) and an electrolyte medium (iodine-based). A schematic of the interior of a DSSC showing the principle of how the device operates is shown in Figure 2.2. The typical basic configuration is as follows: at the heart of the device is the metal oxide layer (mostly ZnO/TiO_2), which is deposited on a fluorinated tin oxide (FTO) coated glass substrate. Attached to the surface of the nanocrystalline film is a monolayer of the charge transfer dyes/QDs. Photoexcitation of the latter results in the injection of an electron into the conduction band of the oxide, leaving the dye in its oxidized state. The dye is restored to its ground state by electron transfer from the electrolyte, usually an organic solvent containing the iodide/triiodide (I^-/I_3^-) redox system. The regeneration of the sensitizer by

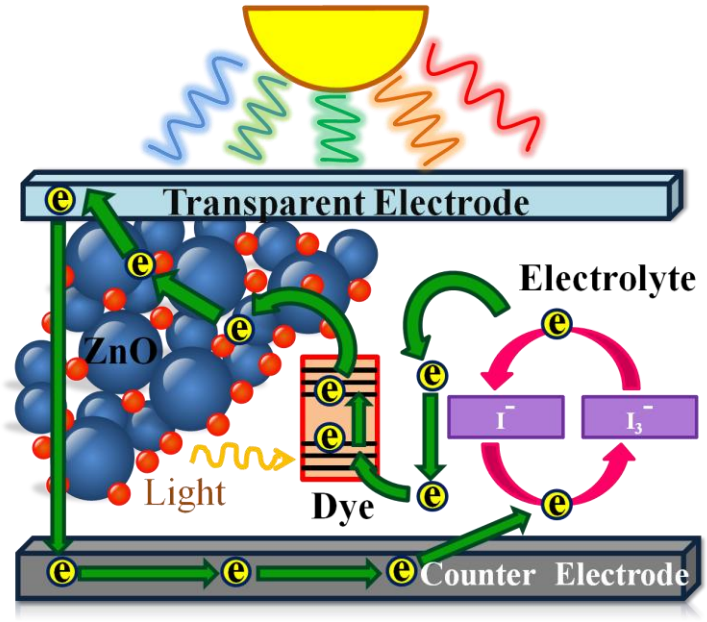

Figure 2.2. *Schematic representation of a ZnO nanoparticle-based DSSC showing different charge migration processes.*

iodide intercepts the recapturing of the conduction band electron by the oxidized dye. The I_3^- ions formed by oxidation of I^- diffuse a short distance (<50 μm) through the electrolyte to the cathode, which is coated with a thin layer of platinum catalyst, where the regenerative cycle is completed by electron transfer to reduce I_3^- to I^-.

In order to quantitatively measure the efficacy of a DSSC, photocurrent−voltage (*I−V or J−V*) measurements under simulated sunlight and incident photon-to-current conversion efficiency (IPCE) under monochromatic light are important.

2.1.7.1. Photourrent−Voltage (*I−V*) Measurements:

A DSSC can be represented by an equivalent electric circuit shown in Figure 2.3, where, I_{ph} is the photocurrent, I_D the diode current, R_S is the series resistance (describes the resistances of the materials) and R_{sh} the shunt resistance.

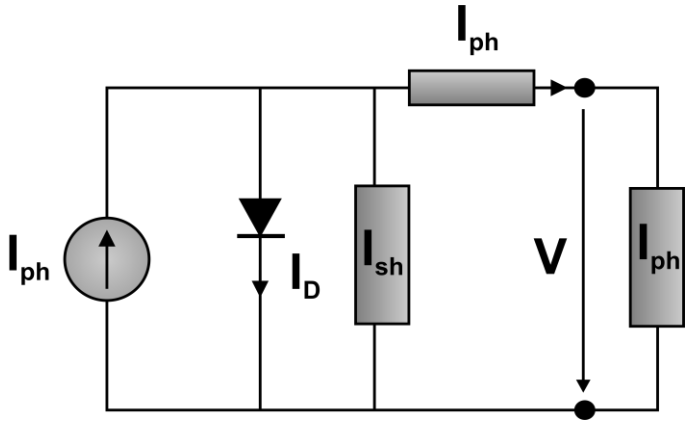

Figure 2.3. *Equivalent electric circuit of a DSSC.*

The semiconductor−metal interface is modelled as a Schottky diode. The equation of such a diode is:

$$I_D = I_S\left[\exp\left(\frac{V + I.R_S}{\eta.V_{th}}\right) - 1\right] \tag{2.22}$$

where, I_S is the saturation current, the ideality factor (typically varies from 1 to 2.4), and V_{th} is the thermal voltage:

$$V_{th} = \frac{k_B.T}{q} \tag{2.23}$$

The equation for the equivalent electric circuit in Figure 2.3 is:

$$I = I_{ph} - I_S \left[\exp\left(\frac{V + I.R_S}{\eta.V_{th}} \right) - 1 \right] - \frac{V + I.R_S}{R_{sh}} \qquad (2.24)$$

During the current–voltage measurements the following parameter will be determined:

A. Short-Circuit Current (I_{SC} or J_{SC}): The current equals the short-circuit current when the applied bias potential is zero:

$$I = I_{ph} - I_S \left[\exp\left(\frac{V + I.R_S}{\eta.V_{th}} \right) - 1 \right] \qquad (2.25)$$

B. Open-Circuit Voltage (V_{OC}): When no current is flowing through the cell the potential equals the open-circuit potential, using equation 2.25 one can find:

$$V_{OC} = \eta.V_{th} \ln\left(\frac{I_{ph}}{I_c} + 1 \right) \qquad (2.26)$$

C. Maximum Power Output (P_{max}): The power delivered from a solar cell at a certain potential equals the product of the current at this potential times the potential:

$$P(V) = I(V).V \qquad (2.27)$$

To obtain a graphic representation of the power one has to vary the potential between V_{OC} and 0. The point where the power is maximum (P_{max}) corresponds to the peak power point (PPP) for the $I–V$ curve. These are the optimal current and potential conditions (I_m, V_m) for the operating cell.

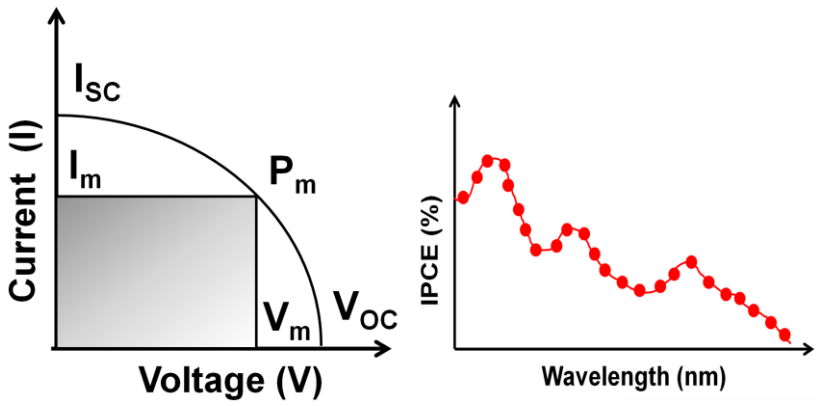

Figure 2.4. *Schematic representation of conventional I–V characteristic diagram (left). Typical IPCE characteristic diagram of a DSSC (right).*

D. Fill Factor (*FF*): The *FF* quantifies the quality of the solar cell, which is the ratio of actual power output ($V_m \times I_m$) versus its 'dummy' power output ($V_{OC} \times I_{SC}$) of a solar cell, as shown in equation 2.28:

$$FF = \frac{V_m I_m}{V_{OC} I_{SC}} \tag{2.28}$$

The *FF* lies between 0.7 and 0.85 for an efficient DSSC. These values are influenced by the values of the series and the shunt resistances. To obtain high *FF* values the shunt resistance has to be as small as possible and the series resistance as high as possible.

E. Photo-conversion Efficiency (η): The overall photo-conversion efficiency is given by the following equation:

$$\eta = \frac{V_m I_m}{P_{in}} = \frac{V_{OC} I_{SC} FF}{P_{in}} \tag{2.29}$$

It expresses the ratio of produced power and the incoming power (P_{in}). The experimental conditions have been fixed worldwide, in order to compare results coming from different places. An approximated power density value of 100 mW/cm^2, at air mass 1.5 global (AM 1.5 G) condition has been set for the incident solar radiation, and the temperature of the cell should be 25 °C. The AM is the ratio of the path-length of incoming sunlight through the atmosphere when the sun is at an angle to the zenith, and the path-length when the Sun is at the zenith.

2.1.7.2. Incident Photon-to-Current Conversion Efficiency (IPCE) Measurements: The sensitivity of a solar cell varies with the wavelength of the incoming light. The IPCE value corresponds to the photocurrent density produced in the external circuit under monochromatic illumination of the cell divided by the photon flux that strikes the cell. From such an experiment the IPCE as a function of wavelength can be calculated from:

$$IPCE(\lambda) = \frac{n_{electrons}(\lambda)}{n_{photons}(\lambda)} = \frac{I(\lambda)/e}{P_{in}(\lambda)/h.\nu} = \frac{I(\lambda)}{\lambda.P_{in}(\lambda)} . \frac{hc}{\nu} \tag{2.30}$$

$$\text{Or,} \qquad IPCE[\%] = 1240[V*nm] \times \frac{I[nA]}{\lambda[nm] \times I_p[nW]} \times 100 \tag{2.31}$$

where, $I(\lambda)$ is the current given by the cell at wavelength, $P_{in}(\lambda)$ the incoming power at wavelength λ, and I_p is the incident light power striking the device. IPCE values provide

practical information about the monochromatic quantum efficiencies of a solar cell. Figure 2.4 (right) shows a typical IPCE spectrum of a standard DSSC.

2.2. Systems:

2.2.1. Proteins: Two types of model proteins; Human Serum Albumin (HSA) and α-Chymotrypsin (CHT) have been used in our studies.

A. Human Serum Albumin (HSA): Serum albumins are multi-domain proteins forming the major soluble protein constituent (60% of the blood serum) of the circulatory system. HSA (molecular weight 66,479 Da) is a heart-shaped tridomain protein (Figure 2.5) with each domain comprising of two identical subdomains A and B with each domain depicting specific structural and functional characteristics. HSA having 585 amino acid residues assumes a solid equilateral triangular shape with sides ~80 Å and depth ~30 Å [25]. Its amino acid sequence comprises of 17 disulfide bridges distributed over all domains, one free thiol (Cys34) in the domain-I and a tryptophan residue (Trp214) in domain-IIA. About 67% of HSA is α-helical while the rest of the structure being turns and extended polypeptides. Each domain contains 10 principle helices (h1-h10). Subdomains A and B share a common motif that includes h1, h2, h3 and h4 for subdomain-A, and h7, h8, h9, h10 for subdomain-B. The non-existence of disulfidelinkage connecting h1 and h3 in subdomain-IA is an exception. HSA is engaged with various physiological functions involving maintenance of osmotic blood pressure, transportation of a wide variety of ligands in and out of the physiological system [26]. The protein binds various kinds of ligands including photosensitizing drugs. The principal binding regions are located in subdomains IIA and IIIA of which IIIA binding cavity is the most active one and binds digitoxin, ibuprofen and tryptophan [27]. Warfarin, however, occupies a single site in domain-IIA. It is known that HSA undergoes reversible conformational transformation with change in pH of the protein solution, which is very essential for picking up and releasing the drugs at sites of differing pH inside the physiological system. At normal pH (pH= 7), HSA assumes the normal form (N) which abruptly changes to fast migrating form (F) at pH values less than 4.3, as this form moves “fast” upon gel electrophoresis. Upon further reduction in pH to less than 2.7 the F-form changes to the fully extended form (E).

On the basic side of the normal pH (above pH = 8), the N-form changes to basic form (B) and above pH = 10, the structure changes to the aged form (A). Serum albumin undergoes an ageing process when stored at a low ionic strength at alkaline pH. The ageing process is catalysed by the free sulfhydryl group and involves sulfhydryl-disulfide interchange that results in the conservation of the sulfhydryl at its original position.

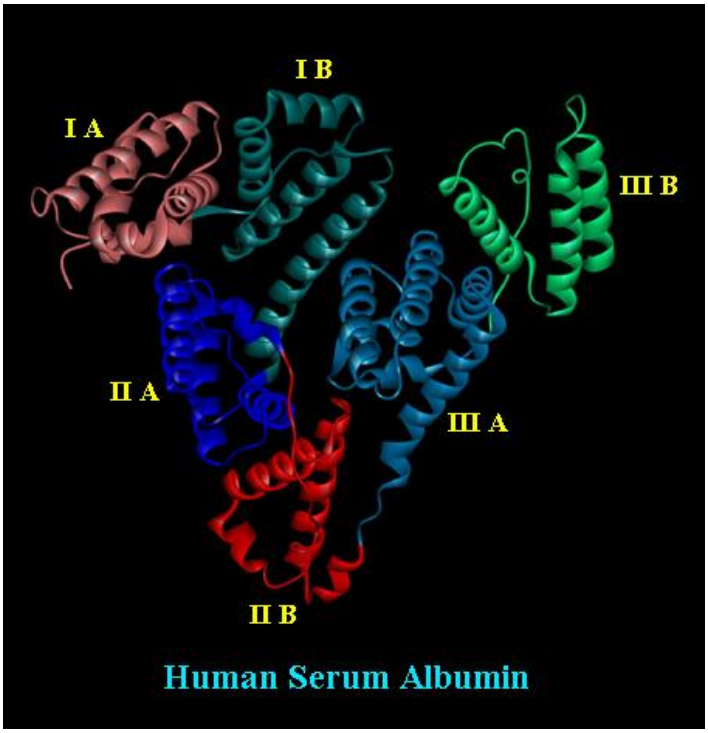

Figure 2.5. *X-ray crystallographic structure (PDB code: 1N5U) of human serum albumin depicting the different domains.*

B. α-Chymotrypsin (CHT): α-Chymotrypsin (CHT) (Figure 2.6) isolated from bovine pancreas is a member of the family serine endopeptidase (molecular weight of 25,191 Da) catalyzing the hydrolysis of peptides in the small intestine [28]. The three dimensional structure of CHT was solved by David Blow [29]. The molecule is a three dimensional ellipsoid of dimensions 51×40×40 Å and comprises of 245 amino acid residues. CHT contains several antiparallel *β*-pleated sheet regions and little α-helix. All charged groups are on the surface of the molecule except the *catalytic triad* of histidine57 (His57),

aspartate102 (Asp102) and serine195 (Ser195) which are essential for catalysis.

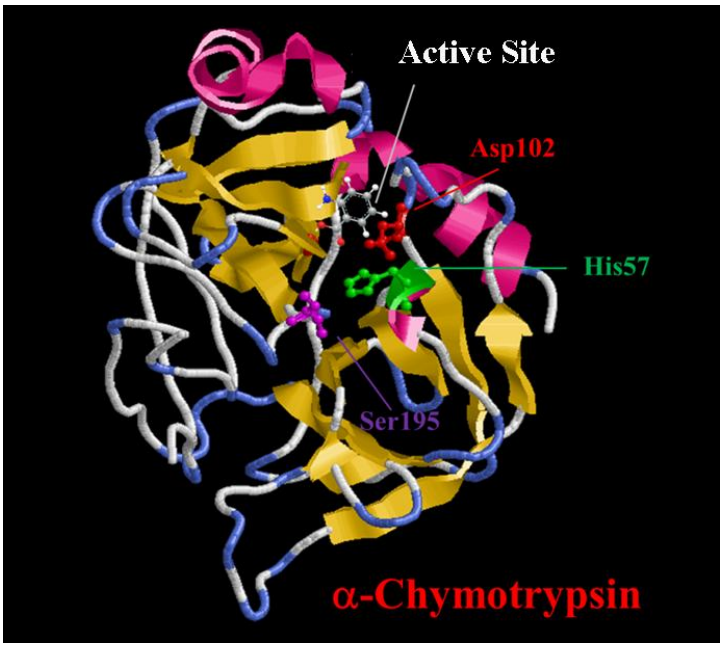

Figure 2.6. *X-ray crystallographic structure (PDB code: 2CHA) of CHT depicting the active catalytic triad (His57, Asp102 and Ser195).*

The Ser195 residue is hydrogen bonded to His57 residue, which in turn is H-bonded to β-carboxyl group of Asp102. An oxyanion hole is formed by amide nitrogen of Gly193 and Ser195. It is selective for hydrolysing peptide bonds on the carboxyl side of the aromatic side chains of tyrosine, tryptophan, and phenylalanine and of large hydrophobic residues such as methionine. It also catalyses the hydrolysis of ester bonds. CHT enhances the rate of peptide hydrolysis by a factor of 10^9. The reaction has two distinct phases, acylation and deacylation of the enzyme. Upon binding of the substrate, the hydroxyl group of the Ser195 attacks the carbonyl group of peptide bond to generate a tetrahedral intermediate. In this transient structure, the oxygen atom of the substrate now occupies the oxyanion hole. The acyl-enzyme intermediate now forms, assisted by proton donation of His57. The N-terminal portion is now released and replaced by water. The acyl-enzyme intermediate subsequently undergoes hydrolysis and the enzyme is regenerated.

2.2.2. Molecular Probes: In this section we will discuss about the different probe molecules that have been used in the course of study.

A. Methylene Blue (MB): MB is a heterocyclic aromatic chemical compound with molecular formula: $C_{16}H_{18}ClN_3S$. It has many uses in a range of different fields. At room-temperature it appears as a solid and is odourless and a dark green powder, which yields a blue solution when dissolved in water. They are widely used as model water contaminant [30]. Its structure is given in Figure 2.7. When dissolved in water, the UV-visible spectrum of MB showed three absorption maxima. The first band was observed at 246 nm and then 291 nm and more intensely 663 nm. The absorption maxima wavelength of MB (λ_{max} = 663 nm) was used for the analysis during decolorization of MB dye.

B. 2,5-Cyclohexadiene-1,4-dione (*p*-Benzoquinone, BQ): BQ (Figure 2.7) is a well-known probe for electron accepting and shuttling for any electron rich material/compound, which readily accepts electron and adapted to be resonance species hydroquinone [31-32]. Large doses could induce local irritation, clonic convulsions, decreased blood pressure and death due to paralysis of the medullary centres.

C. Bilirubin (BR): BR, the yellow-orange breakdown product of normal heme catabolism in mammalian systems, introduces great biological and diagnostic values [33]. Both antioxidant and toxic properties have been attributed to BR [34], which is normally conjugated with glucuronic acid and then excreted in the bile. However, when its conjugation with glucuronic acid is inhibited, as in neonatal jaundice and in hereditary forms of congenital jaundice, excess BR bind and deposit to various tissues, giving rise to severe hyperbilirubinemia and neurotoxicity. Phototherapy, the most effective treatment for jaundice to date, decreases the BR levels in the blood by changing the *ZZ*-BR isomer into water-soluble *ZE*-BR [35-37]. Because this reaction is readily reversible, equilibrium is established between native BR and the *ZE* isomer when BR is photoirradiated in a closed system. The second fastest reaction that occurs when BR is exposed to light is the production of lumirubin, a structural isomer of BR.

D. Di-tetrabutylammonium cis-bis(isothiocyanato)bis(2,2′-bipyridyl-4,4′-dicarboxylato)ruthenium(II) (N719): Metal complexes, in particular the Ru(II) complexes, have been investigated intensively for DSSC application because of their

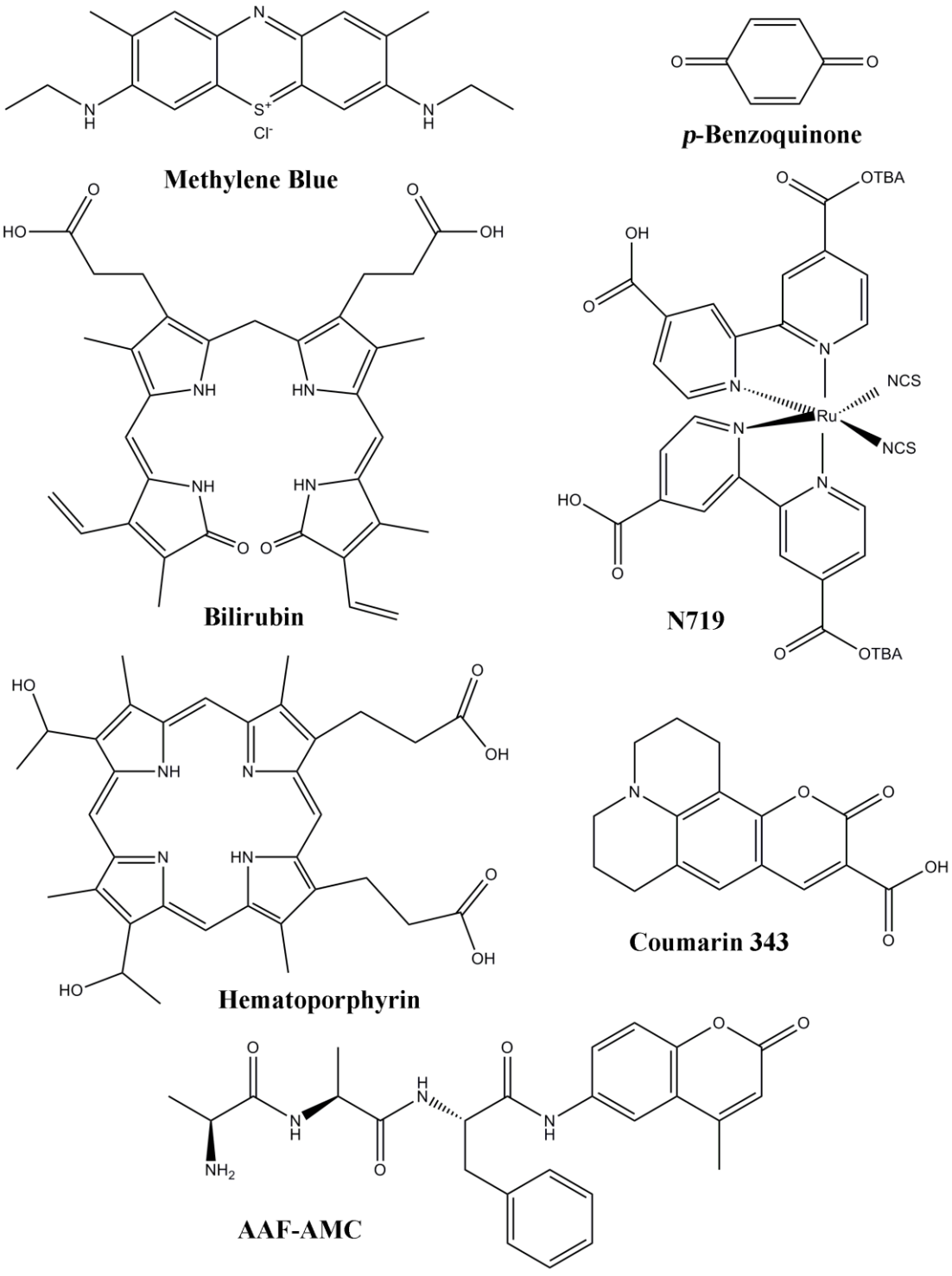

Figure 2.7. *Schematic representation of the fluorescent probes used.*

broad absorption spectra, large value of extinction coefficient (1.4×10^4 M^{-1} cm^{-1}) [38], and favorable photovoltaic properties. N719 (Figure 2.7) consists of a central Ru(II) ion with ancillary ligands having four anchoring groups (COOH). Light absorption in the visible part of the solar spectrum is due to a metal to ligand charge transfer (MLCT) process. The central metal ion is therefore a crucial part of the overall properties of the complexes. Ancillary ligands (bipyridines) can be tuned by different substituents (alkyl, aryl, heterocycle, etc.) to change the photophysical and electrochemical properties and thus improve the photovoltaic performance. Anchoring groups are employed to link the dye with the semiconductor and facilitate the injection of the excited electron into the conduction band of the semiconductor. One can modify any part of the complex to tune the energy levels of the MLCT states and to optimize electron injection and dye regeneration kinetics.

E. 8,13-Bis(1-hydroxyethyl)-3,7,12,17-tetramethyl-21H,23H-porphine-2,18-dipropionic acid (Hematoporphyrin, HP): Since the early 1960's, the hematoporphyrin derivative (HpD) has provided clinical investigators a sensitive means of diagnosis and a selective method for eradication of tumors [1,2]. Its emerging importance in photoradiation therapy is evidenced by research efforts directed at the fundamental problems related to the mechanism of photosensitization and the increasing clinical applications for cancer therapy. They are also found to be a good alternative for Ru(II)-based solar cell dyes.

F. Coumarin 343 (C343): C343 is an ideal system for studying electron transfer into metal oxides, as it is known to undergo fast electron injection [39-40] with ~80−90% efficiency [40-41]. C343 and its derivatives have been successfully used in organic DSSCs [42-44], where the carboxyl group of C343 binds directly to the metal ions on the surface of the nanoparticles [45]. They also have large extinction coefficient though absorption spectrum shows a sharp peak at ~442 nm (4.4×10^4 M^{-1} cm^{-1}) [46].

G. Ala-Ala-Phe-7-amido-4-methylcoumarin (AAF-AMC): AAF-AMC is a fluorescent aromatic tripeptide substrate (Figure 2.7) suitable for cleavage by serine protease. Its concentration is determined by using the extinction coefficient, $\varepsilon = 16$ mM^{-1} cm^{-1} at 325 nm. The rate of catalytic activity is determined by monitoring absorbance of cleaved product (7-amido-4-methylcoumarin) having $\varepsilon = 7.6$ mM^{-1} cm^{-1} at 370 nm in aqueous buffer solution [47].

References

[1] H. Spanggaard, F.C. Krebs, A Brief History of the Development of Organic and Polymeric Photovoltaics, *Sol. Energy Mater. Sol. Cells* 83 (2004) 125.

[2] Y. Shirota, H. Kageyama, Charge Carrier Transporting Molecular Materials and their Applications in Devices, *Chem. Rev.* 107 (2007) 953.

[3] H.B. Gray, J.R. Winkler, Electron Tunneling through Proteins, *Q. Rev. Biophys.* 36 (2003) 341.

[4] G. McLendon, R. Hake, Interprotein Electron Transfer, *Chem. Rev.* 92 (1992) 481.

[5] H. Bassler, Charge Transport in Disordered Organic Photoconductors: A Monte Carlo Simulation Study, *Phys. Status Solidi B* 175 (1993) 15.

[6] V.M. Kenkre, J.D. Andersen, D.H. Dunlap, C.B. Duke, Unified Theory of the Mobilities of Photoinjected Electrons in Naphthalene, *Phys. Rev. Lett.* 62 (1989) 1165.

[7] J.H. Bang, P.V. Kamat, Quantum Dot Sensitized Solar Cells. A Tale of Two Semiconductor Nanocrystals: CdSe and CdTe, *ACS Nano* 3 (2009) 1467.

[8] L. Stryer, Fluorescence Energy Transfer as a Spectroscopic Ruler, *Ann. Rev. Biochem.* 47 (1978) 819.

[9] J.R. Lakowicz, Principles of Fluorescence Spectroscopy, 2nd ed., Kluwer Academic/ Plenum, New York, 1999.

[10] M. Montalti, N. Zaccheroni, L. Prodi, N. O'Reilly, S.L. James, Enhanced Sensitized NIR Luminescence from Gold Nanoparticles via Energy Transfer from Surface-Bound Fluorophores, *J. Am. Chem. Soc.* 129 (2007) 2418.

[11] B.N.J. Persson, N.D. Lang, Electron-Hole Pair Quenching of Excited States Near a Metal, *Phys. Rev. B* 26 (1982) 5409.

[12] J. Gersten, A. Nitzan, Spectroscopic Properties of Molecules Interacting with Small Dielectric Particles, *J. Chem. Phys.* 75 (1981) 1139.

[13] D. Craig, T. Thirunamachandran, Molecular Quantum Electrodynamics, Academic Press, London, 1984.

[14] T.L. Jennings, M.P. Singh, G.F. Strouse, Fluorescent Lifetime Quenching near d = 1.5 nm Gold Nanoparticles: Probing NSET Validity, *J. Am. Chem. Soc.* 128 (2006) 5462.

[15] M.A.H. Muhammed, A.K. Shaw, S.K. Pal, T. Pradeep, Quantum Clusters of Gold Exhibiting FRET, *J. Phys. Chem. C* 112 (2008) 14324.

[16] A. Makhal, S. Sarkar, S.K. Pal, H. Yan, D. Wulferding, F. Cetin, P. Lemmens, Ultrafast Excited State Deactivation of Doped Porous Anodic Alumina Membranes, *Nanotechnology* 23 (2012) 305705.

[17] R. Beaulac, P.I. Archer, J.V. Rijssel, A. Meijerink, D.R. Gamelin, Exciton Storage by Mn^{2+} in Colloidal Mn^{2+} Doped CdSe Quantum Dots, *Nano Lett.* 8 (2008) 2949.

[18] T. Schmidt, M. Scheibner, L. Worschech, A. Forchel, T. Slobodskyy, L.W. Molenkamp, Sign Reversal and Light Controlled Tuning of Circular Polarization in Semimagnetic CdMnSe Quantum Dots, *J. Appl. Phys.* 100 (2006) 123109.

[19] R.N. Bhargava, D. Gallagher, Optical Properties of Manganese-Doped Nanocrystals of ZnS, *Phys. Rev. Lett.* 72 (1994) 416.

[20] J. Yu, H. Liu, Y. Wang, F.E. Fernandez, W. Jia, Irradiation-Induced Luminescence Enhancement Effect of ZnS:Mn^{2+} Nanoparticles in Polymer Films, *Opt. Lett.* 22 (1997) 913.

[21] A. Makhal, S. Sarkar, S.K. Pal, Protein-Mediated Synthesis of Nanosized Mn-Doped ZnS: A Multifunctional, UV-Durable Bio-Nanocomposite, *Inorg. Chem.* 51 (2012) 10203.

[22] B. O'Regan, M. Grätzel, A Low-Cost, High-Efficiency Solar Cell Based on Dye-Sensitized Colloidal TiO_2 Films, *Nature* 353 (1991) 737.

[23] M. Grätzel, Conversion of Sunlight to Electric Power by Nanocrystalline Dye-Sensitized Solar Cells, *J. Photochem. and Photobiol. A* 164 (2004) 3.

[24] M. Grätzel, Photoelectrochemical cells, *Nature* 414 (2001) 338.

[25] X.M. He, D.C. Carter, Atomic Structure and Chemistry of Human Serum Albumin, *Nature* 358 (1992) 209.

[26] J.T. Peters, All about Albumin: Biochemistry, Genetics, and Medical Applications, in, Academic Press, San Diego, CA, 1996.

[27] J. Ghuman, P.A. Zunszain, I. Petitpas, A.A. Bhattacharya, M. Otagiri, S. Curry, Structural Basis of the Drug-binding Specificity of Human Serum Albumin, *J. Mol. Biol.* 353 (2005) 38.

[28] D.L. Nelson, M.M. Cox, Lehninger Principles of Biochemistry, Worth Publishers, New York, 2000.

[29] J.J. Birktoft, D.M. Blow, The Structure of Crystalline Alpha-Chymotrypsin, V. The Atomic Structure of Tosyl-Alpha-Chymotrypsin at 2 Angstroms Resolution, *J. Mol. Biol.* 68 (1972) 187.

[30] N. Xu, Z. Shi, Y. Fan, J. Dong, J. Shi, M.Z.C. Hu, Effects of Particle Size of TiO_2 on Photocatalytic Degradation of Methylene Blue in Aqueous Suspensions, *Ind. Eng. Chem. Res.* 38 (1999) 373.

[31] C. Burda, T.C. Green, S. Link, M.A. El-Sayed, Electron Shuttling Across the Interface of CdSe Nanoparticles Monitored by Femtosecond Laser Spectroscopy, *J. Phys. Chem. B* 103 (1999) 1783.

[32] A. Makhal, P. Kumar, P. Lemmens, S.K. Pal, Manipulation of Spontaneous Emission Dynamics of Organic Dyes in the Porous Silicon Matrix, *J. Fluorescence* 20 (2010) 283.

[33] J.D. Ostrow, Bile Pigments and Jaundice: Molecular, Metabolic and Medical Aspects, Marcel Dekker, New York, 1986.

[34] R. Stocker, A.N. Glazer, B.N. Ames, Antioxidant Activity of Albumin-Bound Bilirubin, *Proc. Natl. Acad. Sci. U.S.A.* 84 (1987) 5918.

[35] D.A. Lightner, A.F. McDonagh, Molecular Mechanisms of Phototherapy for Neonatal Jaundice, *Acc. Chem. Res.* 17 (1984) 417.

[36] A.A. Lamola, W.E. Blumberg, R. McClead, A. Fanaroff, Photoisomerized Bilirubin in Blood from Infants Receiving Phototherapy, *Proc. Natl. Acad. Sci. U.S.A.* 78 (1981) 1882.

[37] S.E. Braslavsky, A.R. Holzwarth, K. Schaffner, Solution Conformations, Photophysics, and Photochemistry of Bile Pigments; Bilirubin and Biliverdin, Dimethyl Esters and Related Linear Tetrapyrroles, *Angew. Chem. Int. Ed.* 22 (1983) 656.

[38] M.K. Nazeeruddin, F.D. Angelis, S. Fantacci, A. Selloni, G. Viscardi, P. Liska, S. Ito, B. Takeru, M. Grätzel, Combined Experimental and DFT-TDDFT Computational Study of Photoelectrochemical Cell Ruthenium Sensitizers, *J. Am. Chem. Soc.* 127 (2005) 16835.

[39] N.A. Anderson, T. Lian, Ultrafast Electron Transfer at the Molecule-Semiconductor Nanoparticle Interface, *Ann. Rev. Phys. Chem.* 56 (2005) 491.

[40] J.M. Rehm, G.L. McLendon, Y. Nagasawa, K. Yoshihara, J. Moser, M. Grätzel, Femtosecond Electron-Transfer Dynamics at a Sensitizing Dye−Semiconductor (TiO_2) Interface, *J. Phys. Chem.* 100 (1996) 9577.

[41] O. Enea, J. Moser, M. Grätzel, Achievement of Incident Photon to Electric Current Conversion Yields Exceeding 80% in the Spectral Sensitization of Titanium Dioxide by Coumarin, *J. Electroanal. Chem.* 259 (1989) 59.

[42] K. Hara, K. Sayama, Y. Ohga, A. Shinpo, S. Suga, H. Arakawa, A Coumarin-Derivative Dye Sensitized Nanocrystalline TiO_2 Solar Cell having a High Solar-Energy Conversion Efficiency up to 5.6%, *Chem. Commun.* (2001) 569.

[43] X. Zhang, J.J. Zhang, Y.Y. Xia, Molecular Design of Coumarin Dyes with High Efficiency in Dye-Sensitized Solar Cells, *J. Photochem. Photobiol. A* 194 (2008) 167.

[44] V. Kandavelu, H.S. Huang, J.L. Jian, T.C.K. Yang, K.L. Wang, S.T. Huang, Novel Iminocoumarin Dyes as Photosensitizers for Dye-Sensitized Solar Cell, *Sol. Energy* 83 (2009) 574.

[45] W.R. Duncan, O.V. Prezhdo, Theoretical Studies of Photoinduced Electron Transfer in Dye-Sensitized TiO_2, *Annu. Rev. Phys. Chem.* 58 (2007) 143.

[46] G.A. Reynolds, K.H. Drexhage, New Coumarin Dyes with Rigidized Structure for Flashlamp-Pumped Dye Lasers, *Optics Commun.* 13 (1975) 222.

[47] R. Biswas, S.K. Pal, Caging Enzyme Function: Alpha-Chymotrypsin in Reverse Micelle, *Chem. Phys. Lett.* 387 (2004) 221.

Chapter 3

Instrumentation and Sample Preparation

In this chapter the details of instrumental setup and sample preparation techniques used in our studies have been described.

3.1. Instrumental Setups:

3.1.1. Steady-state UV-vis Absorption and Emission Measurement: Steady-state UV-vis absorption and emission spectra of the probe molecules were measured with Shimadzu

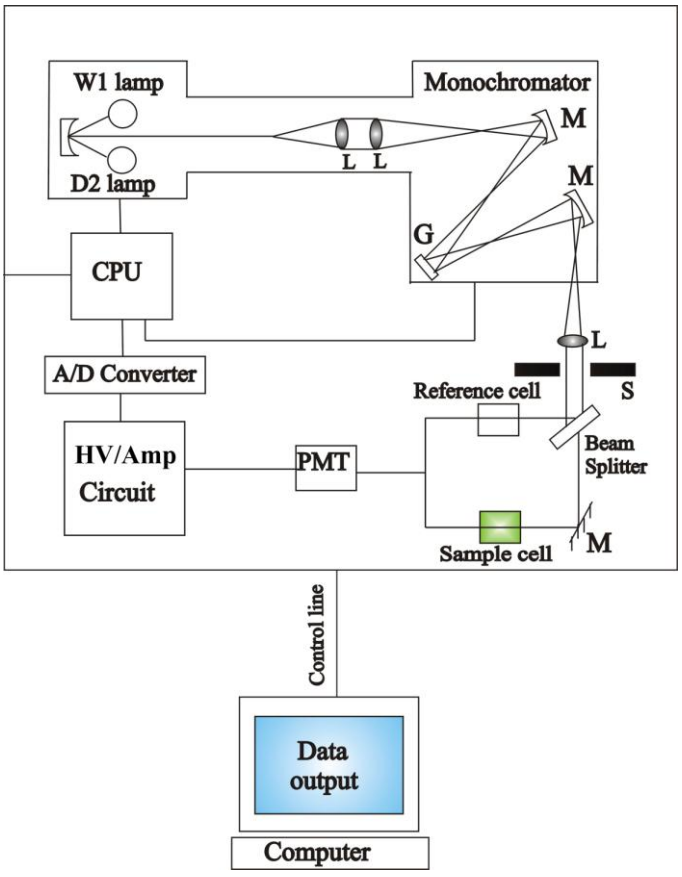

Figure 3.1. *Schematic ray diagram of an absorption spectrophotometer. Tungsten halogen (W1) and Deuterium lamps (D2) are used as light sources in the visible and UV regions, respectively. M, G, L, S, PMT designate mirror, grating, lens, shutter and photomultiplier tube, respectively. CPU, A/D converter and HV/Amp indicate central processing unit, analog to digital converter and High-voltage/Amplifier circuit, respectively.*

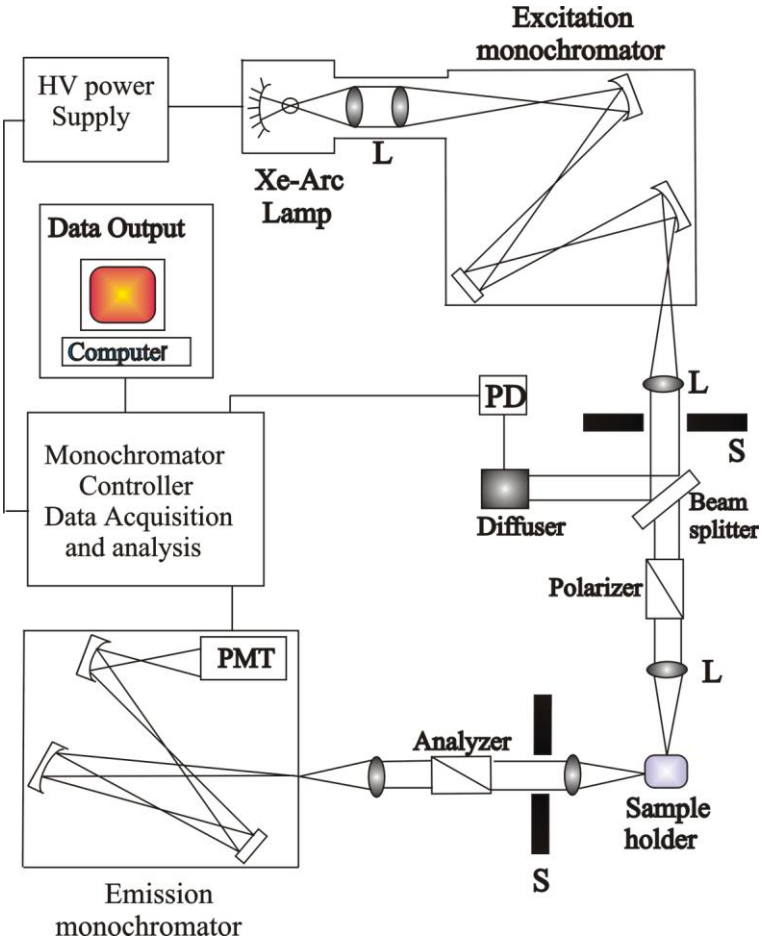

Figure 3.2. *Schematic ray diagram of an emission spectrofluorimeter. M, G, L, S, PMT and PD represent mirror, grating, lens, shutter, photomultiplier tube and reference photodiode, respectively.*

UV-2450 spectrophotometer and Jobin Yvon Fluoromax-3 fluorimeter, respectively. Schematic ray diagrams of these two instruments are shown in Figures 3.1 and 3.2.

3.1.2. Circular Dichroism (CD) Measurement: CD is a form of spectroscopy based on the differential absorption of left and right-handed circularly polarized light. It can be used to determine the structure of macromolecules (including the secondary structure of proteins and the handedness of DNA). The CD measurements were done in a JASCO spectropolarimeter with a temperature controller attachment (Peltier) (Figure 3.3). The CD spectra were acquired using a quartz cell of 1 cm path length. For proteins, the typical concentration used for CD measurements were within 10 μM. The secondary structural data of the CD spectra were analyzed using CDNN deconvolution program.

The working principle of CD measurement is as follows: when a plane polarized light passes through an optically active substance, not only do the left (L) and right (R) circularly polarized light rays travel at different speeds, $c_L \neq c_R$, but these two rays are absorbed to different extents, i.e. $A_L \neq A_R$. The difference in the absorbance of the left and right circularly polarized light, i.e., $\Delta A = A_L - A_R$, is defined as circular dichroism [1]. CD spectroscopy follows Beer-Lambert law. If I_0 is the intensity of light incident on the cell, and I, that of emergent light, then absorbance is given by,

$$A = \log_{10}\left(\frac{I_0}{I}\right) = \varepsilon c l \tag{3.1}$$

where, A is proportional to concentration (c) of optically active substance and optical path length (l). If 'c' is in moles/L and 'l' is in cm, then ε is called the molar absorptivity or molar extinction coefficient. In an optically active medium, two absorbances, A_L and A_R are considered, where $A_L = \log_{10}(I_0/I_L)$ and $A_R = \log_{10}(I_0/I_R)$. At the time of incidence on the sample, intensity of left and right circularly polarized light are same, i.e. $I_0 = I_L = I_R$. Any dicrograph passes periodically changing light through the medium, oscillating between left and right circular polarization, and the difference in absorbances are recorded directly [2].

$$\Delta A = A_L - A_R = \log_{10}\left(\frac{I_0}{I_L}\right) - \log_{10}\left(\frac{I_0}{I_R}\right) = \log_{10}\left(\frac{I_R}{I_L}\right) \tag{3.2}$$

or
$$\Delta A = (\Delta\varepsilon) c l \tag{3.3}$$

As seen from equation 3.2, I_0 does not appear in this final equation, so there is no need for a reference beam. The instruments are, therefore, of single beam type. Most of the CD spectropolarimeters, although they measure differential absorption, produce a CD spectrum in units of ellipticity (θ) expressed in millidegrees versus λ, rather than ΔA versus λ. The relation between ellipticity and CD is given by,

$$\theta = \frac{2.303 \times 180 \times (A_L - A_R)}{4\pi} \text{ degrees} \tag{3.4}$$

To compare the results from different samples, optical activity is computed on a molar or residue basis. Molar ellipticity, $[\theta]$ is defined as,

$$[\theta] = \frac{\theta}{cl} \tag{3.5}$$

where, 'θ' is in degrees, 'c' is in moles/L and 'l' is in cm. The unit of molar ellipticity is deg M^{-1} cm^{-1}.

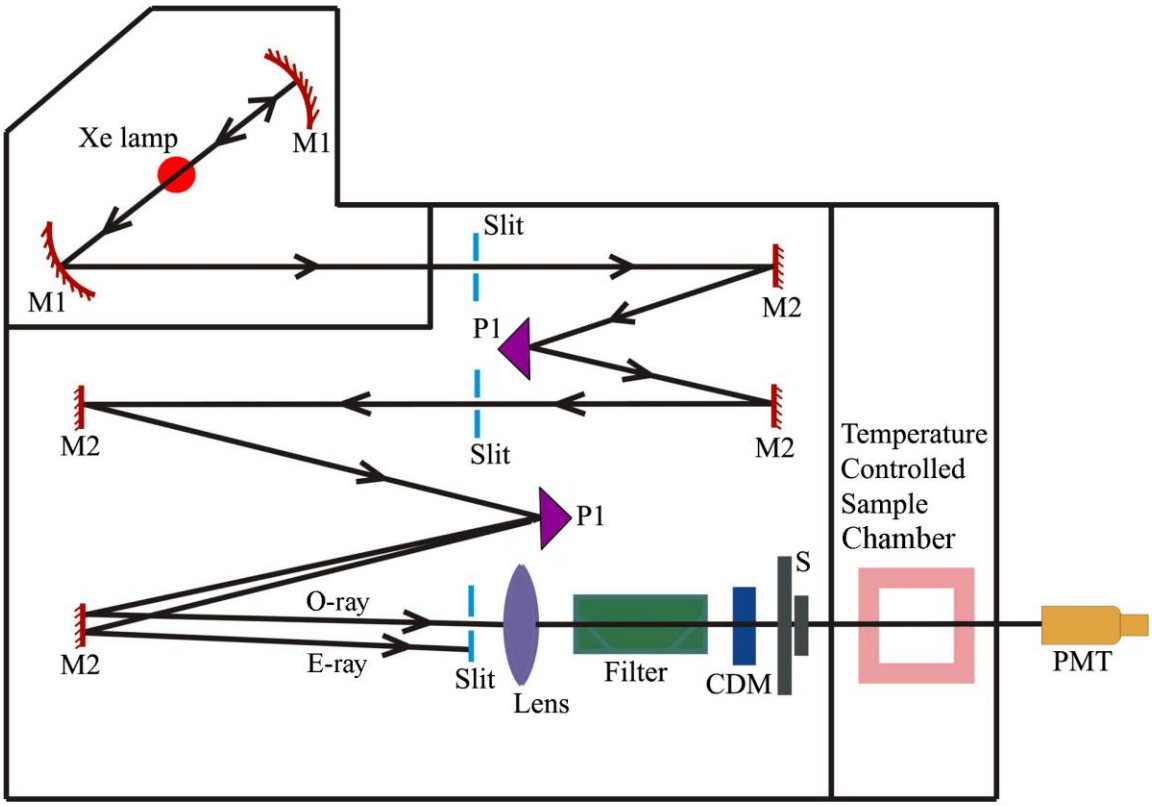

Figure 3.3. *Schematic ray diagram of a Circular Dichroism (CD) spectropolarimeter. M1, M2, P1, S, PMT, CDM, O-ray and E-ray represent concave mirror, plain mirror, reflecting prism, shutter, photomultiplier tube, CD-modulator, ordinary ray and extraordinary ray, respectively.*

3.1.3. Time-Correlated Single Photon Counting (TCSPC) Technique: All the picosecond-resolved fluorescence transients were recorded using TCSPC technique. The schematic block diagram of a TCSPC system is shown in Figure 3.4. TCSPC setup from Edinburgh instruments, U.K., was used during fluorescence decay acquisitions. The instrument response functions (IRFs) of the laser sources at different excitation wavelengths varied between 60 ps to 100 ps. The fluorescence from the sample was detected by a photomultiplier after dispersion through a grating monochromator [3]. For all transients, the polarizer in the emission side was adjusted to be at 54.7° (magic angle) with respect to the polarization axis of excitation beam.

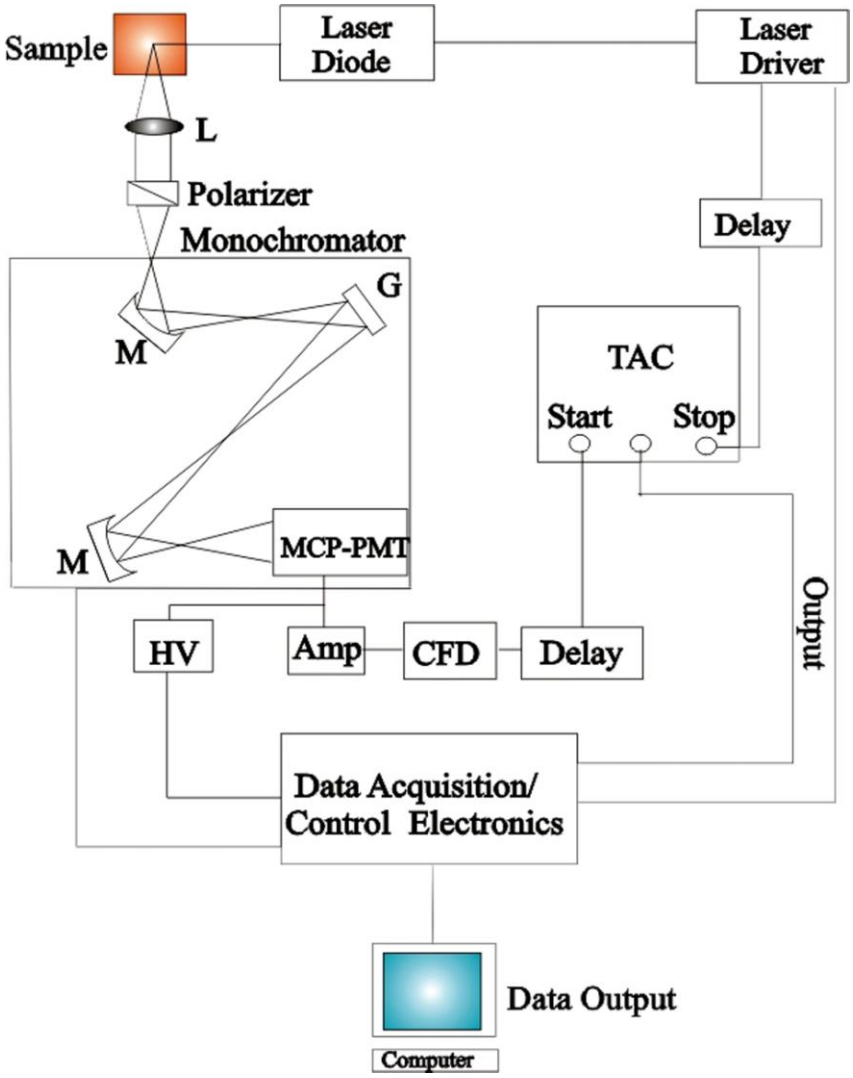

Figure 3.4. *Schematic ray diagram of a time correlated single photon counting (TCSPC) spectrophotometer. A signal from microchannel plate photomultiplier tube (MCP-PMT) is amplified (Amp) and connected to start channel of time to amplitude converter (TAC) via constant fraction discriminator (CFD) and delay. The stop channel of the TAC is connected to the laser driver via a delay line. L, M, G and HV represent lens, mirror, grating and high voltage source, respectively.*

3.1.4. Femtosecond-Resolved Fluorescence Upconversion Technique: The femtosecond-resolved fluorescence spectroscopy was carried out using a femtosecond upconversion setup (FOG 100, CDP, Figure 3.5) in which the sample was excited at 375 nm, using the second harmonic of a mode-locked Ti-sapphire laser with 80 MHz repetition rate (Tsunami, Spectra Physics), pumped by 10 W Millennia (Spectra Physics). The fundamental beam was passed through a periscopic arrangement (*P*) (Figure 3.5) before getting frequency doubled in a nonlinear crystal, NC1 (1 mm BBO, $\theta = 25°$, $\phi = 90°$). This

beam was then sent into a rotating circular cell of 1 mm thickness containing the sample via a dichroic mirror (DM), a polarizer and a mirror (M6). The resulting fluorescence emission was collected, refocused with a pair of lenses (L4 and L5) and mixed with the fundamental beam (750 nm) coming through a delay line to yield an upconverted photon signal in a nonlinear crystal, NC2 (0.5 mm BBO (β-barium borate), $\theta = 10°$, $\phi = 90°$). The upconverted light was dispersed in a double monochromator and detected using photon counting electronics. A cross-correlation function obtained using the Raman scattering from water displayed a full width at half maximum (FWHM) of 165 fs. The femtosecond fluorescence decays were fitted using a Gaussian shape for the exciting pulse.

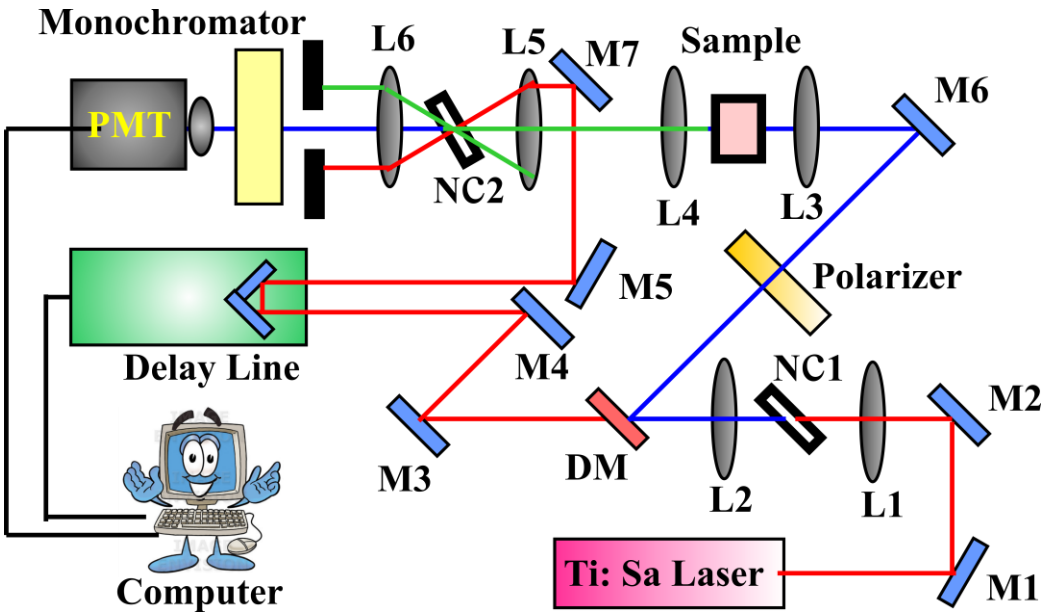

Figure 3.5. *Schematic diagram of a femtosecond fluorescence upconversion experimental setup. A BBO crystal (NC1) is used for second harmonic generation, which provides a pump beam in the UV region. Another BBO crystal (NC2) generates the upconversion signal of pump and probe beams. L and M indicate lenses and mirrors, respectively. M1-M2 and M3, M4, M5, M7 are IR mirrors whereas M6 is a UV mirror. DM is dichroic mirror, and P is periscope.*

3.1.5. Transmission Electron Microscopy (TEM): A JEOL JEM-2100 high-resolution TEM (HRTEM) (Figure 3.6) equipped with an energy dispersive X-ray (EDAX) spectrometer was used to characterize the microscopic structures of samples and to analyze their elemental composition. The sizes of the nanoparticles were determined from the TEM

images obtained at 200 kV. Samples for TEM were prepared by placing a drop of the colloidal solution on a carbon-coated copper grid and allowing the film to evaporate overnight at room-temperature.

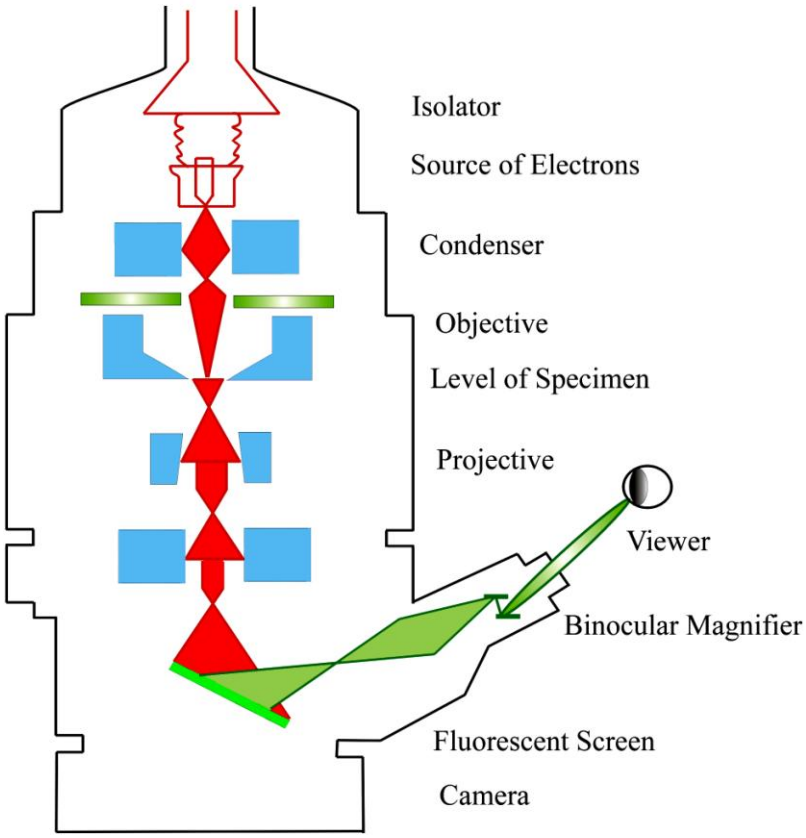

Figure 3.6. *Schematic diagram of a typical transmission electron microscope (TEM). After the transmission of electron beam through a specimen, the magnified image is formed either in the fluorescent screen or can be detected by a CCD camera.*

3.1.6. Scanning Electron Microscopy (SEM): Surface characteristics of Porous silicon samples were done by scanning electron microscope FE (field emission)-SEM; JEOL. Ltd., JSM-6500F. A Electron-gun is attached to SEM and the electrons from filament triggered by 0 KV to 30 KV voltages. These electrons go first through a condenser lens and then through an objective lens, then through an aperture and finally reach to the specimen. The high energy electrons go a bit in the sample and back again give secondary

electrons. The signal from secondary electrons are detected by detector and amplified. The ray diagram of the SEM setup is shown in Figure 3.7.

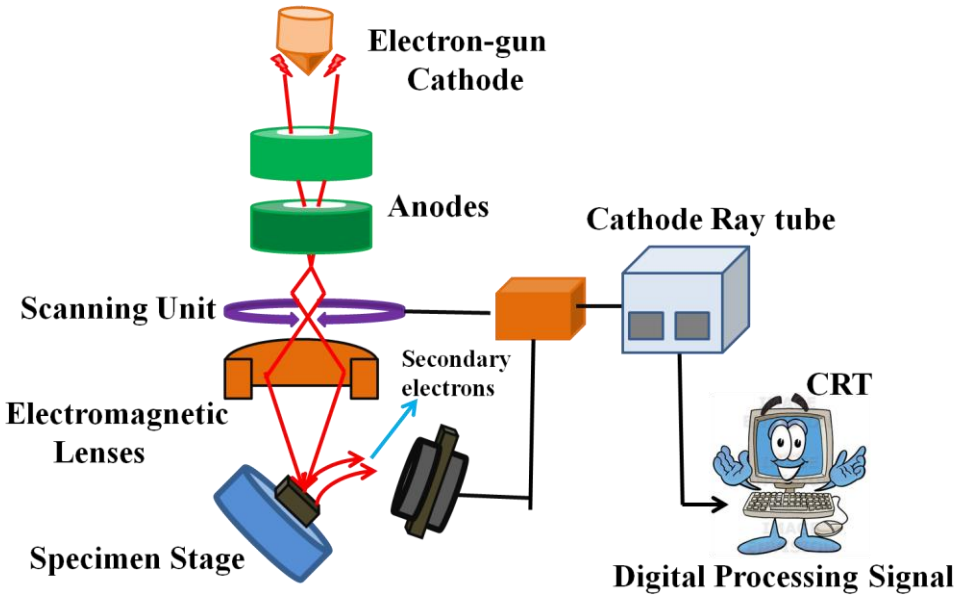

Figure 3.7. *Schematic diagram of typical Scanning Electron Microscope (SEM).*

3.1.7. Thermogravimetric-Differential Thermal Analyzer (TG-DTA) Setup: The thermogravimetric (TG) analysis was carried out using Diamond thermogravimetric (TG)-differential thermal analyzer (DTA) from Perkin Elmer. The TG determines the weight change of a sample whereas the DTA measures the change in temperature between a sample and the reference as a function of temperature and/or time. The schematic of the TG-DTA setup is shown in Figure 3.8. When a weight change occurs on the sample side, the beam holding the platinum pans is displaced. This movement is detected optically and the driving coil current is changed to return the displacement to zero. The detected driving coil current change is proportional to the sample weight change and the output is the TG signal. The DTA detects the temperature difference between the sample holder and the reference holder using the electromotive force of thermocouples, which are attached to the holders. This difference is measured as the DTA signal.

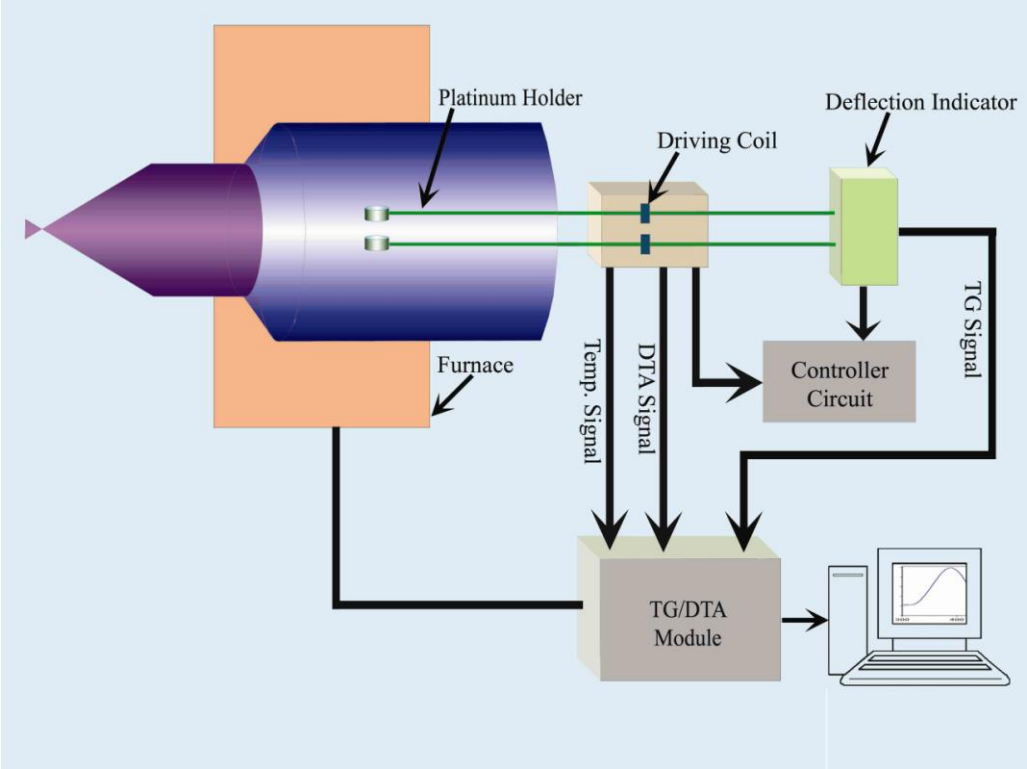

Figure 3.8. *The schematic representation of TG-DTA setup.*

3.1.8. X-ray Diffraction (XRD) Measurement: XRD is a popular and powerful technique for determining crystal structure of crystalline materials. By examining the diffraction pattern, one can identify the crystalline phase of the material. Small angle scattering is useful for evaluating the average interparticle distance while wide-angle diffraction is useful for refining the atomic structure of nanoclusters. The widths of the diffraction lines are closely related to strain and defect size and distribution in nanocrystals. As the size of the nanocrystals decreases, the line width is broadened due to loss of long-range order relative to the bulk. This XRD line width can be used to estimate the size of the particle by using the Debye-Scherrer formula,

$$D = \frac{0.9\lambda}{\beta \cos\theta} \tag{3.6}$$

where, D is the nanocrystal diameter, λ is the wavelength of light, β is the full-width half-maximum (fwhm) of the peak in radians, and θ is the Bragg angle. XRD measurements were performed on a PANalytical XPERT-PRO diffractometer (Figure 3.9) equipped with

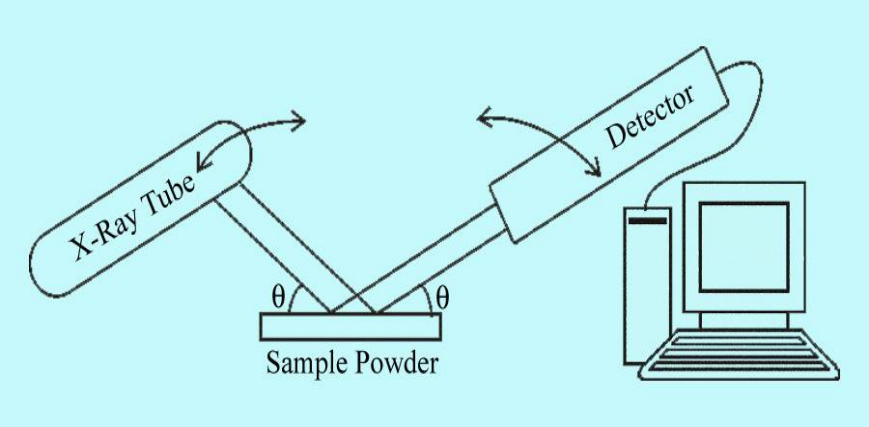

Figure 3.9. *Schematic diagram of X-ray Diffraction (XRD) instrument. By varying the angle θ, the Bragg's Law conditions, nλ=2dsinθ are satisfied by different d-spacings in polycrystalline materials. Plotting the angular positions and intensities of the resultant diffracted peaks of radiation produces a pattern, which is characteristic of the sample.*

CuKα radiation (λ = 1.5418 Å at 40 mA, 40 kV). XRD patterns were obtained by employing a scanning rate of 0.02° s^{-1} in the 2θ range from 15° to 75°.

3.1.9. Fourier Transform Infrared (FTIR) Measurement: FTIR spectroscopy is a technique that can provide very useful information about functional groups in a sample. An infrared spectrum represents the fingerprint of a sample with absorption peaks which correspond to the frequencies of vibrations between the bonds of the atoms making up the material. Because each different material is a unique combination of atoms, no two compounds produce the exact same infrared spectrum. Therefore, infrared spectroscopy can result in a positive identification (qualitative analysis) of every different kind of material. In addition, the size of the peaks in the spectrum is a direct indication of the amount of material present. The two-beam Michelson interferometer is the heart of FTIR spectrometer. It consists of a fixed mirror (M4), a moving mirror (M5) and a beam-splitter (BS1), as illustrated in Figure 3.10. The beam-splitter is a laminate material that reflects and transmits light equally. The collimated IR beam from the source is partially transmitted to the moving mirror and partially reflected to the fixed mirror by the beam-splitter. The two IR beams are then reflected back to the beam-splitter by the mirrors. The detector then sees the transmitted beam from the fixed mirror and reflected beam from the moving mirror, simultaneously. The two combined beams interfere constructively or destructively depending on the wavelength of the light (or frequency in wavenumbers) and

the optical path difference introduced by the moving mirror. The resulting signal is called an interferogram which has the unique property that every data point (a function of the moving mirror position) which makes up the signal has information about every infrared frequency which comes from the source. Because the analyst requires a frequency spectrum (a plot of the intensity at each individual frequency) in order to make identification, the measured interferogram signal cannot be interpreted directly. A means of "decoding" the individual frequencies is required. This can be accomplished *via* a well-known mathematical technique called the Fourier transformation. This transformation is performed by the computer which then presents the user with the desired spectral

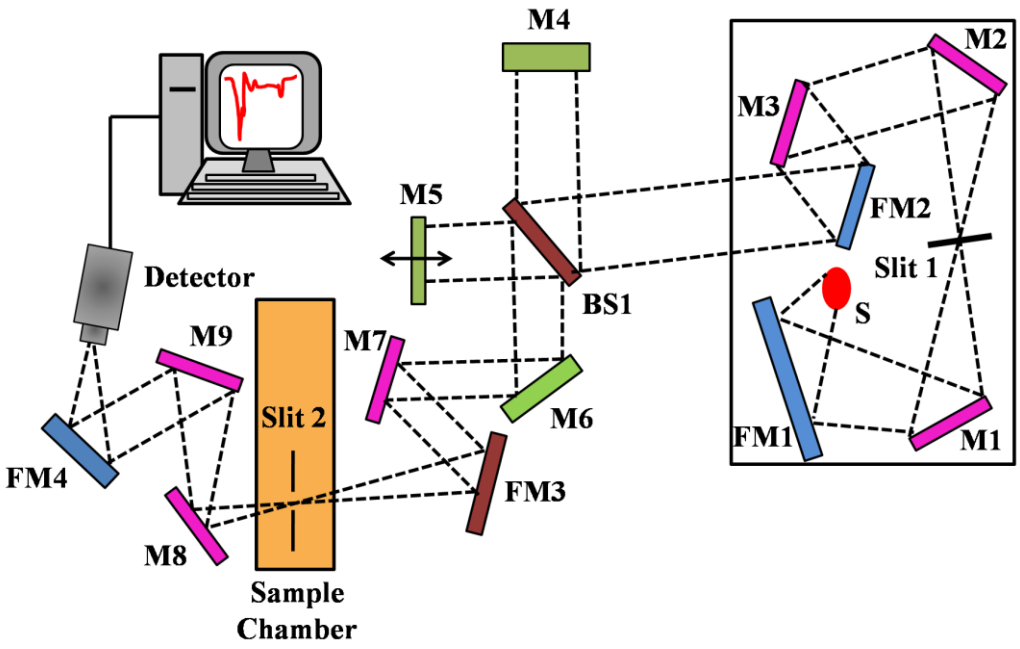

Figure 3.10. *Schematic of Fourier Transform Infrared (FTIR) spectrometer. It is basically a Michelson interferometer in which one of the two fully-reflecting mirrors is movable, allowing a variable delay (in the travel-time of the light) to be included in one of the beams. M, FM and BS1 represent the mirror, focussing mirror and beam splitter, respectively. M5 is a moving mirror.*

information for analysis. FTIR measurements were performed on a JASCO FTIR-6300 spectrometer (transmission mode). For the FTIR measurements, powdered QD samples were mixed with KBr powder and pelletized. The background correction was made using a reference blank of KBr pellet.

3.1.10. Laser Raman Spectroscopy: Raman spectroscopy is a useful technique for the identification of a wide range of substances− solids, liquids, and gases. It is a straightforward, non-destructive technique requiring no sample preparation. Raman spectroscopy involves illuminating a sample with monochromatic light and using a spectrometer to examine light scattered by the sample.

At the molecular level photons can interact with matter by absorption or scattering processes. Scattering may occur either elastically, or inelastically. The elastic process is termed Rayleigh scattering, whilst the inelastic process is termed Raman scattering. The electric field component of the scattering photon perturbs the electron cloud of the molecule and may be regarded as exciting the system to a 'virtual' state. Raman scattering occurs when the system exchanges energy with the photon, and the system subsequently decays to vibrational energy levels above or below that of the initial state. The frequency shift corresponding to the energy difference between the incident and scattered photon is termed the Raman shift. Depending on whether the system has lost or gained vibrational energy, the Raman shift occurs either as an up or down-shift of the scattered photon frequency relative to that of the incident photon. The down-shifted and up-shifted components are called, respectively, the Stokes and anti-Stokes lines. A plot of detected number of photons versus Raman shift from the incident laser energy gives a Raman spectrum. Different materials have different vibrational modes, and therefore characteristic Raman spectra. This makes Raman spectroscopy a useful technique for material identification. There is one important distinction to make between the Raman spectra of gases and liquids, and those taken from solids− in particular, crystals. For gases and liquids it is meaningful to speak of the vibrational energy levels of the individual molecules which make up the material. Crystals do not behave as if composed of molecules with specific vibrational energy levels, instead the crystal lattice undergoes vibration. These macroscopic vibrational modes are called phonons.

In modern Raman spectrometers (LabRAM HR, Jobin Yvon), lasers are used as a photon source due to their highly monochromatic nature, and high beam fluxes (Figure 3.11). This is necessary as the Raman effect is weak, typically the Stokes lines are ~10^5 times weaker than the Rayleigh scattered component. In the visible spectral range, Raman

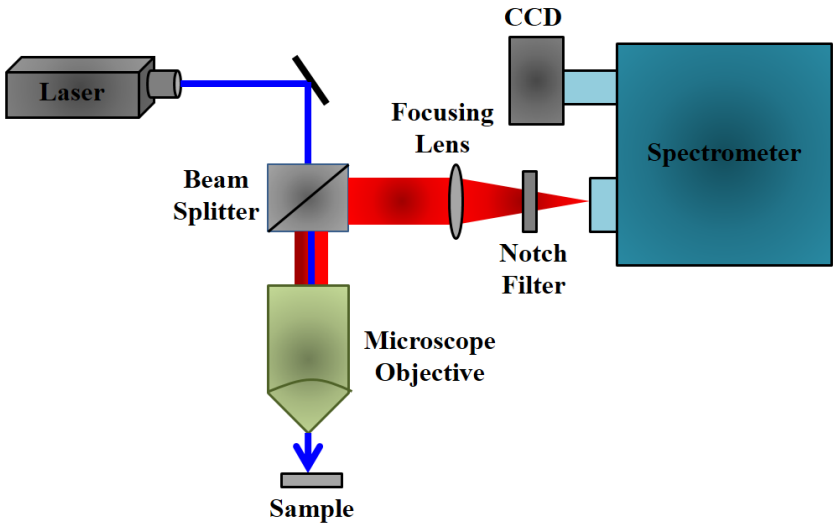

Figure 3.11. *Schematic diagram of a Raman spectrometer is shown.*

spectrometers use notch filters to cut out the signal from a very narrow range centred on the frequency corresponding to the laser radiation. Most Raman spectrometers for material characterization use a microscope to focus the laser beam to a small spot (<1−100 μm diameter). Light from the sample passes back through the microscope optics into the spectrometer. Raman shifted radiation is detected with a charge-coupled device (CCD) detector, and a computer is used for data acquisition and curve fitting. These factors have helped Raman spectroscopy to become a very sensitive and accurate technique.

3.1.11. Water Contact Angle (WCA) Measurements: WCA typically quantifies the wettability of a solid surface by water. A solid surface with high surface energy shows spreading of water with a small WCA (< 90°) and thus called hydrophilic surface. A lower surface energy of a solid shows WCA greater than 90° and called as hydrophobic surface. The WCA measurement thus provides a qualitative estimation on how the surface charges on the solid interacts with the liquid.

The WCA of nanomaterials used in this thesis work was measured by using a water contact angle measurement machine developed in our laboratory (as shown in Figure 3.12). A water droplet of volume 10 μL was dropped on the surface of the nanomaterials and the image of the water droplet was then taken with the help of a microscopic video-camera

attached to a computer. The contact angle was then measured by ImageJ software

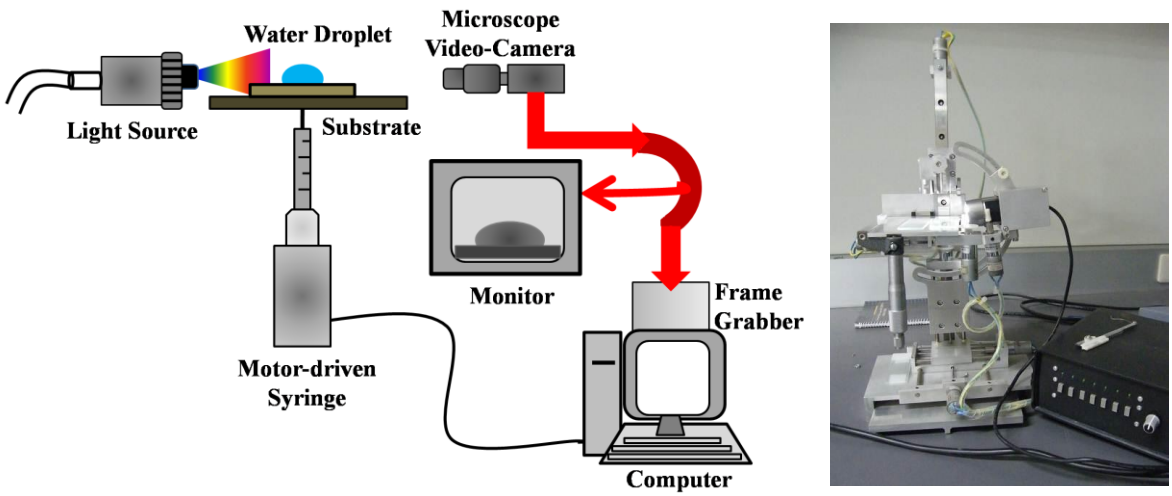

Figure 3.12. *Schematic and the photograph of the water contact angle (WCA) measurement setup.*

and to minimize the error in measurements, the WCA was recorded in 5 different areas on the same sample under the same conditions and finally their average was taken.

3.1.12. Solar Cell Characterization: The characterization of DSSCs and QDSSCs involves the electrical current−voltage ($I-V$) characteristics and incident photon to current conversion efficiency (IPCE) measurements. The $I-V$ characteristics of the solar cells were measured at calibrated 1 sun illumination with intensity 100 mW/cm^2. A small beam solar simulator (SF 150) from Sciencetech equipped with a xenon arc lamp and an air mass (AM) 1.5 filter was used to generate the solar spectrum that was used as the light source for the solar cells. The electrical circuit used to measure the $I-V$ characteristics of the solar cells is shown in Figure 3.13. A Keithley 617 programmable electrometer was programmed with labview software to act as both voltage supplier and current sensing unit to acquire the $I-V$ characteristics of the solar cells.

The short-circuit current (I_{SC}) and open-circuit voltage (V_{OC}) of the solar cells were determined from their respective $I-V$ characteristic curves. The fill factor (FF) and efficiency (η) of the solar cells were calculated by using equation 2.28 and 2.29, respectively. The IPCE of the DSSCs and QDSSCs were measured by using a Czerny-Turner monochromator with a xenon arc lamp as light source. The monochromatic light

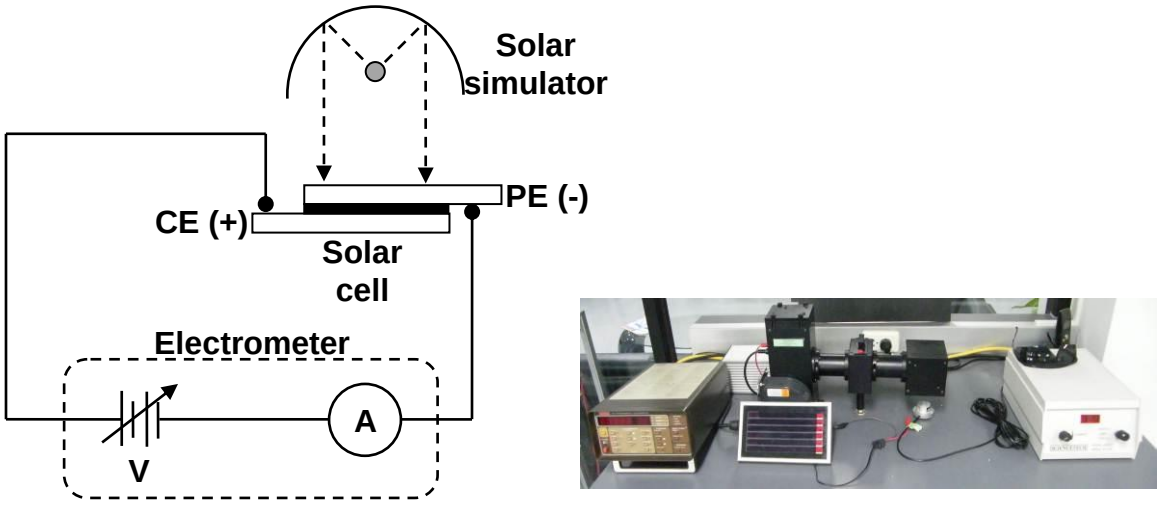

Figure 3.13. *Electrical setup and the photograph of the solar simulator used for the solar cell characterization.*

was allowed to fall on the solar cells and the respective current from the solar cell at every incident wavelength of light was measured by using a digital multimeter (GWInstek GDM-451). The input power at each wavelength of light was measured by using a Kipp & Zonen SPLite pyranometer. Finally, the IPCE was calculated by using equation 2.31.

3.1.13. Photoconductivity Measurement: At a fixed bias voltage, the photocurrent across

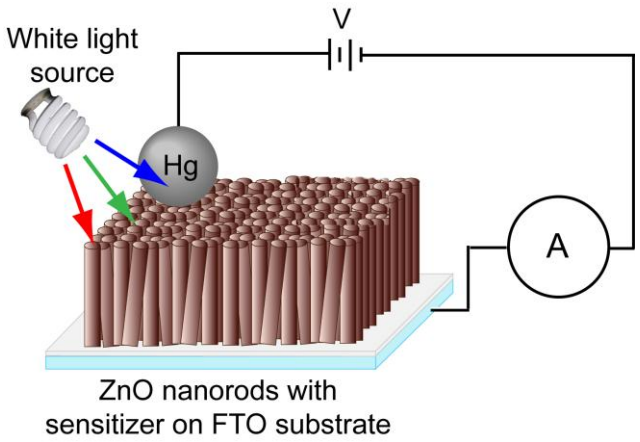

Figure 3.14. *Schematic representation of photoconductivity measurement setup by using FTO as one of the electrodes and a small (4 mm diameter) drop of mercury (Hg) on top of the film as a counter electrode.*

the thickness of the thin films was measured by utilizing FTO as one of the electrodes and a small (4 mm diameter) drop of mercury (Hg) on top of the film as a counter electrode (as

shown in Figure 3.14). The light source (intensity = 25 mW cm^{-2}) was turned on and off in every few seconds, and the obtained current values were continuously recorded using a programmable multimeter (Gwinstek GDM-396).

3.1.14. Fiber-Optic Coupled System for Photocatalytic Measurements: Increased sensitivity in the signal detection in the presence of strong ambient light in our experimental setup lies on the confocal geometry of the excitation and detection sides [4]. As shown in the schematic ray-diagram of the experimental setup (Figure 3.15) the

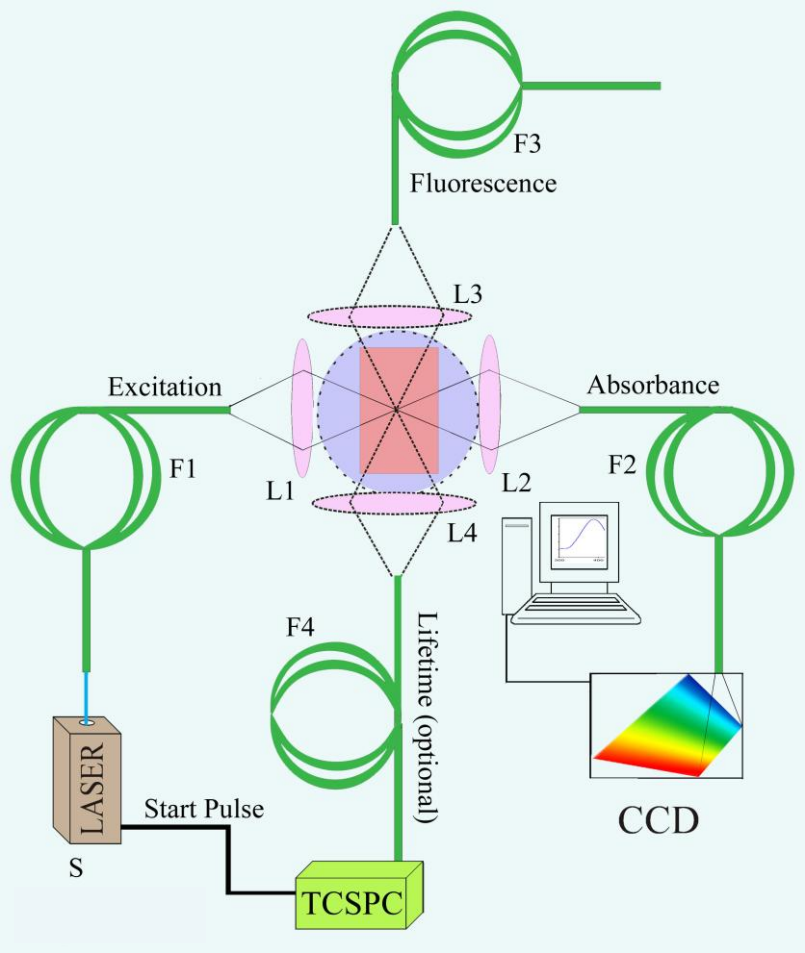

Figure 3.15. *Schematic diagram of the universal setup. S is the source, F1-F4 are the optical fibers, L1-L4 are the fiber coupler lenses, the violate circle represents the ambient light around the sample (reddish rectangle). CCD is the photo-signal detector, connected with computer.*

excitation fiber (400 μM core diameter) carrying laser light is connected to an optical coupler (Ocean Optics, USA, model: 74-UV) in order to focus excitation light at the

middle of a sample holder, which is an all-side polished quartz-cuvette from Starna cells (U.S.A). The numerical aperture (NA) of the excitation fiber (NA=0.45) and focal length of the optical coupling lens (0.5 cm) systems are to achieve out-of-focus rejection by two strategies: firstly by illuminating a single point of the specimen at any one time with a focused beam, so that illumination intensity drops off rapidly above and below the plane of focus and secondly by the use of optical fiber as a collecting unit with similar coupling lens so that light emitted away from the point in the specimen being illuminated is blocked from reaching the detector. The collection fiber is arranged in 'I' geometry and connected with the commercially available CCD based miniaturized spectrograph (Ocean Optics, USA, model: HR4000) in order to measure absorption of the sample of interest. More flexibility in the measurement can also be achieved by using *Shimadzu spectrophotometer (UV-2450)* or *Jobin Yvon (Fluoromax-3)* fluorimeter to measure absorption and photoluminescence, respectively. In order to establish the fact that the absorption of a sample can be measured in presence of strong ambient light effectively, we have placed the quartz cell containing test sample on a home-made UV bath (60W). We have used the same setup in order to investigate the photodegradation of bilirubin [5] and methylene blue [6-7].

3.2. Sample Preparation: In this section the different sample preparation methods have been discussed.

3.2.1. Chemicals used: The chemicals, spectroscopic probes, and proteins were procured from the following sources. Deionized (DI) water, obtained from Millipore, was used to prepare all aqueous solutions. The probes methylene blue (Carlo Erba), Ala-Ala-Phe 7-amido-4-methyl coumarin (Sigma Aldrich), bilirubin (Sigma Aldrich), benzoquinone (Alfa Aesar), Cystine (Sigma Aldrich), and the solar cell dyes N719 (Solaronix, Switzerland), coumarin 343 (Sigma Aldrich), hematoporphyrin (Sigma Aldrich) were used without any further purification. The proteins human serum albumin (HSA) and α-chymotrypsin (CHT) are obtained from Sigma Aldrich. CdSe/ZnS core-shell quantum dots (Maple Red) were purchased from Evident Technology.

3.2.2. Nanoparticles and Nanoporous Membranes:

A. ZnO and ZnO-Au Nanostructures: In order to synthesize colloidal solution of ZnO nanoparticles (NPs), zinc acetate dihydrate, $Zn(CH_3COO)_2.2H_2O$ (Merck), was used as starting material. 40 mL of 2 mM zinc acetate solution was prepared in ethanol (Merck). Then 20 mL of 4 mM NaOH solution in ethanol was added to it under constant stirring. The reaction beaker was then kept in a preheated water bath at 60 °C for 2 h to hydrolyse, after which a transparent ZnO NP colloid was obtained.

ZnO–Au NC colloid was prepared by in situ synthesis of Au NPs on the surface of the ZnO NPs. 5 mL of 1 mM chloroauric acid [$HAuCl_4.H_2O$] (Sigma) ethanolic solution was slowly added to the as-synthesized ZnO NP colloid under constant stirring at room-temperature. The stirring was continued for 15 min. Then 7 mL of 5 mM sodium borohydride, $NaBH_4$ (Sigma), in ethanol solution was added drop-wise to the solution in order to reduce the gold chloride to Au NPs. Immediately after adding $NaBH_4$ the solution becomes red from pale yellow color indicating the formation of the Au NPs in the ZnO NP colloid. The weight ratio between ZnO and Au after the preparation process was found to be 1.3:1 [6].

Detailed processes for the hydrothermal growth of single-crystalline ZnO NRs are described in previous reports [8-9]. In brief, ZnO seed layers were initially deposited on cleaned FTO substrates by spray-pyrolysis method at 350 °C using 10 mM zinc acetate aqueous solution. The seeded FTO substrates were then annealed in air at 350 °C for 1 h and used for the hydrothermal growth of the ZnO NRs. 20 mM aqueous solution of zinc nitrate and hexamethylenetetramine were used as the precursor solution for ZnO NR growth, which was carried out at 90 °C for 40 h. This leads to the growth of ZnO NRs ca. 4−5 μm in length and 100−200 nm in diameter [8, 10]. In order to maintain a constant growth rate of the ZnO NRs during the hydrothermal process, the old precursor solution was replaced with a freshly prepared solution in every 5 h. As-obtained ZnO NR samples were then taken out of the reaction vessel and rinsed thoroughly with DI water to remove unreacted residues. Finally, the samples were annealed in air at 350 °C for 1 h prior to use in our works.

B. CHT-Capped Mn-Doped ZnS: The ZnS:Mn NPs were prepared following a general procedure modified from the reported literature where it was proposed that the growth of

nanostructures with different morphologies, sizes, compositions, and microstructures were mainly controlled by the temperature and time duration of the reaction process [11-20]. Briefly, 50 mL each of 0.2 M *L*-Cys and 20 μM CHT were taken into two different three-necked flasks and 200 μM $NaBH_4$ was added in argon atmosphere with continuous stirring for 45 min. In the next step, 5 mL aqueous solution of 0.1 M zinc acetate was aliquoted into a three-necked round-bottom flask. The mixed solution was adjusted to pH 11.0 by addition of 2 M NaOH and was stirred for 30 min at room-temperature and argon atmosphere. Subsequently, 1.5 mL of 0.01 M manganese acetate was added into the above mixture and stirred for 20 min. 5 mL of 0.1 M deoxygenated Na_2S was then injected into the solution quickly. The mixture was stirred for another 30 min, and then the solution was incubated at 50 °C under air for 2 h to synthesize Cys and enzyme (CHT)-capped ZnS:Mn NPs. Finally, the colloidal NPs were dialyzed against pure water for 4 and 24 h for Cys and CHT-capped NPs, respectively, at 4 °C. In this respect, long-term dialysis is the usual practice for protein-capped systems where excess salts may get absorbed into the protein hydrophobic pockets whereas such effects are absent in Cys-capped systems. The Cys-ZnS and CHT-ZnS samples were prepared as above except for the addition of manganese acetate. The overall synthesis process has been demonstrated in Scheme 7.1.

C. 3-Mercaptopropionic Acid (MPA)-Capped CdTe Quantum Dots (QDs): Several synthetic routes to CdTe QDs have been reported [21-26]. In this study, 0.12 mol of $CdCl_2$ was dissolved in 8 mL of deionized (DI) water, was diluted to 84 mL, and was stirred. To this solution 0.024 mol of trisodium citrate dihydrate, 0.03 mol of Na_2TeO_3 in 8 mL of DI water, 0.011 mol of 3-MPA, and 0.086 mol of $NaBH_4$ were added successively, and were stirred to make the stock solution for CdTe QD synthesis. This stock solution was refluxed for 7, 20, and 30 min in a commercial Panasonic microwave oven (low-power mode) to synthesize QDs with absorption peaks at 440, 500, and 550 nm, respectively. The QDs with 610 nm absorption peak were synthesized by refluxing the stock solution in a commercial oven at 106 °C for 9 h. As-prepared QDs, without any further purification, were used in the fabrication of ZnO NR-based DSSCs.

D. Fabrication of Dye/QD-Sensitized Solar Cells: A 0.5 mM hematoporphyrin (HP) $C_{34}H_{38}N_4O_6$ (Sigma) solution was prepared in anhydrous ethanol under constant stirring at room-temperature for 12 h [27]. The sensitization of the ZnO NRs with HP dye was

carried out in dark and at room-temperature by dipping the ZnO NR samples into the prepared dye solution for 12 h. After the sensitization process, the ZnO NRs were retracted from the dye solution, rinsed with anhydrous ethanol thoroughly (in order to remove any physisorbed dye molecules), and stored in dark for further use. The same sensitization conditions were maintained to anchor another sensitizer N719 on ZnO surface [6, 10].

CdTe QD decorated photoelectrodes (PEs) were fabricated by dipping the ZnO NR coated FTO into CdTe colloid at 60 °C for 3 h [10]. The PEs were removed, were washed with ethanol, and were annealed at 165 °C for 1 h. This cycle was repeated three times to obtain a uniform layer of CdTe particles on the ZnO surface. For cosensitizing the PEs with N719 dye, as-prepared CdTe QD coated PEs were dipped into a 0.5 mM dye N719 in ethanol solution for 24 h in dark at room-temperature. After 24 h, the substrates were withdrawn from the dye solution and were rinsed with ethanol several times in order to remove the excess dye on the film surface. We defined this geometry of the sample as ZnO−QD−N719. In another architecture, we have dipped the ZnO NR with N719 first, and then PEs were coated with CdTe QDs (ZnO−N719−QD architecture). The same procedures were followed to prepare the substrates for time-resolved measurements also only by replacing FTO plates with quartz.

For the fabrication of DSSCs, platinum NPs deposited on FTO substrates were used as counter electrodes. The platinum (Pt) NPs were deposited on the FTO substrates by thermal decomposition of 5 mM platinum chloride, $H_2PtCl_6.H_2O$, Fluka (in isopropanol) at 385 °C for 30 min. The HP-coated ZnO NRs were used as the PEs and the two electrodes were placed on top of each other with a single layer of 50 μm thick Surlyn 1702 (Dupont) as a spacer between the two electrodes. A liquid electrolyte composed of 0.5 M lithium iodide (LiI), 0.05 M iodine (I_2), and 0.5 M 4-tert-butylpyridine (TBP) in acetonitrile was used as the hole conductor and filled in the inter-electrode space by using capillary force, through two small holes (diameter = 1 mm) predrilled on the counter electrode. Finally, the two holes were sealed by using another piece of Surlyn, to prevent the leakage of electrolyte from the cell.

E. Anodic Aluminium Oxide (AAO) Membrane: AAOs are prepared by a standard two-step anodization technique from high-purity (99.99%) aluminium foils of 300 μm thickness, developed by Masuda and co-workers [28]. Before anodization, the aluminium

foils are annealed at 400 °C for 3h to relax grain-induced strain. Next the foils are electro-polished at 18 V for 4 min in a solution of mixed ethanol and $HClO_4$ (C_2H_5OH:$HClO_4$ = 4:1 v/v). The first anodic oxidation process is performed in 0.3 M oxalic acid ($C_2H_2O_4$) with an anodizing voltage of 50 V. After 8h the alumina layer is removed by a mixed aqueous solution of 6% H_3PO_4 and 1.8% H_2CrO_4 at 45 °C for 8 h. The second anodic oxidation process starts under the same conditions as the first one, with 8h of oxidation time to grow the porous alumina layer with a thickness of around 10 μm on the Al foils. After that, a $CuCl_2$ solution (6.8 g $CuCl_2$+100 mL 37% HCl+200 mL distilled water) is used to remove the Al foil on the back side of the AAO. After the sample becomes transparent, the additional barrier layer on the AAO is dissolved by a 5% phosphoric acid solution. The through-hole AAO is coated by an Ag film to be used as a cathode before depositing gold NWs (diameter = 45 nm) in the AAO matrix. Then the deposition process is performed in a solution of 2.25×10^{-3} mol/L $HAuCl_4$ and 0.485 mol/L H_3BO_3, at constant current of 0.04 mA [29].

3.2.3. Measurement of Enzymatic Activity of α-Chymotrypsin (CHT): For the measurement of the enzymatic activity of CHT, AAF-AMC was used as the substrate. The concentration of the substrate was kept an order of magnitude higher than that of the enzyme. The rate of formation of product was followed by measuring the absorbance of product at 370 nm. The absorbance of the product was converted to molar concentration term by using the extinction coefficients of the product at 370 nm wavelength. The specific activity of an enzyme is a common unit, which is defined as the number of enzyme units per mL divided by the concentration of protein in mg/mL. Specific activity values are therefore quoted as units/mg.

References:

[1] A. Rodger, B. Norden, Circular Dichroism and Linear Dichroism, Oxford University Press, 1997.

[2] N. Berova, K. Nakanishi, R.W. Woody, Circular Dichroism: Principles and Applications, Wiley-VCH, 2000.

[3] D.V. O'Connor, D. Philips, Time Correlated Single Photon Counting, Academic Press, London, 1984.

[4] S.S. Sinha, P.K. Verma, A. Makhal, S.K. Pal, A Versatile Fiber-Optic Coupled System for Sensitive Optical Spectroscopy in Strong Ambient Light, *Rev. Sci. Instrum.* 80 (2009) 053109.

[5] S. Sarkar, A. Makhal, S. Baruah, M.A. Mahmood, J. Dutta, S.K. Pal, Nanoparticle-Sensitized Photodegradation of Bilirubin and Potential Therapeutic Application, *J. Phys. Chem. C* 116 (2012) 9608.

[6] S. Sarkar, A. Makhal, T. Bora, S. Baruah, J. Dutta, S.K. Pal, Photoselective Excited State Dynamics in ZnO-Au Nanocomposites and their Implications in Photocatalysis and Dye-Sensitized Solar Cells, *Phys. Chem. Chem. Phys.* 13 (2011) 12488.

[7] A. Makhal, S. Sarkar, S.K. Pal, Protein-Mediated Synthesis of Nanosized Mn-Doped ZnS: A Multifunctional, UV-Durable Bio-Nanocomposite, *Inorg. Chem.* 51 (2012) 10203.

[8] S. Baruah, J. Dutta, pH-Dependent Growth of Zinc Oxide Nanorods, *J. Cryst. Growth* 311 (2009) 2549.

[9] S. Baruah, J. Dutta, Effect of Seeded Substrates on Hydrothermally Grown ZnO Nanorods, *J. Sol-Gel Sci. Tech.* 50 (2009) 456.

[10] S. Sarkar, A. Makhal, K. Lakshman, T. Bora, J. Dutta, S.K. Pal, "Dual-Sensitization" via Electron and Energy Harvesting in CdTe Quantum Dots Decorated ZnO Nanorod-based Dye-Sensitized Solar Cells, *J. Phys. Chem. C* 116 (2012) 14248.

[11] X. Fang, T.Y. Zhai, U.K. Gautam, L. Li, L.M. Wu, Y. Bando, D. Golberg, ZnS Nanostructures: From Synthesis to Applications, *Prog. Mater. Sci.* 56 (2011) 175.

[12] X. Fang, L. Wu, L. Hu, ZnS Nanostructure Arrays: A Developing Material Star, *Adv. Mater.* 23 (2011) 585.

[13] W. Zhou, D.T. Schwartz, F. Baneyx, Single-Pot Biofabrication of Zinc Sulfide Immuno-Quantum Dots, *J. Am. Chem. Soc.* 132 (2010) 4731.

[14] W. Zhou, F. Baneyx, Aqueous, Protein-Driven Synthesis of Transition Metal-Doped ZnS Immuno-Quantum Dots, *ACS Nano* 5 (2011) 8013.

[15] W.S. Zou, D. Sheng, X. Ge, J.Q. Qiao, H.Z. Lian, Room-Temperature Phosphorescence Chemosensor and Rayleigh Scattering Chemodosimeter Dual-Recognition Probe for 2,4,6-Trinitrotoluene Based on Manganese-Doped ZnS Quantum Dots, *Anal. Chem.* 83 (2011) 30.

[16] J. Zhuang, X. Zhang, G. Wang, D. Li, W. Yang, T. Li, Synthesis of Water-Soluble ZnS:Mn^{2+} Nanocrystals by using Mercaptopropionic Acid as Stabilizer, *J. Mater. Chem.* 13 (2003) 1853.

[17] W. Zhang, Y. Li, H. Zhang, X. Zhou, X. Zhong, Facile Synthesis of Highly Luminescent Mn-Doped ZnS Nanocrystals, *Inorg. Chem.* 50 (2011) 10432.

[18] Z. Quan, Z. Wang, P. Yang, J. Lin, J. Fang, Synthesis and Characterization of High-Quality ZnS, ZnS:Mn^{2+}, and ZnS:Mn^{2+}/ZnS (Core/Shell) Luminescent Nanocrystals, *Inorg. Chem.* 46 (2007) 1354.

[19] X.S. Fang, C.H. Ye, L.D. Zhang, Y.H. Wang, Y.C. Wu, Temperature-Controlled Catalytic Growth of ZnS Nanostructures by the Evaporation of ZnS Nanopowders, *Adv. Funct. Mater.* 15 (2005) 63.

[20] Q. Wu, H. Cao, S. Zhang, X. Zhang, D. Rabinovich, Generation and Optical Properties of Monodisperse Wurtzite-Type ZnS Microspheres, *Inorg. Chem.* 45 (2006) 7316.

[21] A.L. Rogach, T. Franzl, T.A. Klar, J. Feldmann, N. Gaponik, V. Lesnyak, A. Shavel, A. Eychmuller, Y.P. Rakovich, J.F. Donegan, Aqueous Synthesis of Thiol-Capped CdTe Nanocrystals: State-of-the-Art, *J. Phys. Chem. C* 111 (2007) 14628.

[22] N. Gaponik, D.V. Talapin, A.L. Rogach, K. Hoppe, E.V. Shevchenko, A. Kornowski, A. Eychmuller, H. Weller, Thiol-Capping of CdTe Nanocrystals: An Alternative to Organometallic Synthetic Routes, *J. Phys. Chem. B* 106 (2002) 7177.

[23] S.F. Wuister, I. Swart, F.V. Driel, S.G. Hickey, C.D.M. Donegaa, Highly Luminescent Water-Soluble CdTe Quantum Dots, *Nano Lett.* 3 (2003) 503.

[24] J.G. Brennan, T. Siegrist, P.J. Carroll, S.M. Stuczynski, P. Reynders, L.E. Brus, M.L. Steigerwald, Bulk and Nanostructure Group II-VI Compounds from Molecular Organometallic Precursors, *Chem. Mater.* 2 (1990) 403.

[25] C.B. Murray, D.J. Norris, M.G. Bawendi, Synthesis and Characterization of Nearly Monodisperse CdE (E = Sulfur, Selenium, Tellurium) Semiconductor Nanocrystallites, *J. Am. Chem. Soc.* 115 (1993) 8706.

[26] F. Aldeek, L. Balan, G. Medjahdi, T. Roques-Carmes, J.P. Malval, C. Mustin, J. Ghanbaja, R. Schneider, Enhanced Optical Properties of Core/Shell/Shell CdTe/CdS/ZnO Quantum Dots Prepared in Aqueous Solution, *J. Phys. Chem. C* 113 (2009) 19458.

[27] S. Sarkar, A. Makhal, T. Bora, K. Lakshman, A. Singha, J. Dutta, S.K. Pal, Hematoporphyrin−ZnO Nanohybrids: Twin Applications in Efficient Visible-Light Photocatalysis and Dye-Sensitized Solar Cells, *ACS Appl. Mater. Interfaces* 4 (2012) 7027.

[28] H. Masuda, K. Fukuda, Ordered Metal Nanohole Arrays Made by a Two-Step Replication of Honeycomb Structures of Anodic Alumina, *Science* 268 (1995) 1466.

[29] A. Makhal, S. Sarkar, S.K. Pal, H. Yan, D. Wulferding, F. Cetin, P. Lemmens, Ultrafast Excited State Deactivation of Doped Porous Anodic Alumina Membranes, *Nanotechnology* 23 (2012) 305705.

Chapter 4

Photoreactivity of Inorganic Nanoparticles in the Proximity of Bilirubin, a Potential Jaundice Marker

4.1. Introduction:

Bilirubin (BR), the yellow-orange breakdown product of normal heme catabolism in mammalian systems, introduces great biological and diagnostic values [1]. Both antioxidant and toxic properties have been attributed to BR [2], which is normally conjugated with glucuronic acid and then excreted in the bile. However, when its conjugation with glucuronic acid is inhibited, as in neonatal jaundice and in hereditary forms of congenital jaundice, excess BR bind and deposit to various tissues, giving rise to severe hyperbilirubinemia and neurotoxicity. The potential to combat jaundice continues to expand with scientific and technological advancements of the diagnostic tools and treatment methodology. Phototherapy, the most effective treatment for jaundice to date, decreases the BR levels in the blood by changing the *ZZ*-BR isomer into water-soluble *ZE*-BR [3-5]. The quantum yield of the photoconversion of *ZZ* to *EE*-isomer was found to be dependent on excitation wavelength, decreasing from excitation at 457.9 to 514.5 nm [6]. However, the formation of structural isomer, *Z*-Lumirubin, was found to follow reverse dependency on the excitation wavelength [7]. Nevertheless, if the levels of unconjugated BR are very high, one may need to have an exchange transfusion that involves taking away some of the patient's blood and replacing it with a blood transfusion. The decrease in serum BR associated with phototherapy was initially argued to be due to oxidative destruction of the pigment. However, substantial quantities of unconjugated BR are found in the bile when phototherapy is administered. This fact and the failure to find much of the expected photooxidation products in excreta of infants or experimental animals after phototherapy led to discarding the idea that photodegradation is a major pathway [8].

Nowadays, use of nanoparticles (NPs) in medical science is a promising direction in nanotechnology [9]. Their applications in drug delivery [10], cancer cell diagnostics

[11], and therapeutics [12] have been active fields of research. It has been found that the large surface area of the mesoporous anatase TiO_2 films, produced by depositing the oxide in colloidal form onto a solid substrate, allows high levels of hemoglobin adsorption [13]. Zinc oxide (ZnO), a wide band-gap (3.37 eV) semiconductor having a high electron−hole binding energy (60 meV), is one of the most attractive and promising materials due to both fundamental research and industrial importance. Although it is less commonly studied and has inferior stability compared to TiO_2, ZnO is more efficient for degradation of various organic compounds [14]. ZnO is also a "green" material that is biocompatible, biodegradable, and nontoxic for medical applications and environmental science [15]. The excitation of ZnO with near UV-light energy has been shown to be sufficient to initiate various redox reactions at the surface of the semiconductor. Because of the small size of particles and high recombination rate, only a fraction (5%) of the produced excitons can be utilized to induce redox processes at the interface. The photocatalytic processes using ZnO and other semiconductors have demonstrated the need to utilize the excitonic recombination in order to achieve higher photocatalytic efficiencies. The photocatalytic property of ZnO has been widely employed for various applications including antibacterial effect, self-cleaning and self-sterilizing materials, as well as degrading organic contaminants in the environment [16-18]. Considering the promising applications of ZnO nanocatalysis, it can be expected that the nanocrystalline ZnO that possesses self-sterilizing property can also photocatalytically decompose BR when it is adsorbed at the surface of the NPs.

In this chapter, we demonstrate the potential use of ZnO NPs with a strong optical absorption in the near-UV region as phototherapeutic agents. The application of defect mediated ZnO photoluminescence (PL) for the degradation of the surface adsorbed BR, in order to enhance the overall efficiency of the BR photodegradation process, is the major interest in the present study. By using a picosecond-resolved fluorescence technique, we have explored the relative contributions of different defect states (mainly, oxygen vacancy centers) in the overall degradation process. Although the photoexcited charge transfer is widely used in the remediation of chemical contaminants, to the best of our knowledge, no effort has been made to utilize the visible emission of ZnO in order to degrade the organic contaminants. To investigate the most effective phototherapeutic ZnO nanostructure, their

physicochemical properties, which include size, shape, morphology and surface chemistry, have also been investigated.

4.2. Results and Discussion:

4.2.1. Nanoparticle-Sensitized Photodegradation of Bilirubin and Potential Therapeutic Application [19]:

The morphological and structural investigation of photocatalysts have been carried out by transmission electron microscopy (TEM) and scanning electron microscopy (SEM). Representative TEM images of various sized (5, 8 and 10 nm) ZnO NPs (Figure 4.1a−d) and SEM images of ZnO agglomerates (200−500 nm, Figure 4.1e) and ZnO nanoflowers (300−400 nm, Figure 4.1f), are shown. High-resolution TEM (HRTEM) image of 5 nm sized ZnO particles are shown in Figure 4.1a, which confirms the particles to be fairly monodispersed and highly crystalline in nature. The lattice fringe width of 0.28 nm indicates the (100) plane of the wurtzite structure of ZnO nanocrystals [20].

The UV-visible absorption spectra of different ZnO colloidal solutions employed in the present study are depicted in Figure 4.2a. The ZnO NPs exhibit a sharp absorbance onset at about 355 nm (3.49 eV), reflecting their uniform size. The peak of the exciton absorption band gradually shifts from 355 to 375 nm (3.49−3.31 eV) as the size increases both in diameter and length. The room-temperature PL spectra from the NP samples all contain a narrow UV-band centred near 368 nm, which is due to exciton recombination and a broad green-band centred at 550 nm (see Figure 4.2b). These broad emission bands originate from the surface defect centers indicating the presence of considerable oxygen vacancies in the crystal lattice of ZnO NPs, whereas, ZnO agglomerate and nanoflower structures contain very little of these defects. The broad green emission band is composed of two bands (P1 & P2, shown in Figure 4.2c as a green and red dotted lines, respectively) typically associated with oxygen deficiency. The doubly charged oxygen vacancies (V_O^{++}), created by capture of a hole by the V_O^{+} center in a depletion region, leads to the P2 emission line. The singly charged center *(V_O^{+})* in the absence of a depletion region turns into a neutral center *($V_O^{\times}$)* upon the capture of an electron (n-type ZnO) from the

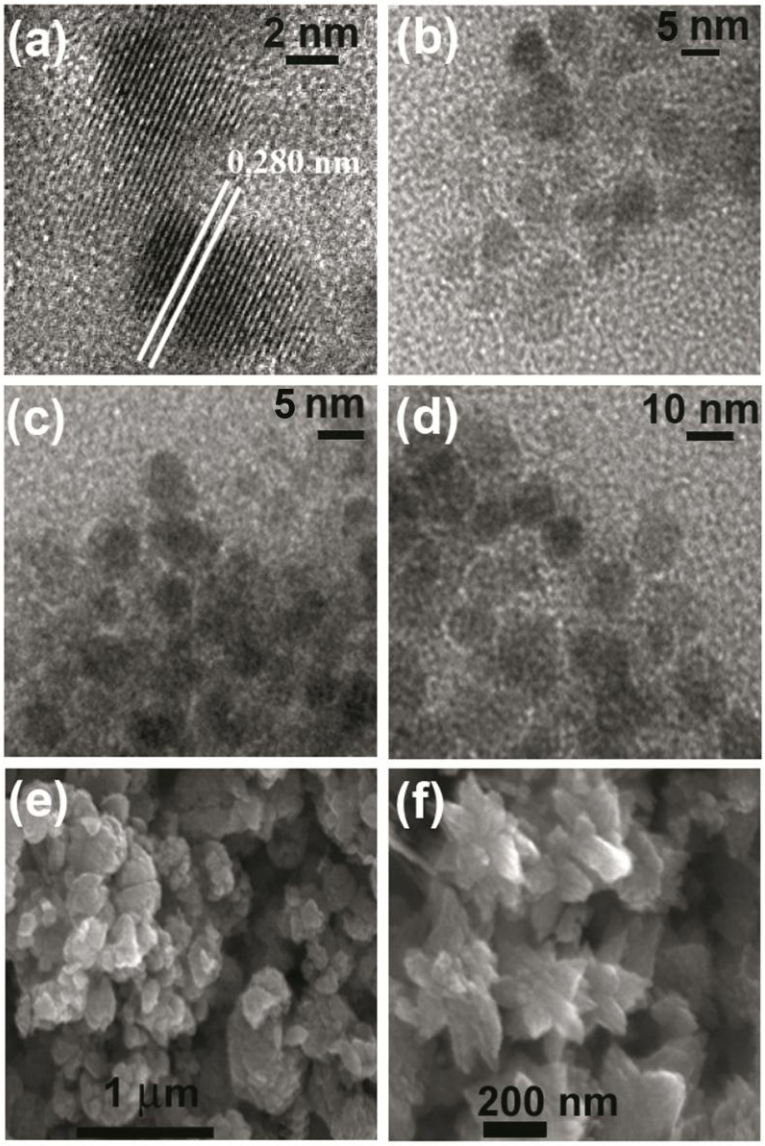

Figure 4.1. *a) High-magnification TEM image of ZnO NP (5 nm). Low-magnification TEM images of various ZnO nanocrystallites b) ZnO NP (5 nm) c) ZnO NP (8 nm) d) ZnO NP (10 nm). SEM images of e) ZnO agglomerates and f) ZnO nanoflowers.*

conduction band, which then recombines with a hole in the valence band giving rise to the P1 emission [21].

As shown in the Figure 4.2d, defect-mediated green emission is suppressed upon gradual addition of BR to the system. Previous study has shown that ZnO PL is sensitive to the presence of various adsorbates like O_2, H_2 and CO which also decreases PL intensity;

however, methanol and formic acid adsorption increased it [22-23]. Herein, we propose

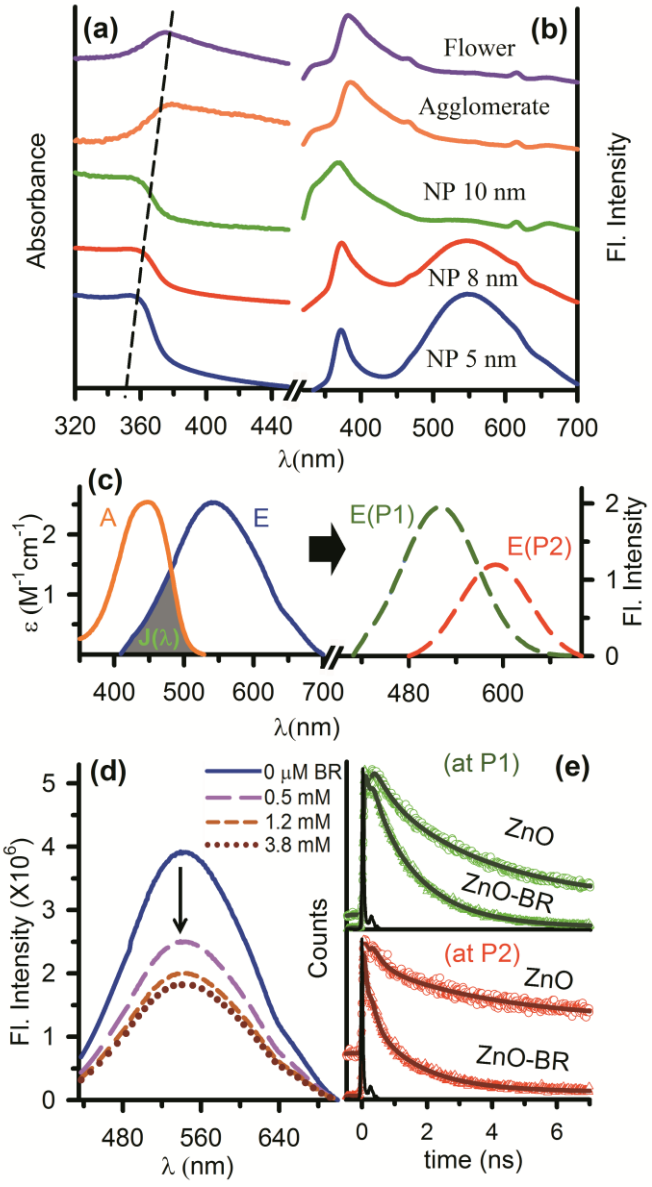

Figure 4.2. *Steady-state a) absorption spectra b) emission spectra (excitation at 320 nm) of ZnO catalysts with various sizes and shapes c) absorption spectra of BR (A, orange) and emission spectra (excitation at 375 nm, Raman extracted) of ZnO NP (E, blue) are shown. A typical emission band is composed of two components P1 and P2 (see text) as shown for the emission curve. An overlapping zone between emission of ZnO NP and absorption of acceptor BR is indicated as gray shaded zone d) PL quenching of ZnO NPs with the increasing concentration of BR e) the picosecond-resolved fluorescence transients of ZnO NP, in the absence and in the presence of acceptor BR (excitation at 375 nm) collected at P1 (green, 520 nm) and P2 (red, 590 nm), are shown.*

FRET from a donor ZnO NP to BR acceptor, which is responsible for the observed inhibition of emission bands. FRET in combination with Förster theory has become an invaluable tool for the assessment of distances in numerous biomolecular assemblies [24-26]. The FRET process is based on the concept of treating an excited donor as an

Table 4.1. Picosecond-resolved luminescence transients of ZnO NPs in the absence and in the presence of BR.[a]

Samples	τ_1 (ns)	τ_2 (ns)	τ_3 (ns)	τ_{avg} (ns)
ZnO NP (520 nm)	32.3 (10.7%)	3.29 (65.3%)	0.497 (24%)	5.73
ZnO NP+BR (520 nm)	15.8 (1.1%)	1.48 (67.7%)	0.216 (31.2%)	1.24
ZnO NP (590 nm)	38.9 (28.5%)	3.19 (31.5%)	0.271 (40%)	12.23
ZnO NP+BR (590 nm)	24.3 (3%)	1.45 (32.2%)	0.153 (64.8%)	1.29

[a]*The emissions from ZnO NPs (probing at 520 and 590 nm) were detected with a 375 nm laser excitation. Numbers in the parentheses indicate relative weightage.*

oscillating dipole that can undergo energy exchange with a second dipole having a similar resonance frequency [26]. In principle, if the fluorescence emission spectrum of the donor molecule overlaps the absorption spectrum of an acceptor molecule, and the two are within a minimal distance from one another (1−10 nm), the donor can directly transfer its excitation energy to the acceptor *via* exchange of a virtual photon. The consideration of Dexter mechanism (orbital overlap) *via* an exchange process associated with the transfer of single charge carriers can be excluded in this study as it is a short-range mechanism (1−10 Å) [27]. The spectral overlap of defect-mediated PL band with that of the BR absorption is shown in Figure 4.2c. It has been reported that the emission centre around 590 nm comes from defect states near the surface layer while the shorter wavelength at 520 nm comes from defects near the bulk of the NPs. Picosecond-resolved fluorescence study (excitation at 375 nm) was performed by monitoring decays at the P1 and P2 peaks. The faster excited state lifetime of the ZnO−BR adduct with respect to that of the free ZnO NP is clearly noticeable from Figure 4.2e. The baseline upliftment comes from the long lifetime component which could not be registered within our experimental time window. The details of the spectroscopic parameters and the fitting parameters of the fluorescence

decays are presented in Table 4.1. From FRET calculations (using equation 2.11 and 2.12b), the effective distances between the donor and the acceptor (r_{DA}) are determined to be 1.48 nm and 1.28 nm for P1 and P2 states, respectively, which support the general understanding that V_O^{++} centers are closer to the surface attached BR compared to V_O^{+} centers. It is to be noted that the smaller value of r_{DA} compared to the radius of the ZnO NPs (~2.5 nm; Figure 4.1a) can be rationalized from the fact that the origin of the PL peaking at P1 and P2 arise essentially from surface defects in the ZnO NPs [28]. The energy transfer efficiencies of the two states are calculated to be 78% and 89%, respectively. Since V_O^{++}/V_O^{+} states are located near the surface, greater energy transfer efficiency *via* doubly charged vacancy centers is well justified. Following the demonstration of relative contributions from different defect states in the energy transfer process, now we proceed to study the effect of transferred energy between the FRET pairs, which finally led to efficient BR degradation in the arena of nanocatalysis.

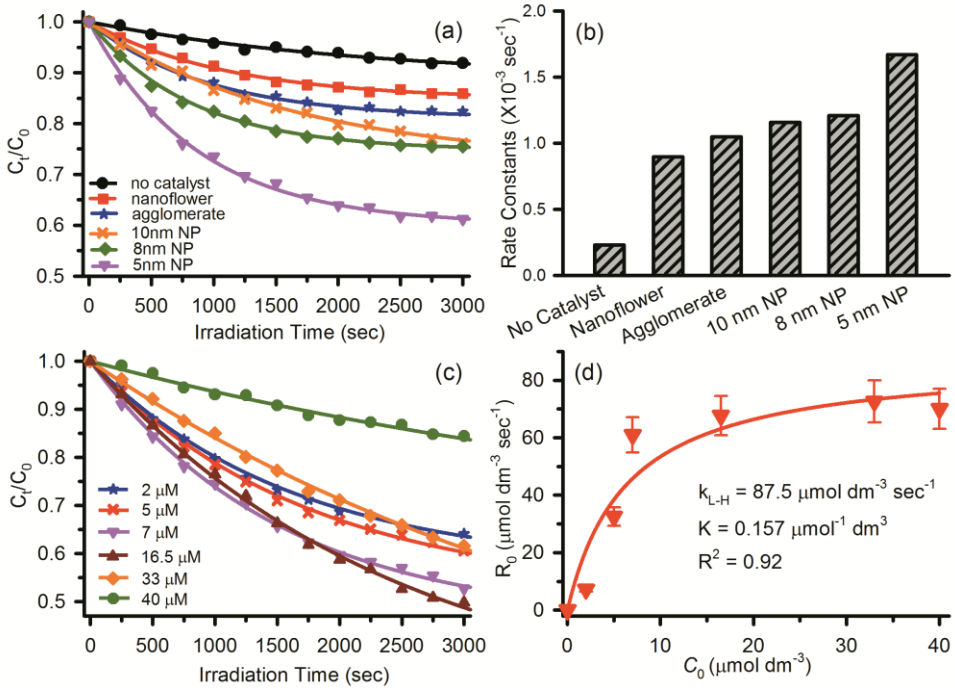

Figure 4.3. *a) Plot of relative concentration (C_t/C_0) versus UV irradiation time for the degradation of BR (monitored at 450 nm), in the presence of various ZnO nanocrystallites. b) Respective rate constants showing 5 nm particles are the most effective catalysts c) (C_t/C_0) versus t with various BR concentrations and d) Langmuir−Hinshelwood (L−H) plot (with 10% error bar) are shown. L−H rate constant (k_{L-H}), Langmuir adsorption coefficient (K), and regression coefficients (R^2) are also provided.*

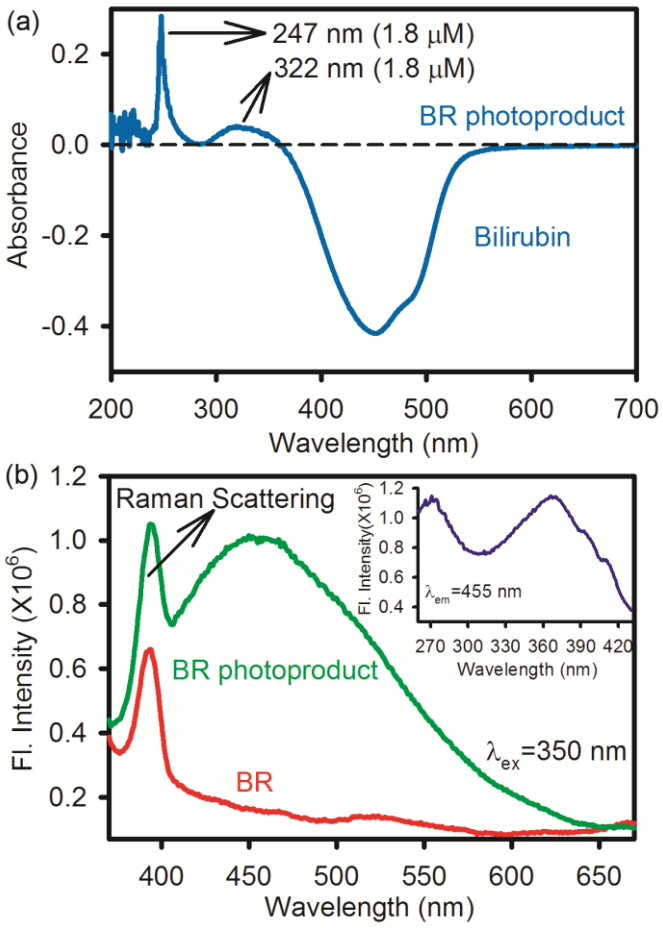

Figure 4.4. *a) Absorbance spectrum of BR photoproduct showing generation of characteristic peaks of MVM. The formation of MVM is associated with degradation of BR characteristic peak. b) Room-temperature PL spectra of BR photoproduct showing broad emission peak centered at 455 nm (excitation at 350 nm). Inset shows excitation spectra monitored at the PL peak.*

The model photocatalytic reaction investigated in this study is the decomposition of BR adsorbed at the surface of ZnO NPs. BR has optical absorption in the UV-visible regions and displays a significant decomposition rate in presence of colloidal ZnO solutions (Figure 4.3). There are some previous studies from our group where photolysis of a test contaminant has been probed in a colloidal semiconductor system [29-30]. BR adsorption on nanostructured hydroxyapatite coating was previously investigated by Yang *et al.* using quartz crystal microbalance and the photocatalytic degradation of adsorbed BR under UV irradiation was studied [31]. It is obvious, the higher the energy transfer from the surface of the ZnO semiconductor, the faster will be the degradation of the surface-

attached BR. The results of BR degradation in the presence and the absence of ZnO catalysts under UV-light are shown in Figure 4.3a, where the relative concentration (C_t/C_0) of BR in solution is plotted against UV-irradiation time. Blank experiments performed for several hours in the absence of catalysts and/or without UV irradiation have only resulted in a negligible change in BR concentration. In this respect, BR degradation under UV irradiation has been performed in a ZnO NP-based flow-device with DMSO:water mixture, and we found characteristic absorbance peaks for BR photooxidation product Methylvinylmaleimide (MVM) at 247 nm and 322 nm (Figure 4.4a). The photoproduct found to be emissive and shows broad emission band centered at 455 nm, as shown in Figure 4.4b. Our results are very much in agreement with previous investigations [32]. In this regard, it is now well-established that MVM does not exhibit the usual enzyme toxicity; therefore, if MVM is being formed *in vivo*, it would be nontoxic [33]. However, the other photoproducts such as configurational (principally, *ZE*-BR) and structural isomer (Lumirubin) are also well expected since ZnO defect-mediated optical radiation transfer is not supposed to interfere with the conventional phototherapy process.

In order to attain the most efficient photodegradation, the process has been investigated for a range of different ZnO morphologies and sizes amongst which ZnO particles with diameter of 5 nm are found to be the most efficient catalyst, as shown in the histogram (Figure 4.3b). Particle shape and size are important parameters for catalysis in general since they directly affect the specific surface influence of a catalyst [34-36]. With a smaller particle size, the surface-to-volume ratio and the number of active surface sites increases, which concomitantly increases the surface charge carrier transfer rate during photocatalysis [37-38]. In order to increase the quantum yield of nanocrystalline photocatalysts, the e−h recombination has to be reduced. An effective method to achieve the separation of e−h is to introduce defects into ZnO lattice. Different mechanisms and different effects of native defects have been proposed in the literature for efficient photocatalytic dye degradation by the use of ZnO [39-41]. It is obvious that the degradation rate increases with increasing ZnO concentration which allows greater contact between organic molecules and photocatalytic active sites. Fig. 4.5 provides the kinetics of the degradation with various surface (ZnO) concentrations (0, 5, 10, 20, 40 and 50 μM) by

keeping the substrate (BR) concentration (3.5 μM) constant, which shows that the degradation rate increases with increasing ZnO concentration (as shown in Table 4.2).

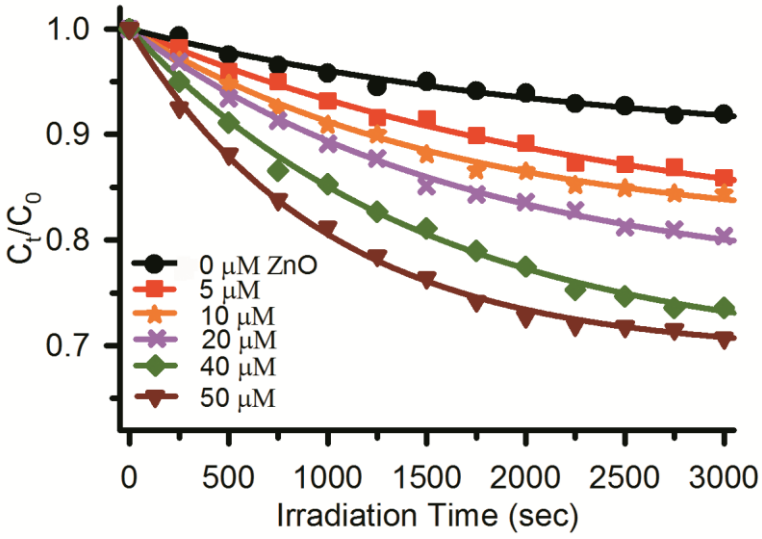

Figure 4.5. *Photodegradation of BR in the presence of different concentrations of ZnO NP (5 nm). Plot of relative concentration (C_t/C_0) versus UV irradiation time for the degradation of BR (monitored at 450 nm).*

Table 4.2. The kinetics parameters[b] for the photodegradation of BR in the presence of different concentrations of catalyst.

Samples	k (s^{-1})	Total amount of degradation (A %) (in 3000 s)	R^2
0 μM ZnO	2.3×10^{-4}	8	0.82
5 μM ZnO	4.04×10^{-4}	14	0.88
10 μM ZnO	5.75×10^{-4}	17	0.91
20 μM ZnO	6.11×10^{-4}	21	0.80
40 μM ZnO	6.55×10^{-4}	27	0.94
50 μM ZnO	1.0×10^{-3}	30	0.83

[b]*Kinetic constants (k), the percentages of total photodegradation (A) and the regression coefficient (R^2). A 320 nm high-pass optical filter was used in the study.*

Now, by keeping the surface concentration fixed, BR-decomposition reaction rate (R_0) is observed to be a function of the substrate initial concentration (C_0). All the photodegradation curves were found to follow a first-order exponential equation, and the results of photocatalytic degradation of BR over nanocrystalline ZnO of varying particle

sizes and shapes are presented in Table 4.3. The rate of photocatalytic decomposition of the BR molecules is typically fitted with the Langmuir−Hinshelwood (L−H) kinetics model [42], as discussed in the section 2.1.6. In this experiment, BR degradation on ZnO NP surface was found to exactly follow the above phenomenon (Figure 4.3c−d). By fitting the observed R_0 versus C_0 curve (using equation 2.19 as fitting equation) for the degradation of BR in presence of same concentration of ZnO, the obtained values of Langmuir–Hinshelwood (L–H) rate constant (k_{L-H}) and Langmuir adsorption coefficient (K) are 87.5 μmol dm^{-3} s^{-1} and 0.157 μmol^{-1} dm^3, respectively. The pattern of the curves and the values of the fitting parameters fall in the range of the observed literature data for various photocatalytic studies [43].

The capability of being reusable is one of the most pivotal criteria for an ideal photocatalyst [44-45]. With the successful exhibition of these NPs as effective

Table 4.3. The kinetics parameters[c] for the photodegradation of BR in the absence and presence of ZnO.

Samples	k (s^{-1})	Total amount of degradation (A%) (in 3000 s)	R^2
ZnO size and morphology dependent study (10 μM BR)			
No Catalyst	2.3×10^{-4}	8	0.82
ZnO nanoflower	8.98×10^{-4}	18	0.78
ZnO agglomerate	1.05×10^{-3}	14	0.88
ZnO NP (~10 nm)	1.16×10^{-3}	23	0.85
ZnO NP (~8 nm)	1.21×10^{-3}	25	0.89
ZnO NP (~5 nm)	1.67×10^{-3}	37	0.86
BR concentration dependent study (50 μM ZnO)			
2 μM BR	3.6×10^{-4}	36	0.92
5 μM BR	6.5×10^{-4}	39	0.94
7 μM BR	8.7×10^{-4}	47	0.93
16.5 μM BR	4.1×10^{-4}	50	0.97
33 μM BR	2.2×10^{-4}	39	0.98
40 μM BR	1.7×10^{-4}	17	0.99

[c]*Kinetic constants (k), the percentages of total photodegradation (A) and regression coefficient (R^2). A 320 nm high-pass optical filter was used in the study.*

photocatalysts, the regeneration of the NPs in the process of photocatalysis was further confirmed from the similar rate of photodegradation of BR for three cycles. The results,

given in Figure 4.6c, demonstrate that these NPs can indeed serve as highly effective and convenient recyclable photocatalysts. The change in concentration of BR solution for multiple steps also fit very well to the exponential decay profile with regression coefficient, $R^2 \geq 0.94$, and the rate constants were determined to be almost the same ($\sim 3.8\times10^{-4}$ s^{-1}) for the multiple cycles.

In order to apply our findings into a model application, we have designed a flow-device consisting of two glass plates (separated by a spacer) as shown in Figure 4.6d. Polycrystalline ZnO NP (diameter ~5 nm) thin films were grown on one of the glass plates by spray pyrolysis technique and BR solution was passed through the channel in a very slow flow rate (2 mL/30 min). The whole system was kept over a UV source and total amount of BR degradation was found to be 4% and 37% in the absence and presence of ZnO NPs, respectively, under the same flow-rate condition. Therefore, it is clear from our results that BR can be degraded by careful utilization of nonradiative recombination in ZnO. We like to emphasize two potential advantages of using such NP-based flow-device

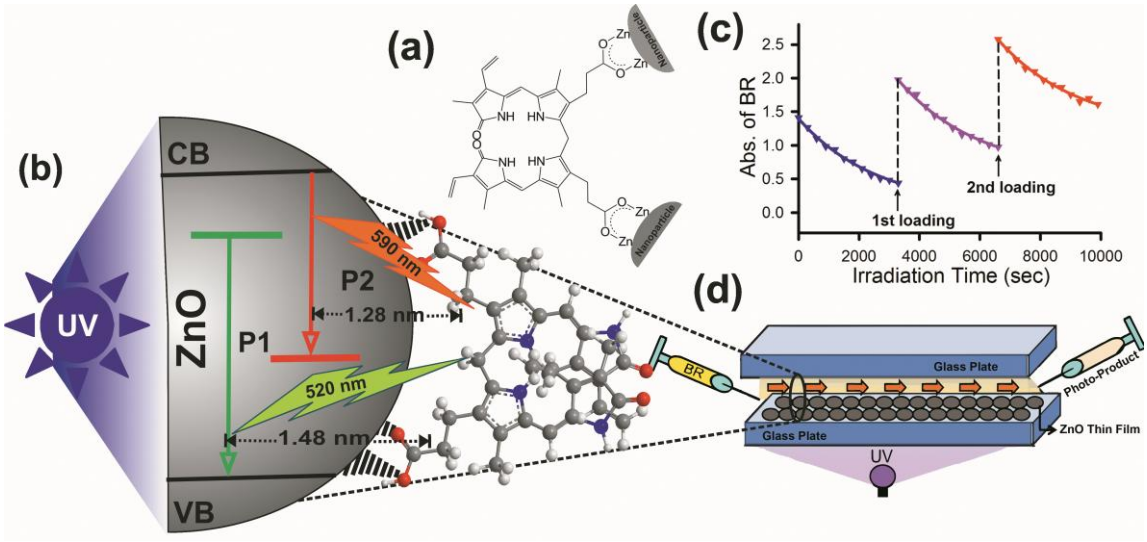

Figure 4.6. *a) Molecular structure of BR and its attachment to the surface of ZnO NPs. b) Representation of the ZnO NP−BR adducts depicting FRET dynamics from different oxygen vacancy centers of ZnO NPs (gray big ball) to surface adsorbed BR (shown in ball-stick model) molecules. c) Photocatalytic degradation curves (abs. versus t) of BR in ZnO suspension under UV-light irradiation for three repeated cycles. d) A schematic representation of our designed system/device using ZnO NPs as phototherapeutic agents.*

in the purification of BR-containing blood. Firstly, the recyclable NPs need minimum recharging that can easily be done by passing an aqueous solution with pH at 8 followed by deionized water. Secondly, the exposure of the BR-containing blood to the harmful UV radiation can be avoided using the high pass filter action of the NPs layer. Although Zn^{2+} being biologically trace element, cytotoxic response of a critical ZnO concentration (3.75 ppm) has been reported [46]. However, the risk of toxicity caused by ZnO in our designed system can be excluded since ZnO NPs have been deposited by spray pyrolysis technique and after passing 500 mL of both water and ethanol through the flow-device it was found that a very negligible amount of ZnO NPs (~30 μM) leached from glass plate (Figure 4.7), which is a much lower value compared to *in vitro* toxic concentration of $(Zn^{2+})_{aq}$ (400 μM) [47], thus eliminates the risk of cytotoxicity.

Since serum albumins are the most abundant proteins in plasma and BR is mostly bound to albumin in blood, we have further extended BR degradation in presence of HSA protein by using ZnO NP-based flow-device. The whole system was kept over an UV source and BR−HSA complex solution was passed through the channel in a very slow flow rate (2 mL/40 min). As shown in Figure 4.8a, the total amount of BR degradation is found

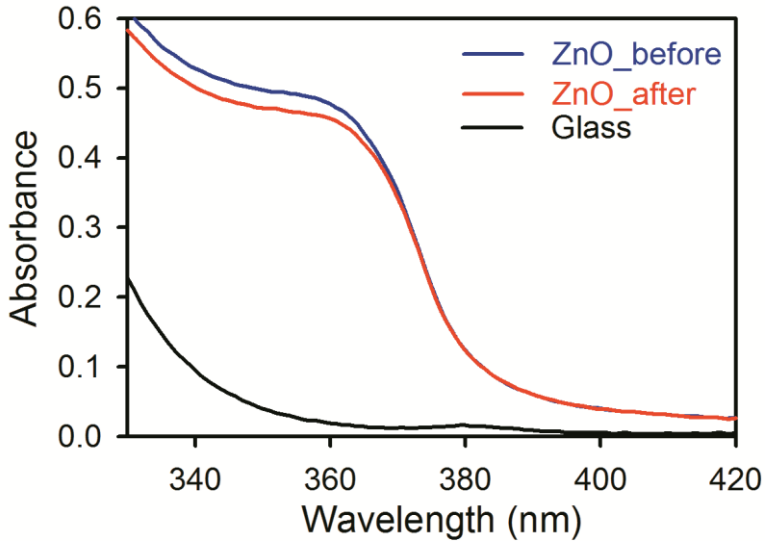

Figure 4.7. *Absorbance spectra of ZnO NPs (before and after passing 500 mL water and ethanol) deposited by spray-pyrolysis technique and only glass plate.*

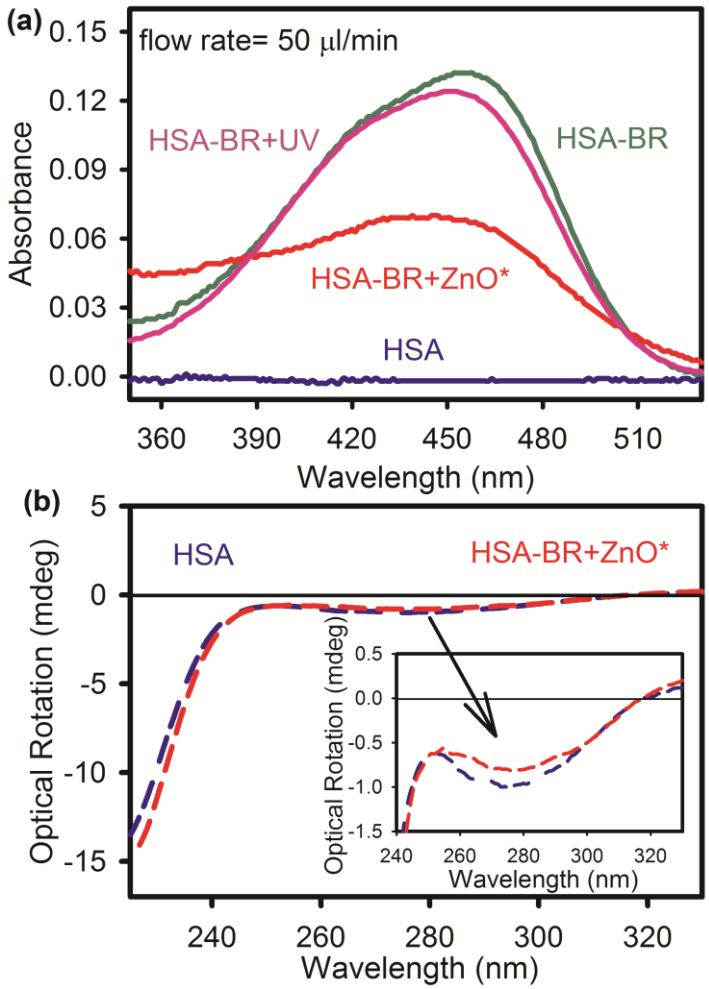

Figure 4.8. *a) UV-vis spectral changes of BR−HSA complex solution in the absence of UV (green), upon UV irradiation in presence (red) and absence (pink) of ZnO NPs. The absorbance spectrum of HSA is shown for reference. b) Circular dichroism (CD) spectra of native HSA protein and HSA−BR complex solution in the presence of UV irradiated ZnO NPs. The near UV (inset) and far UV spectra reveal less than 2% change in tertiary and secondary structures, respectively.*

to be 6% and 51% in the absence and presence of ZnO NPs, respectively, under the same flow rate condition. Therefore, it is concluded that BR can be degraded significantly, even if, they are bound to HSA protein. Figure 4.8b shows circular dichroism (CD) spectra of native proteins and the ejected BR−HSA photoproduct, which was obtained after passing BR−HSA complex solution throughout the NP-based flow-device. From the CD spectra, a very negligible perturbation of the secondary and tertiary (inset) structure of the NP-associated enzyme HSA is clearly noticeable.

4.3. Conclusion:

To conclude, we present a novel mechanism for ZnO NP-sensitized BR degradation *via* FRET process, as schematically shown in Figure 4.6b. The efficient degradation in presence of smaller ZnO NPs containing higher concentration of defect states is attributed to the FRET from NP defect states to surface attached BR which introduces a pathway to degrade BR. ZnO NP has several advantages for BR photocatalysis under UV irradiation. First, these catalysts are easily prepared and the method does not need specialized equipments or reagents. Second, these NPs have been demonstrated to work as recyclable photocatalyst and exhibit excellent photocatalytic activity for the degradation of BR in multiple cycles. Finally, ZnO, which has huge absorption band at the near UV range, can protect the harmful effect of UV-light. These advantages substantially make this recyclable ZnO NP photocatalyst promising to be useful in the future technology of BR phototherapy. We have also proposed a FRET-based phototherapeutical device/system involving ZnO NP thin film in order to degrade BR in blood. Further technological refinement of the ZnO-based "nanotherapy" and rigorous clinical trial are likely to offer better phototherapeutic improvements in the treatment of hyperbilirubinemia.

References

[1] J.D. Ostrow, Bile Pigments and Jaundice: Molecular, Metabolic and Medical Aspects, Marcel Dekker, New York, 1986.

[2] R. Stocker, A.N. Glazer, B.N. Ames, Antioxidant Activity of Albumin-Bound Bilirubin, *Proc. Natl. Acad. Sci. U.S.A.* 84 (1987) 5918.

[3] D.A. Lightner, A.F. McDonagh, Molecular Mechanisms of Phototherapy for Neonatal Jaundice, *Acc. Chem. Res.* 17 (1984) 417.

[4] A.A. Lamola, W.E. Blumberg, R. McClead, A. Fanaroff, Photoisomerized Bilirubin in Blood from Infants Receiving Phototherapy, *Proc. Natl. Acad. Sci. U.S.A.* 78 (1981) 1882.

[5] S.E. Braslavsky, A.R. Holzwarth, K. Schaffner, Solution Conformations, Photophysics, and Photochemistry of Bile Pigments; Bilirubin and Biliverdin, Dimethyl Esters and Related Linear Tetrapyrroles, *Angew. Chem. Int. Ed.* 22 (1983) 656.

[6] G. Agati, F. Fusi, R. Pratesi, A.F. McDonagh, Wavelength-Dependent Quantum Yield for Z-E Isomerasation of Bilirubin Complexed with Human Serum Albumin, *Photochem. Photobiol.* 55 (1992) 185.

[7] A.F. McDonagh, G. Agati, F. Fusi, R. Pratesi, Quantum Yields for Laser Photocyclization of Bilirubin in the presence of Human Serum Albumon. Dependence of Quantum Yield on Excitation Wavelength, *Photochem. Photobiol.* 50 (1989) 305.

[8] A.F. McDonagh, L.A. Palma, D.A. Lightner, Blue Light and Bilirubin Excretion, *Science* 208 (1980) 145.

[9] J.Z. Zhang, Biomedical Applications of Shape-Controlled Plasmonic Nanostructures: A Case Study of Hollow Gold Nanospheres for Photothermal Ablation Therapy of Cancer, *J. Phys. Chem. Lett.* 1 (2010) 686.

[10] G.F. Paciotti, L. Myer, D. Weinreich, D. Goia, N. Pavel, R.E. McLaughlin, L. Tamarkin, Colloidal Gold: A Novel Nanoparticle Vector for Tumor Directed Drug Delivery, *Drug Delivery* 11 (2004) 169.

[11] X. Wu, H. Liu, J. Liu, K.N. Haley, J.A. Treadway, J.P. Larson, N. Ge, F. Peale, M.P. Bruchez, Immunofluorescent Labeling of Cancer Marker Her2 and Other Cellular Targets with Semiconductor Quantum Dots, *Nat. Biotechnol.* 21 (2002) 41.

[12] L.R. Hirsch, R.J. Stafford, J.A. Bankson, S.R. Sershen, B. Rivera, R.E. Rrice, J.D. Hazle, N.J. Halas, J.L. West, Nanoshell-Mediated Near-Infrared Thermal Therapy of Tumors under Magnetic Resonance Guidance, *Proc. Natl. Acad. Sci. U.S.A.* 100 (2003) 13549.

[13] E. Topoglidis, C.J. Campbell, A.E.G. Cass, J.R. Durrant, Factors that Affect Protein Adsorption on Nanostructured Titania Films. A Novel Spectroelectrochemical Application to Sensing, *Langmuir* 17 (2001) 7899.

[14] Y. Li, W. Xie, X. Hu, G. Shen, X. Zhou, Y. Xiang, X. Zhao, P. Fang, Comparison of Dye Photodegradation and its Coupling with Light-to-Electricity Conversion over TiO_2 and ZnO, *Langmuir* 26 (2010) 591.

[15] J. Zhou, N.S. Xu, Z.L. Wang, Dissolving Behavior and Stability of ZnO Wires in Biofluids- A Study on Biodegradability and Biocompatibility of ZnO Nanostructures, *Adv. Mater.* 18 (2006) 2432.

[16] P.V. Kamat, R. Huehn, R. Nicolaescu, A "Sense and Shoot" Approach for Photocatalytic Degradation of Organic Contaminants in Water, *J. Phys. Chem. B* 106 (2002) 788.

[17] J.M. Herrmann, Heterogeneous Photocatalysis: Fundamentals and Applications to the Removal of Various Types of Aqueous Pollutants, *Catal. Today* 53 (1999) 115.

[18] P.C. Maness, S. Smolinski, D.M. Blake, Z. Huang, E.J. Wolfrum, W.A. Jacoby, Bactericidal Activity of Photocatalytic TiO_2 Reaction: toward an Understanding of Its Killing Mechanism, *Appl. Environ. Microbiol.* 65 (1999) 4094.

[19] S. Sarkar, A. Makhal, S. Baruah, M.A. Mahmood, J. Dutta, S.K. Pal, Nanoparticle-Sensitized Photodegradation of Bilirubin and Potential Therapeutic Application, *J. Phys. Chem. C* 116 (2012) 9608.

[20] X. Wang, X. Kong, Y. Yu, H. Zhang, Synthesis and Characterization of Water-Soluble and Bifunctional ZnO-Au Nanocomposites, *J. Phys. Chem. C* 111 (2007) 3836.

[21] J.D. Ye, S.L. Gu, F. Qin, S.M. Zhu, S.M. Liu, X. Zhou, W. Liu, L.Q. Hu, R. Zhang, Y. Shi, Y.D. Zheng, Correlation Between Green Luminescence and Morphology Evolution of ZnO Films, *Appl. Phys. A* 81 (2005) 759.

[22] H. Idriss, M.A. Barteau, Photoluminescence from Zinc Oxide Powder To Probe Adsorption and Reaction of O_2, CO, H_2, HCOOH, and CH_3OH, *J. Phys. Chem.* 96 (1992) 3382.

[23] H. Idriss, R.M. Andrews, M.A. Barteau, Application of Luminescence Techniques to Probe Surface-Adsorbate Interactions on Oxide Single Crystals, *J. Vac. Sci. Technol. A* 11 (1993) 209.

[24] R.M. Clegg, [18] Fluorescence Resonance Energy Transfer and Nucleic Acids, *Methods Enzymol.* 211 (1992) 353.

[25] D.M.J. Lilley, T.J. Wilson, Fluorescence Resonance Energy Transfer as a Structural Tool for Nucleic Acids, *Curr. Opin. Chem. Biol.* 4 (2000) 507.

[26] J.R. Lakowicz, Principles of Fluorescence Spectroscopy, 2nd ed., Kluwer Academic/ Plenum, New York, 1999.

[27] J.H. Warner, A.R. Watt, E. Thomsen, N. Heckenberg, P. Meredith, H. Rubinsztein-Dunlop, Energy Transfer Dynamics of Nanocrystal-Polymer Composites, *J. Phys. Chem. B* 109 (2005) 9001.

[28] A. Makhal, S. Sarkar, T. Bora, S. Baruah, J. Dutta, A.K. Raychaudhuri, S.K. Pal, Dynamics of Light Harvesting in ZnO Nanoparticles, *Nanotechnology* 21 (2010) 265703.

[29] S. Baruah, S.S. Sinha, B. Ghosh, S.K. Pal, A.K. Raychaudhuri, J. Dutta, Photoreactivity of ZnO Nanoparticles in Visible Light: Effect of Surface States on Electron Transfer Reaction, *J. Appl. Phys.* 105 (2009) 074308.

[30] S. Sarkar, A. Makhal, T. Bora, S. Baruah, J. Dutta, S.K. Pal, Photoselective Excited State Dynamics in ZnO-Au Nanocomposites and their Implications in Photocatalysis and Dye-Sensitized Solar Cells, *Phys. Chem. Chem. Phys.* 13 (2011) 12488.

[31] Z. Yang, C. Zhang, Adsorption and Photocatalytic Degradation of Bilirubin on Hydroxyapatite Coatings with Nanostructural Surface, *J. Mol. Catal. A: Chem.* 302 (2009) 107.

[32] W.E. Kurtin, Spectroscopy and Photochemistry of Bilirubin Photoproducts. I. Methylvinylmaleimide, *Photochem. Photobiol.* 27 (1978) 503.

[33] D.A. Lightner, G.B. Quistad, Methylvinylmleimide from Bilirubin Photooxidation, *Science* 175 (1971) 324.

[34] R. Narayanan, M.A. El-Sayed, Shape-Dependent Catalytic Activity of Platinum Nanoparticles in Colloidal Solution, *Nano Lett.* 4 (2004) 1343.

[35] A. Mclaren, T.V. Solis, G. Li, S.C. Tsang, Shape and Size Effects of ZnO Nanocrystals on Photocatalytic Activity, *J. Am. Chem. Soc.* 131 (2009) 12540.

[36] M. Auffan, J. Rose, J.Y. Bottero, G.V. Lowry, J.P. Jolivet, M.R. Wiesner, Towards a Definition of Inorganic Nanoparticles from an Environmental, Health and Safety Perspective, *Nat. Nanotech.* 4 (2009) 634.

[37] C. Burda, X.B. Chen, R. Narayanan, M.A. El-Sayed, Chemistry and Properties of Nanocrystals of Different Shapes, *Chem. Rev.* 105 (2005) 1025.

[38] M. Murdoch, G.I.N. Waterhouse, M.A. Nadeem, J.B. Metson, M.A. Keane, R.F. Howe, J. Llorca, H. Idriss, The Effect of Gold Loading and Particle Size on Photocatalytic Hydrogen Production from Ethanol over Au/TiO_2 Nanoparticles, *Nat. Chem.* 3 (2011) 489.

[39] J.C. Wang, P. Liu, X.Z. Fu, Z.H. Li, W. Han, X.X. Wang, Relationship Between Oxygen Defects and the Photocatalytic Property of ZnO Nanocrystals in Nafion Membranes, *Langmuir* 25 (2009) 1218.

[40] M.Y. Guo, A.M.C. Ng, F. Liu, A.B. Djuri, W.K. Chan, H. Su, K.S. Wong, Effect of Native Defects on Photocatalytic Properties of ZnO, *J. Phys. Chem. C* 115 (2011) 11095.

[41] D.S. Bohle, C.J. Spina, Cationic and Anionic Surface Binding Sites on Nanocrystalline Zinc Oxide: Surface Influence on Photoluminescence and Photocatalysis, *J. Am. Chem. Soc.* 131 (2009) 4397.

[42] M.R. Hoffmann, S.T. Martin, W.Y. Choi, D.W. Bahnemann, Environmental Applications of Semiconductor Photocatalysis, *Chem. Rev.* 95 (1995) 69.

[43] Y. Xu, C.H. Langford, Variation of Langmuir Adsorption Constant Determined for TiO_2-Photocatalyzed Degradation of Acetophenone under Different Light Intensity, *J. Photochem. Photobiol. A* 133 (2000) 67.

[44] J. Das, D. Khushalani, Nonhydrolytic Route for Synthesis of ZnO and its Use as a Recyclable Photocatalyst, *J. Phys. Chem. C* 114 (2010) 2544.

[45] T.J. Kuo, C.N. Lin, C.L. Kuo, M.H. Huang, Growth of Ultralong ZnO Nanowires on Silicon Substrates by Vapor Transport and Their Use as Recyclable Photocatalysts, *Chem. Mater.* 19 (2007) 5143.

[46] T.J. Brunner, P. Wick, P. Manser, P. Spohn, R.N. Grass, L.K. Limbach, A. Bruinink, W.J. Stark, In Vitro Cytotoxicity of Oxide Nanoparticles: Comparison to Asbestos, Silica, and the Effect of Particle Solubility, *Environ. Sci. Technol.* 40 (2006) 4374.

[47] R.D. Palmiter, Protection Against Zinc Toxicity by Metallothionein and Zinc Transporter 1, *Proc. Natl. Acad. Sci. U.S.A.* 101 (2004) 4918.

Chapter 5

Excited State Dynamics of Electron/Energy Transfer in Metal−Semiconductor Nanocomposites and their Implications in the Proximity of Organic Dyes

5.1. Introduction:

Quantum dots and metal nanoparticles (NPs) are of great interest because of their unique electronic, optical, and magnetic properties [1-5]. In particular, noble metal NPs having diameters below 10 nm have been the focus of recent works [6-7] due in part to their enhanced reactivities. For example, Au NPs of 3 to 8 nm diameter have been shown to tune the catalytic properties of TiO_2 [8-10]. In the structure of composite nanocluster-based dye-sensitized solar cells (DSSCs), Au NPs are employed to facilitate efficient charge separation, thus serving as a Schottky barrier for reducing the rate of electron−hole recombination [11]. Tetsu *et al.* [12] studied the enhancement of anodic photocurrents induced by visible light irradiation in a device based on Au NPs deposited on TiO_2 films. Their data indicate that using Au Schottky contacts in photovoltaic cells may yield improved device performance. In an earlier investigation [13] by Kamat and co-workers, it was shown that the photoelectrochemical performance of nanostructured TiO_2 films could be improved by coupling to noble metal NPs. Using the hypothesis of Fermi level equilibration, it has been possible to understand the increase in the photovoltage of TiO_2−Au films [13-14] as well as the charging effects in metal−semiconductor colloids [15-18]. Although there have been many attempts to obtain improved device performance with metal−semiconductor nanocomposites (NCs), the mechanism of charge separation as well as the excitation-dependent interfacial charge transfer kinetics in the nanoscale regime are yet to be fully understood.

The improved performance of photoactive processes and devices has typically been achieved with composite nanostructures based on semiconductor oxides, such as TiO_2 and ZnO, modified with noble metal NPs. A systematic study of the energetics of such NC

systems is important for tailoring the properties of next-generation nanodevices. The mediating role of noble metals in storing and shuttling photogenerated electrons from the semiconductor to an acceptor in a photocatalytic process can be understood by designing metal−semiconductor NC structures. Among direct band-gap crystals, ZnO has a wide band gap of 3.37 eV and a large exciton binding energy of 60 meV at room temperature. Two photoluminescence (PL) bands are usually found: a relatively weak and narrow UV emission band (band-gap emission) around 370 nm (3.35 eV), which is just below the onset of absorption, and a much stronger and broader visible emission band with a maximum near 550 nm (2.25 eV). The UV emission band is due to the radiative annihilation of excitons, the high binding energy of which permits observation even at significantly elevated temperatures [19]. The green emission is known to come from the defect centers located near the surface of the NPs [20]. Numerous studies have been conducted to improve the band-gap emission by controlling the influence of defect states for the improvement of emission efficiency in semiconductors [21-22]. In an earlier study [23] with ZnO−Pt NCs, it was reported that the band-gap emission is enhanced substantially, while the defect emission is suppressed. The underlying mechanism behind enhancement of the band-gap emission and quenching of the defect-mediated green emission is a combination of the energy transfer between defects and surface plasmon (SP) resonance in Pt NPs, as well as electron–hole pair generation and recombination processes in ZnO nanorods (NRs). A similar study [24] with Au-capped ZnO NRs also indicates that the suppression of the green emission might be due to a combined effect of Au SP and passivation of the ZnO NR surface traps.

The present study is aimed at elucidating the mechanism of pronounced intrinsic emission from colloidal ZnO and ZnO−Au NCs upon above band-edge and below band-gap excitation. To probe the correlation between dynamics of photogenerated carrier trapping at the defect sites and kinetics of charge migration from ZnO and ZnO−Au semiconductors, methylene blue (MB) degradation was examined using UV-light and optical filters. Photostability and luminescence studies from a ZnO−Au NC colloidal dispersion show that Förster resonance energy transfer (FRET) dynamics from donor semiconductor to gold acceptor can be observed. Finally, we have designed a model DSSC based on ZnO NPs which leads to an increase in short-circuit photocurrent (J_{sc}) and

improved overall efficiency (η) in the presence of Au NPs. The reason behind the giant improvement in efficiency is also clarified by photoconductivity measurements of the ZnO NP and ZnO−Au NC thin films.

5.2. Results and Discussion:

5.2.1. Photoselective Excited State Dynamics in ZnO−Au Nanocomposites and their Implications in Photocatalysis and Dye-Sensitized Solar Cells [25]:

The structure, crystalline phase, size, and morphology of ZnO NPs and ZnO−Au NCs were determined (with TEM). Representative HRTEM images of the ZnO−Au NCs are illustrated in Figure 5.1a, where the measured average diameters are 6 and 8 nm for ZnO and Au NPs, respectively. From TEM observation it was found that, the ZnO−Au NCs are fairly monodispersed and their shapes are different from that of the spherical ZnO NPs due

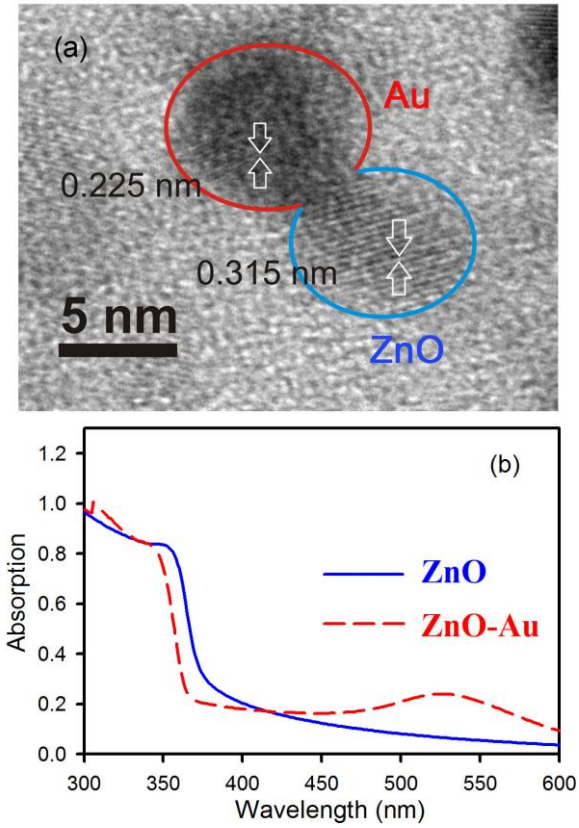

Figure 5.1. *a) HRTEM image of dumbbell-like ZnO−Au NCs with Au attached to the ZnO surface. b) Steady-state absorption spectra of bare ZnO NPs (blue) and ZnO−Au NCs (red) showing the SP band at 520 nm.*

to the incorporation of Au components. The higher contrast of Au observed in the TEM image is due to the higher electron density of metallic Au compared to semiconducting ZnO. The relevant TEM images are shown in Figure 5.2a−c. After the synthesis of ZnO−Au NCs, the Zn:Au weight ratio was calculated by using a field emission-type scanning electron microscope. From EDAX analysis it was found to be 1.3:1 as shown in the table below.

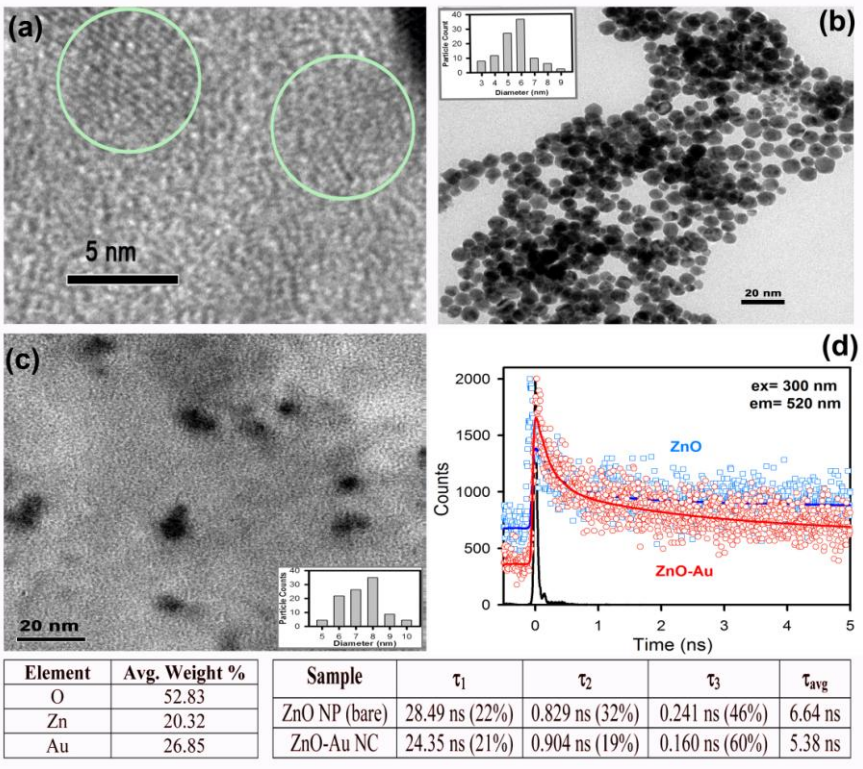

Element	Avg. Weight %
O	52.83
Zn	20.32
Au	26.85

Sample	τ_1	τ_2	τ_3	τ_{avg}
ZnO NP (bare)	28.49 ns (22%)	0.829 ns (32%)	0.241 ns (46%)	6.64 ns
ZnO-Au NC	24.35 ns (21%)	0.904 ns (19%)	0.160 ns (60%)	5.38 ns

Figure 5.2. *a) HRTEM image of bare ZnO NPs. b) TEM image of bare ZnO NPs (inset shows particle size distribution of ZnO NPs). c) TEM image of ZnO−Au NCs (inset shows particle size distribution of Au NPs attached to ZnO NPs). Table (left) shows EDAX analysis of ZnO−Au NCs by using a field emission-type SEM. Table (right) shows picosecond-resolved luminescence transients of ZnO NPs in the presence and absence of Au NPs. The numbers in the parentheses indicate relative weightage. d) The emissions from ZnO NPs and ZnO−Au NCs (probing at 520 nm) were detected with a 300 nm laser excitation.*

The visible absorption spectrum of gold grown onto the ZnO NPs was clearly characterized by the plasmon resonance peak of Au NPs. Figure 5.1b shows the absorption spectra of the ZnO−Au NCs and pure ZnO NPs. It is generally believed that the band-edge absorption of semiconductor in the quantum-confined size regime (≤ 7 nm) is dependent

on the particle size [26]. There is no distinct variation in absorption characteristics in the range 300−420 nm, which implies that no apparent growth of ZnO NPs occurred during the formation of Au on ZnO NPs. An SP band, resulting from Au in the ZnO−Au NCs, centered at ~525 nm can also be observed in the NC (Figure 5.1b). In Figure 5.3a, we have plotted the excitation spectra of bare ZnO NPs and ZnO−Au NCs monitored at the emission peaks (368 nm and 550 nm, respectively). The room-temperature PL spectra of both the bare ZnO NPs and ZnO−Au NCs (Figure 5.3b) are comprised of one broad

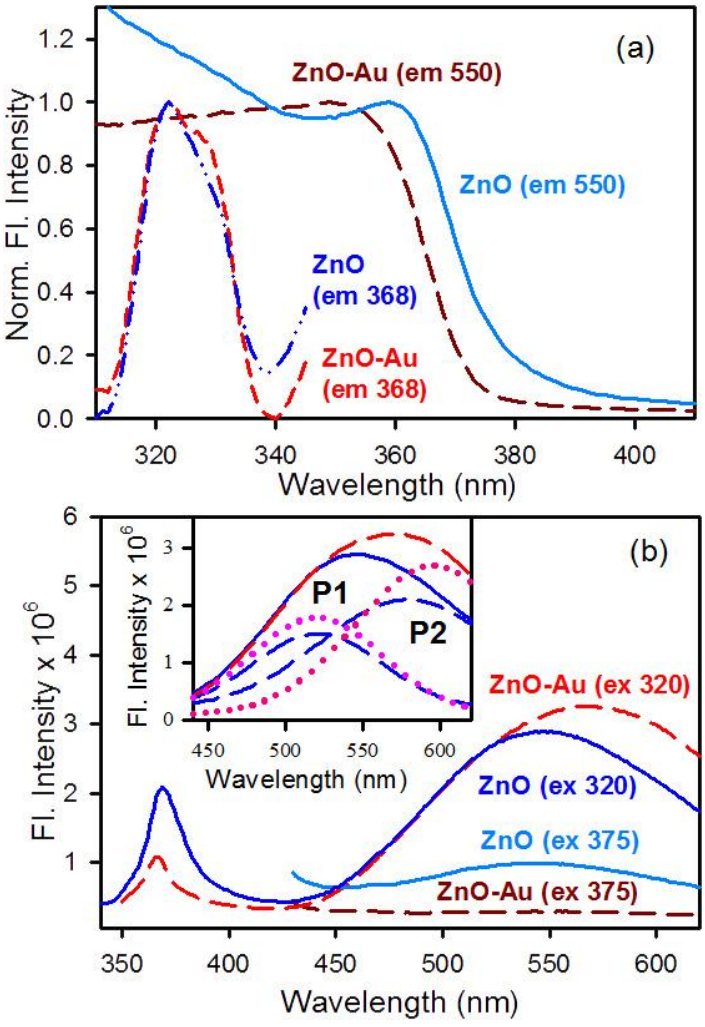

Figure 5.3. *a) Excitation spectra of ZnO NPs (blue) and ZnO−Au NCs (red) monitored at 368 nm and 550 nm. b) Steady-state emission spectra of ZnO NPs (blue) and ZnO−Au NCs (red) are shown (excitation at 320 and 375 nm). The inset shows that the defect related green emission is composed of two bands, P1 and P2.*

emission band upon excitation below the band-gap (λ_{ex} = 375 nm) and two emission bands upon excitation above the band-edge (λ_{ex} = 320 nm). The narrow UV band centered at 368 nm is due to exciton recombination. Analysis of the broad emission observed in our sample in the blue-green region shows that it is composed of two emission bands (shown as dotted lines in Figure 5.3b, inset), which are marked as P1 and P2 [27]. The characteristics of each emission band depend upon whether it arises from a doubly-charged vacancy center V_O^{++} (P2) or a singly-charged vacancy center V_O^{+} (P1). The V_O^{++} center, created by capture of a hole by the V_O^{+} center in a depletion region, leads to the P2 emission line. The singly-charged center (V_O^{+}) in the absence of a depletion region turns into a neutral center ($V_O^{\times}$) upon the capture of an electron (n-type ZnO) from the conduction band, which then recombines with a hole in the valence band giving rise to the P1 emission [28]. The spectral content of the blue-green band is determined by the relative weight of the two overlapping emission peaks.

As shown in Figure 5.3b, when below band-gap excitation (λ_{ex} = 375 nm) was used, the defect-related emission is suppressed in the presence of Au NPs. Herein, we propose FRET from donor ZnO NP to Au acceptor, which is responsible for the observed suppression of emission bands. The spectral overlap of the ZnO emission spectrum with that of the Au absorption spectrum is shown in Figure 5.4a. The faster excited-state lifetime of the ZnO−Au NC with respect to that of the free ZnO NP is clearly noticeable from Figure 5.4b. Details of the spectroscopic parameters and the fitting parameters of the fluorescence decays are tabulated in Table 5.1. In order to estimate FRET efficiency of the donor (ZnO) and hence to determine distances of donor−acceptor pairs, we followed the methodology described in chapter 13 of reference [29]. In this case the spectral overlap integral, J (equation 2.9) is found to be 2.82×10^{16}. From the average lifetime calculation for the ZnO−Au NC, we obtain the effective distance between the donor and the acceptor, $r_{DA} \approx 2.55$ nm, using equation 2.11 and 2.12b. It is to be noted that the smaller value of r_{DA} compared to the radius of the ZnO NPs (~3 nm; Figure 5.1a) can be rationalized from the fact that the origin of the PL peaking at 550 nm arises essentially from surface defects in the ZnO NPs [30]. Moreover, comparing the PL spectra of bare ZnO NPs and ZnO−Au NCs upon excitation above the band-edge, it was observed that the emission due to

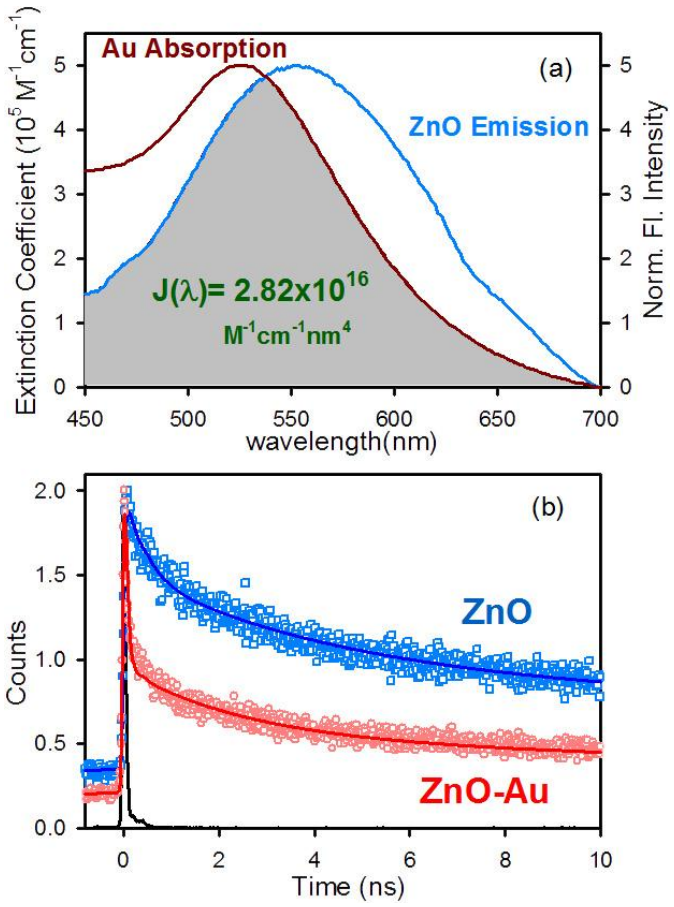

Figure 5.4. *a) SP band of Au NPs and emission spectra of ZnO NPs are shown. An overlapping zone between emission of ZnO NPs and absorption of acceptor Au is indicated as a gray shaded zone. b) The picosecond-resolved fluorescence transients of ZnO NPs, in the absence (blue) and presence of acceptor Au (red) (excitation at 375 nm) collected at 550 nm.*

excitonic recombination is suppressed, while the defect-related emission is red-shifted in the presence of Au NPs. In this respect, we have shown that the energy is transferred from the Vo^{+} center to Au NPs, which leads to a reduction in the PL intensity at 520 nm. The energy transfer efficiency (*E*) is found to be ~19% (Figure 5.2d), which is much lower value compared to that of below band-gap excitation (E = ~85%). In retrospect, excited electrons are preferentially trapped by V_O^{++} center, which is originated by V_O^{+} center by capturing a hole. The formation of V_O^{++} centers is more favourable upon band-edge excitation since the photogenerated holes have enough time to migrate during thermalization of highly excited electrons. This leads to more facile recombination of excited electrons *via* V_O^{++} centers, and this recombination pathway is supported by the appreciable red-shift observed in ZnO−Au NCs upon above band-edge excitation.

However, the decrease in band-edge emission intensity in the presence of Au NPs is well understood, whereby, Au acts as a sink that can store and shuttle photogenearted electrons [16, 31]. As per our understanding, the optical activity of surface defect states in the overall emission of the semiconductor solely depends on the excitation wavelength.

Table 5.1. Dynamics of picosecond-resolved luminescence transients of ZnO NPs in the presence and absence of Au NPs[a] and the kinetics parameters[b] for the photoselective degradation of MB in the presence of ZnO and ZnO−Au nanocolloids.

DYNAMICS STUDY				
Samples	τ_1 **(ns)**	τ_2 **(ns)**	τ_3 **(ns)**	τ_{avg} **(ns)**
ZnO NP (bare)	47.58 (41%)	3.78 (23%)	0.280 (36%)	20.48
ZnO−Au NC	33.34 (8%)	2.60 (10%)	0.051 (82%)	2.97
KINETICS STUDY [y=A exp(−kt) + y_0]				
Samples and Filters	k **(sec^{-1})**		A **(%)**	R^2
ZnO (420 HP)	1.055×10^{-3}		2.66	0.96
ZnO−Au (420 HP)	1.388×10^{-3}		2.78	0.93
ZnO (460 LP)	2.203×10^{-3}		11.68	0.97
ZnO−Au (460 LP)	2.528×10^{-3}		29.31	0.99
ZnO (320 HP−460 LP)	2.340×10^{-3}		23.55	0.99
ZnO−Au (320 HP−460 LP)	2.287×10^{-3}		19.65	0.99

[a]The emissions from ZnO NPs and ZnO−Au NCs (probing at 550 nm) were detected with a 375 nm laser excitation. Numbers in the parentheses indicate relative weightage. [b]kinetic constants (k), regression coefficients (R^2) and the percentages of photoselective degradation (A). Parentheses indicate the optical filters used in the study.

It was reported by several researchers that in the presence of metal NPs in close proximity to semiconductor NPs, enhanced photocatalytic degradation of test solutions was observed. Thus we compared the role of a Au layer in promoting photogenerated charges in ZnO−Au and ZnO colloids by carrying out photoreduction of a test contaminant; MB is known to be an excellent probe for the study of interfacial electron transfer in colloidal semiconductor systems [32]. In general, the higher the charge migration from the surface

of the ZnO semiconductor, the faster will be the degradation of the surface-attached MB. We have used a fiber-optic based system for the measurement of light-induced chemical processes with spectroscopic precision. To demonstrate the sensitivity and usefulness of our designed system, we previously conducted a detailed study of the photodeteriotion of vitamin B2 (riboflavin) in aqueous phase [33]. In order to obtain different excitations we have used three different types of filters placed on a home-made UV bath (60 W; normally used for water purification). The optical filters, namely 420 high-pass (HP), 460 low-pass

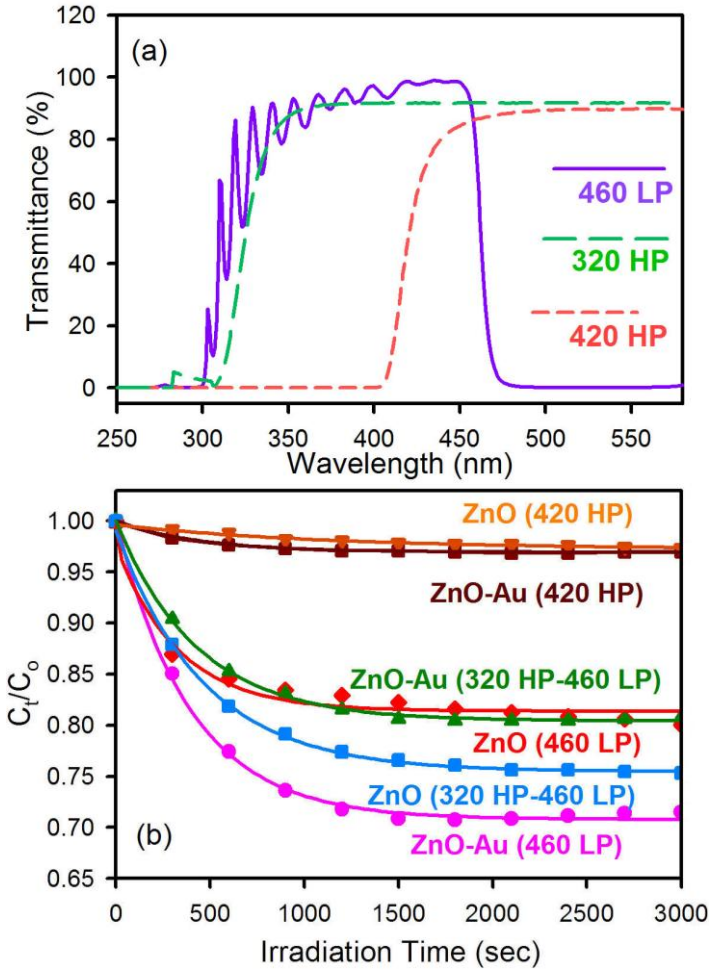

Figure 5.5. *a) The transmittance spectra of 320 HP (green), 420 HP (red) and 460 LP (violet) optical filters are shown. b) Plot of relative concentration (C_t/C_0) versus time for the degradation of MB (monitored at 655 nm) is shown. The degradation is performed in the presence of colloidal solutions of ZnO NPs and ZnO−Au NCs under different excitation conditions (parentheses indicate the optical filters used for the desired excitation).*

(LP) and 320 HP, were chosen in order to achieve controlled and preferential excitation. The characteristics of the optical filters are shown in Figure 5.5a, which clearly depicts that 420 HP (passes light above 420 nm) is only used for the SP excitation of Au NPs, 460 LP (passes light below 460 nm) is used for the above band-edge excitation of ZnO, and the combined use of 320 HP and 460 LP (passes light above 320 nm and below 460 nm) leads to preferential excitation of below band-gap excitation of ZnO. In Figure 5.5b, the relative concentration (C_t/C_0) of MB in solution is plotted with respect to UV-irradiation time, the results of which indicate the photodegradation of MB upon continued UV-irradiation. It is to be noted that there was no obvious change in the concentration of MB stored in the dark for several hours (data are not shown here). Under selective UV radiation we have recorded the absorption peak of MB (at 655 nm) at 5 sec intervals, using SPECTRA SUITE software supplied by Ocean Optics, and plotted it against the time of photoirradiation. All the photodegradation curves were found to follow a first-order exponential equation, and the kinetic parameters are represented in Table 5.1. The decrease in the absorbance at 655 nm implies the generation of the colourless photoproduct leuco methylene blue (LMB). Note that in the present study we are interested in exploring the long-time photodegradation of MB (for several min). To compare the photodegradation of MB in the presence of ZnO NPs and ZnO−Au NCs with a 420 HP filter, it is clearly shown that no considerable change in absorbance peak at 655 nm takes place upon Au SP excitation. The photodegradation rates are found to be 1.055×10^{-3} sec^{-1} and 1.388×10^{-3} sec^{-1}, and the percentages of total photodegradation (i.e., the value of A in the first-order kinetic equation shown in Table 5.1) are 2.66 and 2.78 for ZnO and ZnO−Au NCs, respectively. It reveals that electron transfer from Au NPs to MB is not allowed upon direct excitation of Au. Upon, replacing the 420 HP filter with a 460 LP filter, we observed an increase in the photodegradation rates in the presence of Au NPs ($k_{ZnO}=2.203\times10^{-3}$ sec^{-1}, $k_{ZnO-Au}= 2.258\times10^{-3}$ sec^{-1}), and the percentage of photodegradation also improved from $A_{ZnO}= 11.68$ to $A_{ZnO-Au}= 29.31$. This is attributed to improved charge separation in the presence of Au NPs, which also can store and shuttle excited electrons, thereby suppressing recombination. Such Au NP-stabilized ZnO NPs behave as more efficient electron accumulators (at the conduction band) than the bare oxide [34]. In retrospect, the photodegradation rate of MB was observed to decrease ($k_{ZnO}= 2.340\times10^{-3}$ sec^{-1}, $k_{ZnO-Au}=$

2.287×10^{-3} sec^{-1}), and the percentage of total photodegradation was found to be much lower (A_{ZnO}= 23.55, A_{ZnO-Au}= 19.65) in the presence of Au NPs when we used combined optical filters of 320 HP and 460 LP. This happens because excited electrons of ZnO can easily occupy the defect centers and resonantly transfer their energy to Au NPs via nonradiative processes (FRET, as previously discussed). As a consequence, in presence of Au, excited electrons are unable to migrate from the ZnO surface to perform the reduction of MB. Thus, it is important to note that the differences in rate constants are not significant, whereas considerable differences in the magnitude of total photodegradation are observed during above band-edge and below band-gap excitation of ZnO and ZnO−Au NCs. This is due to the fact that the total number of active electrons available for carrying out MB degradation is different for ZnO and ZnO−Au NCs for any particular excitation. Our study clearly demonstrates that the role of incorporated metal on semiconductor for facilitating redox reactions is solely dependent on the excitation of the semiconductor.

The efficient charge migration in metal−semiconductor NCs is expected to lead to improved DSSC performance of ZnO−Au NCs compared to bare ZnO [35]. Thus, we measured and directly compared the IPCE (using equation 2.31) of ZnO and ZnO−Au-based DSSCs. Each of the two examined ZnO and ZnO−Au-based cells contained the same sensitizer dye N719 and I^-/I_3^- electrolyte, to allow for a fair comparison. The IPCE curves of the two cells are presented in Figure 5.6a, which shows a broad spectral response in the range 440 to 600 nm. Significant enhancement in photocurrent generation is seen upon deposition of Au NPs on the ZnO electrodes. The enhancement in the photocurrent generation efficiency is indicative of the fact that the Au NPs assist in the charge separation within the nanostructured ZnO film as well as improve the interfacial charge transfer processes. Figure 5.6b shows the photocurrent−voltage (J−V) characteristics for solar cells, constructed using the bare ZnO NPs and ZnO−Au NCs. The short-circuit current density (J_{SC}) and the open-circuit voltage (V_{OC}) of the ZnO−Au NC-based DSSC were 261.87 μA/cm^2 and 0.605 V, respectively, which are much higher than that of the bare ZnO-based DSSC (J_{SC} = 7.5 μA/cm^2, V_{OC} = 0.394 V). The calculated values of *FF* and the overall power conversion efficiency of the ZnO-based DSSC were 30% and 0.012%, respectively, which are substantially improved in the presence of gold (*FF* = 53%

and η = 0.8%). Table 5.2 summarizes the measured and calculated values obtained from each $J-V$ curve.

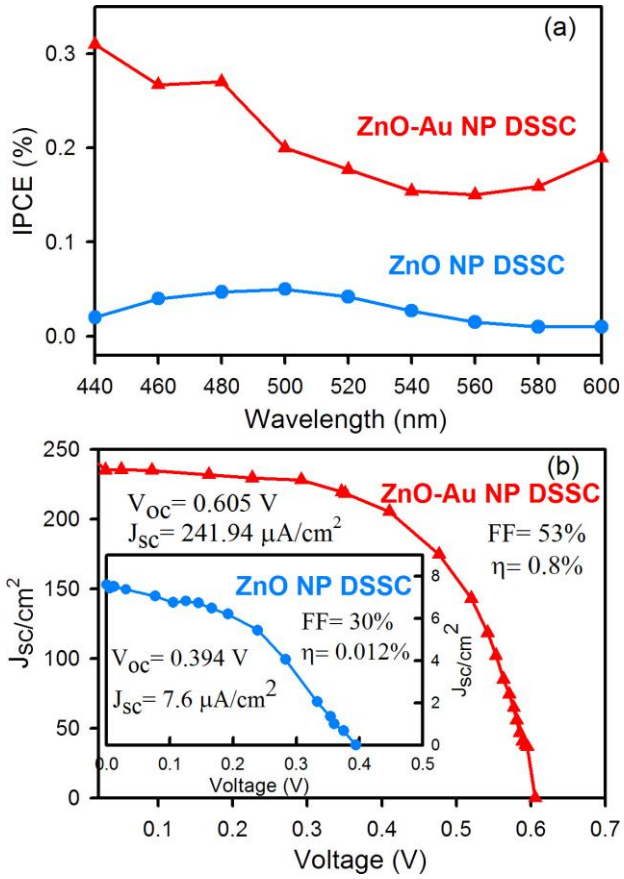

Figure 5.6. *a) Dependence of the incident photon conversion efficiency on the incident wavelength for ZnO NP (blue) and ZnO−Au NC (red) films cast on an FTO plate. b) Photocurrent-voltage (J−V) characteristics of ZnO−Au NC and ZnO NP (inset) based DSSC (with 10.5 klux illumination intensity at the area of 0.16 cm^2 from a 90 W xenon lamp).*

Table 5.2. Device performance[c] of the DSSCs with ZnO NP and ZnO−Au NC.

Device with N719	V_{OC} (V)	J_{SC} (µA/cm^2)	*FF* (%)	η (%)
ZnO NP	0.394	7.5	44	0.012
ZnO−Au NC	0.605	261.87	53	0.8

[c]*short-circuit photocurrent densities (J_{SC}/cm^2), open-circuit voltage (V_{OC}), fill factor (FF), and efficiency (η) (see equations 2.28−2.29).*

The photoconductivity measurement [36-37] (as discussed in section 3.1.12) of the ZnO NP and ZnO−Au NC thin films were necessary in order to further understand the electron mobility (i.e. performance of the semiconductor) and charge transfer mechanism. Figure 5.7 shows the photocurrent response for the ZnO NP and ZnO−Au NC thin films, where an improved photocurrent was observed for the ZnO−Au NC thin film (~70 µA) under illuminated condition compared to the ZnO NP thin film (~1.5 µA). This shows that the photogenerated electrons in ZnO NPs (from visible-light absorption by the intermediate

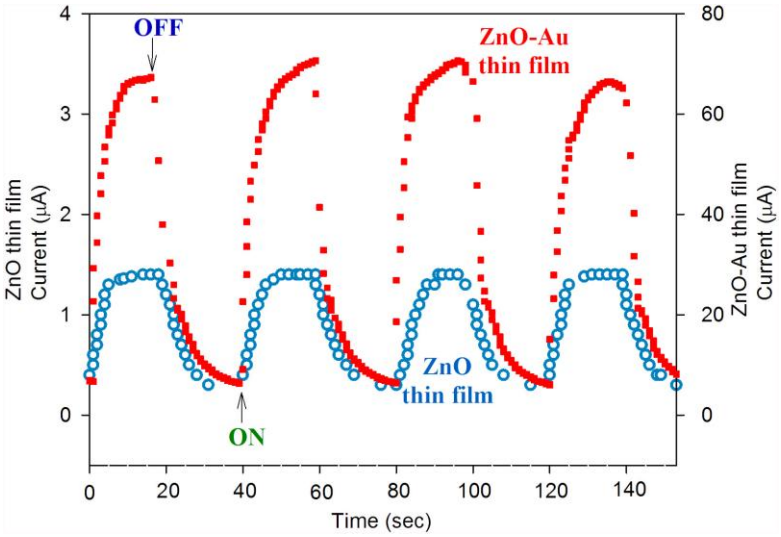

Figure 5.7. *Photocurrent responses of ZnO NP and ZnO−Au NC thin films under bias voltage of 5V. The photocurrent was measured across the thickness of the films with 25 mW/cm^2 incident power from a halogen light source.*

Vo$^+$ center) are transferred to Au NPs, as mentioned earlier contributing in enhanced photocurrent of the ZnO−Au NC thin films compared to the ZnO NP. In case of the model DSSC shown here, a similar mechanism is responsible for the enhanced photocurrent observed (Figure 5.6b) in the presence of Au NPs along with the ZnO NPs. Some of the injected electrons from the excited N719 dye to the CB of ZnO are captured by the intermediate defect sites of ZnO (V_O^+) resulting in poor photocurrent and fill factor of DSSC. However, in the presence of Au NPs in the ZnO thin film, we have observed higher photocurrent (J_{SC} = 261.87 µA/cm^2) and fill factor (*FF* = 53%) compared to the ZnO NP DSSC (J_{SC} = 7.5 µA/cm^2 and *FF* = 44%). Thus, it is noted that the ratios of improved

photocurrent response (70:1.5) and short-circuit current (261.9:7.5) for ZnO and ZnO−Au

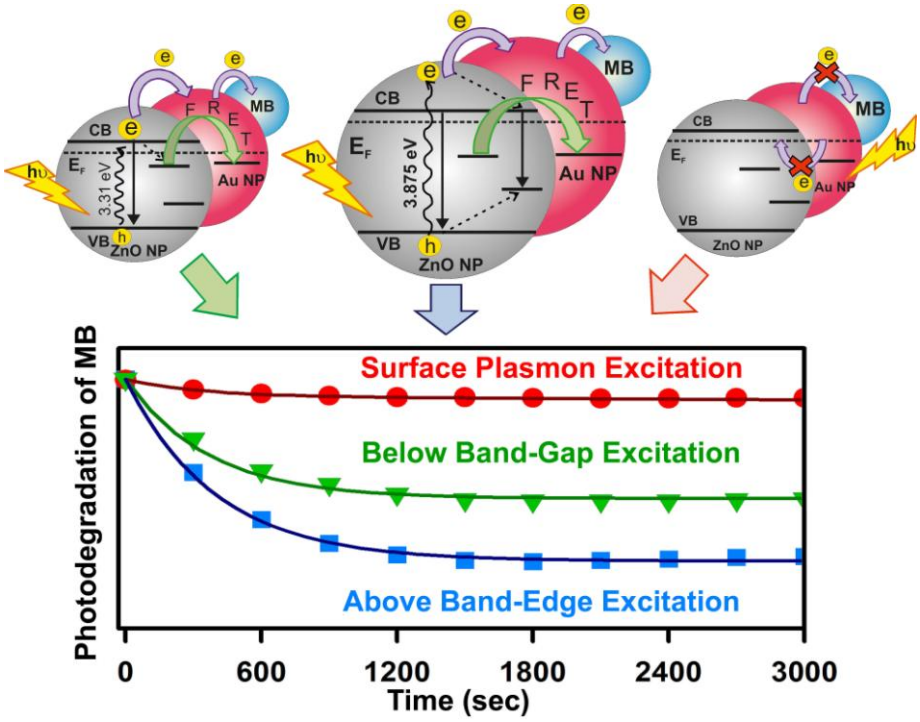

Scheme 5.1. *Schematic representation of the metal−semiconductor system: The system consists of a semiconductor ZnO NP (gray big ball) containing appreciable amounts of defect states on which Au NP (red big ball) is fabricated. MB (small blue ball) is bound to the ZnO−Au NC by surface adsorption. The dynamics of charge separation and interparticle charge/energy migration of the entire structure is shown. Thereafter, photodegradation of MB under different excitation conditions is also shown by a graph, which reveals the mediating role of Au NP in photocatalysis.*

semiconductors are comparable. The improvement observed in the overall device performance is mainly due to increased conductivity by transferring the trapped electrons in Vo^{+} centers of ZnO to Au NPs, which then contribute to the photocurrent as well as the fill factor of the DSSC. It is worth noting that the efficiency obtained from the model DSSC with the use of NPs is lower than the maximum efficiency reported [38] with NRs, which were employed to provide higher surface area and better charge transport. The overall mechanistic explanations for the excitation-dependent recombination processes and the catalytic activity of Au NPs in the ZnO−Au NCs have been schematically shown in Scheme 5.1.

5.2.2. Highly Efficient ZnO−Au Schottky Barrier Dye-Sensitized Solar Cells: Role of Gold Nanoparticles on the Charge Transfer Process [35]:

The surface morphology of hydrothermally grown ZnO NRs and *in situ* deposited Au NP coated ZnO NRs are shown in Figure 5.8, where the diameter of the ZnO NRs was found to vary from ~500 to 700 nm and length from ~8 to 9 μm. The distribution of the Au NPs over the ZnO NR surface is found fairly uniform as can be observed from Figure 5.8c. The cross-sectional SEM image indicates (Figure 5.8d) that the Au NPs grow almost homogeneously over the complete length of the ZnO NRs.

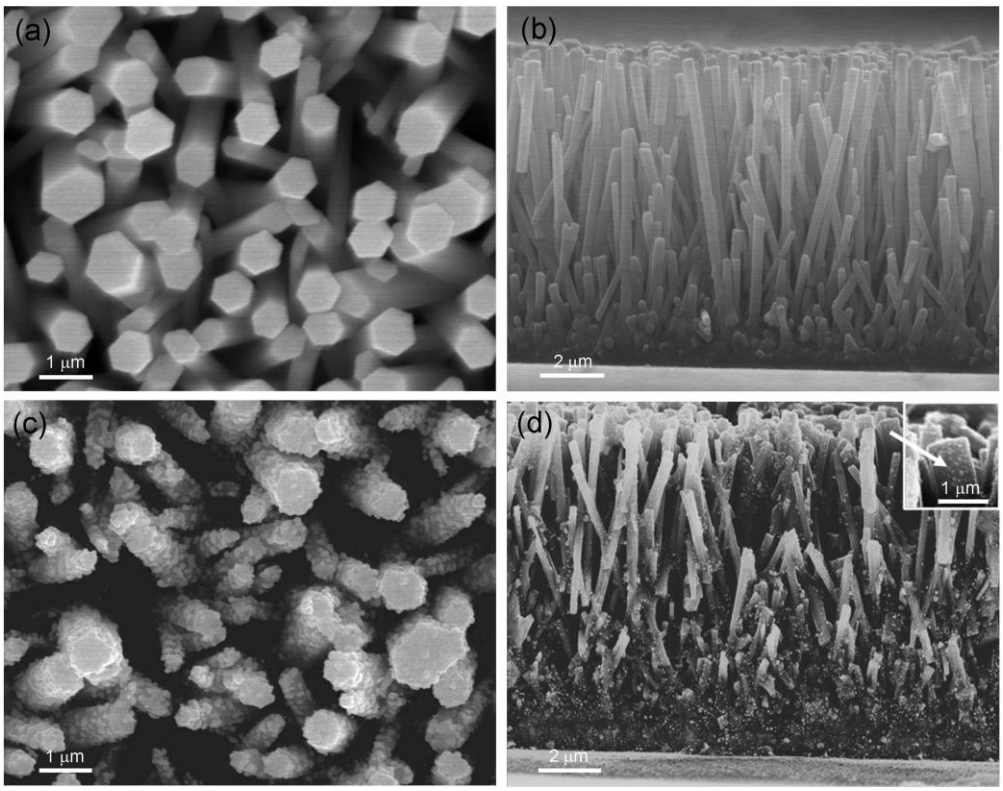

Figure 5.8. *FESEM images showing the a) top view, b) cross-sectional view of the bare ZnO nanorod photoelectrode, and c) top view, d) cross-sectional view of the ZnO−Au NC photoelectrode. Inset in d) shows the magnified FESEM image of the Au NPs synthesized on the surface of the ZnO NRs using 0.01 mM $HAuCl_4.H_2O$ aqueous solution.*

The optical absorptions of the ZnO NR and ZnO−Au NC photoelectrode are shown in Figure 5.9a. Due to the SP absorption in the Au NPs, a higher optical absorption of the ZnO−Au NC photoelectrode near 520 nm was observed. The optical absorption of the

ZnO−Au photoelectrode was compared with the absorption of Au NP colloid (particle size ~20 nm), which indicates that the Au NPs in both the systems were of comparable sizes, that was further verified from TEM image. A typical HRTEM image of one single Au NP on ZnO NR surface is shown in Figure 5.9b.

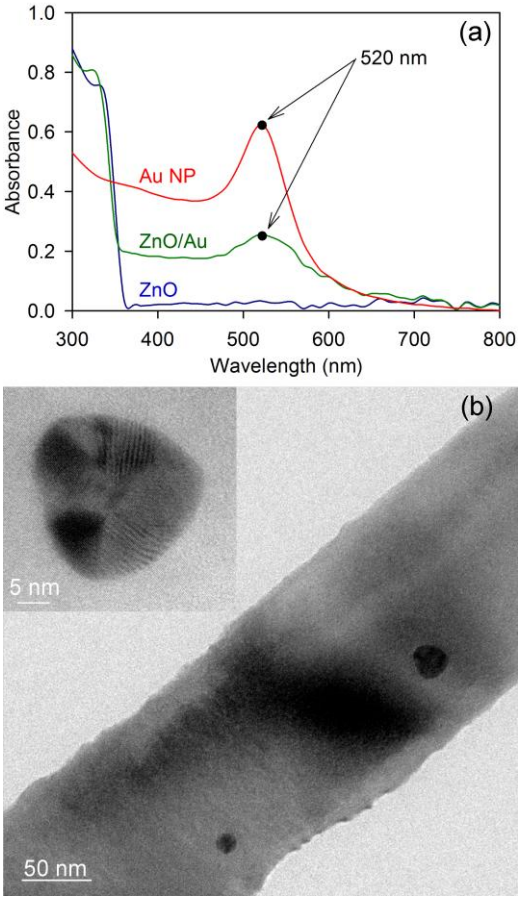

Figure 5.9. *a) Optical absorption of ZnO NR, ZnO−Au NC photoelectrode and Au NP colloid (particle size ~20 nm) and b) TEM image of Au NPs in situ deposited on the surface of a ZnO NR. Inset in b) shows the magnified image of a single Au NP on the ZnO NR surface with nanoparticle diameter ~20 nm.*

The solar cells with ZnO NRs and ZnO−Au NC photoelectrodes in absence of dye N719 were initially prepared to study the photovoltaic behavior of the ZnO−Au nanocomposite system. The *J*−*V* characteristics of these solar cells are shown in Table 5.3. Upon illumination with light intensity of 100 mW/cm^2 (AM 1.5 G), the bare ZnO NR solar cell exhibited short-circuit current density (J_{SC}) of 18.80 μA/cm^2 and open-circuit voltage

(V_{OC}) of 0.27 V. On the other hand, the ZnO−Au NC solar cell, under illumination, demonstrated higher J_{SC} (82.46 μA/cm^2) as well as V_{OC} (0.39 V) compared to the bare ZnO NR solar cell, which is mainly attributed to the higher optical absorption of the ZnO−Au photoelectrode due to the SP absorption in Au NPs. In case of the ZnO−Au solar cells

Table 5.3. *J*−*V* characteristics of bare ZnO NR and ZnO−Au NC solar cells in the absence of dye N719, measured at 1 sun illumination (100 mW/cm^2).[d]

Parameters	Bare ZnO DSSC	ZnO−Au DSSC
V_{OC} (V)	0.27	0.39
J_{SC} (μA/cm^2)	18.80	82.46
FF (%)	30.94	52.05
η (%)	0.002	0.017

[d]*The active area of all the solar cells was maintained at 0.25 cm^2 during these experiments.*

without any sensitizer dye molecules, the photoexcited electrons in the Au NPs are transferred to the conduction band (CB) of ZnO, which then diffuse through the ZnO NRs towards the conducting FTO substrate resulting in higher photocurrent and photovoltage, as observed. The injection of the excited electrons from Au NPs to the CB of ZnO is believed to be facilitated by the existence of the Schottky barrier at the ZnO−Au interface, which provides a unidirectional pathway for the electrons from Au to the CB of ZnO. Upon injection, the regeneration of the Au NPs occurs by capturing electrons from the redox electrolyte (I^-/I_3^-) present in the cell.

The solar cell performance in presence of dye was then studied by fabricating three sets of ZnO NR and ZnO−Au NC solar cells each with dye N719 and their *J*−*V* characteristics were measured under 1 sun, AM 1.5 illuminations, as shown in Table 5.4. In Figure 5.10a, the best *J*−*V* characteristics obtained for both bare ZnO NR and ZnO−Au NC DSSCs are shown. It was found that the photocurrent of the ZnO NR DSSC improved upon the incorporation of Au NPs in the ZnO NR photoelectrode. For the ZnO−Au NC DSSC, ~35% improvement in J_{SC} (14.89 mA/cm^2) was obtained compared to the bare ZnO NR DSSC (11.01 mA/cm^2) and the overall power conversion efficiency improved from 5.34% to 6.49%. In Figure 5.10b, the photocurrent response of bare ZnO NR and ZnO−Au

NC DSSC measured at different incident wavelengths are shown. Due to the SP absorption of Au NPs, an improved photocurrent response was observed above 500 nm illumination in case of the ZnO−Au NC DSSC compared to the bare ZnO NR DSSC. The improved device performance observed in case of the ZnO−Au NC DSSC can also be attributed to the presence of the Schottky barrier at the ZnO−Au interface, which would block the back electron transfer from the CB of ZnO to the I^-/I_3^- redox electrolyte. In ZnO−Au NC system, due to the higher work function of Au (5.1 eV) [11] compared to ZnO (4.2 eV) [39],

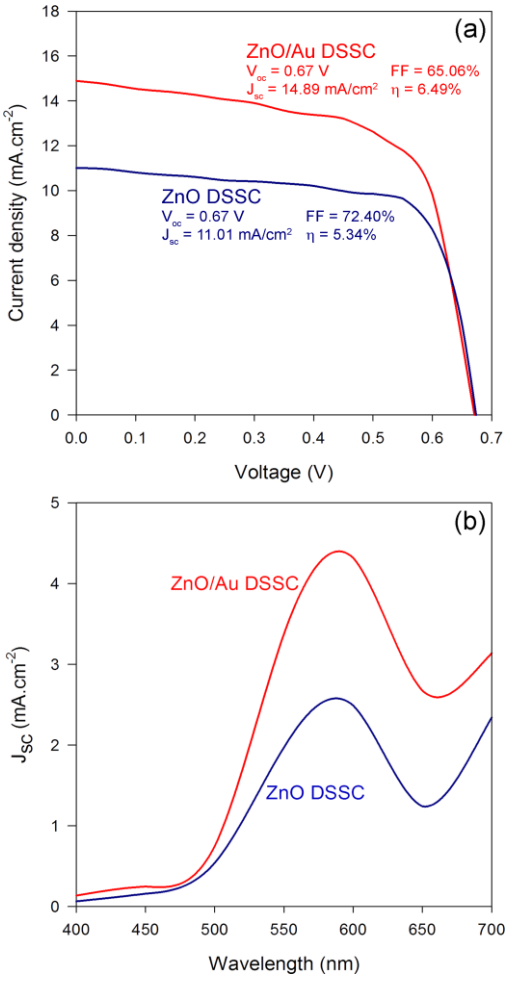

Figure 5.10. *a) J−V characteristics of the bare ZnO NR and ZnO−Au NC DSSC, measured at 1 sun (AM 1.5 G) illumination and b) short-circuit photocurrent density of the bare ZnO nanorod and ZnO−Au NC DSSCs measured at different incident wavelengths. The active area of all the DSSCs was maintained at 0.1 cm^2.*

Table 5.4. *J*−*V* characteristics of the bare ZnO NRs and ZnO−Au NC DSSCs, measured at 1 sun illumination (100 mW/cm^2).[e]

Parameters	ZnO DSSC			ZnO−Au DSSC		
	Cell I	Cell II	Cell III	Cell I	Cell II	Cell III
V_{OC} (V)	0.67	0.67	0.67	0.67	0.65	0.66
J_{SC} (mA/cm^2)	10.98	11.01	10.84	14.89	14.28	14.45
FF (%)	71.55	72.40	70.31	65.06	63.00	65.78
η (%)	5.27	5.34	5.11	6.49	5.85	6.28

[e]*The active area of all the DSSCs was maintained at 0.1 cm^2 during these experiments.*

a Schottky barrier forms at the ZnO−Au interface. Upon light irradiation, the electrons from excited dye molecules are injected to the Au NPs embedded on the surface of ZnO NRs resulting in an electron accumulation in the Au NP. As a result, the Fermi energy level of the Au NPs is pushed closer to the CB of the ZnO and transfer of electrons from Au NPs to the CB of ZnO could occur to establish charge equilibrium in the system. Some of the electrons from dye can also directly injected to the CB of the ZnO. The formation of the Schottky barrier at the ZnO−Au NC system and the possible electron transfer path in ZnO−Au DSSC is schematically represented in Scheme 5.2. The charge transfer

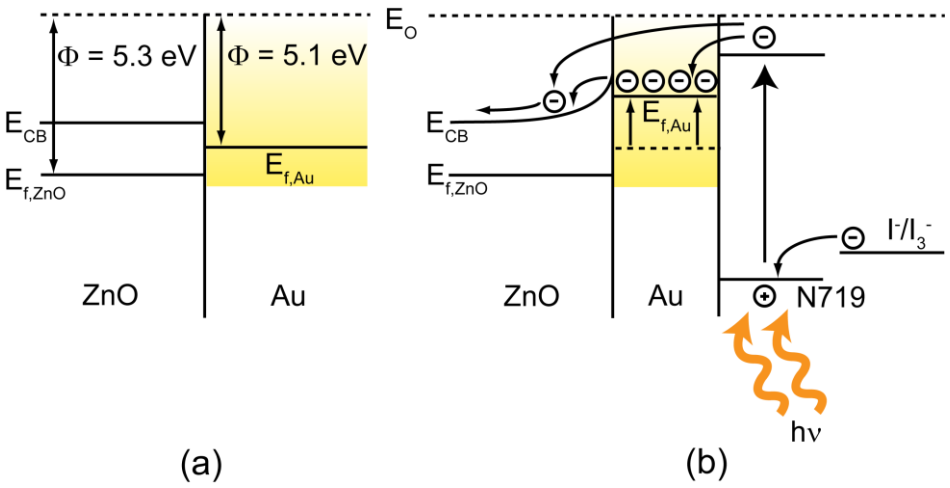

Scheme 5.2. *a) Energy band positions and formation of the Schottky barrier in the ZnO−Au NC system and b) possible electron transfer path in the ZnO−Au NC DSSC, where the dashed line (in Au) represents the position of the Fermi level of Au before electron injection from dye N719. E_o represents the vacuum energy level.*

mechanism in the ZnO−Au NC system was followed by comparing the dynamics of electron transfer from dye molecules to the bare ZnO and ZnO−Au NC system through time-correlated single photon count (TCSPC) spectroscopic technique. For these experiments, dye N719 was replaced by a fluorescent dye, namely Coumarin 343 (C343). Similar to dye N719, the carboxylic group of C343 binds directly to the Zn atoms on the surface of the ZnO NRs [40] and has been used in DSSC applications [41-42]. The steady-state photoluminescence (PL) of the C343 dye peaking at ~480 nm is shown in

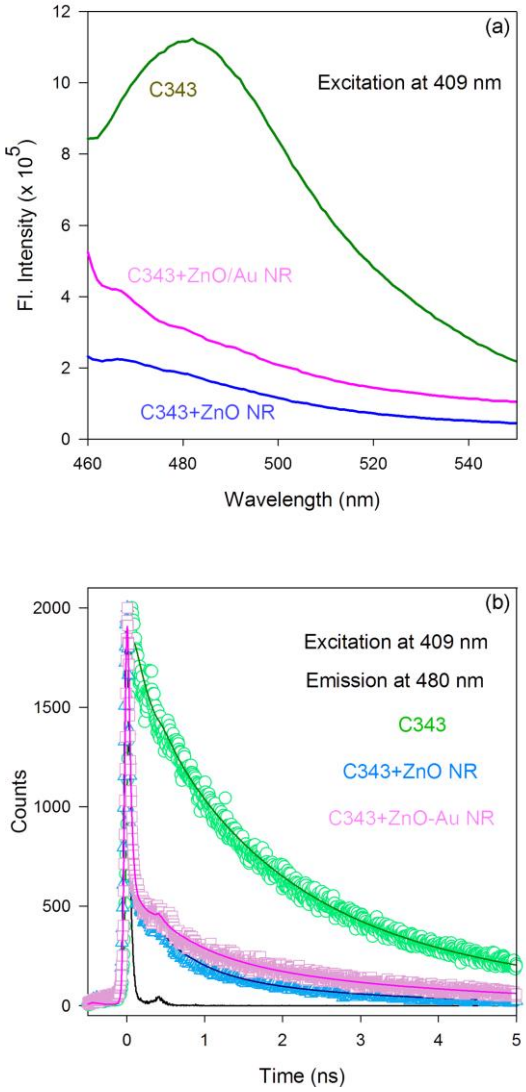

Figure 5.11. *a) PL spectra and b) PL transients of C343 dye observed at 480 nm in the presence and absence of bare ZnO NR and ZnO−Au NCs. All the samples were excited at 409 nm laser wavelength.*

Figure 5.11a, where the quenching of the PL intensity of C343 dye can be clearly observed in the presence of both ZnO NRs and ZnO−Au NCs. The PL transient measured at 480 nm (excitation at 409 nm) in the presence and absence of ZnO NRs and ZnO−Au NC systems are shown in Figure 5.11b. From the fluorescence decay study, we have observed a very sharp decay in the fluorescence intensity of the C343 dye in the presence of ZnO NR or ZnO−Au NC system. These sharp decays, observed here, indicate efficient electron transfer from the sensitizer to the semiconductor system. The various decay time constants obtained after deconvolution of the fluorescence decay curves are given in Table 5.5.

Table 5.5. Dynamics of picosecond-resolved luminescence transients of C343 dye in the presence and absence of bare ZnO NR and ZnO−Au NC.[f]

Samples	τ_1 (ns)	τ_2 (ns)	τ_3 (ns)	τ_{avg} (ns)
C343 (bare)	3.9 (26%)	1.49 (48%)	0.191 (26%)	1.77
C343 + ZnO	2.5 (2%)	0.56 (4%)	0.015 (94%)	0.09
C343 + ZnO−Au	3.3 (3%)	0.69 (3%)	0.016 (94%)	0.13

[f]*The emissions from C343 dye (probing at 480 nm) were detected with a 409 nm laser excitation. Numbers in the parentheses indicate relative weightage.*

The fraction of electrons following the fastest decay path (τ_3 in Table 5.5) increased sharply from 26% to 94% in the presence of both ZnO NR and ZnO−Au NC systems, confirming the presumption that efficient electron transfer from the sensitizer dye molecules to the semiconductor system takes place. We have observed similar fluorescence decay time constants (τ_3) in both ZnO NR and ZnO−Au NC systems, indicating that the dynamics of charge transfer process from the surface adsorbed sensitizer to the CB of the semiconductor is same in both the systems.

The performance of the ZnO−Au NC DSSC was further studied for solar cells with larger active areas. The *J*−*V* characteristics for bare ZnO NR and ZnO−Au NC DSSC with active areas of 0.25 cm^2 and 1 cm^2 are shown in Table 5.6. For active area of 0.25 cm^2, the J_{SC} of the ZnO−Au DSSC was observed to increase from 7.98 mA/cm^2 to 8.61 mA/cm^2 as compared to the bare ZnO NR DSSC. The V_{OC} and fill factor (*FF*) was also increased from 0.63 V to 0.66 V and from 47.92% to 57.53% respectively, indicating lower charge

recombination at the photoelectrode due to the existence of the Schottky barrier in the ZnO−Au NC DSSC compared to the bare ZnO NR DSSC. As a result, the overall power conversion efficiency improved from 2.41% to 3.27%.

Table 5.6. *J*−*V* characteristics of bare ZnO NR and ZnO−Au NC DSSCs with different active areas measured at 1 sun illumination (100 mW/cm^2).

Active area (cm^2)	ZnO NR DSSC				ZnO−Au NC DSSC			
	V_{OC} (V)	J_{SC} (mA/cm^2)	*FF* (%)	η (%)	V_{OC} (V)	J_{SC} (mA/cm^2)	*FF* (%)	η (%)
0.25	0.63	7.98	47.92	2.41	0.66	8.61	57.53	3.27
1.00	0.54	2.25	41.16	0.50	0.67	3.80	45.52	1.16

Similar results were observed in case of 1 cm^2 active area ZnO NR and ZnO−Au NC DSSC. The overall power conversion efficiency (PCE) improved from 0.5% to 1.16% in case of the ZnO−Au DSSC (J_{SC} = 3.80 mA/cm^2, V_{OC} = 0.67 V and *FF* = 45.52%) compared to the bare ZnO NR DSSC (J_{sc} = 2.25 mA/cm^2, V_{OC} = 0.54 V and *FF* = 41.16%). The lower PCE observed in case of large area DSSCs compared to the small area DSSCs is mainly attributed to the increase in the sheet resistance of the conducting FTO substrates resulting overall increase in the series resistance (R_s) of the large area DSSCs, which plays an important role in the solar cell performance [43-44]. Table 5.7 shows the series resistance (R_s) value of the ZnO−Au NC DSSC for different active area of the solar cells calculated by using one diode equivalent circuit model for DSSC as described by Murayama et al. [45]. It can be observed that with increasing active area of the DSSCs from 0.1 cm^2 to 1 cm^2, R_s considerably increases from 5.13 Ω to 27.08 Ω, affecting the performance of the solar cells significantly.

The dependency of the device performance on the amount of Au NPs in the photoelectrode was further studied by varying the dipping time of the ZnO NR photoelectrodes in 0.01 mM $HAuCl_4.H_2O$ solution from 30 min to 2 h. The *J*−*V* characteristics of these ZnO−Au NC DSSCs with active area of 1 cm^2 were shown in Table 5.8. Initially the overall performance of the ZnO−Au DSSC with increasing amount of Au NPs in the photoelectrode by increasing the dipping time from 30 min to 1 h was observed

Table 5.7. Series resistance (R_s) of ZnO−Au NC DSSC measured for different active areas of the solar cells using one diode equivalent circuit model for DSSC.

Active area (cm^2)	R_s (Ω)
0.10	5.13
0.25	10.10
1.00	27.08

to increase. But for higher amount of incorporated Au NPs in the ZnO NR photoelectrode by increasing the dipping time more than 1 h demonstrated a continuous drop in all the *J*−*V* parameters. The J_{sc} was observed to decrease from 3.80 mA/cm^2 to 2.40 mA/cm^2,

Table 5.8. *J*−*V* characteristics of ZnO−Au NC DSSCs with increasing amount of Au NPs in the photoelectrode as a function of the dipping time of ZnO NR photoelectrodes in the $HAuCl_4.H_2O$ aq. solution (0.01 mM).[g]

Dipping time (h)	V_{OC} (V)	J_{SC} (mA/cm^2)	*FF* (%)	η (%)
0.50	0.64	3.10	41.58	0.83
1.00	0.67	3.80	45.52	1.16
1.50	0.65	2.90	34.33	0.65
2.00	0.62	2.40	31.31	0.47

[g]The J−V characteristics were measured at 1 sun illumination (100mW/cm^2) and active area of all the DSSCs was maintained at 1 cm^2 during these experiments.

whereas, V_{OC} and *FF* also dropped from 0.67 to 0.62 V and 45.52% to 31.31%, respectively, when the dipping time was increased from 1 to 2 h, which results a retardation in power conversion efficiency from 1.16% to 0.47%.

The reduction in the DSSC performances observed with higher amount of Au NPs in the photoelectrode is believed to arise due to the agglomeration of the Au NPs on the ZnO NR surface. With smaller size of Au NPs, the energy levels in Au are discrete and a greater shift in the Fermi levels is expected for a small electron accumulation in the Au NPs [10, 46]. Since Au NPs form agglomerate to make larger particles, more electron accumulation is required to achieve the upward shift of the Fermi level. As a result, most of the accumulated electrons from the larger Au NPs recombine with the oxidized dye

N719 molecules or with the I^-/I_3^- redox electrolyte before they are transferred to the CB of ZnO and thus results in poor photocurrent as well as *FF*, as observed.

5.3. Conclusion:

In conclusion, the present study provides a mechanistic explanation for the excitation-dependent recombination processes and the catalytic activity of Au NPs in the ZnO–Au NCs, as schematically shown in Scheme 5.1. A better understanding of the charge transfer processes at the semiconductor/metal interface is crucial for optimizing the performance of such catalysts. Our results demonstrate that the excited ZnO NPs resonantly transfer visible optical radiation to the Au NPs upon below band-gap excitation of the semiconductor. A singly charged vacancy center of the ZnO semiconductor is demonstrated to be responsible for the visible optical radiation transfer from ZnO NPs to Au NPs, whereas, a combination of the energy transfer between surface defects and SP of Au NPs, as well as thermalization of photogenerated electron–hole pairs and their recombination in the ZnO NPs is believed to take place simultaneously upon above band-edge excitation. We observe that the prepared ZnO–Au NCs are stable and efficient enough for the environmental purification of organic pollutants. As a low-cost photovoltaic cell, the incident photon-to-current conversion efficiency and short-circuit current are significantly improved in the presence of Au NPs which is attributed to the better electron mobility of the ZnO–Au semiconductor. This approach may give rise to a new class of multifunctional materials with possible applications in energy conversion devices and biofunctionalized materials.

In addition, DSSCs with ZnO NRs in proximity to Au NPs were successfully fabricated as the photoelectrode and their performances were compared with the bare ZnO NR DSSCs and discussed. Incorporation of Au NPs into the ZnO NR photoelectrode led to higher optical absorption by the photoelectrode and high dye intake, resulting in an ~35% enhancement in the photocurrent in the case of the ZnO−Au NC DSSC with J_{SC} equal to 14.89 mA/cm^2 compared to the bare ZnO NR DSSC with J_{SC} equal to 11.01 mA/cm^2. As a result, the overall power-conversion efficiency was increased from 5.34% to 6.49% for the small-area (0.1 cm^2) ZnO−Au NC DSSC. The time-resolved fluorescence studies were conducted by using Coumarin 343 dye, to demonstrate an ultrafast carrier migration from sensitizing dyes to the semiconductors. In the case of the large area ZnO−Au DSSCs,

efficiency dropped to 3.27% and 1.16% for active areas equal to 0.25 cm^2 and 1 cm^2, respectively, which was mainly attributed to the increased sheet resistance of the FTO substrates. For higher amounts of Au NPs incorporated into the ZnO NR photoelectrode, an ~60% reduction in the overall PCE of the ZnO−Au DSSC was observed, suggesting that the amount of Au NPs in the ZnO NR photoelectrode is crucial for optimizing the performance of the ZnO−Au NC DSSC.

References

[1] C.B. Murry, C.R. Kagan, M.G. Bawendi, Self-Organization of CdSe Nanocrystallites into Three-Dimensional Quantum Dot Superlattices, *Science* 270 (1995) 1335.

[2] A. Henglein, Small-Particle Research: Physicochemical Properties of Extremely Small Colloidal Metal and Semiconductor Particles, *Chem. Rev.* 89 (1989) 1861.

[3] T.Y. Olson, J.Z. Zhang, Structural and Optical Properties and Emerging Applications of Metal Nanomaterials, *J. Mater. Sci. Technol.* 24 (2008) 433.

[4] M.A. Sliem, T. Hikov, Z.A. Li, M. Spasova, M. Farle, D.A. Schmidt, M.H. Newen, R.A. Fischer, Interfacial Cu/ZnO Contact by Selective Photodeposition of Copper onto the Surface of Small ZnO Nanoparticles in Non-Aqueous Colloidal Solution, *Phys. Chem. Chem. Phys.* 12 (2010) 9858.

[5] X. Fang, T.Y. Zhai, U.K. Gautam, L. Li, L.M. Wu, Y. Bando, D. Golberg, ZnS Nanostructures: From Synthesis to Applications, *Prog. Mater. Sci.* 56 (2011) 175.

[6] S. Link, M.A. El-Sayed, Spectral Properties and Relaxation Dynamics of Surface Plasmon Electronic Oscillations in Gold and Silver Nanodots and Nanorods, *J. Phys. Chem. B* 103 (1999) 8410.

[7] R. Jin, Y.C. Cao, C.A. Mirkin, K.L. Kelly, G.C. Schatzand, J.G. Zheng, Photoinduced Conversion of Silver Nanospheres to Nanoprisms *Science* 294 (2001) 1901.

[8] P.V. Kamat, Photophysical, Photochemical and Photocatalytic Aspects of Metal Nanoparticles, *J. Phys. Chem. B* 106 (2002) 7729.

[9] M. Valden, X. Lai, D.W. Goodman, Onset of Catalytic Activity of Gold Clusters on Titania with the Appearance of Nonmetallic Properties, *Science* 281 (1998) 1647.

[10] M. Haruta, Size and Support-Dependency in the Catalysis of Gold, *Catal. Today* 36 (1997) 153.

[11] Z.H. Chen, Y.B. Tang, C.P. Liu, Y.H. Leung, G.D. Yuan, L.M. Chen, Y.Q. Wang, I. Bello, J.A. Zapien, W.J. Zhang, C.S. Lee, S.T. Lee, Vertically Aligned ZnO

Nanorod Arrays Sentisized with Gold Nanoparticles for Schottky Barrier Photovoltaic Cells, *J. Phys. Chem. C* 113 (2009) 13433.

[12] T. Yang, T. Tetsu, Mechanisms and Applications of Plasmon-Induced Charge Separation at TiO_2 Films Loaded with Gold Nanoparticles, *J. Am. Chem. Soc.* 127 (2005) 7632.

[13] V. Subramanian, E.E. Wolf, P.V. Kamat, Semiconductor−Metal Composite Nanostructures. To What Extent Do Metal Nanoparticles Improve the Photocatalytic Activity of TiO_2 Films?, *J. Phys. Chem. B* 105 (2001) 11439.

[14] N. Chandrasekharan, P.V. Kamat, Improving the Photoelectrochemical Performance of Nanostructured TiO_2 Films by Adsorption of Gold Nanoparticles, *J. Phys. Chem. B* 104 (2000) 10851.

[15] A. Wood, M. Giersig, P. Mulvaney, Fermi Level Equilibration in Quantum Dot−Metal Nanojunctions, *J. Phys. Chem. B* 105 (2001) 8810.

[16] V. Subramanian, E.E. Wolf, P.V. Kamat, Green Emission to Probe Photoinduced Charging Events in ZnO-Au Nanoparticles.Charge Distribution and Fermi-Level Equilibration, *J. Phys. Chem. B* 107 (2003) 7479.

[17] M. Jakob, H. Levanon, Charge Distribution between UV-Irradiated TiO_2 and Gold Nanoparticles: Determination of Shift in the Fermi Level, *Nano Lett.* 3 (2003) 353.

[18] C. Li, L. Li, Z. Du, H. Yu, Y. Xiang, Y. Li, Y. Cai, T. Wang, Rapid and Ultrahigh Ethanol Sensing Based on Au-Coated ZnO Nanorods, *Nanotechnology* 19 (2008) 035501.

[19] K. Shibahara, N. Kuroda, S. Nishino, H. Matsunami, Fabrication of p-n Junction Diodes Using Homoepitaxially Grown 6H-SiC at Low Temperature by Chemical Vapor Deposition, *Jpn. J. Appl. Phys.* 26 (1987) 1815.

[20] Y.W. Heo, D.P. Norton, S.J. Pearton, Origin of Green Luminescence in ZnO Thin Film Grown by Molecular-Beam Epitaxy, *J. Appl. Phys.* 98 (2005) 073502.

[21] C.C. Lin, H.P. Chen, H.C. Liao, S.Y. Chen, Enhanced Luminescent and Electrical Properties of Hydrogen-Plasma ZnO Nanorods Grown on Wafer-Scale Flexible Substrates, *Appl. Phys. Lett.* 86 (2005) 183103.

[22] N. Ohashi, T. Ishigaki, N. Okada, T. Sekiguchi, I. Sakaguchi, H. Haneda, Effect of Hydrogen Doping on Ultraviolet Emission Spectra of Various Types of ZnO, *Appl. Phys. Lett.* 80 (2002) 2869.

[23] J.M. Lin, H.Y. Lin, C.L. Cheng, Y.F. Chen, Giant Enhancement of Bandgap Emission of ZnO Nanorods by Platinum Nanoparticles, *Nanotechnology* 17 (2006) 4391.

[24] C.W. Cheng, E.J. Sie, B. Liu, C.H.A. Huan, T.C. Sum, H.D. Sun, H.J. Fan, Surface Plasmon Enhanced Band Edge Luminescence of ZnO Nanorods by Capping Au Nanoparticles, *Appl. Phys. Lett.* 96 (2010) 071107.

[25] S. Sarkar, A. Makhal, T. Bora, S. Baruah, J. Dutta, S.K. Pal, Photoselective Excited State Dynamics in ZnO-Au Nanocomposites and their Implications in Photocatalysis and Dye-Sensitized Solar Cells, *Phys. Chem. Chem. Phys.* 13 (2011) 12488.

[26] M. Haase, H. Weller, A. Henglein, Photochemistry and Radiation Chemistry of Colloidal Semiconductors. 23. Electron Storage on Zinc Oxide Particles and Size Quantization, *J. Phys. Chem.* 92 (1988) 482.

[27] J.D. Ye, S.L. Gu, F. Qin, S.M. Zhu, S.M. Liu, X. Zhou, W. Liu, L.Q. Hu, R. Zhang, Y. Shi, Y.D. Zheng, Correlation Between Green Luminescence and Morphology Evolution of ZnO Films, *Appl. Phys. A* 81 (2005) 759.

[28] M. Ghosh, A.K. Raychaudhuri, Shape Transition in ZnO Nanostructures and Its Effect on Blue-Green Photoluminescence, *Nanotechnology* 19 (2008) 445704.

[29] J.R. Lakowicz, Principles of Fluorescence Spectroscopy, 2nd ed., Kluwer Academic/ Plenum, New York, 1999.

[30] A. Makhal, S. Sarkar, T. Bora, S. Baruah, J. Dutta, A.K. Raychaudhuri, S.K. Pal, Dynamics of Light Harvesting in ZnO Nanoparticles, *Nanotechnology* 21 (2010) 265703.

[31] V. Subramanian, E.E. Wolf, P.V. Kamat, Catalysis with TiO_2/Gold Nanocomposites. Effect of Metal Particle Size on the Fermi Level Equilibration, *J. Am. Chem. Soc.* 126 (2004) 4943.

[32] S. Baruah, S.S. Sinha, B. Ghosh, S.K. Pal, A.K. Raychaudhuri, J. Dutta, Photoreactivity of ZnO Nanoparticles in Visible Light: Effect of Surface States on Electron Transfer Reaction, *J. Appl. Phys.* 105 (2009) 074308.

[33] S.S. Sinha, P.K. Verma, A. Makhal, S.K. Pal, A Versatile Fiber-Optic Coupled System for Sensitive Optical Spectroscopy in Strong Ambient Light, *Rev. Sci. Instrum.* 80 (2009) 053109.

[34] P.D. Cozzoli, M.L. Curri, A. Agostiano, Efficient Charge Storage in Photoexcited TiO_2 Nanorod-Noble Metal Nanoparticle Composite Systems, *Chem. Commun.* (2005) 3186.

[35] T. Bora, H.H. Kyaw, S. Sarkar, S.K. Pal, J. Dutta, Highly Efficient ZnO/Au Schottky Barrier Dye-Sensitized Solar Cells: Role of Gold Nanoparticles on the Charge Transfer Process, *Beilstein J. Nanotechnol.* 2 (2011) 681.

[36] L. Hu, J. Yan, M. Liao, L. Wu, X. Fang, Ultrahigh External Quantum Efficiency from Thin SnO_2 Nanowire Ultraviolet Photodetectors, *Small* 7 (2011) 1012.

[37] X. Fang, Y. Bando, M. Liao, U.K. Gautam, C. Zhi, B. Dierre, B. Liu, T. Zhai, T. Sekiguchi, Y. Koide, D. Golberg, Single-Crystalline ZnS Nanobelts as Ultraviolet-Light Sensors, *Adv. Mater.* 21 (2009) 2034.

[38] K. Keis, E. Magnusson, H. Lindstrom, S.E. Lindquist, A. Hagfeldt, A 5% Efficient Photoelectrochemical Solar Cell Based on Nanostructured ZnO Electrodes, *Sol. Energy Mater. Sol. Cells* 73 (2002) 51.

[39] L.J. Brillson, L. Yicheng, ZnO Schottky Barriers and Ohmic Contacts, *J. Appl. Phys.* 109 (2011) 121301.

[40] W.R. Duncan, O.V. Prezhdo, Theoretical Studies of Photoinduced Electron Transfer in Dye-Sensitized TiO_2, *Annu. Rev. Phys. Chem.* 58 (2007) 143.

[41] X. Zhang, J.J. Zhang, Y.Y. Xia, Molecular Design of Coumarin Dyes with High Efficiency in Dye-Sensitized Solar Cells, *J. Photochem. Photobiol. A* 194 (2008) 167.

[42] K. Hara, K. Sayama, Y. Ohga, A. Shinpo, S. Suga, H. Arakawa, A Coumarin-Derivative Dye Sensitized Nanocrystalline TiO_2 Solar Cell having a High Solar-Energy Conversion Efficiency up to 5.6%, *Chem. Commun.* (2001) 569.

[43] M.W. Denhoff, N. Drolet, The Effect of the Front Contact Sheet Resistance on Solar Cell Performance, *Sol. Energy Mater. Sol. Cells* 93 (2009) 1499.

[44] K. Onoda, S. Ngamsinlapasathian, T. Fujieda, S. Yoshikawa, The Superiority of Ti Plate as the Substrate of Dye-Sensitized Solar Cells, *Sol. Energy Mater. Sol. Cells* 91 (2007) 1176.

[45] M. Murayama, T. Mori, Evaluation of Treatment Effects for High-Performance Dye-Sensitized Solar Cells using Equivalent Circuit Analysis, *Thin Solid Films* 509 (2006) 123.

[46] P.V. Kamat, Quantum Dot Solar Cells. Semiconductor Nanocrystals as Light Harvesters, *J. Phys. Chem. C* 112 (2008) 18737.

Chapter 6

Metal Oxide Semiconductors in the Simultaneous Proximity of Organic Dyes and Quantum Dots

6.1. Introduction:

Dye-sensitized solar cells (DSSCs) are based on solar light harvesting through the sensitizing dye (SD) attached to a wide band-gap semiconductor, first introduced by Grätzel et al. [1] The SD is an essential constituent in nanocrystalline DSSCs that has a potential for future photovoltaic applications owing to the lower fabrication costs of solar cells with acceptable conversion efficiencies [1-2]. The most successful and widely used dye employed in DSSCs are ruthenium complexes [3-5], ($Ru(dcbpy)_2(NCS)_2$), N_3 (dcbpy = 4,4-dicarboxy-2,2′-ipyridine), and bis(tetrabutylammonium) salt N719, which have fairly broad optical absorption spectra ($\Delta\lambda \approx 350$ nm) but low molar extinction coefficients (5,000−20,000 M^{-1} cm^{-1}). Alternative organic dyes have recently been developed with substantially higher molar extinction coefficients (50,000−200,000 M^{-1} cm^{-1}) but show narrow spectral bandwidths ($\Delta\lambda \approx 250$ nm) [6-8]. Dye cocktails lead to a broader absorption spectra [9], but due to the absence of dyes that absorb efficiently in the red part of the spectrum, generally a lower efficiency is achieved. As dyes with strong absorptivity do not typically exhibit broad absorption overlapping the solar spectra, this is one of the major pitfalls of using dyes as photosensitizers in solar cells.

Many efforts have been made to introduce stronger light absorber and to widen the spectral response of the photosensitizers. In recent times, the use of quantum dots (QDs) as light harvesters has stimulated a lot of interest due to its higher extinction coefficient compared to conventional dyes [10] for efficient light energy conversion [11-14]. Because of the size quantization property, the optical and electronic properties of the semiconductor QDs can be engineered to further tune the response of QD solar cells (QDSCs) [15-17]. In addition, QDs open up new possibilities for the utilization of hot electrons [18] or multiple charge carrier generation with a single photon [19]. Multiple carrier generation in PbSe

nanocrystals has shown that two or more excitons can be generated with a single photon of energy greater than the band-gap [20]. The performance of a QDSC is currently limited by a number of factors, including a limited choice of electrolytes with which QDs are chemically compatible, insufficient passivation of recombination channels (usually attributed to surface traps), and limited QD loading capacities [21]. Recent studies have shown that it is possible to stabilize CdS QD-based DSSCs by coating the QD-sensitized nanoporous electrodes with a thin amorphous TiO_2 layer which enables the use of various QD sensitizers in the presence of iodine-based electrolytes [22]. Utilizing two sensitizing layers of SD N719 and CdS QDs separated by an amorphous titanium dioxide (TiO_2) layer, a significant increase in cell efficiency compared to a QD monolayer cell has been reported [23]. In a more recent study, Grätzel *et al.* have used cobalt complex (Co^{2+}/Co^{3+}) as an electrolyte in the cells which permits direct contact between the QDs and the electrolyte. Choi *et al.* have recently demonstrated the coupling of semiconductor nanocrystal and a red-NIR organic dye with complementary spectral absorption in the visible region [24].

Utilization of two sensitizers (one acting as energy donor while the other as an acceptor) can be very useful in order to achieve both broadening of optical absorption region in DSSCs as well as increasing the absolute loading of absorbing media on the semiconductor. This novel approach is based on Förster resonance energy transfer (FRET) which has recently experienced a significant interest of several groups [25-30] including ours [31-32]. The use of FRET between covalently linked energy donor molecules to the SD which are attached to the semiconductor (titania) surface has been demonstrated in the literature [33], where higher excitation transfer efficiency (> 89%) between attached dye molecules and a subsequent improvement in the device external quantum efficiency of 5−10% between 400 and 500 nm spectral range has been reported. The overall enhancement of power conversion efficiency of the DSSC was still low (< 9%) that was argued to arise due to an increase in the open-circuit voltage rather than an increase in the short-circuit photocurrent density. Recently, it has been demonstrated that unattached, highly luminescent chromophores inside liquid electrolyte can absorb high energy photons and efficiently transfer the energy to the anchored near-infrared SD leading to an increase in optical absorption efficiency [34]. In another work, enhancement in photovoltaic device performance has been reported using long-range resonant energy transfer from a dissolved

luminescent dopant confined in the interwire spaces of a nanowire array electrode to an acceptor species confined to the surface of the nanowires [28].

In this contribution, we demonstrate that size tunable CdTe QDs capped with 3-mercaptopropionic acid (MPA), assembled in a N719-sensitized solar cell, can absorb visible-light in the 'gaps' where SD N719 has lower absorption and/or does not absorb any light. In this design, QDs serve as a cosensitizer which can directly transfer electrons to ZnO nanorods (NRs). Moreover, the QDs which are not in a direct attachment to the ZnO NR surfaces, harvest the absorbed energy to nearby dye molecules via FRET, rather than contributing directly as sensitizers. By using steady-state and picosecond-resolved fluorescence spectroscopy, we have demonstrated that photoluminescence (PL) from QDs can be useful to excite the SD molecule for an enhanced light absorption. The consequence of QD-mediated electron and light-harvesting processes on the overall performance of a model QD-assembled DSSC has also been demonstrated.

6.2. Results and Discussion:

6.2.1. "Dual-Sensitization" *via* Electron and Energy Harvesting in CdTe Quantum Dots Decorated ZnO Nanorod-based Dye-Sensitized Solar Cells [35]:

The morphological characterization by SEM (Figure 6.1a) indicates the formation of arrays of ZnO NRs with a preferential growth direction along the polar facets in the [0002] direction of the ZnO hexagonal wurtzite crystal. The NRs growing perpendicular to the substrate are nearly uniform in length (~3 μm) and possess a characteristic hexagonal cross-section with diameter in the range of ~180 nm. Inset shows the magnified top-view of a typical single NR decorated with CdTe QDs. Figures 6.1b−c show the TEM images of two distinctly different sizes of CdTe QDs (QD1 and QD2), which are found to be ~4±0.2 and ~5±0.4 nm in diameter. As shown in the insets of Figures 6.1b−c, HRTEM image reveals the fringes of CdTe with a lattice spacing of 0.33 nm and 0.25 nm corresponding to (111) and (220) planes of cubic CdTe crystal, which are in good agreement with previous reports [36]. Both the absorption and PL spectra of CdTe QDs exhibit "quantum size-effect", as shown in Figure 6.2. The tunable absorption bands of CdTe QDs can be

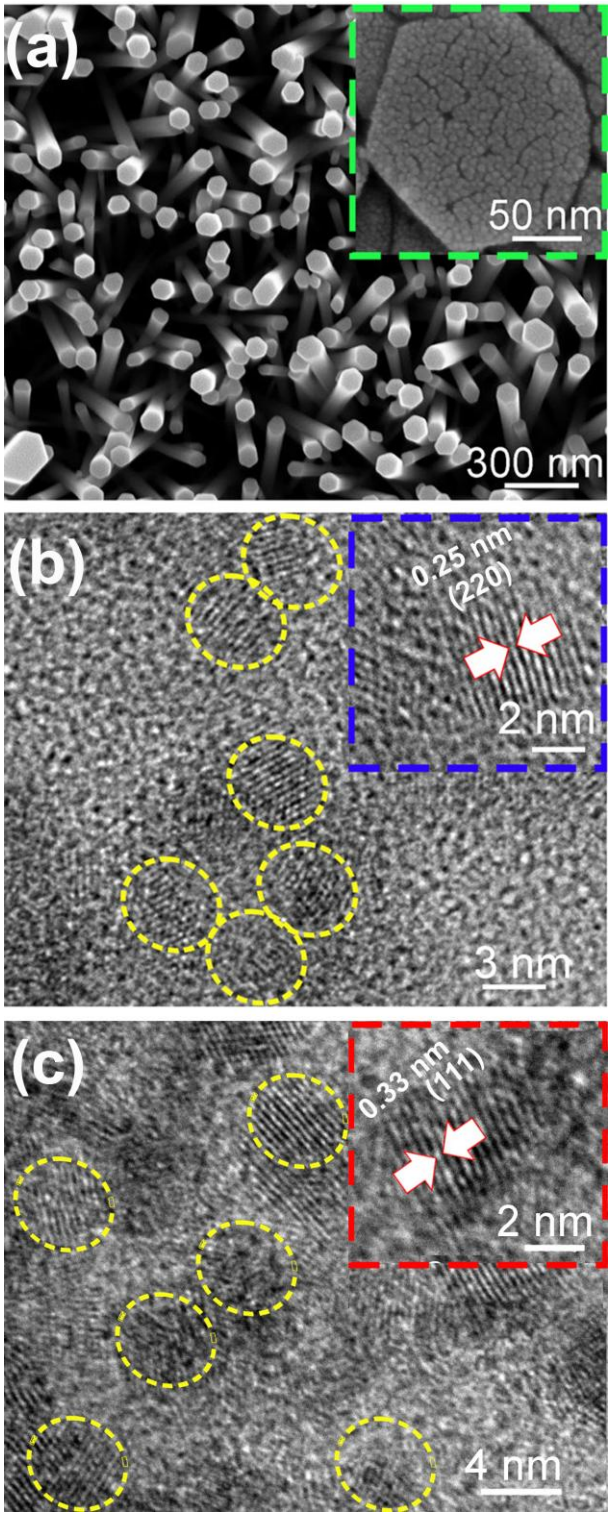

Figure 6.1. *a) Top-view SEM image of vertically aligned ZnO NRs decorated on an FTO plate; the inset shows a closer view of hexagonal shaped ZnO NR on which CdTe QDs are attached. TEM images of b) QD1 and c) QD2 (two representative QDs) are shown; the insets show their corresponding HRTEM image.*

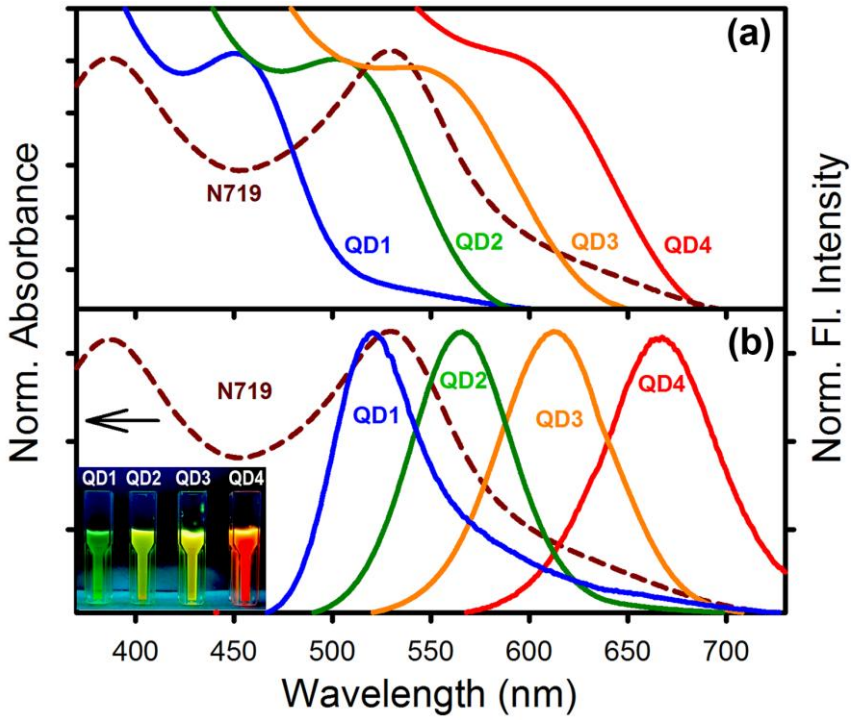

Figure 6.2. *a) Normalized absorption spectra of the sensitizing dye N719 and 3-MPA-capped CdTe QDs with average diameters of 4 nm (QD1), 5 nm (QD2), 7 nm (QD3), and 9 nm (QD4). b) Significant overlap between absorption spectra of N719 and photoluminescence (PL) spectra of four different-sized CdTe QDs is shown.*

so adjusted that they preferentially cover the 'gaps' of sensitizer N719 absorption, i.e. where sensitizer has none or very low extinction coefficient (Figure 6.2a). As can be observed in Figure 6.2b, there are significant overlaps between the optical absorption of sensitizer N719 and the emission bands of CdTe QDs, which is one of the foremost criteria for FRET dynamics. As shown in Figure 6.3, upon 375 nm excitation, strong emissions of CdTe QDs (deposited on a quartz plate) were suppressed in the presence of sensitizer N719. Herein, we propose FRET from donor CdTe QDs to N719 acceptor [37], which is responsible for the observed suppression of the emission bands. The donor thus decays to the ground state while the acceptor is still excited. It results in the excitation of the acceptor from an indirect process, i.e., the acceptor effectively captures photons that are not directly absorbed by it. The faster excited-state lifetime of the CdTe−N719 composite with respect to that of the free QDs is clearly noticeable in Figure 6.4. Details of the

spectroscopic parameters and the fitting parameters of the fluorescence decays are

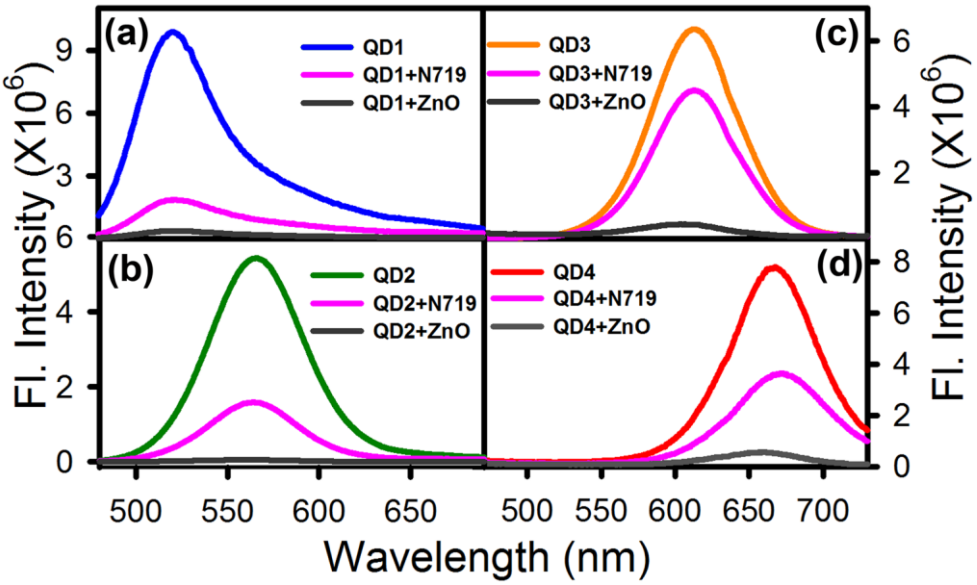

Figure 6.3. *Steady-state emission quenching of different-sized CdTe QDs (a, QD1; b, QD2; c, QD3; d, QD4) in the presence of sensitizing dye N719 and ZnO NRs. Excitation was at 375 nm.*

tabulated in Table 6.1. The quantum yields (Q_D) of the donors in the absence of acceptor are measured with respect to a reference dye Rhodamine 123 (Q_D = 0.9) and presented in Table 6.2. From the average lifetime calculation for the CdTe–N719 adduct, we obtain the effective distance (using equation 2.11 and 2.12b) between the donor and the acceptor, r_{DA} to be 3.72±0.03, 4.14±0.06, 4.38±0.08 and 4.22±0.04 nm for QD1 to QD4, respectively. It is to be noted that the insignificant variations in donor–acceptor distances compared to the radii of the QDs (measured from TEM image) can be rationalized from the fact that the origin of the PL arises essentially from surface states in the CdTe QDs [17]. Both the degree of overlap and distance between donor and acceptor have been accounted simultaneously for FRET efficiency estimation. The energy transfer efficiency from QD to N719 is observed to decrease with a subsequent decrease in overlap integral, which is consistent with previous studies [38-39]. The calculated FRET parameters are also presented in Table 6.2.

Although FRET is an interesting phenomenon that requires neither physical contact nor charge exchange, however, direct attachment of the CdTe QDs with the ZnO NRs

leads to photoinduced electron transfer (PET) from QDs to the conduction band of ZnO. Similar PET studies have been reported in the literature, which is a fundamental

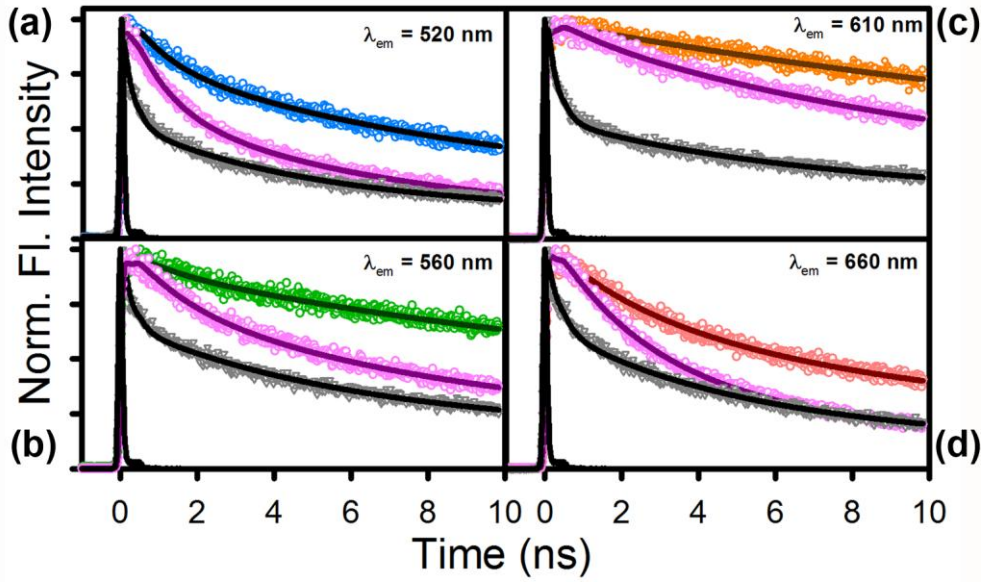

Figure 6.4. *The picosecond-resolved fluorescence transients of four different-sized CdTe QDs (a, QD1; b, QD2; c, QD3; d, QD4) in the absence and presence of sensitizing dye N719 (pink) and ZnO NRs (gray). The excitation wavelength was at 375 nm.*

process of QDSSC that ultimately pilots a direct sensitization of the solar cell performance.[17, 40-41] The rate of charge recombination, energy transfer and charge injection processes (see equations 6.1−6.3) dictate the emission decay of CdTe QDs:

$$CdTe + h\nu \rightarrow CdTe(e+h) \rightarrow CdTe + h\nu' \quad \text{(recombination)} \quad (6.1)$$

$$dye + h\nu' \rightarrow dye^* \quad \text{(energy harvesting)} \quad (6.2)$$

$$CdTe(e+h) + ZnO \rightarrow CdTe(h) + ZnO(e) \quad \text{(electron harvesting)} \quad (6.3)$$

Figure 6.4 shows the emission decay of CdTe QDs anchored to ZnO NR films on a quartz plate, recorded with 375 nm diode laser excitation. As observed in the previous studies, both heterogeneity of samples and varying degree of surface defects introduce multiexponential decay behavior to the charge recombination process [16-17]. A significant decrease in QD lifetime, however, was observed in the presence of ZnO NRs. In particular, the fast component, which contributes nearly 61% of the decay, shows a major decrease in lifetime from 0.93±0.03 to 0.21±0.02 ns in the smallest QD−ZnO

composite. For the smallest QD (i.e. QD1), the apparent rate constant for charge injection into ZnO NRs was estimated to be 1.7×10^{8} s^{-1} (by using equation 2.5), whereas, the rate of energy transfer from QD1 to N719 is 6.7×10^{7} s^{-1}. Therefore, it is evident that the charge injection from the excited CdTe to the ZnO NRs occurs with a rate constant that is an order of magnitude higher than that of energy transfer between CdTe to N719. It should be noted that the above estimation of average lifetimes takes into account both short and long-lived components. A major population of the charge injection process occurs with a greater rate constant (as high as 10^{9} s^{-1}) if we compare only the fast component of the emission transients. For example, ~61% of the emission decay of CdTe QDs on ZnO surface occurs with a lifetime of 0.21±0.02 ns, indicating the major fraction of the charge injection event occurs on an ultrafast time scale.

In order to investigate the mechanism of cosensitization of CdTe QDs in the layered architectures (Figures 6.5a−b) related to DSSC fabrication, picosecond-resolved fluorescence study was performed (Figure 6.5c). The fluorescence transient of the bare QDs not in the vicinity of N719 or ZnO is shown in the figure as a reference. In the ZnO−QD−N719 architecture (Figure 6.5a), QDs are sandwiched between ZnO NRs and N719. In these conditions, QDs can either directly transfer electrons to the conduction band (CB) of ZnO NRs or can nonradiatively transfer energy to sensitizer N719. The fluorescence decay parameters, as shown in Table 6.3, are comparable to the distinct lifetimes of an electron transfer process (Table 6.1). Therefore, the picosecond-resolved fluorescence transient of CdTe QDs in the ZnO−QD−N719 architecture reveals a “direct injection” of charge carriers from QDs to ZnO NRs *via* PET. It is to note that the role of the capping ligands of the colloidal QDs has been demonstrated to have paramount importance on the efficient charge separation at the QD/polymer interface [42]. In this respect, the electron transfer pathway is found to prevail over the FRET process with short chain 3-MPA ligands associated to CdTe QDs. In the other architecture, ZnO−N719−QD (Figure 6.5b), the QDs are separated by a layer of N719 molecules from the ZnO NRs whereby light harvesting could only occur through FRET from QDs to N719. It is being conventional that the N719 dye binds the ZnO by using its carboxylic groups [43], as a result the residual chains of N719 are free and away from the ZnO, which allows them to interlace with the 3-MPA ligands of the QDs via efficient hydrophilic interactions. This

sort of an association results in an average distance between the donor and the acceptor, which lies within the Förster radius and allows an efficient energy transfer. The assorted lifetimes (Table 6.3) of the QDs in this particular configuration are comparable to the decay parameters of the energy transfer route (as shown in Table 6.1), which reveals

Table 6.1. Dynamics of picosecond-resolved luminescence transients of CdTe QDs (QD1−QD4) in the presence and absence of sensitizer N719 and ZnO NRs.[a]

Sample	Observed wavelength	τ_1 (ns)	τ_2 (ns)	τ_3 (ns)	τ_{avg} (ns)	$k_{nr} \times 10^7$ (s^{-1})
QD1 (abs 445 nm)	520 nm	0.93±0.03 (30%)	6.80±0.15 (38%)	35.80±0.45 (32%)	14.30±0.21	
QD1+N719	520 nm	0.90±0.03 (40%)	4.80±0.12 (38%)	23.40±0.38 (22%)	7.30±0.14	k_{FRET} = 6.70±0.16
QD1+ZnO	520 nm	0.21±0.02 (61%)	4.20±0.05 (25%)	21.30±0.23 (14%)	4.20±0.05	k_{PET} = 17.00±0.40
QD2 (abs 500 nm)	560 nm	1.10±0.15 (15%)	9.90±0.78 (33%)	40.20±0.95 (52%)	24.30±0.77	
QD2+N719	560 nm	1.20±0.08 (25%)	7.50±0.20 (43%)	34.90±0.50 (32%)	14.70±0.27	k_{FRET} = 2.60±0.10
QD2+ZnO	560 nm	0.21±0.02 (52%)	4.70±0.07 (25%)	26.20±0.16 (23%)	7.30±0.06	k_{PET} =10.00±0.40
QD3 (abs 550 nm)	610 nm	0.84±0.05 (3%)	16.20±0.88 (45%)	43.60±0.9 (52%)	29.90±0.87	
QD3+N719	610 nm	0.80±0.08 (7%)	8.80±0.27 (32%)	28.30±0.68 (61%)	20.10±0.51	k_{FRET} = 1.60±0.03
QD3+ZnO	610 nm	0.22±0.07 (61%)	4.30±0.12 (13%)	27.40±0.14 (26%)	7.80±0.02	k_{PET} = 9.50±0.06
QD4 (abs 610 nm)	660 nm	2.35±0.17 (27%)	8.10±0.94 (36%)	31.80±1.40 (37%)	15.30±0.90	
QD4+N719	660 nm	2.18±0.06 (36%)	7.10±0.30 (36%)	27.30±1.00 (28%)	10.90±0.41	k_{FRET} = 2.60±0.07
QD4+ZnO	660 nm	0.27±0.02 (49%)	4.30±0.50 (31%)	21.70±0.13 (20%)	5.80±0.19	k_{PET} = 10.70±0.20

[a] The emission from CdTe QDs (emission at 520, 560, 610 and 660 nm, respectively) was detected with 375 nm laser excitation. k_{nr} represents nonradiative (FRET/PET) rate constant. Numbers in the parenthesis indicate relative weightages.

Table 6.2. Various FRET parameters[b] obtained for different-sized CdTe QDs and N719 dye molecules.

FRET pairs	$J(\lambda)\times10^{14}$ ($M^{-1}cm^{-1}nm^4$)	Q_D	R_0 (nm)	E_{TR} (%)	r_{DA} (nm) from FRET	r (nm) from TEM
QD1+N719	9.2±0.2	0.18±0.01	3.69±0.05	0.490±0.003	3.72±0.03	2.00±0.11
QD2+N719	7.5±0.3	0.29±0.02	3.86±0.07	0.400±0.008	4.14±0.06	2.50±0.20
QD3+N719	5.1±0.2	0.45±0.03	3.90±0.07	0.330±0.002	4.38±0.08	3.50±0.14
QD4+N719	3.6±0.1	0.40±0.02	3.61±0.04	0.290±0.012	4.22±0.04	4.50±0.25

[b]*Overlap integral ($J(\lambda)$), quantum yield (Q_D) in the absence of acceptor, Förster distance (R_0), FRET efficiency calculated from time-resolved study (E_{TR}) and donor−acceptor distance (r_{DA}) between the FRET pairs and radii (r) of QDs measured from TEM images.*

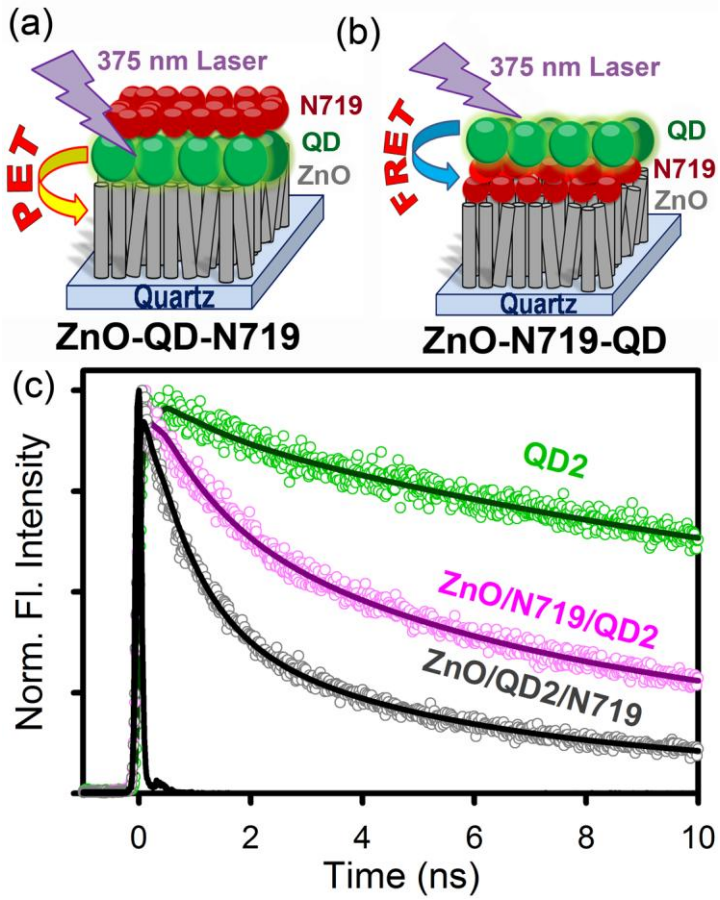

Figure 6.5. *Two different architectures of CdTe QD decorated dye-sensitized ZnO NR substrates, namely, a) ZnO−QD−N719 and b) ZnO−N719−QD. c) The picosecond-resolved fluorescence transients of CdTe QD2 showing PET and FRET in two different architectures. The excitation wavelength was 375 nm and the emission was monitored at 560 nm.*

Table 6.3. Dynamics of picosecond-resolved luminescence transients of CdTe QDs (QD1−QD4) in the presence and absence of sensitizer N719 and ZnO NRs.[c]

Sample	Observed wavelength	τ_1 (ns)	τ_2 (ns)	τ_3 (ns)	τ_{avg} (ns)	$k_{nr}\times10^7$ (s^{-1})
QD2 (abs 500 nm)	560 nm	1.10±0.15 (15%)	9.90±0.78 (33%)	40.20±0.95 (52%)	24.30±0.77	
ZnO−N719−QD2	560 nm	1.20±0.18 (33%)	7.00±0.65 (45%)	32.00±0.86 (22%)	10.60±0.54	5.30±0.31
ZnO−QD2−N719	560 nm	0.72±0.09 (59%)	4.50±0.45 (33%)	22.80±0.82 (8%)	7.30±0.27	9.60±0.38

[c]*The emission from CdTe QD (emission at 560 nm) was detected with 375 nm laser excitation. Numbers in the parenthesis indicate relative weightages.*

that an additional "indirect-excitation" of N719 can be introduced by using the sensitivity of FRET and this type of engineered solar cells should contribute to higher photocurrents. The nonradiative rate constants (k_{nr}) in these two architectures, as presented in Table 6.3, are almost analogous to the k_{nr} values of the individual systems that lead to either energy or electron transfer pathways (Table 6.1).

The effectiveness of QD decoration in solar cell performance was evaluated by employing them in a photoelectrochemical cell with the two different architectures (Figures 6.5a−b) as discussed before. The use of CdTe QDs as a sensitizer in photoelectrochemical cells have been investigated by several research groups [17, 27, 43-44]. The DSSC devices fabricated with N719 dye as sensitizer in the presence and the absence of CdTe QDs (QD1 and QD2) were characterized by wavelength-dependent photocurrent spectroscopy (Figure 6.6a−b) and photocurrent−voltage ($J-V$) measurements (Figure 6.6c); the resulting photovoltaic parameters are summarized in Table 6.4. The wavelength-dependent photocurrent is the number of electrons collected under known photon intensity that was evaluated from the short-circuit photocurrent (J_{SC}) measured for different incident wavelengths (λ). The inset of Figure 6.6a shows the wavelength-dependent incident power of the monochromator. The photocurrent versus wavelength plot of the ZnO−QD−N719 architecture is presented in Figure 6.6a, which shows a spectral response in the range of 350 to 750 nm. In devices without any modification of the dye sensitizer with QDs, the broad photocurrent spectrum is attributed to the photogenerated

charge carrier in sensitizer N719 [28]. As shown in the figure, the presence of QD1 (abs. at 440 nm) and QD2 (abs. at 500 nm) into the sensitization process lead to a dramatic increase in the photocurrent in the spectral region of blue photons indicating the occurrence of a direct injection of electrons from QDs to ZnO NRs, similar to the

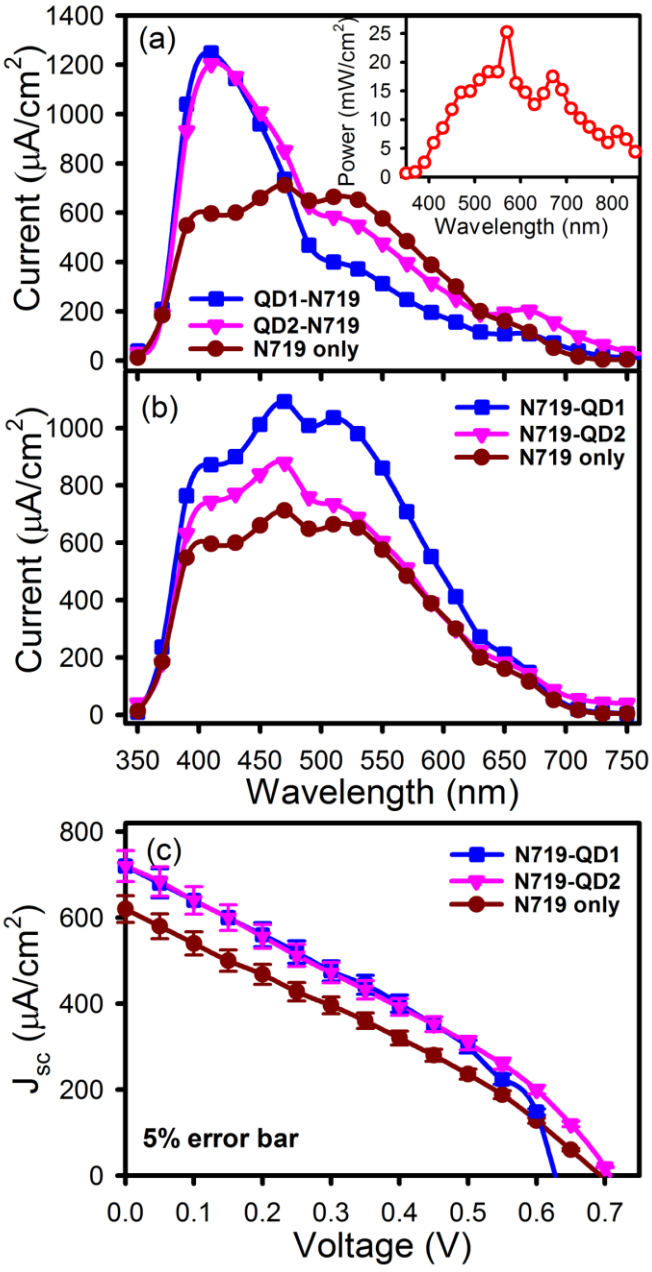

Figure 6.6. *Photocurrent vs. wavelength spectra for DSSCs comprised of a) ZnO−QD−N719 and b) ZnO−N719−QD architectures, respectively. The inset shows incident power vs wavelength plot. c) Photocurrent−voltage (J−V) characteristics for ZnO−N719−QD architecture.*

Table 6.4. Device performance[d] of the DSSCs made of two different architecture of QD loading.

Device with N719	V_{OC} (V)	J_{SC} (μA/cm^2)	*FF* (%)	η (%)
ZnO−N719−QD1	0.63±0.04	720±36	35.27±2.70	0.16±0.01
ZnO−N719−QD2	0.71±0.03	720±29	30.99±1.31	0.16±0.01
ZnO−N719	0.69±0.05	620±33	29.92±0.50	0.13±0.01

[d]*short-circuit photocurrent densities (J_{SC}/cm^2), open-circuit voltage (V_{OC}), fill factor (FF), and efficiency (η).*

observations made by the picosecond-resolved fluorescence studies (Figure 6.5c). In this case, it is to be noted that dye (N719) loading was lower in ZnO−QD−N719 architecture compared to that of ZnO−N719 assembly due to prior attachment of QD to the ZnO NRs. Therefore, at 530 nm (maximum optical absorption in N719) the photocurrent was found to be lower in ZnO−QD−N719 compared to ZnO−N719 system. Hence, a fair comparison of wavelength-dependent photocurrent and overall device performance of these architectures is not likely when the amounts of dye present in different architectures are not similar. For a better assessment, we engineered devices with similar dye loading in ZnO−N719−QD and ZnO−N719 solar cells. The ZnO−N719−QD architecture shows increased photocurrent (Figure 6.6b) compared to ZnO−N719 system throughout the spectral region as additional photogenerated charge carriers from N719 dye (*via* FRET) adds up to the net photocurrent. Figure 6.6c shows the $J-V$ characteristics of solar cells with ZnO−N719−QD architecture as compared to solar cells sensitized with dye only. As shown in Table 6.4, the calculated values of FF and the overall power conversion efficiencies of ZnO−N719 based DSSCs are found to improve in the presence of QD assembly. Overall, the analysis of photodevice data in the measured ZnO−N719−QD configuration reflects similarly the cosensitization of CdTe QDs tagged with the sensitivity of FRET as observed by the picosecond-resolved fluorescence study (Figure 6.5c).

The photoconductivity measurement [32] (as discussed in section 3.1.13) of the ZnO NR, ZnO−N719 and ZnO−N719−QD thin films were carried out in order to better understand the contribution of QDs *via* FRET to the net photocurrent in the devices. Figure 6.7 shows the photocurrent response for the ZnO NR (inset), ZnO−N719 and

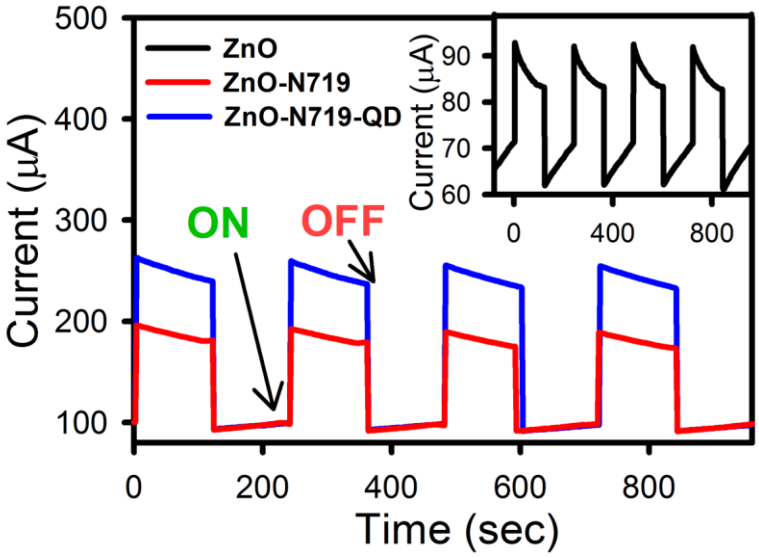

Figure 6.7. *Photocurrent responses of ZnO NRs (inset), ZnO−N719, and ZnO−N719−QD2 arrays under bias voltage of 2.5 V. The photocurrent was measured across the thickness of the films with 25 mW cm^{-2} incident power from a halogen light source.*

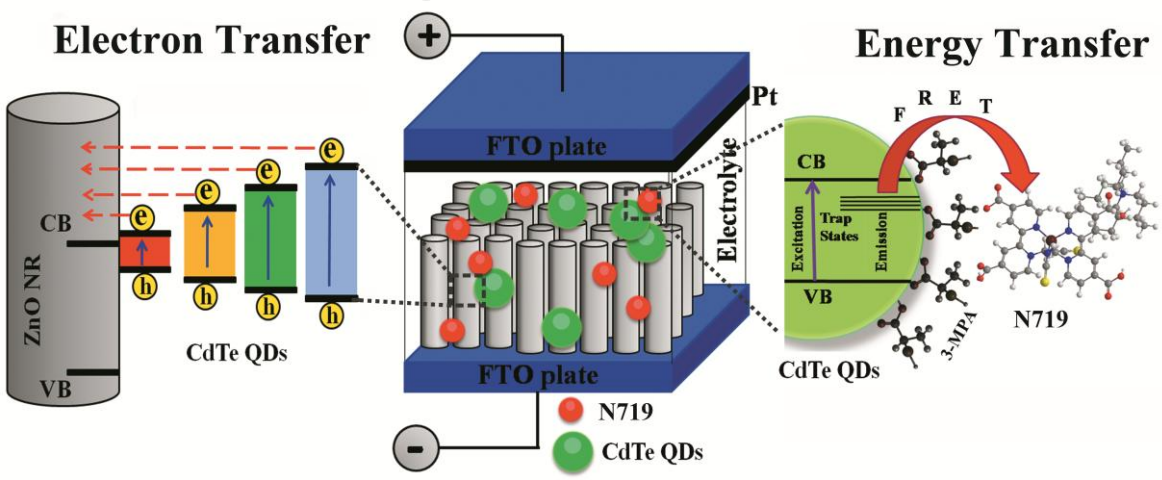

Scheme 6.1. *Dual-sensitization in QD-decorated DSSCs: the system consists of a fluorinated tin oxide (FTO) on which semiconductor ZnO NR (gray cylinder) is fabricated. The sensitizer dye N719 (small red circle) and 3-MPA-capped CdTe QDs (big green circle) are bound to ZnO NR by surface adsorption. The directly attached QDs lead to sensitization via efficient charge injection from excited semiconductor nanocrystal, CdTe into ZnO NR. Moreover, the QDs that are within the close proximity of sensitizing dye N719 introduce an additional indirect excitation of N719 by using the sensitivity of FRET. The upshot of the above dual-sensitization mode is found to be reflected in the overall solar cell performance.*

ZnO−N719−QD2 thin films. An improved photocurrent was observed for the ZnO−N719−QD2 thin film (~260 μA) under illuminated conditions compared to the ZnO−N719 thin film (~190 μA). This shows that an additional "indirect excitation" of N719 can be obtained by decorating the dye molecules with CdTe QDs. For the model DSSCs prepared with the same arrangement of ZnO−N719−QD, we observed a similar enhancement of photocurrent (Figure 6.6c) in the presence of CdTe QDs, which further confirms the contribution of FRET towards the improvement of efficient energy harvesting in dual-sensitized solar cells.

6.3. Conclusion:

In conclusion, by using spectroscopic techniques we have demonstrated the utilization of dual-sensitization in DSSCs, as schematically represented in Scheme 6.1. The steady-state and the time-resolved luminescence measurements on 3-MPA-capped CdTe QDs reveal the size-dependent charge injection characteristics to ZnO photoelectrodes. The QDs which are not in a direct contact with the semiconductor can harvest visible-light which resonantly transfer to SD N719 and offers an "indirect excitation" of the SD. To investigate the improvement of light-harvesting due to QD decoration in a DSSC, wavelength-dependent photocurrent, photocurrent−voltage (*J*−*V*) characteristics and photoconductivity measurements were performed for both the QD-assembled and reference (only sensitizing dye) devices. The cosensitization in the presence of CdTe QDs leads to a significant increment in photocurrent throughout the visible spectral region and also enhances the short-circuit current density as additional photogenerated charge carriers from N719 dye (*via* FRET) adds up to the net photocurrent. As we continue to modify, study, and improve such FRET pair sensitizers, the realization of truly inexpensive, stable, and efficient DSSCs grows nearer.

References

[1] B. O'Regan, M. Grätzel, A Low-Cost, High-Efficiency Solar Cell Based on Dye-Sensitized Colloidal TiO_2 Films, *Nature* 353 (1991) 737.

[2] M. Grätzel, Photoelectrochemical Cells, *Nature* 414 (2001) 338.

[3] M.K. Nazeeruddin, F.D. Angelis, S. Fantacci, A. Selloni, G. Viscardi, P. Liska, S. Ito, B. Takeru, M. Grätzel, Combined Experimental and DFT-TDDFT Computational Study of Photoelectrochemical Cell Ruthenium Sensitizers, *J. Am. Chem. Soc.* 127 (2005) 16835.

[4] M.K. Nazeeruddin, C. Klein, P. Liska, M. Grätzel, Synthesis of Novel Ruthenium Sensitizers and Their Application in Dye-Sensitized Solar Cells, *Coord. Chem. Rev.* 249 (2005) 1460.

[5] A.B.F. Martinson, J.W. Elam, J.T. Hupp, M.J. Pellin, ZnO Nanotube Based Dye-Sensitized Solar Cells, *Nano Lett.* 7 (2007) 2183.

[6] J.H. Yum, P. Walter, S. Huber, D. Rentsch, T. Geiger, F. Nüesch, F.D. Angelis, M. Grätzel, M.K. Nazeeruddin, Efficient Far Red Sensitization of Nanocrystalline TiO_2 Films by an Unsymmetrical Squaraine Dye, *J. Am. Chem. Soc.* 129 (2007) 10320.

[7] A. Burke, L. Schmidt-Mende, S. Ito, M. Grätzel, A Novel Blue Dye for Near-IR 'Dye-Sensitized' Solar Cell Applications, *Chem. Commun.* (2006) 234.

[8] W.M. Campbell, K.W. Jolley, P. Wagner, K. Wagner, P.J. Walsh, K.C. Gordon, L. Schmidt-Mende, M.K. Nazeeruddin, Q. Wang, M. Grätzel, D.L. Officer, Highly Efficient Porphyrin Sensitizers for Dye-Sensitized Solar Cells, *J. Phys. Chem. C* 111 (2007) 11760.

[9] S.Q. Fan, R.J. Cao, Y.X. Xi, M. Gao, M.D. Wang, D.H. Kim, C.W. Kim, J.J. Ko, CdSe Quantum Dots As Co-Sensitizers of Organic Dyes in Solar Cells for Red-Shifted Light Harvesting, *Optoelectron. Adv. Mat.* 3 (2009) 1027.

[10] W. Yu, L.H. Qu, W.Z. Guo, X.G. Peng, Experimental Determination of the Extinction Coefficient of CdTe, CdSe, and CdS Nanocrystals, *Chem. Mater.* 15 (2003) 2854.

[11] P.V. Kamat, Meeting the Clean Energy Demand: Nanostructure Architectures for Solar Energy Conversion, *J. Phys. Chem. C* 111 (2007) 2834.

[12] Q. Zhang, X. Guo, X. Huang, S. Huang, D. Li, Y. Luo, Q. Shen, T. Toyoda, Q. Meng, Highly Efficient CdS/CdSe-Sensitized Solar Cells Controlled by the Structural Properties of Compact Porous TiO_2 Photoelectrodes, *Phys. Chem. Chem. Phys.* 13 (2011) 4659.

[13] S. Ruhle, M. Shalom, A. Zaban, Quantum-Dot-Sensitized Solar Cells, *Chem. Phys. Chem.* 11 (2010) 2290.

[14] M. Shalom, S. Ruhle, I. Hod, S. Yahav, A. Zaban, Energy Level Alignment in CdS Quantum Dot Sensitized Solar Cells Using Molecular Dipoles, *J. Am. Chem. Soc.* 131 (2009) 9876.

[15] P.V. Kamat, Quantum Dot Solar Cells. Semiconductor Nanocrystals as Light Harvesters, *J. Phys. Chem. C* 112 (2008) 18737.

[16] A. Kongkanand, K. Tvrdy, K. Takechi, M. Kuno, P.V. Kamat, Quantum Dot Solar Cells. Tuning Photoresponse through Size and Shape Control of CdSe-TiO_2 Architecture, *J. Am. Chem. Soc.* 130 (2008) 4007.

[17] J.H. Bang, P.V. Kamat, Quantum Dot Sensitized Solar Cells. A Tale of Two Semiconductor Nanocrystals: CdSe and CdTe, *ACS Nano* 3 (2009) 1467.

[18] R.T. Ross, A.J. Nozik, Efficiency of Hot-Carrier Solar Energy Converters, *J. Appl. Phys.* 53 (1982) 3813.

[19] R.D. Schaller, V.M. Agranovich, V.C. Klimov, High-Efficiency Carrier Multiplication through Direct Photogeneration of Multi-Excitons *via* Virtual Single-Exciton States, *Nat. Phys.* 1 (2005) 189.

[20] R.D. Schaller, V.I. Klimov, High Efficiency Carrier Multiplication in PbSe Nanocrystals: Implications for Solar Energy Conversion, *Phys. Rev. Lett.* 92 (2004) 186601.

[21] P.V. Kamat, K. Tvrdy, D.R. Baker, J.G. Radich, Beyond Photovoltaics: Semiconductor Nanoarchitectures for Liquid-Junction Solar Cells, *Chem. Rev.* 110 (2010) 6664.

[22] M. Shalom, S. Dor, S. Ruhle, L. Grinis, A. Zaban, Core/CdS Quantum Dot/Shell Mesoporous Solar Cells with Improved Stability and Efficiency Using an Amorphous TiO_2 Coating, *J. Phys. Chem. C* 113 (2009) 3895.

[23] M. Shalom, J. Albero, Z. Tachan, E. Martínez-Ferrero, A. Zaban, E. Palomares, Quantum Dot-Dye Bilayer-Sensitized Solar Cells: Breaking the Limits Imposed by the Low Absorbance of Dye Monolayers, *J. Phys. Chem. Lett.* 1 (2010) 1134.

[24] H. Choi, R. Nicolaescu, S. Paek, J. Ko, P.V. Kamat, Supersensitization of CdS Quantum Dots with a Near-Infrared Organic Dye: Toward the Design of Panchromatic Hybrid-Sensitized Solar Cells, *ACS Nano* 5 (2011) 9238.

[25] S. Giménez, A.L. Rogach, A.A. Lutich, D. Gross, A. Poeschl, A.S. Susha, I. Mora-Seró, T. Lana-Villarreal, J. Bisquert, Energy Transfer versus Charge Separation in Hybrid Systems of Semiconductor Quantum Dots and Ru-Dyes as Potential Co-Sensitizers of TiO_2-based Solar Cells, *J. Appl. Phys.* 110 (2011) 014314.

[26] L. Etgar, J. Park, C. Barolo, V. Lesnyak, S.K. Panda, P. Quagliotto, S.G. Hickey, M.K. Nazeeruddin, A. Eychmuller, G. Viscardi, M. Grätzel, Enhancing the Efficiency of a Dye Sensitized Solar Cell due to the Energy Transfer between CdSe Quantum Dots and a Designed Squaraine Dye, *RSC Adv.* 2 (2012) 2748.

[27] A. Ruland, C. Schulz-Drost, V. Sgobba, D.M. Guldi, Enhancing Photocurrent Efficiencies by Resonance Energy Transfer in CdTe Quantum Dot Multilayers: Towards Rainbow Solar Cells, *Adv. Mater.* 23 (2011) 4573.

[28] K. Shankar, X. Feng, C.A. Grimes, Enhanced Harvesting of Red Photons in Nanowire Solar Cells: Evidence of Resonance Energy Transfer, *ACS Nano* 3 (2009) 788.

[29] S. Buhbut, S. Itzhakov, E. Tauber, M. Shalom, I. Hod, T. Geiger, Y. Garini, D. Oron, A. Zaban, Built-in Quantum Dot Antennas in Dye-Sensitized Solar Cells, *ACS Nano* 4 (2010) 1293.

[30] S. Buhbut, S. Itzhakov, D. Oron, A. Zaban, Quantum Dot Antennas for Photoelectrochemical Solar Cells, *J. Phys. Chem. Lett.* 2 (2011) 1917.

[31] A. Makhal, S. Sarkar, T. Bora, S. Baruah, J. Dutta, A.K. Raychaudhuri, S.K. Pal, Role of Resonance Energy Transfer in Light Harvesting of Zinc Oxide-Based Dye-Sensitized Solar Cells, *J. Phys. Chem. C* 114 (2010) 10390.

[32] S. Sarkar, A. Makhal, T. Bora, S. Baruah, J. Dutta, S.K. Pal, Photoselective Excited State Dynamics in ZnO-Au Nanocomposites and their Implications in Photocatalysis and Dye-Sensitized Solar Cells, *Phys. Chem. Chem. Phys.* 13 (2011) 12488.

[33] C. Siegers, J. Hohl-Ebinger, B. Zimmermann, U. Würfel, R. Mülhaupt, A. Hinsch, R. Haag, A Dyadic Sensitizer for Dye Solar Cells with High Energy Transfer Efficiency in the Device, *Chem. Phys. Chem.* 8 (2007) 1548.

[34] B.E. Hardin, E.T. Hoke, P.B. Armstrong, J.H. Yum, P. Comte, T. Torres, J.M.J. Frechet, M.K. Nazeeruddin, M. Grätzel, M.D. McGehee, Increased Light Harvesting in Dye-Sensitized Solar Cells with Energy Relay Dyes, *Nat. Photonics* 3 (2009) 406.

[35] S. Sarkar, A. Makhal, K. Lakshman, T. Bora, J. Dutta, S.K. Pal, "Dual-Sensitization" via Electron and Energy Harvesting in CdTe Quantum Dots Decorated ZnO Nanorod-based Dye-Sensitized Solar Cells, *J. Phys. Chem. C* 116 (2012) 14248.

[36] M. Pehnt, D.L. Schulz, C.J. Curtis, K.M. Jones, D.S. Ginley, Nanoparticle Precursor Route to Low Temperature Spray Deposition of CdTe Thin Films, *Appl. Phys. Lett.* 67 (1995) 2176.

[37] I. Mora-Sero, D. Gross, T. Mittereder, A.A. Lutich, A.S. Susha, T. Dittrich, A. Belaidi, R. Caballero, F. Langa, J. Bisquert, A.L. Rogach, Nanoscale Interaction Between CdSe or CdTe Nanocrystals and Molecular Dyes Fostering or Hindering Directional Charge Separation, *Small* 6 (2010) 221.

[38] M. Li, S.K. Cushing, Q. Wang, X. Shi, L.A. Hornak, Z. Hong, N. Wu, Size-Dependent Energy Transfer between CdSe/ZnS Quantum Dots and Gold Nanoparticles, *J. Phys. Chem. Lett.* 2 (2011) 2125.

[39] S. Batabyal, A. Makhal, K. Das, A.K. Raychaudhuri, S.K. Pal, Ultrafast Dynamics of Excitons in Semiconductor Quantum Dots on a Plasmonically Active Nano-Structured Silver Film, *Nanotechnology* 22 (2011) 195704.

[40] I. Robel, M. Kuno, P.V. Kamat, Size-Dependent Electron Injection from Excited CdSe Quantum Dots into TiO_2 Nanoparticles, *J. Am. Chem. Soc.* 129 (2007) 4136.

[41] I. Mora-Sero, J. Bisquert, T. Dittrich, A. Belaidi, A.S. Susha, A.L. Rogach, Photosensitization of TiO_2 Layers with CdSe Quantum Dots: Correlation between Light Absorption and Photoinjection, *J. Phys. Chem. C* 111 (2007) 14889.

[42] E. Martínez-Ferrero, J. Albero, E. Palomares, Materials, Nanomorphology, and Interfacial Charge Transfer Reactions in Quantum Dot/Polymer Solar Cell Devices, *J. Phys. Chem. Lett.* 1 (2010) 3039.

[43] R.S.J. Aga, D. Jowhar, A. Ueda, Z. Pan, W.E. Collins, R. Mu, K.D. Singer, J. Shen, Enhanced Photoresponse in ZnO Nanowires Decorated with CdTe Quantum Dot, *Appl. Phys. Lett.* 91 (2007) 232108.

[44] X. Cao, P. Chen, Y. Guo, Decoration of Textured ZnO Nanowires Array with CdTe Quantum Dots: Enhanced Light-Trapping Effect and Photogenerated Charge Separation, *J. Phys. Chem. C* 112 (2008) 20560.

Chapter 7

Photoinduced Dynamical Processes and Promising Applications of a Potential Bio-Nanocomposite

7.1. Introduction:

The critical role that dopants play in semiconductor structure has stimulated research on the properties and the potential applications of doped semiconductor nanoparticles (NPs) [1-2]. The control of optoelectronic properties of such semiconductor NPs using different doping is found to be quite efficient [3], such as, large magneto-optical effect [4-5], efficient sensitized impurity luminescence [4, 6-8] and quantum size effects on impurity-carrier binding energies [9]. Manganese (Mn)-doped zinc chalcogenide NPs have been explored as an alternatives to popularly used CdSe QDs with advantages of lower toxicity and larger Stokes shift [10]. The synthesis of such Mn-doped zinc sulphide (ZnS) NPs (diameter <5 nm) by the solvothermal method [11] has already been reported. However, the synthesis of high-quality Mn-doped ZnS NPs (diameter <5 nm) characterized by a sharp exciton absorption peak and uniform diameter is still a great challenge. In an earlier study [12] various levels in the Mn-doped ZnS nanocluster with relatively smaller diameter (1.2 nm) in reverse micellar environments leading to different relaxation dynamics have been reported. Tunability of the electronic energy depending on the diameter of high-quality Mn-dopped ZnS nanorod has also been evident in recent literature [10].

The use of proteins and peptides to direct the *in vitro* syntheses of inorganic materials is attractive for a number of reasons [13]. First, peptides and proteins make bio-enabled syntheses of inorganic materials inherently “green” processing which is facilitated at or near room-temperature, in aqueous solutions. Second, proteins and peptides can exquisitely control the size, shape, optical properties and crystal structure of the inorganic product. The major benefit of using peptides and proteins is to produce materials with highly specific or multiple functions; such proteins and peptides may direct the arrangement of enzymatically active composites or produce materials that specifically

recognize substrates. To be a suitable biolabelling agent, NPs should have high luminescence efficiency, biocompatibility, and proper surface groups for coupling with biomolecules. To date, however, the obtained doped nanocrystals barely meet these requirements. The consequence of using capping agents on the electronic and defect states of Mn-doped ZnS NPs, which leads to a large enhancement of photoluminescence (PL) intensity of the nanomaterials, has been reported [14-15]. However, a detailed study on the photoselective excited state dynamics and electron migration in such NPs in a biological macromolecular environment is sparse in literature and is one of the motives of the present work. The studies are important in the context that the interaction of NPs with proteins [16] has emerged as a key parameter in nanomedicine and nanotoxicology [17].

Here we have followed a simple, faster and "green" phosphine free colloidal chemical route [18] for the synthesis of enzyme-capped high-quality Mn-doped ZnS bio-nanocomposites (BNCs), as schematically shown in Scheme 7.1. The enzyme α-Chymotrypsin (CHT)-capped multifunctional BNCs, with average diameter <5 nm, are found to be extremely soluble and stable in aqueous solution for several weeks. To investigate the specific role of enzyme environments on the nanomaterial surface, we have also synthesized Cysteine (Cys, sulphur containing amino group)-capped ZnS NPs with <5 nm diameter, as a control sample. While steady-state absorption and emission spectroscopy explore various electronic states of the Cys/CHT-capped BNCs, picosecond-resolved emission using various excitation/detection wavelengths reveals the relaxation of electrons from specific states which was further supported by the photocatalysis of a test contaminant. Irradiation induced luminescence enhancement (IILE) [19] technique with different excitation intensities has been studied to explore the interaction of the enzyme with surface states and to justify efficacy of the protein capping agent that shield against deep-UV induced surface damage of the NP surface. In this respect, more biomolecules irrespective of CHT are also promising that may give rise to a new class of multifunctional BNCs with possible biological applications. For example, Lipase L1 enzyme contains an unusual extra domain, making a tight intramolecular interaction with the main catalytic domain through a Zn^{2+}-binding coordination which may offer more novel ZnS BNCs using lipase as a potential host matrix [20].

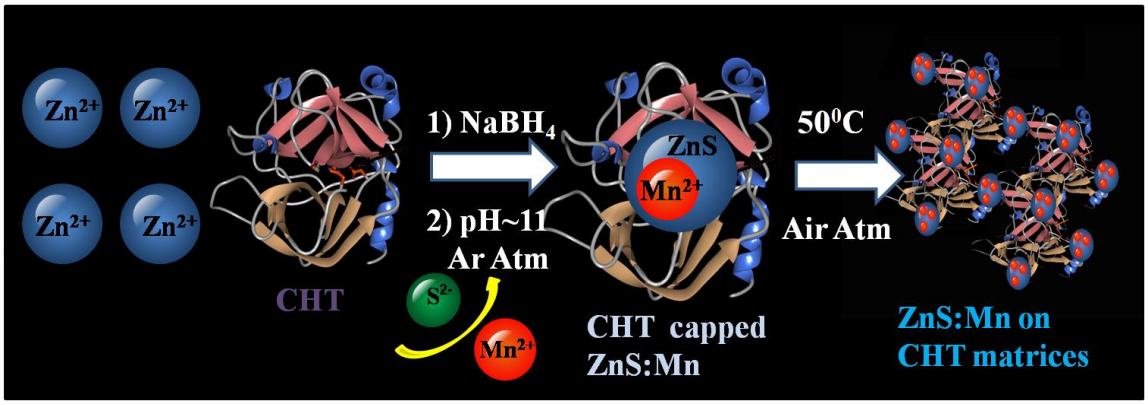

Scheme 7.1. *Synthetic strategy of enzyme mediated Mn-doped ZnS BNCs.*

7.2. Results and Discussion:

7.2.1. Protein-Mediated Synthesis of Nanosized Mn-Doped ZnS: A Multifunctional, UV-Durable Bio-Nanocomposite [21]:

7.2.1.1. Characterization of NPs in the BNCs: Figure 7.1 shows a set of transmission electron microscopic (TEM) images of CHT and Cys-capped, with/without Mn-doped ZnS NPs. It has to be noted that the shape of the NPs in the protein matrix is relatively quasi-spherical compared to that of the Cys-capped NPs. The observation could be consistent with the fact that the NPs in the protein matrix are associated with a number of sulphur containing Cys residues from various locations of a protein which essentially direct the shape of the NPs to be quasi-spherical. On the other hand, plenty of free Cys residues in the solution for the Cys-capped NPs lead to uniform growth of the NPs and make the shape to be spherical. The corresponding high-resolution TEM (HRTEM) images (right insets, Figure 7.1a−d) clearly demonstrate lattice fringes with an observed d-spacing of ~0.31 nm and ~0.23 nm for CHT and Cys-capped NPs, respectively, which are in good agreement with the high-crystallinity in the materials with zinc-blende structures [10, 22]. The particle sizes are estimated by fitting our experimental TEM data on 100 particles which provides the average diameter of 3 nm and 2.7 nm for CHT and Cys-capped NPs (left insets, Figure 7.1b, d), respectively. It is noticeable that CHT-capped NPs are fairly monodispersed in the protein matrix while for Cys-Zns:Mn, some of the particles are

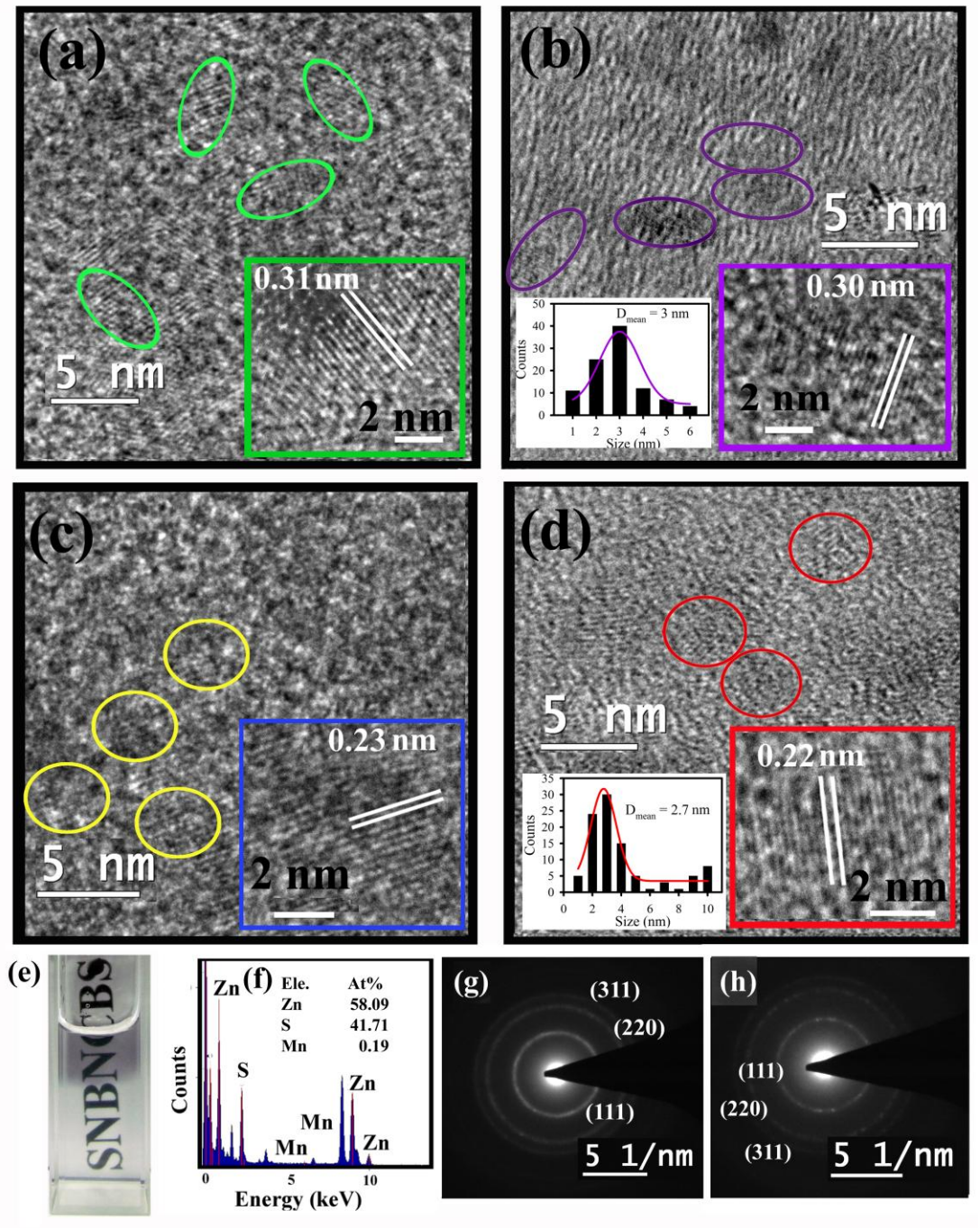

Figure 7.1. *Transmission electron microscopy (TEM) and high-resolution TEM images (inset) of a) CHT-ZnS, b) CHT-ZnS:Mn, c) Cys-ZnS, d) Cys-ZnS:Mn NPs. Inset left of figure b) and d) represent the size distribution analysis of CHT-ZnS NPs and Cys-ZnS:Mn NPs, respectively. Inset right of figure b) and d) represent the size distribution analysis of CHT-ZnS NPs and Cys-ZnS:Mn NPs, respectively. e) Optically transparent solution of CHT-ZnS:Mn BNCs under daylight, f) Energy-dispersive X-ray spectroscopy (EDAX) analysis and atomic percentages elements, g) and h) represent selected area electron diffraction (SAED) analysis of CHT-ZnS and CHT-ZnS:Mn BNCs, respectively.*

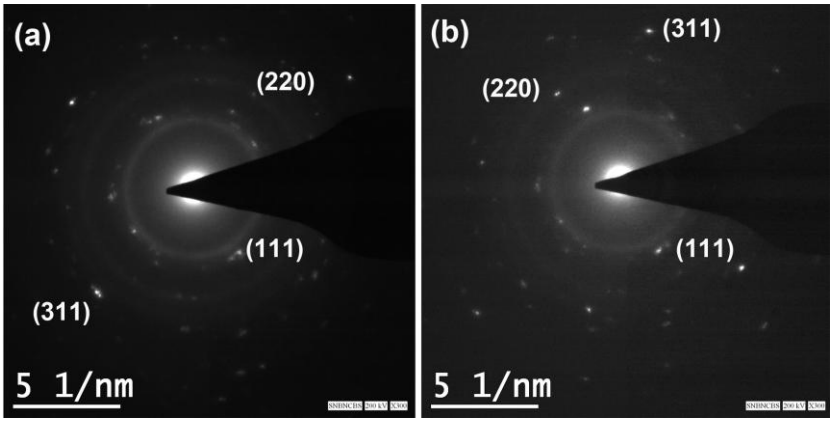

Figure 7.2. *Selected-area electron diffraction (SAED) pattern of a) Cys-ZnS and b) Cys-ZnS:Mn nanoparticles.*

agglomerated up to 10 nm. Owing to the amino group capping on the surface, all the BNCs can be steadily dispersed in water to form an optically transparent solution (Figure 7.1e). Further confirmation of the composition and the crystal structure of as-prepared NPs are also evident from Energy-dispersive X-ray spectroscopy (EDAX) and selected area electron diffraction (SAED) analysis. EDAX analysis (Figure 7.1f) of the CHT-capped NPs reveals the incorporation of Mn with atomic contribution of 0.2% as dopant. A detailed analysis of SAED pattern of CHT-capped (Figure 7.1g−h) and Cys-capped NPs (Figure 7.2) exhibit concentric rings along with some diffraction spots probably from larger particles. The rings have been indexed to (111), (220) and (311) planes of the cubic ZnS phase [23-24].

A typical XRD pattern for CHT-ZnS and CHT-ZnS:Mn BNCs is shown in Figure 7.3. The spectrum shows three diffraction peaks at 2θ values of 28.9°, 32.4°, 47.5°, and 56.5° which appear because of reflection from the (111), (200), (220), and (311) planes of the cubic phase of ZnS, respectively. The obtained peak positions correspond to zinc blended type patterns for all the samples [25-26]. Particle sizes from XRD patterns were estimated using Scherrer's equation $D = \frac{0.9\lambda}{\beta \cos\theta}$, where D is the mean grain size, λ is the X-ray wavelength (for CuKα radiation, λ = 0.15406 nm), θ is the diffraction angle (in radian), and β is full width at half-maximum. The grain size of CHT-ZnS and CHT-

ZnS:Mn BNCs, as calculated by using Scherrer's equation, is in range of ~20.7 nm. It must

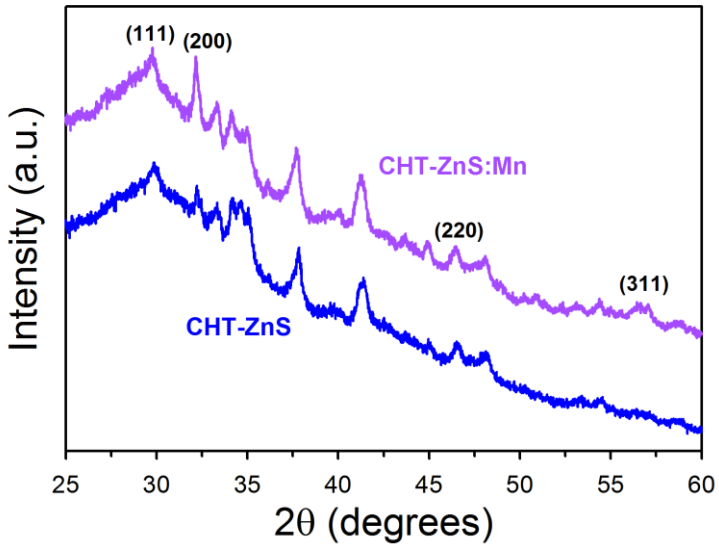

Figure 7.3. *XRD pattern of CHT-ZnS and CHT-ZnS:Mn BNCs at room temperature.*

be emphasized that the distinction between XRD and TEM data may be due to the presence of more than one crystallite in single grain, and the size determined by diffraction methods corresponds to the magnitude of the coherent crystal regions, that is, to regions where the periodic arrangement of the atoms is perfect and continuous. Furthermore, there may be some extent of agglomeration among the particles during the preparation of the samples for XRD measurement where the aqueous solution of the BNCs was lyophilized using Heto Power Dry LL1500 freeze dryer instrument and the powder form was used for XRD study. Therefore, the size obtained by diffraction cannot always be simply compared to the sizes determined by other techniques.

Many NPs in solution bear an electrostatic charge on their surface that hampers the interparticle interaction/aggregation by electrostatic repulsion. This surface charge of NPs is very important for defining the composition of the produced BNCs and also has an impact on their subsequent biodistribution. Generally, the zeta potential (ζ potential) gives information on the surface charge of the NPs and can be used to detect protein binding to the NP surface as this will change the overall surface charge [17, 27]. The increase in

electrophoretic mobility from −1.35 (Cys-ZnS:Mn) to −2.93 μm.cm/V.s (CHT-ZnS:Mn) confirmed the charging of the colloid surface through protein attachment. A change in the

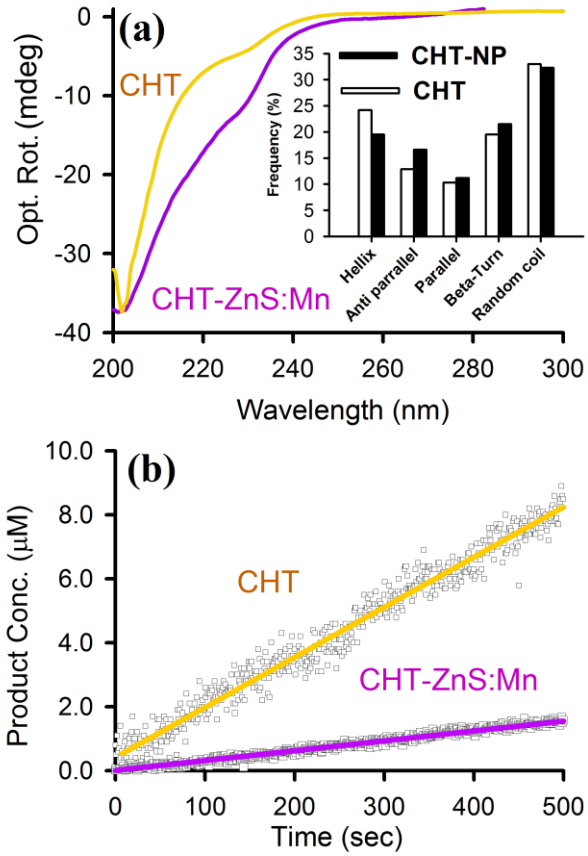

Figure 7.4. *a) Circular dichroism (CD) spectra of native CHT and CHT-ZnS:Mn BNCs. Inset showing the deconvolution of CD spectra for different fragments of enzyme with native CHT, b) the enzyme activity kinetics at 270 nm of native CHT and CHT-ZnS:Mn.*

ζ potential of the particles was observed from approximately −17.2 mV for a Cys-ZnS:Mn surface [28] to −37.3 mV, as expected for CHT-stabilized particles [29].

7.2.1.2. Protein Structure and Enzymatic Activity in the BNCs: Figure 7.4a shows circular dichroism (CD) spectra of the BNCs in aqueous solution and it has been compared with the spectrum of free CHT as a reference. From the CD spectra, a significant perturbation of the secondary structure of the NP-associated enzyme CHT is clearly noticeable. A careful analysis of the secondary structure (inset) of CHT upon attachment with NPs illustrates the variation in the content of helix and antiparallel β-sheet. The

consequences of the structural perturbation on the enzymatic activity of CHT in the BNCs are also evident from Figure 7.4b. In comparison to free enzymes, the NP-associated enzymes in BNCs show a significant retardation of the rate of formation of product (7-amido-4-methyl-coumarin) from the substrate (AAF-AMC). We have estimated that the activity of the BNCs to be 3.8 units/mg, which is significantly retarded compared to that of the free enzyme (21.3 units/mg) in aqueous solutions [30]. It is to be noted that the possibility of CHT to be remained as a free enzyme is negligibly small by considering 1:1 binding between CHT and NP since the concentration of the NP (~ 25 μM) is comparable to the initial enzyme concentration (20 μM) in the medium.

7.2.1.3. Optical Spectroscopy and Ultrafast Dynamics of the BNCs: We show the optical characterization of these BNC samples in terms of UV-visible absorption spectra

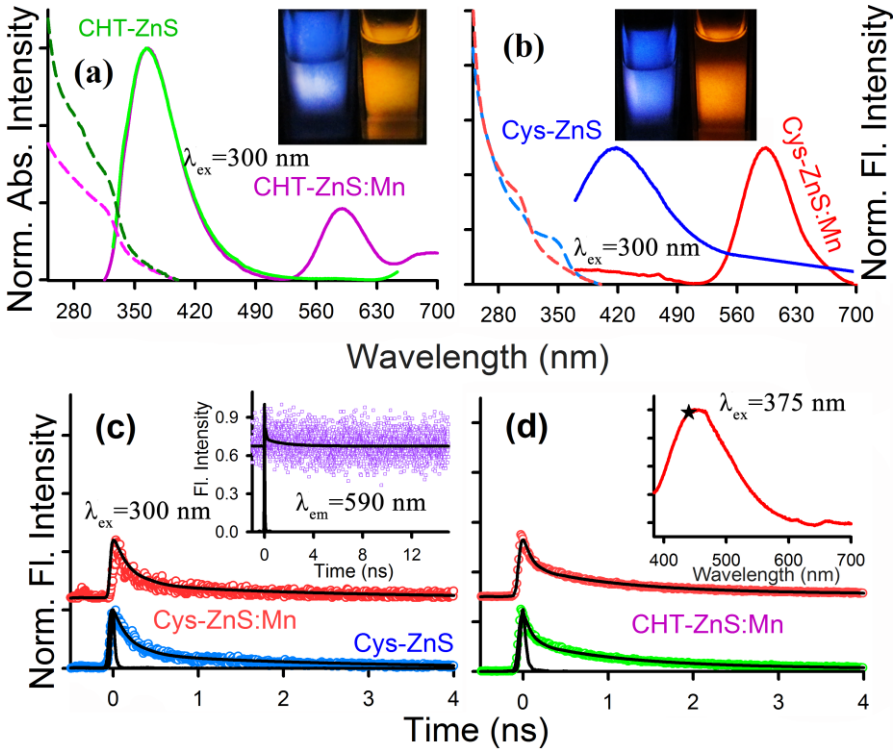

Figure 7.5. *a) The optical absorption and steady-state emission spectra of a) CHT-ZnS and CHT-ZnS:Mn BNCs and b) Cys-ZnS, Cys-ZnS:Mn NPs, respectively. Inset of a) and b) shows PL photos of the corresponding solutions upon 300 nm excitation. c) The picosecond-resolved fluorescence transients of Cys-ZnS and Cys-ZnS:Mn NPs (excitation at 300 nm) collected at 420 nm and inset shows fluorescence transient of Cys-ZnS:Mn NPs collected at 590 nm. d) The picosecond-resolved fluorescence transients of CHT-ZnS:Mn NPs (excitation at 375 nm) collected at 460 nm (to avoid Raman scattering) and 590 nm. Inset shows PL spectra upon 375 nm excitation. A star sign represents the appearance of Raman scattering upon 375 nm excitation.*

and fluorescence spectra in Figure 7.5. The UV-vis absorption spectra (Figure 7.5a, b) show distinct absorption-edge at 320 nm for all the Cys and CHT-capped samples. Effective mass approximation [31] for the estimation of particle size from the shoulder of the absorption spectra of all samples at 320 nm reveals relatively larger particle size (5.3 nm) compared to that observed in the TEM image. The discrepancy could be due to the quasi-broad particle size distribution as evidenced in the TEM studies. It has also been shown earlier that UV-vis spectroscopy essentially reveals larger particles of samples containing multiple particle size distribution [32-33].

The room-temperature PL spectra (Figure 7.5a, b) of doped and undoped ZnS NPs have been recorded at an excitation wavelength of 300 nm (4.13 eV). As shown in Figure 7.5b, Cys-capped undoped ZnS NPs show one broad emission band centered at ~420 nm, which is attributed to defect-state recombinations, possibly at the surface. Since, an excess of the cations have been used in the synthesis procedure, we expect sulphur vacancies at the surface giving rise to Zn dangling bonds that form shallow donor levels. Thus, the recombination is mainly between these shallow donor levels and the valence band. Becker *et al.* reported that S^{2-} vacancies even in bulk ZnS lead to emission at 428 nm [34]. Upon Mn incorporation in nanocrystal samples, blue ZnS emission is quenched, whereas an orange emission band develops at ~590 nm (Figure 7.5b), corresponding to the spin

Table 7.1. Picosecond-resolved luminescence transients of Cys/CHT-capped ZnS NPs with/without Mn-doping.[a]

Samples	Excitation wavelength (nm)	Detection wavelength (nm)	τ_1 (ns)	τ_2 (ns)	τ_{avg} (ns)
Cys-ZnS	300	420	0.20 (79%)	2.34 (21%)	0.65
Cys-ZnS:Mn	300	420	0.50 (88%)	3.49 (12%)	0.86
Cys-ZnS:Mn	300	590	4.5 (69%)	42.0 (31%)	16.1
CHT-ZnS:Mn	375	460	0.08 (92%)	2.89 (8%)	0.31
CHT-ZnS:Mn	375	590	0.13 (90%)	3.21 (10%)	0.44

[a]*The emissions from ZnS NPs (probing at 420, 460 and 590 nm) were detected with a 300 and 375 nm laser excitation. Numbers in the parentheses indicate relative weightage.*

forbidden $^4T_1 - ^6A_1$ Mn d-d transition in a tetrahedral site [35-37]. The insets of Figure 7.5a−b show PL photographs from the undoped (blue) and doped (orange) solutions upon 300 nm excitation. In the CHT-capped BNCs, NP associated proteins show a strong emission band centered at 367 nm (Figure 7.5a) which possibly augments ZnS PL band at 420 nm [38]. In the picosecond-resolved emission study (Figure 7.5c), the excited-state population of charge carriers in Cys-ZnS:Mn NPs are monitored at 420 nm followed by excitation at 300 nm. It is to be noted that Cys-ZnS and Cys-ZnS:Mn sample solutions show almost the same decay pattern (time constants) when both the decays are monitored at 420 nm. This phenomenon reveals that the ZnS PL quenching upon Mn-doping is either static in nature or may be too fast to be resolved in our TCSPC instrument with IRF of 60 ps. The inset of Figure 7.5c shows the time-resolved PL decay of Cys-ZnS:Mn NPs monitored at 590 nm. The PL transient is not completed in our experimental time window revealing higher values of time constants which are reported to be 1−2 ms in previous studies [7, 12]. Such a long lifetime makes the luminescence from the NPs readily distinguishable from the background luminescence from ZnS, which has a very short lifetime. On the other hand, in the cases of CHT-ZnS and CHT-ZnS:Mn BNCs, the strong emission from the protein essentially masks the ZnS emission and show characteristic decay of the intrinsic tryptophan residues of the protein in the picosecond-resolved transients at 420 nm (data are not shown). However, it is to be noted that CHT-ZnS:Mn samples show almost same decay pattern when detected at 590 nm (Figure 7.6) and as a

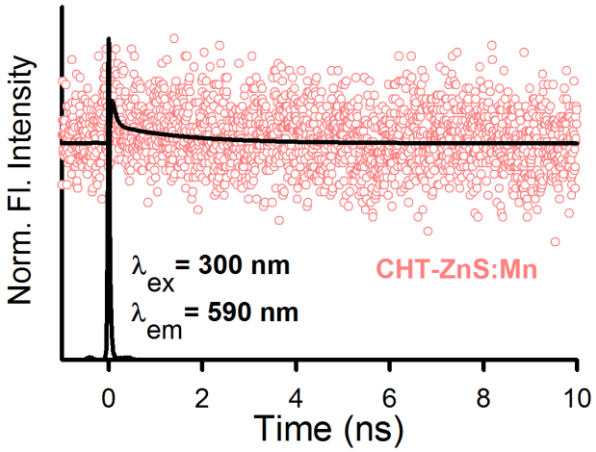

Figure 7.6. *Time-resolved PL decay of CHT-ZnS:Mn NPs monitored at 590 nm (λ_{ex}=300 nm).*

consequence, these advantages make them ideal candidates as fluorescence labelling agents, especially in biology [33]. Upon below band-edge excitation (with 375 nm i.e. 3.3 eV), no Mn emission peak is noticeable in the doped NPs (Figure 7.5d, inset). The picosecond-resolved fluorescence decays (excitation at 375 nm) monitored at 460 (to avoid Raman scattering at 428 nm) and 590 nm are shown in Figure 7.5d which exhibits similar time constants of ZnS. The observation suggests that the below band-gap excitation is not sufficient to excite the doped material (Mn) *via* energy transfer from the host's conduction band to the Mn state [33]. Considering that the excitation process generates an electron−hole pair across the band-gap (3.9 eV) of the ZnS nanocrystal host, the present results make it obvious that there is a more efficient excitonic energy transfer from the host to the doped Mn site compared to that of the defect states in these materials; revealing a strong coupling between the Mn d-levels and the host states [39]. The energy transfer is unlikely to occur directly from the semiconductor trap (defect) states to the low-lying Mn d-states. This observation demonstrates that the trap states are not in a direct coupling with the Mn d-states and Mn-doping do not affect the trap state lifetimes of the excited state electrons at the host ZnS surface. Details of the spectroscopic parameters and the fitting parameters of the PL decays are tabulated in Table 7.1.

7.2.1.4. Photocatalytic Activity of the BNCs: To investigate the efficacy of the host protein matrix in promoting photogenerated charges from ZnS NP to a surface adsorbed molecule, we have performed photocatalysis of an organic dye methylene blue (MB). Bulk ZnS semiconductor with a large band-gap (3.6 eV) produces electron−hole pairs under UV-light that initiates the formation of surface radicals capable of oxidizing adsorbed organic and biological pollutants [40-41]. As a photocatalyst, ZnS has been examined for degradation of water pollutants, reduction of toxic heavy metals, and water-splitting for H_2 evolution [42-44]. In this work, photocatalytic activity was quantified by carrying out photoreduction of a test contaminant MB (Figure 7.7a) which is known to be an excellent probe for the study of interfacial electron transfer in colloidal semiconductor systems [45-46]. It is obvious that higher the charge migration from the surface of the ZnS semiconductor, the faster will be the degradation of the surface-attached MB. Under selective UV radiation, we have recorded the absorption peak of MB (at 655 nm) at 90 sec intervals, using SPECTRA SUITE software supplied by Ocean Optics, and plotted it

against the time of photoirradiation. The decrease in the absorbance at 655 nm implies the reduction of MB to colourless leuco methylene blue (LMB). Results of MB degradation in the presence and absence of 25 μM ZnS photocatalysts under UV light are shown in Figure 7.7b, where the relative concentration (C_t/C_0) of MB in solution is plotted with respect to

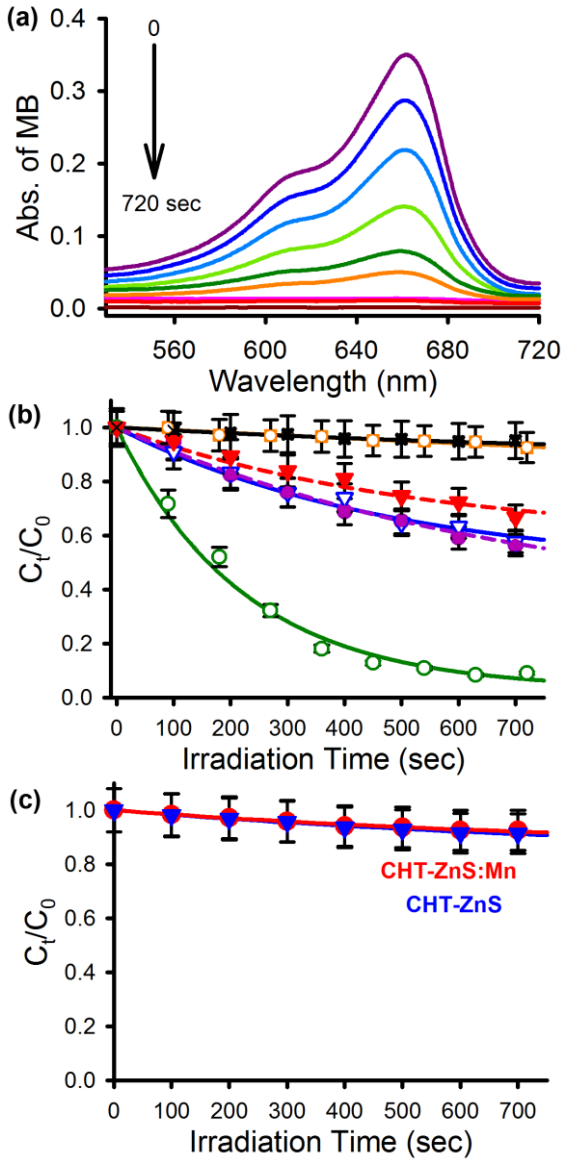

Figure 7.7. *a) Time dependent UV-vis spectral changes of MB in the presence of CHT-ZnS BNCs under UV-light irradiation. b) Plot of relative concentration (C_t/C_0) versus irradiation time for the degradation of MB (monitored at 655 nm) is shown. The degradation is performed in the presence of BNCs: CHT-ZnS (empty circle), CHT-ZnS:Mn (filled circle), Cys-ZnS (empty triangle), Cys-ZnS:Mn (filled triangle), only CHT (empty square), no catalysts (crossed). c) Plot of C_t/C_0 versus irradiation time in the presence of CHT-ZnS (filled triangle) and CHT-ZnS:Mn (filled circle) upon selective excitation with a 350 nm HP filter.*

UV irradiation time. The control experiments performed for several hours in the absence of catalysts and/or without UV-irradiation have only resulted in a negligible change in the MB concentration. All the photodegradation curves were found to follow a first-order exponential equation $y = A\exp(-kt) + y_0$, and the kinetic parameters are represented in Table 7.2. The percentages of total photodegradation (i.e., the value of *A* in the first-order kinetic equation shown in Table 7.2) are found to be enhanced in CHT-ZnS compared to Cys-capped NPs. This observation clearly reveals the molecular recognition of MB molecules by ZnS-attached protein, which can effectively host both ZnS and MB molecules; consequently the electron transfer process is facilitated when electron donor and acceptor molecules come to a close proximity. It is to be noted that CHT contains amino acids with aromatic rings in their side-chains which can act as hydrophobic host sites where the organic dye MB (with aromatic rings) can be incorporated efficiently [47]. It is also revealed that the photocatalytic activity of photocatalyst decreases upon Mn-doping which is consistent with the fact that excited electrons of ZnS can resonantly transfer their energy to Mn^{2+} state *via* nonradiative processes. As a consequence, in the presence of Mn, excited electrons are unable to migrate from the ZnS surface to perform the reduction of MB. In contrast, Cys is not comprised of hydrophobic aromatic rings in its

Table 7.2. The kinetics parameters[b] for the photodeterioration of methylene blue (MB) in the absence and presence of ZnS.

Samples	k (s^{-1})	Total amount of degradation (A%) (in 720 sec)	R^2
Above band-edge excitation			
CHT-ZnS	4.5×10^{-3}	94	0.95
CHT-ZnS:Mn	2.0×10^{-3}	45	0.94
Cys-ZnS	1.9×10^{-3}	41	0.90
Cys-ZnS:Mn	1.4×10^{-3}	32	0.95
CHT	1.1×10^{-3}	8	0.94
No Catalyst	9.9×10^{-4}	7	0.88
Below band-gap excitation			
CHT-ZnS	1.1×10^{-3}	10	0.92
CHT-ZnS:Mn	1.0×10^{-3}	9	0.94

[b]*kinetic constants (k), percentages of photoselective degradation (A) and the regression coefficients (R^2).*

side-chain which can provide efficient binding of MB molecules in order to facilitate the electron transfer from ZnS to MB. Therefore, the photocatalytic activity itself becomes very poor for Cys-ZnS NPs which decreased further with Mn-doping.

We have also performed the photocatalysis of MB under selective below band-gap excitation of ZnS NPs to investigate the role of surface trap states in the semiconductor. For this, a 350 nm (3.3 eV) high-pass (HP) filter was used to excite ZnS BNCs, which effectively excite electrons to its trap states (below band-gap) rather than exciting electrons to the conduction band of semiconductor (as evidenced by the PL study). From the photodegradation of MB in the presence of ZnS and ZnS:Mn BNCs with a 350 HP filter, it is clearly shown that no considerable change in the absorbance peak at 655 nm takes place upon below band-gap excitation (Figure 7.7c). It reveals that the electron transfer is not allowed from ZnS/ZnS:Mn to MB upon direct excitation of electrons to the trap states in BNCs.

7.2.1.5. Irradiation Induced Luminescence Enhancement (IILE) Effect of the BNCs: To investigate the efficacy of the protein-shell around the BNCs against the UV damage of the encapsulated NPs, we have performed IILE studies (section 2.1.5) under different irradiance doses on both CHT and Cys-capped nanostructures. Earlier, several mechanisms have been proposed to explain the increase in quantum efficiency for UV-irradiated ZnS:Mn NPs [48-49]. More recently, the model involving the migration of electron from ZnS band to the Mn^{2+} state is found to be more acceptable and further justified by experimental evidences [50]. Being exposed under the UV-irradiation, the population of the surface quench centres of the NPs decreases because of either photochemical or photophysical processes; luminescence of Mn^{2+} ions is thus enhanced. The reported studies on the IILE in a polymeric host matrices and shell capping reveal the minimum damages on NPs surfaces [15, 50]. Our experimental observations of the IILE detection wavelength (at 590 nm) [51] from various Mn-doped samples, as shown in Figures 7.8a−d, reveal common temporal characteristics. At the beginning, the emission intensity decreases following a plateau region and finally increases monotonically. We have divided the IILE spectra of CHT and Cys-capped NPs into three different zones, short-term degradation (STD) [52], plateau (stable) and IILE, respectively. It is obvious from the figures that the

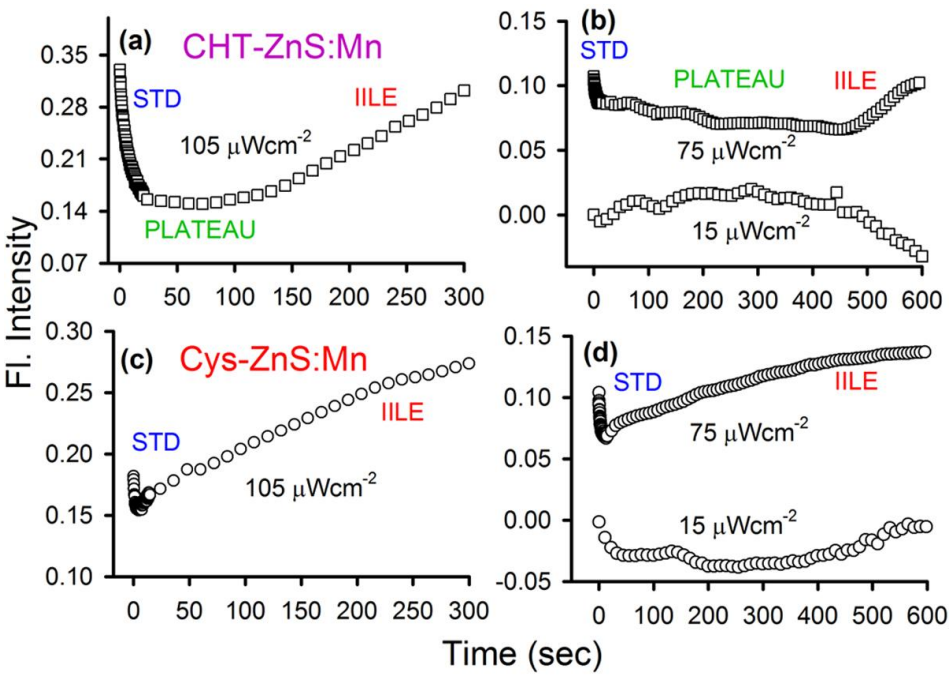

Figure 7.8. *Dose-dependent IILE spectra of (a–b) CHT-ZnS:Mn and (c−d) Cys-ZnS:Mn. Figures clearly demonstrate the individual stable and damage zones of both the systems due to IILE effect.*

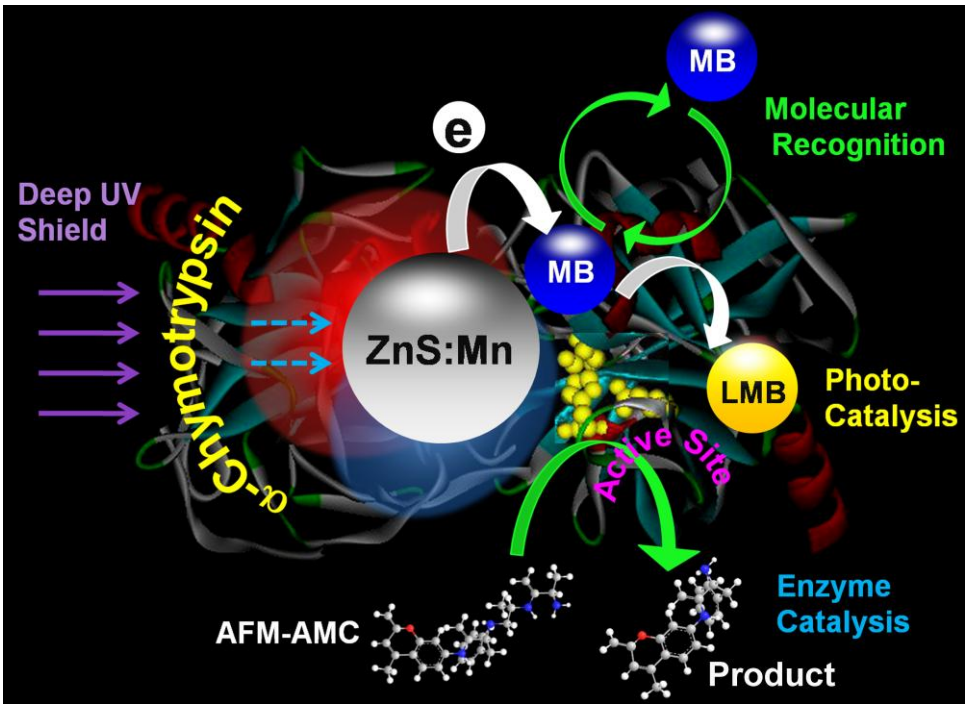

Scheme 7.2. *Schematic representation of a CHT-ZnS:Mn BNCs revealing its multifunctional nature towards molecular recognition, efficient photocatalysis, active enzyme catalysis and deep-UV durability.*

stable zones for the Cys-capped NPs are negligibly small compared to that of the CHT-capped BNCs under similar UV exposure. In the first few seconds of UV irradiation, a sudden drop of the initial intensity on a short time scale (assigned as STD zone) was observed, for both Cys and CHT-capped systems, which can be attributed, for the sudden excitation the defect state oxygen in the conduction band act, as a quenching source and equilibrated within few seconds. The indications of surface damage of Cys-capped NPs at lower UV doses (15 μW cm^{-2} dose and 75 μW cm^{-2}) in the STD and IILE processes are still observed (Figure 7.8d). A negligible damage of the NPs in the BNCs under similar UV exposure (15 μW cm^{-2} and 75 μW cm^{-2} dose) is clearly evident from the Figure 7.8b. The observation is consistent with the fact that enzyme has relatively more protecting ability against the UV-induced photochemical/photophysical damage on the surface NPs compared to that of the Cysteine amino acid.

7.3. Conclusion:

In this report, we show that biomolecules and nanoparticles can be linked to prepare a novel bio-nanocomposite (BNC) that is able to recognize and efficiently reduce target organic molecules. A simple, fast, water soluble and green phosphine free colloidal synthesis strategy has been developed for the preparation of multifunctional protein (enzyme)-capped ZnS NPs with/without transitional metal-ion doping. While HRTEM and XRD confirm the crystallinity of the BNCs, CD spectroscopy clearly reveals the structural detainment of the host enzyme. The enzymatic activity of the as-prepared BNCs confirms functional intactness of the enzyme to a certain extent. The photocatalytic study by probing an organic dye in the presence of BNCs reveals the molecular recognition of such dyes by the BNCs. The IILE experiments demonstrate the protecting ability of the protein as a capping host against the deep UV damage of the NPs. The overall functionality of the synthesized BNCs is schematically represented in Scheme 7.2. Our studies may find relevance in the use of water soluble, stable, enzyme-capped Mn-doped ZnS BNCs for photonic device and bio-imaging applications.

References

[1] R. Beaulac, P.I. Archer, J.V. Rijssel, A. Meijerink, D.R. Gamelin, Exciton Storage by Mn^{2+} in Colloidal Mn^{2+} Doped CdSe Quantum Dots, *Nano Lett.* 8 (2008) 2949.

[2] T. Schmidt, M. Scheibner, L. Worschech, A. Forchel, T. Slobodskyy, L.W. Molenkamp, Sign Reversal and Light Controlled Tuning of Circular Polarization in Semimagnetic CdMnSe Quantum Dots, *J. Appl. Phys.* 100 (2006) 123109.

[3] J.D. Bryan, D.R. Gamelin, Doped Semiconductor Nanocrystals: Synthesis, Characterization, Physical Properties, and Applications, *Prog. Inorg. Chem.* 54 (2005) 47.

[4] D.J. Norris, N. Yao, F.T. Charnock, T.A. Kennedy, High-Quality Manganese-Doped ZnSe Nanocrystals, *Nano Lett.* 1 (2001) 3.

[5] N.S. Norberg, G.L. Parks, G.M. Salley, D.R. Gamelin, Giant Excitonic Zeeman Splittings in Colloidal Co^{2+}-Doped ZnSe Quantum Dots, *J. Am. Chem. Soc.* 128 (2006) 13195.

[6] N. Pradhan, X. Peng, Efficient and Color-Tunable Mn-Doped ZnSe Nanocrystal Emitters: Control of Optical Performance via Greener Synthetic Chemistry, *J. Am. Chem. Soc.* 129 (2007) 3339.

[7] A.A. Bol, A. Meijerink, Long-lived Mn^{2+} emission in nanocrystaline ZnS:Mn^{2+}, *Phys. Rev. B* 58 (1998) R15997.

[8] A. Aboulaich, M. Geszke, L. Balan, J. Ghanbaja, G. Medjahdi, R. Schneider, Water-Based Route to Colloidal Mn-Doped ZnSe and Core/Shell ZnSe/ZnS Quantum Dots, *Inorg. Chem.* 49 (2010) 10940.

[9] N.S. Norberg, G.M. Dalpian, J.R. Chelikowsky, D.R. Gamelin, Energetic Pinning of Magnetic Impurity Levels in Quantum-Confined Semiconductors, *Nano. Lett.* 6 (2006) 2887.

[10] Z. Deng, L. Tong, M. Flores, S. Lin, J. Cheng, H. Yan, Y. Liu, High-Quality Manganese-Doped Zinc Sulfide Quantum Rods with Tunable Dual-Color and Multiphoton Emissions, *J. Am. Chem. Soc.* 133 (2011) 5389.

[11] T. Charinpanitkul, A. Chanagul, J. Dutta, U. Rungsardthong, W. Tanthapanichakoon, Effects of Cosurfactant on ZnS Nanoparticle Synthesis In Microemulsion, *Sci. Tech. Adv. Mater.* 6 (2005) 266.

[12] B.A. Smith, J.Z. Zhang, A. Joly, J. Liu, Luminescence Decay Kinetics of Mn^{2+}-Doped ZnS Nanoclusters Grown in Reverse Micelles, *Phys. Rev. B* 62 (2000) 2021.

[13] M.B. Dickerson, K.H. Sandhage, R.R. Naik, Protein- and Peptide-Directed Syntheses of Inorganic Materials, *Chem. Rev.* 108 (2008) 4935.

[14] M. Konishi, T. Isobe, M. Senna, Enhancement of Photoluminescence of ZnS : Mn Nanocrystals by Hybridizing with Polymerized Acrylic Acid, *J. Lumin.* 93 (2001) 1.

[15] D. Gallagher, W.E. Heady, J.M. Racz, R.N. Bhargava, Homogeneous Precipitation of Doped Zinc Sulfide Nanocrystals for Photonic Applications, *J. Mater. Res.* 10 (1995) 870.

[16] M. Mahmoudi, I. Lynch, M.R. Ejtehadi, M.P. Monopoli, F.B. Bombelli, S. Laurent, Protein-Nanoparticle Interactions: Opportunities and Challenges, *Chem. Rev.* 111 (2011) 5610.

[17] M. Lundqvist, J. Stigler, T. Cedervall, G. Elia, I. Lynch, K.A. Dawson, Nanoparticle Size and Surface Properties Determine the Protein Corona with Possible Implications for Biological Impacts, *Proc. Natl. Acad. Sci. U.S.A.* 105 (2008) 14265.

[18] C.B. Murray, D.J. Norris, M.G. Bawendi, Synthesis and Characterization of Nearly Monodisperse CdE (E = Sulfur, Selenium, Tellurium) Semiconductor Nanocrystallites, *J. Am. Chem. Soc.* 115 (1993) 8706.

[19] A.B. Cruz, Q. Shen, T. Toyoda, The Effect of Ultraviolet Irradiation on the Photothermal, Photoluminescence and Photoluminescence Excitation Spectra of Mn-doped ZnS Nanoparticles, *Thin Solid Films* 499 (2006) 104.

[20] W.C. Choi, M.H. Kim, H.S. Ro, S.R. Ryu, T.K. Oh, J.K. Lee, Zinc in Lipase L1 from *Geobacillus Stearothermophilus* L1 and Structural Implications on Thermal Stability, *FEBS Lett.* 579 (2005) 3461.

[21] A. Makhal, S. Sarkar, S.K. Pal, Protein-Mediated Synthesis of Nanosized Mn-Doped ZnS: A Multifunctional, UV-Durable Bio-Nanocomposite, *Inorg. Chem.* 51 (2012) 10203.

[22] X. Lu, J. Yang, Y. Fu, Q. Liu, B. Qi, C. Lu, Z. Su, White Light Emission from Mn^{2+} Doped ZnS Nanocrystals through the Surface Chelating of 8-Hydroxyquinoline-5-Sulfonic Acid, *Nanotechnology* 21 (2010) 115702.

[23] M. Hudlikar, S. Joglekar, M. Dhaygude, K. Kodam, Latex-Mediated Synthesis of ZnS Nanoparticles: Green Synthesis Approach, *J. Nanopart. Res.* 14 (2012) 865.

[24] Z. Quan, Z. Wang, P. Yang, J. Lin, J. Fang, Synthesis and Characterization of High-Quality ZnS, ZnS:Mn^{2+}, and ZnS:Mn^{2+}/ZnS (Core/Shell) Luminescent Nanocrystals, *Inorg. Chem.* 46 (2007) 1354.

[25] J. Zhuang, X. Zhang, G. Wang, D. Li, W. Yang, T. Li, Synthesis of Water-Soluble ZnS:Mn^{2+} Nanocrystals by using Mercaptopropionic Acid as Stabilizer, *J. Mater. Chem.* 13 (2003) 1853.

[26] R. Maity, K.K. Chattopadhyay, Synthesis and Optical Characterization of ZnS and ZnS:Mn Nanocrystalline Thin Films by Chemical Route, *Nanotechnology* 15 (2004) 812.

[27] K. Rezwan, A.R. Studart, J. Voros, L.J. Gauckler, Change of ζ Potential of Biocompatible Colloidal Oxide Particles upon Adsorption of Bovine Serum Albumin and Lysozyme, *J. Phys. Chem. B* 109 (2005) 14469.

[28] J.D.G. Duran, M.C. Guindo, A.V. Delgado, F. Gonzalez-Caballero, Stability of Monodisperse Zinc Sulfide Colloidal Dispersions, *Langmuir* 11 (1995) 3648.

[29] M. Balastre, J. Persello, A. Foissy, J.F. Argillier, Binding and Ion-Exchange Analysis in the Process of Adsorption of Anionic Polyelectrolytes on Barium Sulfate, *J. Colloid Interface Sci.* 219 (1999) 155.

[30] S.S. Narayanan, S.S. Sinha, S.K. Pal, Structural and Functional Characterization of Luminescent Silver Protein Nanobioconjugates, *J. Phys. Chem. C* 112 (2008) 12716.

[31] L.E. Brus, A Simple Model for the Ionization Potential, Electron Affinity, and Aqueous Redox Potentials of Small Semiconductor Crystallites, *J.Chem. Phys.* 79 (1983) 5566.

[32] Y. Dieckmann, H. Clfen, H. Hofmann, A.P. Fink, Particle Size Distribution Measurements of Manganese-Doped ZnS Nanoparticles, *Anal. Chem.* 81 (2009) 3889.

[33] P. Wu, L. Miao, H. Wang, X. Shao, X. Yan, A Multidimensional Sensing Device for the Discrimination of Proteins Based on Manganese-Doped ZnS Quantum Dots, *Angew. Chem. Int. Ed.* 50 (2011) 8118.

[34] G. Bacher, H. Schomig, M. Scheibner, A. Forchel, A.A. Maksimov, A.V. Chernenko, P.S. Dorozhkin, V.D. Kulakovskii, T. Kennedy, T.L. Reinecke, Spin-Spin Interaction in Magnetic Semiconductor Quantum Dots, *Physica E* 26 (2005) 37.

[35] R.N. Bhargava, D. Gallagher, Optical Properties of Manganese-Doped Nanocrystals of ZnS, *Phys. Rev. Lett.* 72 (1994) 416.

[36] K. Sooklal, B.S. Cullum, S.M. Angel, C.J. Murphy, Photophysical Properties of ZnS Nanoclusters with Spatially Localized Mn^{2+}, *J. Phys. Chem.* 100 (1994) 4551.

[37] L. Levy, N. Feltin, D. Ingert, M.P. Pileni, Three Dimensionally Diluted Magnetic Semiconductor Clusters $Cd_{1-y}Mn_yS$ with a Range of Sizes and Compositions: Dependence of Spectroscopic Properties on the Synthesis Mode, *J. Phys. Chem. B* 101 (1997) 9153.

[38] M.R. Kim, J.H. Chung, D. Jang, Spectroscopy and Dynamics of Mn^{2+} in ZnS Nanoparticles, *Phys. Chem. Chem. Phys.* 11 (2009) 1003.

[39] M. Tanaka, Photoluminescence Properties of Mn^{2+}-doped II-VI Semiconductor Nanocrystals, *J. Lumin.* 100 (2002) 163.

[40] H. Fujiwara, H. Hosokawa, K. Murakoshi, Y. Wada, S. Yanagida, Surface Characteristics of ZnS Nanocrystallites Relating to Their Photocatalysis for CO_2 Reduction, *Langmuir* 14 (1998) 5154.

[41] B. Xia, I.W. Lenggoro, K. Okuyama, Synthesis and Photoluminescence of Spherical ZnS:Mn^{2+} Particles, *Chem. Mater.* 14 (2002) 4969.

[42] H. Yin, Y. Wada, T. Kitamura, S. Yanagida, Photoreductive Dehalogenation of Halogenated Benzene Derivatives Using ZnS or CdS Nanocrystallites as Photocatalysts, *Environ. Sci. Technol.* 35 (2001) 227.

[43] A. Kudo, M. Sekizawa, Photocatalytic H_2 Evolution under Visible Light irradiation on Ni-doped ZnS Photocatalyst, *Chem. Commun.* (2000) 1371.

[44] A. Kudo, M. Sekizawa, Photocatalytic H_2 Evolution under Visible Light Irradiation on $Zn_{1-x}Cu_xS$ Solid Solution, *Catal. Lett.* 58 (1999) 241.

[45] S. Sarkar, A. Makhal, T. Bora, S. Baruah, J. Dutta, S.K. Pal, Photoselective Excited State Dynamics in ZnO-Au Nanocomposites and their Implications in Photocatalysis and Dye-Sensitized Solar Cells, *Phys. Chem. Chem. Phys.* 13 (2011) 12488.

[46] S. Baruah, S.S. Sinha, B. Ghosh, S.K. Pal, A.K. Raychaudhuri, J. Dutta, Photoreactivity of ZnO Nanoparticles in Visible Light: Effect of Surface States on Electron Transfer Reaction, *J. Appl. Phys.* 105 (2009) 074308.

[47] H. Hachisako, T. Yamazaki, H. Ihara, C. Hirayama, K. Yamada, Formation of Specific Hydrophobic Sites for Incorporation of Methylene Blue by Laterally Arranged L-Glutamate Residues in Anionic, Crystalline Bilayer Aggregates, *J. Chem. Soc., Perkin Trans. 2* (1994) 1671.

[48] I. Yu, T. Isobe, M. Senna, Optical Properties and Characteristics of ZnS Nanoparticles with Homogeneous Mn Distribution, *J. Phys. Chem. Solids* 57 (1996) 373.

[49] C. Jin, J. Yu, L. Sun, K. Dou, S. Hou, J. Zhao, Y. Chen, S. Huang, Luminescence of Mn^{2+} Doped ZnS Nanocrystallites, *J. Lumin.* 66-67 (1996) 315.

[50] L. Cao, J. Zhang, S. Ren, S. Huang, Luminescence Enhancement of Core-Shell ZnS:Mn/ZnS Nanoparticles, *Appl. Phys. Lett.* 80 (2002) 4300.

[51] J. Yu, H. Liu, Y. Wang, F.E. Fernandez, W. Jia, Irradiation-Induced Luminescence Enhancement Effect of ZnS:Mn^{2+} Nanoparticles in Polymer Films, *Opt. Lett.* 22 (1997) 913.

[52] H. Jeong, D. Zou, T. Tsutsui, C. Ha, Short-Term Degradation Behaviors of Light Emitting Diodes Made of Polyurethane Derivative with Large Permanent Dipoles on the Side Chain, *Thin Solid Films* 363 (2000) 279.

Chapter 8

Ultrafast Photoinduced Energy/Electron Transfer from a Technologically Important Nanoporous Host Membrane to Various Inorganic/Organic Guests

8.1. Introduction:

Anodic aluminium oxide (AAO) membranes prepared through a typical electrochemical procedure [1-3] possess highly ordered nanopores with controllable and homogeneous dimensions arranged in a close-packed pattern [4]. The demonstrated dimensions of inter-pore spacing ranging from 50 to 400 nm and pore size from 25 to 300 nm are suitable for both quantum electronic effects and photonic crystals. Nowadays, AAO is an important material for a variety of nanotechnological applications because its unique nanoporous honeycomb structure can act as a template for the fabrication of other nanostructured materials [5-11]. For example, AAO membranes are used as a template to grow different nanoscale materials like rare earth elements (Tb, Eu) [12], polymers DBO-PPV (Poly(2,5-dibutoxy-1,4-phenylenevinylene)) [13], MEH-PPV (Poly(2-methoxy-5-(2-ethylhexyloxy)-1,4-phenylenevinylene)) [14]), sensors [15], photonic crystal [16-17], energy storage and solar cells [18], magnetic storage devices [19], cell cultures [20] and drug delivery systems [21]. To enable the studies of the interesting properties appearing for nanocomposites or nanodevices related to AAO films, a complete understanding of the self-properties of the AAO membranes is essential and necessary. Although many studies devoted to this topic have been made, the origin of blue photoluminescence (PL) is controversially discussed. In general there are two main points of view to explain this phenomenon. The first one suggests that the observed blue emission band is caused by singly ionized oxygen vacancies (F^+ centers) [22-24]. The other viewpoint is based on an assumption of Yamamoto *et al.* [25] that oxalate impurities can be incorporated into the film during its formation which would transform into luminescent centers with the blue PL band around 470 nm. Although, using AAO membranes prepared in H_2SO_4, a similar PL phenomenon

was observed by Du *et al.* Electron paramagnetic resonance measurements of the AAO membrane prepared in oxalic acid also reveal that the blue PL band arises from F^+ centers [22, 24]. Therefore, it is already a well accepted fact that the blue PL band of AAO arises from F^+ centers. However, AAO membranes used in our experiments are annealed at 500 °C to drive out any organic contaminants, mostly the oxalate impurities. Until now, most research works have focused on the magnetic and opto-electronic properties of nanoscopic materials and their fabrication mechanisms using AAO as a template material [26]. Recently, there is growing interest in incorporating laser dyes into solid media for device applications, and some luminescent mechanisms have been discussed [27]. Jia *et al.* have discussed the luminescence mechanisms of morin and morin-protein (trypsin and lysozome) embedded into AAO films [28]. They have shown that the interaction of morin and remaining aluminium in AAO film and coexistence of embedded dye and protein may be responsible for the PL appearance and enhancement, respectively.

In contrast to the previously reported studies, this work deals with the photoinduced charge transfer from electrochemically grown AAO membranes by anodizing aluminum in oxalic acid solutions, and by studying their optical properties. Our aim is to establish the AAO membrane as an advantageous light-harvesting material depicting both energy and electron transport ability in the presence of organic molecules and inorganic nanostructures. By using the femtosecond (fs)-resolved fluorescence upconversion techniques, we have investigated charge transfer dynamics of AAO membranes in a complexation with benzoquinone (BQ) which is well known as an electron acceptor [29]. In this work, we have explored the Förster resonance energy transfer (FRET) dynamics from AAO membranes to nanopore-embedded Maple Red (Map Red) QDs and gold nanowires (NWs). The use of FRET has been contemplated as an alternative mechanism for charge separation and a way to improve exciton harvesting [30]. In inorganic QD-based solar cells, the use of FRET to transfer the exciton generated in the QD to a high mobility conducting channel has been proposed as a way to bypass the traditional limitations of charge separation and transport [31-32]. We report here on the use of FRET to boost the harvesting capacity of a light-harvesting device. By using steady-state and picoseconds (ps)-resolved fluorescence spectroscopy, we have demonstrated that defect-mediated PL from AAO membranes can be used to excite the guest QDs/Au NWs for the enhancement

of light absorption possibility. In this context, nanosurface energy transfer (NSET) [33], one of the other prevailing pathways of nonradiative quenching, is conclusively found to prevail in AAO−Au composites. A detailed demonstration of the ultrafast excited-state deactivation of porous AAO membrane in the presence of various fluorescence quenchers is schematically represented in Scheme 8.1. This work may find its application to improve the efficiency of light-harvesting devices.

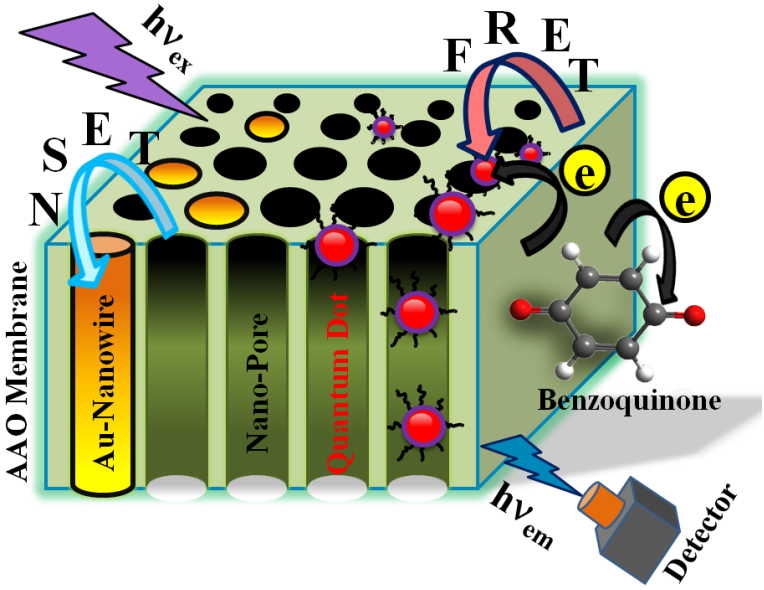

Scheme 8.1. *Schematic illustration of the ultrafast excited state deactivation associated with both the electron and energy transfer reactions from host porous AAO membrane to various guest organic molecules and inorganic nanostructures.*

8.2. Results and Discussion:

8.2.1. Ultrafast Excited State Deactivation of Doped Porous Anodic Alumina Membranes [34]:

The side-view of a scanning electron micrograph of porous alumina template is shown in Figure 8.1a, which reveals that the nanopores are uniform and highly ordered. The inset (left side) shows a top-view with ~48 nm periodic pores separated by ~64 nm. The pore diameter can easily be controlled by the anodization conditions, for example, the electrolyte type, concentration, applied voltage, and temperature. The thickness is adjusted by varying the time of the second anodization [6]. The right inset of Figure 8.1a shows a

cross-view of Au wires in a typical sample. The length of these wires is controlled by the

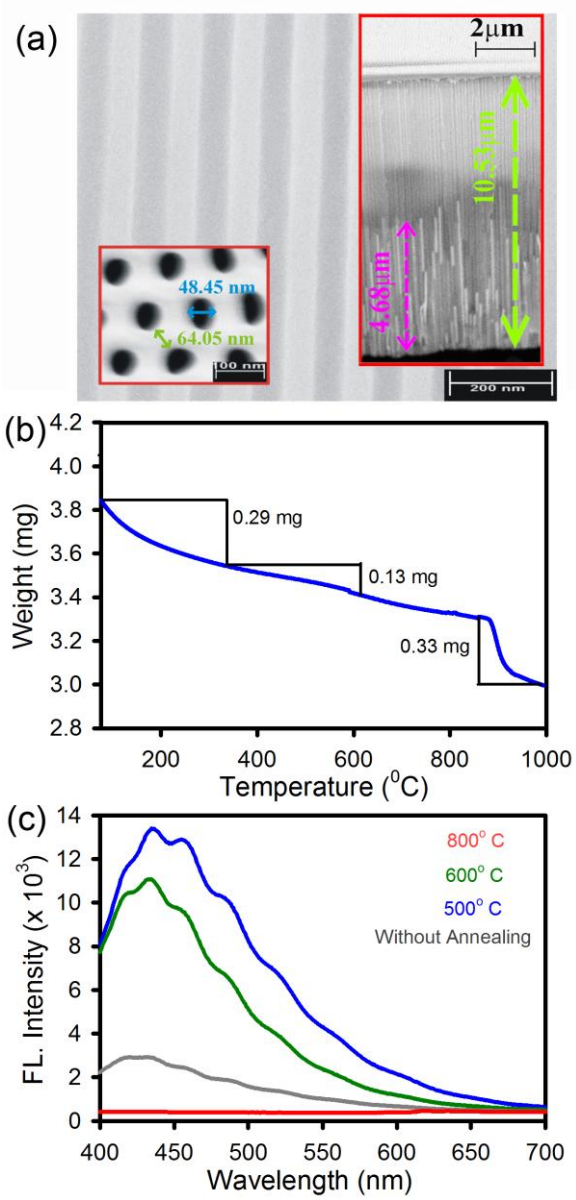

Figure 8.1. *a) Side-view of AAO using electron microscopy showing uniform and highly-ordered nanopores. Left inset shows a top-view with periodic pores. Right inset shows a side-view on Au wires in AAO. Different Au wire lengths at the edge are induced by breaking the sample for microscopy. b) Thermogravimetric analysis curve for the as-prepared AAO membranes. c) PL spectra of the as-anodized AAO and the AAO membranes annealed at different temperatures.*

deposition time. Figure 8.1b shows the thermogravimetric analysis (TGA) of the as-prepared AAO where three weight loss regions are prominent resembling the TGA curve

reported by Sun *et al.* [35] The weight loss for the first section (room-temperature−335 °C) is mainly attributed to desorption of weakly bound water from the surface and inner walls of nanopores. In the second section (335−615 °C), oxalate impurities are decomposed [36] and the third section (855−990 °C) indicates a strong phase transition. Figure 8.1c shows the PL spectra (excitation at 375 nm) of AAO membranes with/without annealed at different temperatures. It is obvious that an intensive and broad PL emission band appears at ~450 nm [37] which originates from singly-ionized oxygen vacancies (F^+ centers) in AAO membranes [22]. The intensity of this band increases with elevated annealing temperature (T_a) and reaches to a maximum for the sample at T_a = 500 °C, but drastically decreases with further increase in T_a [22, 35]. This phenomenon is well understood by considering the fact that during the heat treatment, oxygen in porous alumina membranes and oxygen diffusing from air into the membranes possibly react with the remaining aluminum in AAO, to form new alumina, and newly formed alumina may contain many oxygen vacancies. With a further increase in annealing temperature the PL intensity of AAO membranes becomes weak, due to the fact that at very high temperatures the annihilation rate of oxygen vacancies becomes faster than the formation rate. The generation of new defect states upon air-annealing, and the annihilation of defect states with increasing temperature are very common phenomena [22, 38]. Therefore, only a few F^+ centers remain intact in porous alumina membranes, resulting in a sudden drop in the PL intensity. A similar broad green emission band at room-temperature is also well-known for ZnO NPs which has been studied in detail and demonstrated to be originated from oxygen vacancy centers near the surface [39-41]. In particular, the origin of the blue-green emission peaking at 495 nm was demonstrated to be singly positive oxygen vacancy centers located at ~2 nm from the surface of the ZnO NPs [39-41]. In the present study, all optical experiments were carried out with the AAO membranes annealed at 500 °C to obtain the maximum PL intensity and also to avoid any influence of organic contaminants mostly the oxalate impurities. The emission bands and TGA analysis results obtained at different T_a thus confirm the purity of AAO membranes used in our experiments.

We have investigated the defect-mediated blue band emission of AAO membrane in the absence and the presence of various emission quenchers impregnated in the AAO

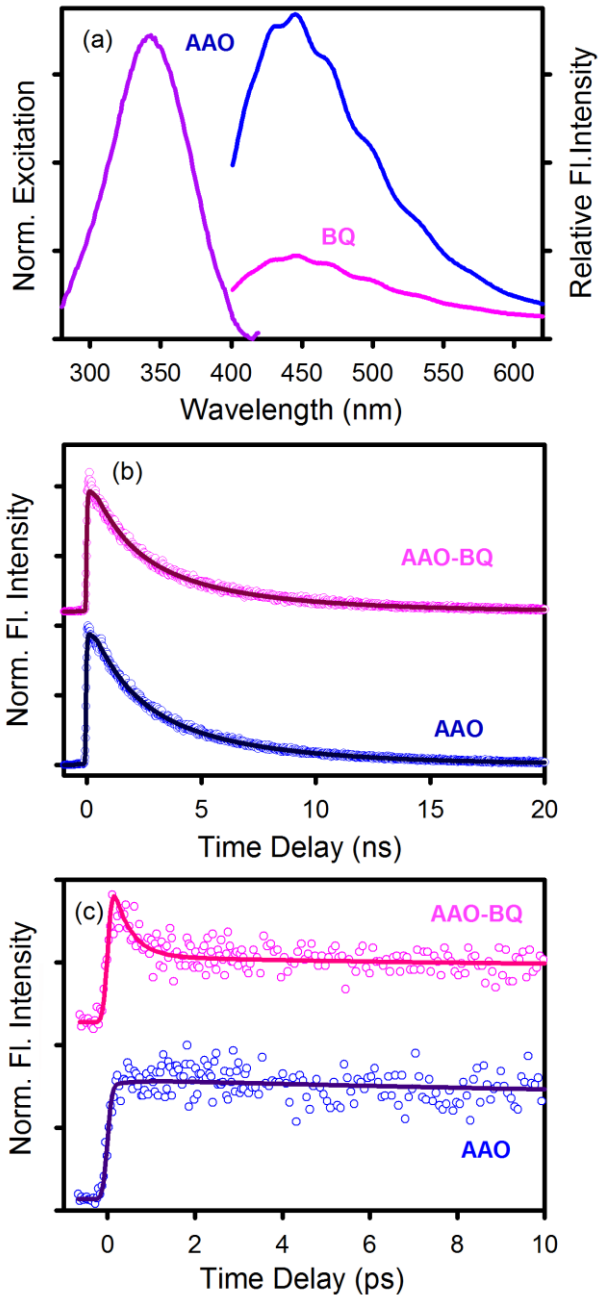

Figure 8.2. *a) Normalized excitation spectra and emission spectra of AAO membranes, in the absence and the presence of BQ. b) The picosecond-resolved fluorescence transients of AAO membranes, in the absence (blue) and the presence of BQ (pink) (excitation at 375 nm) monitored at 450 nm. c) The femtosecond-resolved fluorescence transients of bare AAO (blue) and BQ impregnated AAO (pink) (excitation at 375 nm) collected at 450 nm showing faster decay.*

nanopores. Figure 8.2a represents the excitation spectra of bare AAO membranes and the room-temperature PL spectra of AAO. In order to investigate the electron transfer

dynamics from the AAO membranes upon excitation, we have studied the complexation of the membrane with an organic molecule, *p*-benzoquinone (BQ), which is well known as an electron acceptor [29]. Infrared spectroscopic studies have shown that the carbonyl stretch vibration of the BQ is lowered in frequency as soon as the BQ adsorbs on the semiconductor surface [29]. The adsorbed BQ then acts as an electron acceptor and removes the photoexcited electron from the semiconductor conduction band in less time than the laser pulse duration (<120 fs) [40, 42-43]. The steady-state and time (ps and fs)-resolved PL quenching (at 450 nm) of AAO upon complexation with BQ are shown in Figure 8.2a−c. The ps-resolved study on AAO−BQ system exhibits timescales comparable to bare AAO depicting the fact that excited state electron transfer process must be too fast to be resolved in our ps-resolved luminescence study. Therefore, we have extended the study to the fs-timescale for a better understanding of excited electron transfer process from AAO to the LUMO of BQ molecules. The sharp fluorescence decay (Figure 8.2c) of AAO in the presence of BQ at the same excitation of 375 nm generates a new time constant of ~400 fs (59%). Note that this short decay component is comparable to those reported for CdSe−BQ adduct (~600 fs) which was demonstrated to arise due to electron transfer from QD core to the surface attached BQ [43]. The resemblance of the electron transfer dynamics of BQ-embedded AAO with those of the CdSe−BQ system clearly signifies the ultrafast photoinduced electron transfer dynamics from the host AAO to the organic guest molecule BQ.

As shown in Figure 8.3a, defect-mediated blue emission of bare AAO is noticeably quenched when it is impregnated with Map Red QDs or gold NWs. The ps-resolved faster excited state lifetimes of the AAO−Map Red and AAO−Au adducts with respect to that of the bare AAO is clearly noticeable from Figure 8.3b. Herein, we propose FRET from a donor AAO to Map Red or gold acceptors, which is responsible for the observed inhibition of emission bands. FRET in combination with Förster theory has become an invaluable tool for the assessment of distances in numerous biomolecular assemblies [44-46]. The FRET process is based on the concept of treating an excited donor as an oscillating dipole that can undergo energy exchange with a second dipole having a similar resonance frequency [46]. In principle, if the fluorescence emission spectrum of the donor overlaps

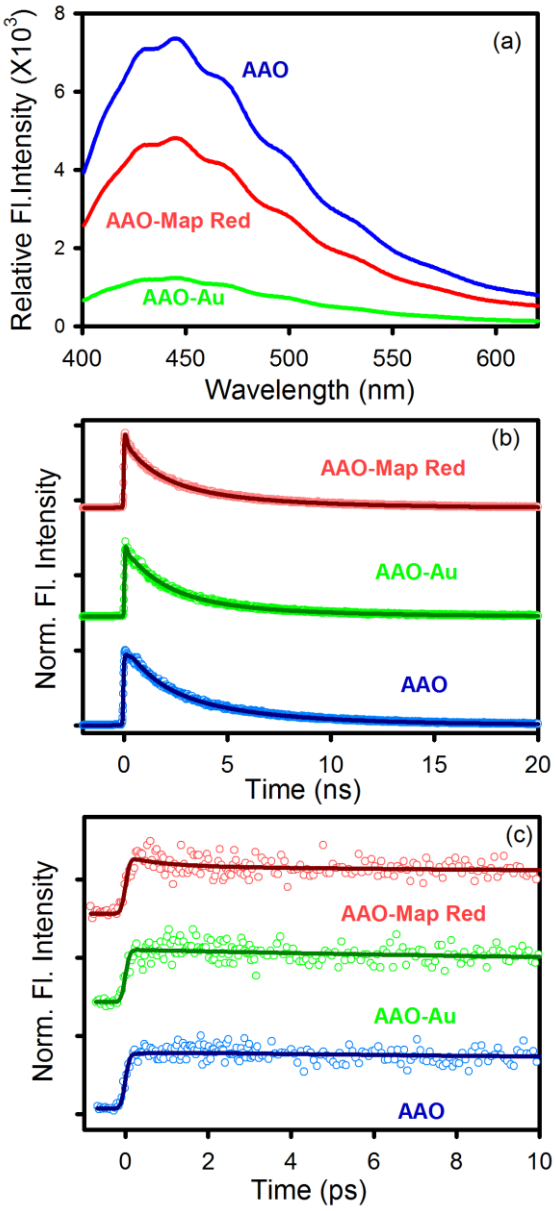

Figure 8.3. *a) Steady state emission spectra of AAO membranes, in the absence and the presence of gold NWs and Map Red, b) picosecond-resolved fluorescence transients (excitation at 375 nm, monitored at 450 nm) and c) femtosecond-resolved fluorescence transients of bare AAO (blue) and Au NWs (green), Map Red (red) impregnated AAO (excitation at 375nm) collected at 450 nm.*

the absorption spectrum of an acceptor, and the two are within a minimal distance from one another (1−10 nm), the donor can directly transfer its excitation energy to the acceptor *via* exchange of a virtual photon. The spectral overlap of the AAO emission spectrum with that of the Map Red and Au absorption spectrum is shown in Figure 8.4a and 8.4b,

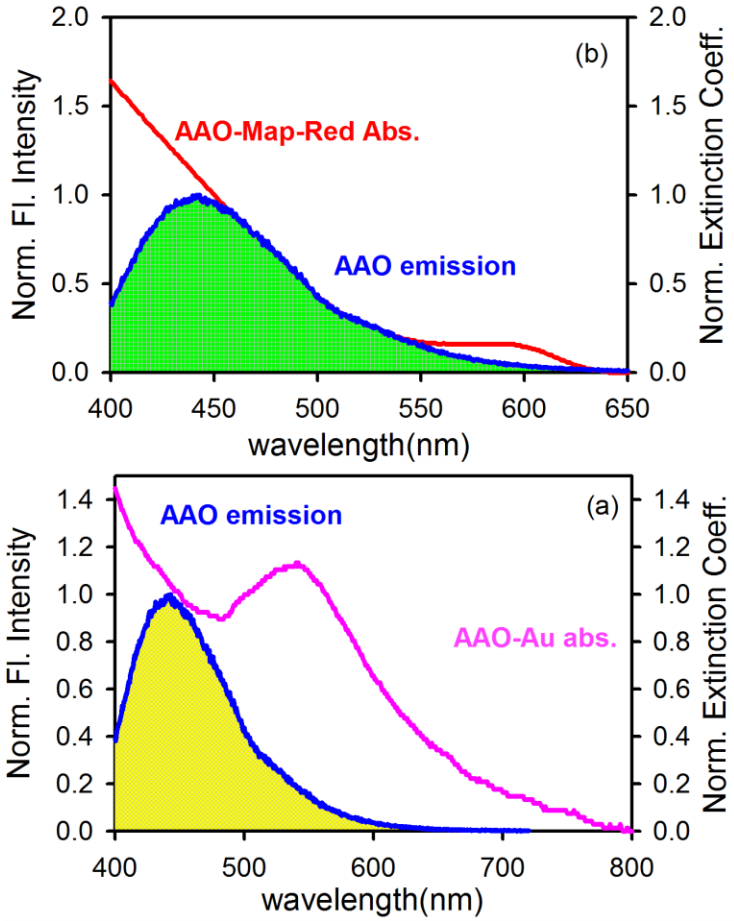

Figure 8.4. *a) Steady state absorption spectra of acceptor Map Red (red) and emission spectra of donor AAO (blue) are shown. b) Steady state absorption spectra of acceptor gold NWs (red) and emission spectra of donor AAO (blue) The overlap zones have been shown in green and yellow, respectively.*

respectively. The details of the spectroscopic parameters and the fitting parameters of the luminescence transients are given in Table 8.1 and Table 8.2. From the average lifetime calculation for AAO−Map Red and AAO−Au complex, we obtain the effective distance between the donor and the acceptor, $r_{DA} \approx 5.2$ and 21.5 nm for AAO−Map Red and AAO−Au, respectively (using equation 2.11 and 2.12b). For AAO−QD complexation, the effective D−A distance is essentially the distance from donor singly-positive oxygen vacancy states to the centre of the acceptor QDs. However, the expected separation of donor and acceptor is supposed to be the radius of Map Red QDs (~3.0 nm, data not shown) [43]. By using FRET measurement on AAO−QD system, we have estimated the

Table 8.1. Picosecond-resolved luminescence transients of bare AAO & AAO in the presence of several quenchers.[a]

Sample	τ_1 (ns)	τ_2 (ns)	τ_3 (ns)	τ_{av} (ns)
AAO	1.47 (46%)	4.54 (48%)	10.5 (6%)	3.49
AAO−BQ	1.42 (49%)	4.54 (46%)	10.5 (5%)	3.30
AAO−Map Red	0.15 (38%)	1.7 (37%)	5.5 (25%)	2.06
AAO−Au	0.79 (37%)	2.9 (50%)	7.8 (13%)	2.76

[a]*The emission from AAO membrane (emission at 450 nm) was detected with 375 nm laser excitation. Numbers in the parenthesis indicate relative weightages.*

Table 8.2. Femtosecond decay periods of luminescence measured with AAOs (bare) & AAOs in the presence of several quenchers.[b]

Sample	τ_1 (ps)	τ_2 (ps)	τ_3 (ps) (fixed)
AAO		44.2 (28%)	1472 (72%)
AAO−BQ	0.40 (59%)	8.4 (6%)	1472 (35%)
AAO−Map Red	0.87 (17%)	12.2 (14%)	1472 (69%)
AAO−Au		35.5 (35%)	1472 (65%)

[b]*The emission from AAO membrane (emission at 450 nm) was detected with 375 nm laser excitation. Numbers in the parenthesis indicate relative weightages.*

D−A distance of 4.4 nm which reveals that the donor F^+ centers are located within (5.2−3.0) nm = 2.2 nm from AAO surface boundary. Note that the exact position of oxygen vacancy centers in AAO membrane is very much consistent with ZnO NPs [39-41]. In contrast, by using FRET technique, the D−A distance for AAO−Au system is found to be 18.4 nm which is a larger value compared to the D−A distance between F^+ centers and metal surface considering the fact that the donor F^+ center transfers energy to the surface plasmon of the impregnated Au NWs, at the distance of ~2.2 nm. The observation is thus raising question about the validity of FRET in the determination of D−A distance in the case of AAO−Au system.

The D−A separations can also be calculated using another prevailing technique, nanosurface energy transfer (NSET) [47-48], in which the energy transfer efficiency depends on the inverse of the fourth power of the D−A separation [49]. For the calculation

of D−A separation, we have used the useful formulations as discussed in section 2.1.2. In our present system, c is the speed of light, Φ_D is the quantum yield of the donor (0.005), ω is the angular frequency for the donor (4.2×10^{15} s^{-1}), ω_F is the angular frequency for bulk gold (8.4×10^{15} s^{-1}), d is the D−A separation, μ is the dipole moment, τ_D is the average lifetime of the donor (3.48 ns), and k_F is the Fermi wave-vector for bulk gold (1.2×10^8 cm^{-1}) [50-51]. In our case we used k_{NSET} as $k_{NSET} = \frac{1}{\tau_{donor-acceptor}} - \frac{1}{\tau_{donor}}$, where, $\tau_{donor-acceptor}$ is the average lifetime of the AAO−Au system. The calculated D−A distance (using equation 2.15) is found to be 2.7 nm, which reflects the separation of donor F^+ centers from Au surface and also justify the location of F^+ centers from AAO surface (~2.2 nm from surface boundary). A demonstration of the excited state energy transfer *via* FRET and NSET mechanism is revealed in Scheme 8.2 and effective D−A distances are shown in presence of different acceptors. Furthermore, it is to be noted that fs-resolved luminescence

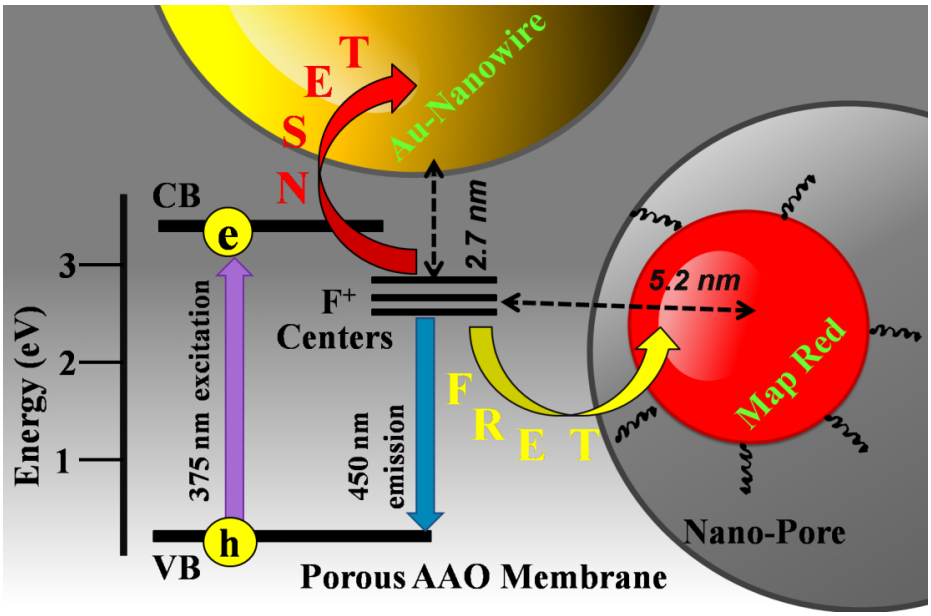

Scheme 8.2. *Schematic illustration of the FRET and NSET mechanism between donor F^+ centers in AAO membrane to the acceptors Map Red QDs and Au NWs showing their corresponding donor−acceptor distances.*

transients (Figure 8.3c) reveal a faster lifetime component of 0.87 ps which is associated with the excited-state of AAO−Map Red adduct and arises due to charge transfer from

AAO to the conduction band of QDs. Therefore, it is clear that both the electron and energy transfer processes are coupled in the deactivation process of the excited AAO when it is embedded to Map Red QDs. However, no faster time constants are detectable from the fs-resolved luminescence transients AAO−Au composite which suggests that the deactivation of AAO excited states occurs only *via* NSET process.

8.3. Conclusion:

In summary, AAOs with ordered pore size ~50 nm were synthesized using electrochemical methods which provide defect-mediated emission band near 450 nm. The present study provides a mechanistic explanation for the ultrafast excited state deactivation by considering every single aspect of quenching mechanisms, namely charge transfer, FRET and NSET from host AAO membrane to different guest molecules. The shorter lifetime as well as significant steady-state quenching was found when the AAO is impregnated with the well-known electron acceptor BQ, which accounted for fs-resolved charge transfer from the AAO conduction band to the BQ. We have also demonstrated that photoexcited AAO can transfer its energy to the impregnated QDs (Map Red) and Au NWs *via* FRET and NSET techniques, respectively. Based on these techniques, the location of the oxygen defect center is assigned and their distance from the surface adsorbed acceptor molecules is reported. Our present experiments and results will be beneficial to the understanding of the charge carrier or energy transfer processes from photoexcited AAOs to various acceptor molecules and it may find its applications in the use of porous alumina in the light-harvesting devices.

References

[1] G.E. Thompson, R.C. Furneaux, G.C. Wood, J.A. Richardson, J.S. Goode, Nucleation and Growth of Porous Anodic Films on Aluminium, *Nature* 272 (1978) 433.

[2] H. Masuda, K. Fukuda, Ordered Metal Nanohole Arrays Made by a Two-Step Replication of Honeycomb Structures of Anodic Alumina, *Science* 268 (1995) 1466.

[3] H. Masuda, F. Hasegwa, S. Ono, Self-Ordering of Cell Arrangement of Anodic Porous Alumina Formed in Sulfuric Acid Solution, *J. Electrochem. Soc.* 144 (1997) L127.

[4] C.K.Y. Ng, A.H.W. Ngan, Precise Control of Nanohoneycomb Ordering over Anodic Aluminum Oxide of Square Centimeter Areas, *Chem. Mater.* 23 (2011) 5264.

[5] Y. Zhang, G.H. Li, Y.C. Wu, B. Zhang, W.H. Song, L. Zhang, Antimony Nanowire Arrays Fabricated by Pulsed Electrodeposition in Anodic Alumina Membranes, *Adv. Mater.* 14 (2002) 1227.

[6] D. Chen, W. Zhao, T.P. Russell, P3HT Nanopillars for Organic Photovoltaic Devices Nanoimprinted by AAO Templates, *ACS Nano* 6 (2012) 1479.

[7] X. Mei, D. Kim, H.E. Ruda, Q.X. Guo, Molecular-Beam Epitaxial Growth of GaAs and InGaAs/GaAs Nanodot Arrays using Anodic Al_2O_3 Nanohole Array Template Masks, *Appl. Phys. Lett.* 81 (2002) 361.

[8] W.C. Hu, D.W. Gong, Z. Chen, L.M. Yuan, K. Saito, C.A. Grimes, P. Kichambare, Growth of Well-Aligned Carbon Nanotube Arrays on Silicon Substrates using Porous Alumina Film as a Nanotemplate, *Appl. Phys. Lett.* 79 (2001) 3083.

[9] M.S. Sander, A.L. Prieto, R. Gronsky, T. Sands, A.M. Stacy, Fabrication of High-Density, High Aspect Ratio, Large-Area Bismuth Telluride Nanowire Arrays by Electrodeposition into Porous Anodic Alumina Templates, *Adv. Mater.* 14 (2002) 665.

[10] M.S. Sander, R. Gronsky, T. Sands, A.M. Stacy, Structure of Bismuth Telluride Nanowire Arrays Fabricated by Electrodeposition into Porous Anodic Alumina Templates, *Chem. Mater.* 15 (2003) 335.

[11] L. Liu, W. Lee, Z. Huang, R. Scholz, U. Gösele, Fabrication and Characterization of a Flow-through Nanoporous Gold Nanowire/AAO Composite Membrane, *Nanotechnology* 19 (2008) 335604.

[12] J.C. Pivin, N.V. Gaponenko, I. Molchan, R. Kudrawiec, J. Misiewicz, L. Bryja, G.E. Thompson, P. Skeldon, Comparison of Terbium Photoluminescence from Ion Implanted and Sol–Gel-Derived Films, *J. Alloys. Compd.* 341 (2002) 272.

[13] Y. Zhao, D. Yang, C. Zhou, Q. Yang, D. Que, Photoluminescence Properties of the Composite of Porous Alumina and Poly (2,5-dibutoxy-1,4 phenylenevinylene), *J. Lumin.* 105 (2003) 57.

[14] T.P. Nguyena, S.H. Yanga, P.L. Rendua, H. Khan, Optical Properties of Poly(2-methoxy-5-(2′-ethyl-hexyloxy)-phenylene vinylene) Deposited on Porous Alumina Substrates, *Composites A* 36 (2005) 515.

[15] F. Rumiche, H.H. Wang, W.S. Hu, J.E. Indacochea, M.L. Wang, Anodized Aluminum Oxide (AAO) Nanowell Sensors for Hydrogen Detection, *Sensors Actuators B* 134 (2008) 869.

[16] H. Masuda, M. Ohya, H. Asoh, M. Nakao, M. Nohtomi, T. Tamamura, Photonic Crystal Using Anodic Porous Alumina, *Jpn. J. Appl. Phys.* 38 (1999) 1403.

[17] H. Masuda, M. Yamada, F. Matsumoto, S. Yokoyama, S. Mashiko, M. Nakao, K. Nishio, Lasing from Two-Dimensional Photonic Crystals Using Anodic Porous Alumina, *Adv. Mater.* 18 (2006) 213.

[18] A. Aguilera, V. Jayaraman, S. Sanagapalli, R.S. Singh, V. Jayaraman, K. Sampson, V.P. Singh, Porous Alumina Templates and Nanostructured CdS for Thin Film Solar Cell Applications, *Sol. Energy Mater. Sol. Cells* 90 (2006) 713.

[19] K. Nielsch, R.B. Wehrspohn, J. Barthel, J. Kirschner, U. Gösele, S.F. Fischer, H. Kronmüller, Hexagonally Ordered 100 nm Period Nickel Nanowire Arrays, *Appl. Phys. Lett.* 79 (2001) 1360.

[20] J. Hua, J.H. Tiana, J. Shia, F. Zhanga, D.L. Heb, L. Liuc, D.J. Jungc, J.B. Baib, Y. Chen, Cell Culture on AAO Nanoporous Substrates with and without Geometry Constrains, *Microelectron. Eng.* 88 (2011) 1714.

[21] S. Simovic, D. Losic, K. Vasilev, Controlled Drug Release from Porous Materials by Plasma Polymer Deposition, *Chem. Commun.* 46 (2010) 1317.

[22] Y. Du, W.L. Cai, C.M. Mo, J. Chen, L.D. Zhang, X.G. Zhu, Preparation and Photoluminescence of Alumina Membranes with Ordered Pore Arrays, *Appl. Phys. Lett.* 74 (1999) 2951.

[23] Y. Li, G.H. Li, G.W. Meng, L.D. Zhang, F. Phillipp, Photoluminescence and Optical Absorption Caused by the F^+ Centres in Anodic Alumina Membranes, *J. Phys.:Condens. Matter* 13 (2001) 2691.

[24] W. Chen, H.G. Tang, C.S. Shi, J. Deng, J.Y. Shi, Y.X. Zhou, S.D. Xia, Y.X. Wang, S.T. Yin, Investigation on the Origin of the Blue Emission in Titanium Doped Sapphire: Is F^+ Color Center the Blue Emission Center?, *Appl. Phys. Lett.* 67 (1995) 317.

[25] Y. Yamamoto, N. Baba, S. Tajima, Coloured Materials and Photoluminescence Centres in Anodic Film on Aluminium, *Nature* 289 (1981) 572.

[26] C.R. Martin, Nanomaterials: A Membrane-based Synthetic Approach, *Science* 266 (1994) 1961.

[27] G. Shi, C.M. Mo, W.L. Cai, L.D. Zhang, Photoluminescence of ZnO Nanoparticles in Alumina Membrane with Ordered Pore Arrays, *Solid State Commun.* 115 (2000) 253.

[28] R. Jia, Y. Shen, H. Luo, X. Chen, Z. Hu, D. Xue, Photoluminescence Properties of Morin and Lysozyme Molecules Absorbed on Anodic Porous Alumina Membrane, *Appl. Surf. Sci.* 233 (2004) 343.

[29] C. Burda, T.C. Green, S. Link, M.A. El-Sayed, Electron Shuttling Across the Interface of CdSe Nanoparticles Monitored by Femtosecond Laser Spectroscopy, *J. Phys. Chem. B* 103 (1999) 1783.

[30] Y.X. Liu, M.A. Summers, S.R. Scully, M.D. McGehee, Resonance Energy Transfer from Organic Chromophores to Fullerene Molecules, *J. Appl. Phys.* 99 (2006) 093521.

[31] S. Lu, A. Madhukar, Nonradiative Resonant Excitation Transfer from Nanocrystal Quantum Dots to Adjacent Quantum Channels, *Nano Lett.* 7 (2007) 3443.

[32] Y. Yang, W. Rodríguez-Córdoba, X. Xiang, T. Lian, Strong Electronic Coupling and Ultrafast Electron Transfer between PbS Quantum Dots and TiO_2 Nanocrystalline Films, *Nano Lett.* 12 (2012) 303.

[33] C.S. Yun, A. Javier, T. Jennings, M. Fisher, S. Hira, S. Peterson, B. Hopkins, N.O. Reich, G.F. Strouse, Nanometal Surface Energy Transfer in Optical Rulers, Breaking the FRET Barrier, *J. Am. Chem. Soc.* 127 (2005) 3115.

[34] A. Makhal, S. Sarkar, S.K. Pal, H. Yan, D. Wulferding, F. Cetin, P. Lemmens, Ultrafast Excited State Deactivation of Doped Porous Anodic Alumina Membranes, *Nanotechnology* 23 (2012) 305705.

[35] X. Sun, F. Xu, Z. Li, W. Zhang, Photoluminescence Properties of Anodic Alumina Membranes with Ordered Nanopore Arrays, *J. Lumin.* 121 (2006) 588.

[36] D. Dollimore, The Thermal Decomposition of Oxalates. A Review, *Thermochim. Acta* 117 (1987) 331.

[37] G.S. Huang, X.L. Wu, Y.F. Mei, X.F. Shao, G.G. Siu, Strong Blue Emission from Anodic Alumina Membranes with Ordered Nanopore Array, *J. Appl. Phys.* 93 (2003) 582.

[38] A.B. Djurišić, Y.H. Leung, K.H. Tam, Y.F. Hsu, D. L., W.K. Ge, Y.C. Zhong, K.S. Wong, W.K. Chan, H.L. Tam, K.W. Cheah, W.M. Kwok, D.L. Phillips, Defect Emissions in ZnO Nanostructures, *Nanotechnology* 18 (2007) 095702.

[39] A. Makhal, S. Sarkar, T. Bora, S. Baruah, J. Dutta, A.K. Raychaudhuri, S.K. Pal, Dynamics of Light Harvesting in ZnO Nanoparticles, *Nanotechnology* 21 (2010) 265703.

[40] A. Makhal, S. Sarkar, T. Bora, S. Baruah, J. Dutta, A.K. Raychaudhuri, S.K. Pal, Role of Resonance Energy Transfer in Light Harvesting of Zinc Oxide-Based Dye-Sensitized Solar Cells, *J. Phys. Chem. C* 114 (2010) 10390.

[41] S. Sarkar, A. Makhal, T. Bora, S. Baruah, J. Dutta, S.K. Pal, Photoselective Excited State Dynamics in ZnO-Au Nanocomposites and their Implications in Photocatalysis and Dye-Sensitized Solar Cells, *Phys. Chem. Chem. Phys.* 13 (2011) 12488.

[42] Y. Lou, X. Chen, A.C. Samia, C. Burda, Femtosecond Spectroscopic Investigation of the Carrier Lifetimes in Digenite Quantum Dots and Discrimination of the Electron and Hole Dynamics via Ultrafast Interfacial Electron Transfer, *J. Phys. Chem. B* 107 (2003) 12431.

[43] A. Makhal, H. Yan, P. Lemmens, S.K. Pal, Light Harvesting Semiconductor Core-Shell Nanocrystals: Ultrafast Charge Transport Dynamics of CdSe-ZnS Quantum Dots, *J. Phys. Chem. C* 114 (2010) 627.

[44] R.M. Clegg, [18] Fluorescence Resonance Energy Transfer and Nucleic Acids, *Methods Enzymol.* 211 (1992) 353.

[45] D.M.J. Lilley, T.J. Wilson, Fluorescence Resonance Energy Transfer as a Structural Tool for Nucleic Acids, *Curr. Opin. Chem. Biol.* 4 (2000) 507.

[46] J.R. Lakowicz, Principles of Fluorescence Spectroscopy, 2nd ed., Kluwer Academic/Plenum, New York, 1999.

[47] M. Montalti, N. Zaccheroni, L. Prodi, N. O'Reilly, S.L. James, Enhanced Sensitized NIR Luminescence from Gold Nanoparticles via Energy Transfer from Surface-Bound Fluorophores, *J. Am. Chem. Soc.* 129 (2007) 2418.

[48] B.N.J. Persson, N.D. Lang, Electron-Hole Pair Quenching of Excited States Near a Metal, *Phys. Rev. B* 26 (1982) 5409.

[49] J. Gersten, A. Nitzan, Spectroscopic Properties of Molecules Interacting with Small Dielectric Particles, *J. Chem. Phys.* 75 (1981) 1139.

[50] T.L. Jennings, M.P. Singh, G.F. Strouse, Fluorescent Lifetime Quenching near d = 1.5 nm Gold Nanoparticles: Probing NSET Validity, *J. Am. Chem. Soc.* 128 (2006) 5462.

[51] M.A.H. Muhammed, A.K. Shaw, S.K. Pal, T. Pradeep, Quantum Clusters of Gold Exhibiting FRET, *J. Phys. Chem. C* 112 (2008) 14324.

Chapter 9

Photosensitization Dynamics of Metal Oxide Semiconductors by Medicinally Important Porphyrins: Towards '*Two-in-One*' Applications

9.1. Introduction:

Light-harvesting nanohybrids (LHNs) are of intense current interest, as the simple search for individual nanoparticles no longer incites broad scientific interests for specific high-end applications. Most of these LHNs are composed of an inorganic nanostructure associated with an organic pigment. For example, association of a ruthenium-based sensitizing dye (SD) N719 with TiO_2 or ZnO nanomaterials leads to very efficient LHNs for dye-sensitized solar cell (DSSC) applications [1-4]. The cost, rarity, and environmental issues of ruthenium complexes limit their wide application and encourage exploration of less-expensive, stable, and safer sensitizers. In this respect, porphyrin and porphyrin derivatives have shown promise for the replacement of ruthenium-based dyes for cost-effective and steady photovoltaic conversion of solar energy to electrical energy, because of their strong absorption in the region of 400−450 nm (B or Soret band) as well as 500−700 nm (Q bands). Several types of model porphyrins have been synthesized and their photophysical and electrochemical properties at the organic dye−semiconductor interface has been intensively studied [5-20]. These reports have revealed that the efficiency of porphyrin-sensitized solar cells can be increased by adding donor groups to the porphyrin ring, attaching bulky substituents to the phenyl groups, or by introducing double or triple bonds between the porphyrin ring and the anchoring carboxylic group (COOH). For e.g., Yalla *et al.* introduced long alkoxyl groups into the porphyrin ring and achieved an unprecedented 12.3% energy conversion efficiency in combination with a cobalt-based electrolyte and a complementary dye Y123 [21]. More recently, boron dipyrromethene compound has been synthesized and coadsorbed on TiO_2 nanoparticles with porphyrin dyes, which lead to a significant enhancement of energy conversion efficiency [11].

Along with successful recognition of efficient DSSCs, harvesting solar energy has also attracted a lot of attention to reduce organic pollutants at very low concentration by means of visible-light photocatalysis (VLP). In both the applications, the basic building block is a sensitizer, which absorbs visible-light from the sun, thereby initiating electron migration upon photoexcitation. The decisive use of various sensitizers including quantum dots in the system is found to be one of the key considerations in the realization of resourceful LHNs for efficient electron migration from sensitizers to the nanoparticulate film of a wide band-gap oxide semiconductor, and eventually the charge separation determines the VLP activity and the quality of DSSCs [22]. In this respect, due to its large band gap (3.3 eV), the popular photocatalyst ZnO can only utilize about 4% of the incoming solar energy, thus restricting its practical applications in a model VLP process. Therefore, a visible-light-activated catalyst is desired that can take the benefit of utilizing a superior portion of the solar spectrum and would be much more effective in ecological cleanup. In the view point of effective utilization of visible solar radiation, efforts have been made to trigger a photocatalyst under visible-light by extending its photoresponse to the visible region by metal-ion doping [23], nonmetal doping [24-25], noble metal deposition [26], narrow-band-gap semiconductors coupling [27-29], conducting polymer sensitization [30], and dye-sensitization [31-33]. In the latter approach, the excited dye molecule transfers an electron into the conduction band of the semiconductor, leading to the formation of a cationic radical of the dye. The injected electron then reacts with the dioxygen adsorbed on the surface of the metal oxide (MO), and generates active species involved in the process such as $O_2^{\bullet-}$, $dye^{\bullet+}$, as shown in equations 9.1−9.4:

$$dye + h\upsilon \rightarrow dye^{*} \tag{9.1}$$

$$dye^{*} + MO \rightarrow dye^{\bullet+} + MO(e_{CB}^{-}) \tag{9.2}$$

$$MO(e_{CB}^{-}) + O_2 \rightarrow MO + O_2^{\bullet-} \tag{9.3}$$

$$dye^{\bullet+}, O_2^{\bullet-} + R \rightarrow \mathrm{Pr}oduct \tag{9.4}$$

The subsequent radical chain reactions lead to the degradation and mineralization of a contaminant (R) and concurrently water in the media acts as an electron donor to regenerate the sensitizer dye [33]. For example, Zhao *et al.* has demonstrated a dye-sensitization system incorporating $Pt(dcbpy)Cl_2$ (dcbpy = 4,4′-dicarboxy-2,2′-bipyridine)

on titania for the visible-light degradation of aqueous organic pollutant 4-chlorophenol in the presence of oxygen [31]. Another study by Sun *et al.* has also demonstrated that aluminum phthalocyanine loaded on TiO_2 is a good sensitizer for degradation of substituted phenols in aerated aqueous solution under visible light irradiation [32]. Although various organic−inorganic LHNs are found to be active for energy conversion, we come up with an approach to achieve both the eco-friendly VLP process and cost-effective DSSC with a model LHN.

In the first part of this work, a hydrothermally grown, vertically oriented ZnO nanorods (NRs) were sensitized with hematoporphyrin (HP), the first isolated porphyrin which came from the ejection of iron from protohaemin and the hydration of the two vinyl side chains to form α-hydroxyethyl groups in their place. To obtain a better understanding of the physical properties of HP-sensitized ZnO LHNs, we have analyzed the attachment of porphyrin molecules to ZnO surfaces by using FTIR and Raman spectroscopic studies. Upon the binding of HP on ZnO surfaces, the ultrafast charge transfer processes were investigated by using steady-state and picosecond-resolved fluorescence techniques. After demonstrating HP−ZnO LHN as an efficient electron transfer mediator, we approached to employ the same nanohybrid in twin applications of efficient VLP process and to the fabrication of stable DSSCs. To the best of our knowledge, this sort of twin applications has not been reported previously by using a less-expensive, more stable, and safer HP−ZnO nanohybrid. To implement this approach, it is essential that rates of heterogeneous electron transfer for the nanohybrid layer be characterized as a function of structural parameters, including surface hydrophilicity, molecular interactions, and nature of anchoring of the chromophores.

9.2. Results and Discussion:

9.2.1. Hematoporphyrin−ZnO Nanohybrids: Twin Applications in Efficient Visible-Light Photocatalysis and Dye-Sensitized Solar Cells [34]:

9.2.1.1. Structural Characterization of HP−ZnO LHNs: Figure 9.1a shows the photographs of bare (left) and HP-sensitized (right) ZnO NRs decorated on FTO plates under daylight and their respective morphological characterization by SEM images are

shown. The contrast difference is clearly noticeable from the two SEM images that were

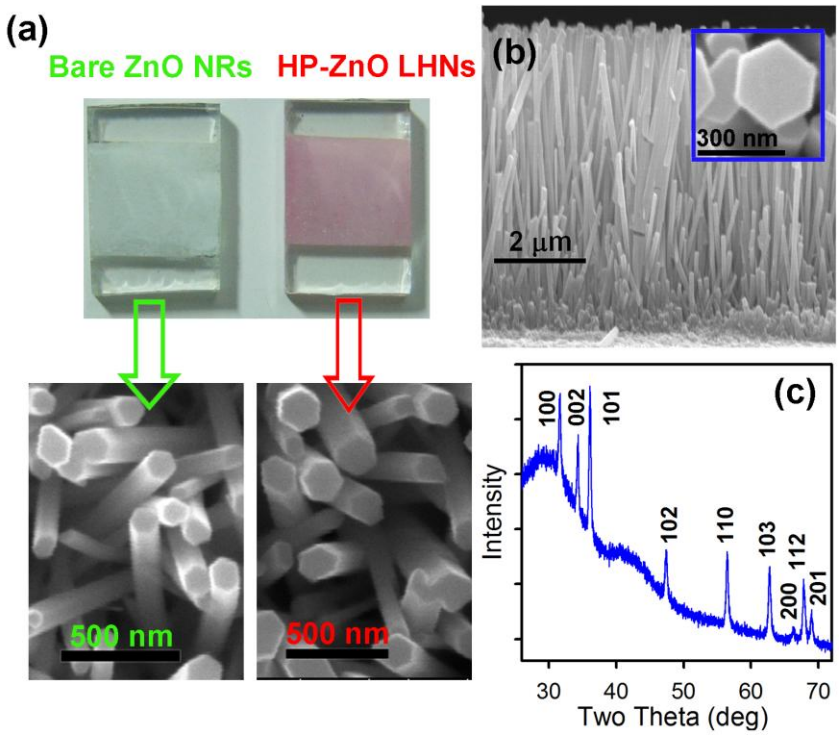

Figure 9.1. *a) Photographs of bare (left) and HP-sensitized (right) ZnO NRs decorated on FTO plates and their respective SEM images under daylight. b) The side-view and magnified top-view (inset) SEM images of vertically aligned, hexagonal ZnO NRs. c) XRD pattern of as-prepared ZnO NRs.*

taken under the same experimental conditions for a fare comparison. The side-view SEM image (Figure 9.1b) indicates the formation of arrays of ZnO NRs with a preferential growth direction along the polar facets in the [0002] direction of the ZnO hexagonal structure. The NRs growing perpendicular to the substrate are nearly uniform in length (~4−5 μm) and possess a characteristic hexagonal cross-section with a diameter of ~180 nm (inset). On the basis of the XRD results (Figure 9.1c), the crystallographic phase of these ZnO NRs belongs to the wurtzite-type [35].

9.2.1.2. Steady-State Absorption & PL Spectra of HP−ZnO LHNs: The formation of HP−ZnO nanohybrids are characterized by UV-vis spectroscopy. As shown in Figure 9.2a, ZnO NRs do not show considerable absorption above 410 nm, but the optical absorption increases in the UV region down to 360 nm which reaching a plateau at ~350 nm. Bare HP

exhibits a strong Soret absorption at 396 nm together with weak Q bands at 500 Q_y (1←0), 533 Q_y (0←0), 569 Q_x (1←0), and 622 nm Q_x (0←0) [36]. In this respect, the removal of a metal ion from the center of a porphyrin molecule (which is the case in HP) results in the appearance of these four weak bands in the visible region, which have been assigned

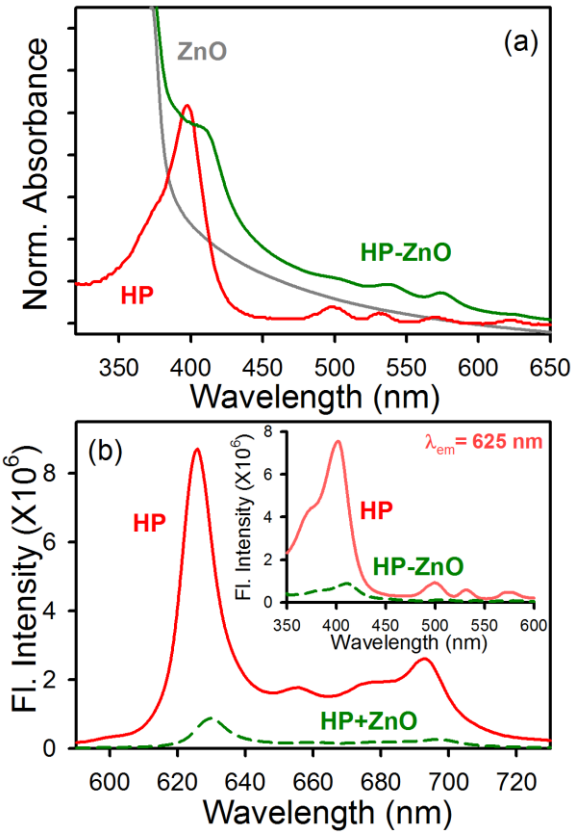

Figure 9.2. *a) UV/Vis absorption spectra of ZnO NRs (gray), HP (red) and HP-ZnO LHNs (green) in ethanol. b) Room temperature PL spectra (excitation wavelength was at 409 nm) of bare HP (red) and ZnO-anchored HP (green) are shown. Inset shows the excitation spectra of HP monitored at 625 nm.*

to the splitting of doubly degenerate states into the vibration components. Relative to HP, HP−ZnO nanohybrid exhibits a 12 nm bathochromic shift and a weaker intensity of Soret band [37]. These changes are obvious when compared to the absorption spectrum of HP, and it is reasonable to conclude that HP−ZnO LHNs are formed by the covalent binding of ZnO and anchoring groups of HP rather than only physical adsorption. As shown in Figure 9.2b, HP molecules are highly emissive as the photogenerated charge carriers undergo

radiative recombination. Upon 409 nm laser excitation, the strong emission of HP was found to be suppressed when anchored to ZnO NRs. The dramatic quenching of HP

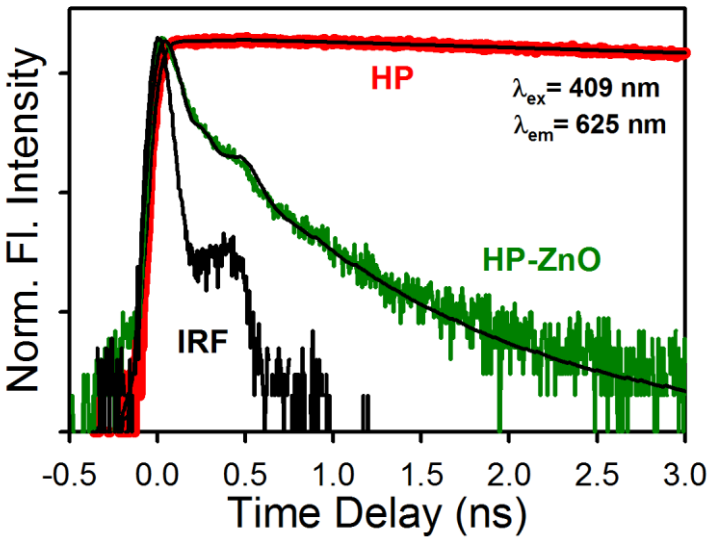

Figure 9.3. *Fluorescence decay profiles of HP−ZnO LHNs (green) and free HP (red) in ethanol.*

emission by ZnO NRs observed in the composite film is indicative of the fact that radiative decay becomes a minor pathway. The inset of Figure 9.2b shows the excitation spectra of bare HP and HP−ZnO LHNs monitored at the emission peak (625 nm). The excitation spectra of HP also show parallel maxima at 400 (Soret), 500, 532, and 574 nm. In addition, the excitation spectra for HP−ZnO LHNs also reveal ~12 nm bathochromic shift which is in accordance to the observations made from the absorption spectra. Because of the interference of the absorption of ZnO NRs with the excitation wavelength of 409 nm, it is difficult to obtain a quantitative estimate of HP emission quenching which was further established by monitoring the emission decay of HP and HP−ZnO LHNs.

9.2.1.3. Picosecond-Resolved Fluorescence Spectra of HP−ZnO LHNs: By using picosecond-resolved fluorescence technique, we probed the excited-state interactions of HP−ZnO LHNs, which was prepared by following the procedure discussed in section 3.2.2D. As shown in Figure 9.3, the fluorescence decay curve of HP was fitted with single exponential decay, which showed a lifetime of 10.38±0.06 ns depicting HP molecules were monomeric in ethanolic solution [9]. A significant decrease in HP fluorescence lifetime

(τ_{avg}) is observed in the presence of ZnO NRs and two fluorescence lifetimes are obtained which are summarized in Table 9.1. In particular, a faster component of 0.05±0.01 ns generates which contributes nearly 97% of the decay in HP−ZnO composite. Based on the results presented in Figures 9.2b and 9.3, we can conclude that an additional nonradiative pathway competes with the fluorescence of excited HP molecules. The apparent rate constant, k_{nr}, is determined for the nonradiative processes by comparing the lifetimes of HP in the absence (τ_0) and the presence (τ) of ZnO NRs, using equation 2.5. The apparent rate constant for the nonradiative process is estimated to be $(1.66\pm0.24)\times10^{10}$ s^{-1}. As reported in previous studies, such k_{nr} values represent electron transfer from LUMO of HP to the conduction band of ZnO semiconductor and rules out the possibility of self-quenching due to the aggregation of HP molecules on ZnO surface [14, 38-39]. This indicates that the charge injection between excited HP and ZnO NRs is an ultrafast process and it can be modulated by controlling the nature of anchoring of HP to the semiconductor surface.

9.2.1.4. FTIR Analysis of HP−ZnO LHNs: The dye used in this study, HP, contains two carboxylic groups, which possesses strong binding ability to the surface of ZnO. Three possible binding modes have been previously proposed for the surface adsorption of carboxylate on metal oxides [40-42]: (i) the monodentate (esterlike) linkage, (ii) bidentate chelating, and (iii) the bidentate bridging. Infrared vibrational spectroscopy usually provides a powerful tool to distinguish these binding modes. Generally, the frequency difference between the antisymmetric and symmetric stretching vibration ($\Delta = \nu_{as}-\nu_s$) of carboxylate group is in the order of Δ(monodentate) > Δ(ionic) ~ Δ(bridging) > Δ(bidentate). For the pure dye, the stretching vibration band of carboxylic group is located at 1714 cm^{-1}, as shown in Figure 9.4a. After coordinating to ZnO surface, this vibration band splits into two bands (1693 and 1416 cm^{-1}, respectively). The band located at 1693 cm^{-1} is ascribed to the antisymmetric stretching vibration of coordinated carboxylate group, while the shoulder band at 1416 cm^{-1} corresponds to the symmetric vibration. Therefore, the Δ value estimated for HP adsorbed on the pure ZnO is found to be (1693−1416) = 277 cm^{-1} which is a much larger value and suggests that the binding mode of HP on ZnO is dominantly the monodentate esterlike linkage. In a previous study, Zhao *et al.* also reported monodentate binding of Rhodamine B dyes with TiO_2 and Al(III)-

Table 9.1. Dynamics of picosecond-resolved luminescence transients of HP and HP−ZnO LHNs.[a]

Sample	τ_1 (ns)	τ_2 (ns)	τ_{avg} (ns)	$k_{nr}\times10^{10}$ (sec^{-1})
HP (bare)		10.38±0.06 (100%)	10.38±0.06	
HP−ZnO	0.05±0.01 (97%)	0.47±0.02 (3%)	0.06±0.01	1.66±0.24

[a]*The emission (monitored at 625 nm) was detected with 409 nm laser excitation. k_{nr} represents nonradiative rate constant. Numbers in the parenthesis indicate relative weightages.*

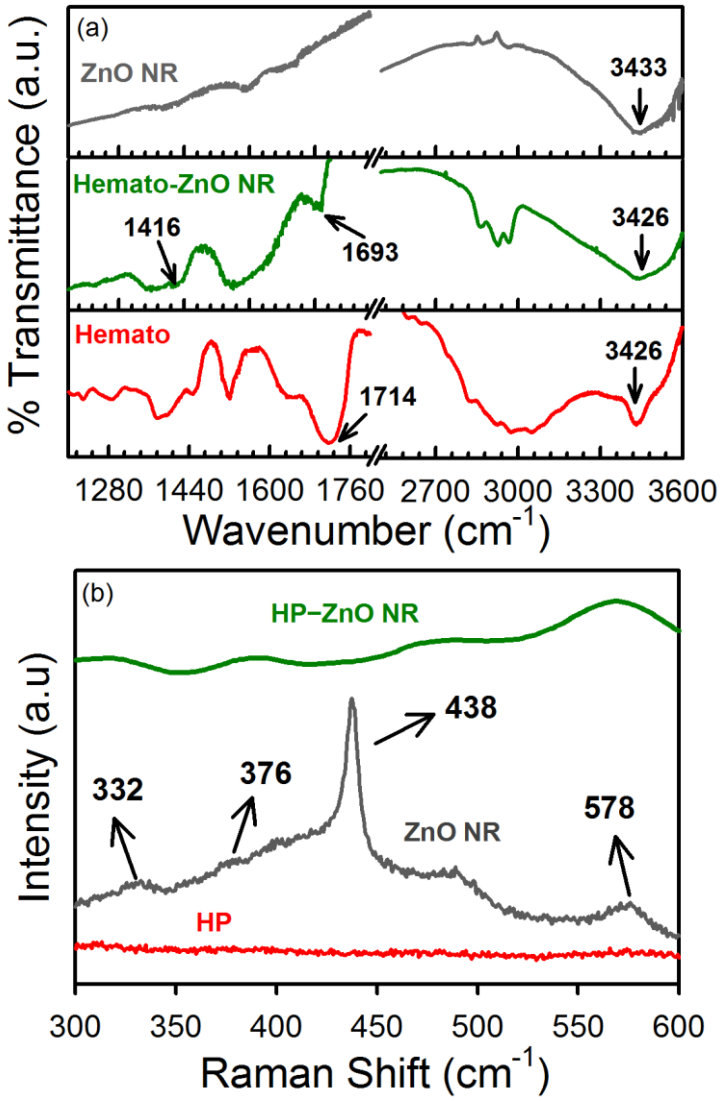

Figure 9.4. *a) FTIR and b) Raman spectra of HP (red), ZnO NRs (gray) and HP−ZnO LHNs (green).*

modified TiO_2 nanoparticles, with Δ value of 262 and 281 cm^{-1}, respectively [43].

9.2.1.5. Raman Spectra of HP−ZnO LHNs: The Raman spectra collected from HP, ZnO NRs and HP−ZnO LHNs in the wavenumber region of 300−600 cm^{-1} are shown in Figure 9.4b. As evidenced from the figure, HP molecules do not show an obvious peak in the experimental range. The Raman spectrum of the ZnO NR arrays exhibits four vibration peaks at 332, 376, 438, and 578 cm^{-1} thus indicating the presence of wurtzite structure [9, 44]. The peaks at 376 and 578 cm^{-1} correspond to the polar transverse A_1 and longitudinal E_1 optical phonon mode, respectively; the peak at 332 cm^{-1} is attributed to the E_2^{high}–E_2^{low} mode; and the strong peak at 438 cm^{-1} can be assigned to the nonpolar optical phonon E_2 mode of the ZnO NRs at high frequency, which is associated with oxygen deficiency [9, 45]. After binding HP to ZnO, the E_2 mode characteristic band of ZnO, associated to defect centers, is significantly perturbed. This is an indicative of the passivation of ZnO surface states upon HP assembly. The presence of other characteristic bands indicates good retention of ZnO wurtzite structure and crystal shape during the sensitization of ZnO NRs with HP.

9.2.1.6. Visible-Light Photocatalysis of MB by HP−ZnO LHNs: In order to apply our findings into a model application, we designed a flow-device consisting of two glass plates (separated by a spacer) as illustrated in Figure 4.6d. The research was aimed to clarify (1) the efficiency of the HP−ZnO LHNs for the degradation of dye pollutants under visible-light irradiation, (2) the effect of dye-sensitization time on the degradation efficiency, and (3) the mechanism of catalytic enhancement of photodegradation of dye pollutants under visible irradiation. As dye-sensitized systems solely rely on trapped conduction band electrons to reduce dioxygen to superoxide, many dyes simply cannot survive this severe oxidative stress [30-32, 46-48]. The optical response of the visible-light source was found to be effective in the region of 420−950 nm with a maximum intensity at 620 nm (Figure 9.5b, inset). The present work identifies a highly stable photocatalytic material, HP−ZnO, which promotes the visible-light sensitized (λ > 420 nm) decomposition of aqueous MB, a representative organic pollutant, in the presence of air without the need for any undesirable sacrificial electron donors to promote regeneration of surface-bound sensitizer molecules. Figure 9.5a shows the change of absorption spectra of MB solution when exposed to

visible-light in the absence and the presence of ZnO NRs and HP−ZnO LHNs at two

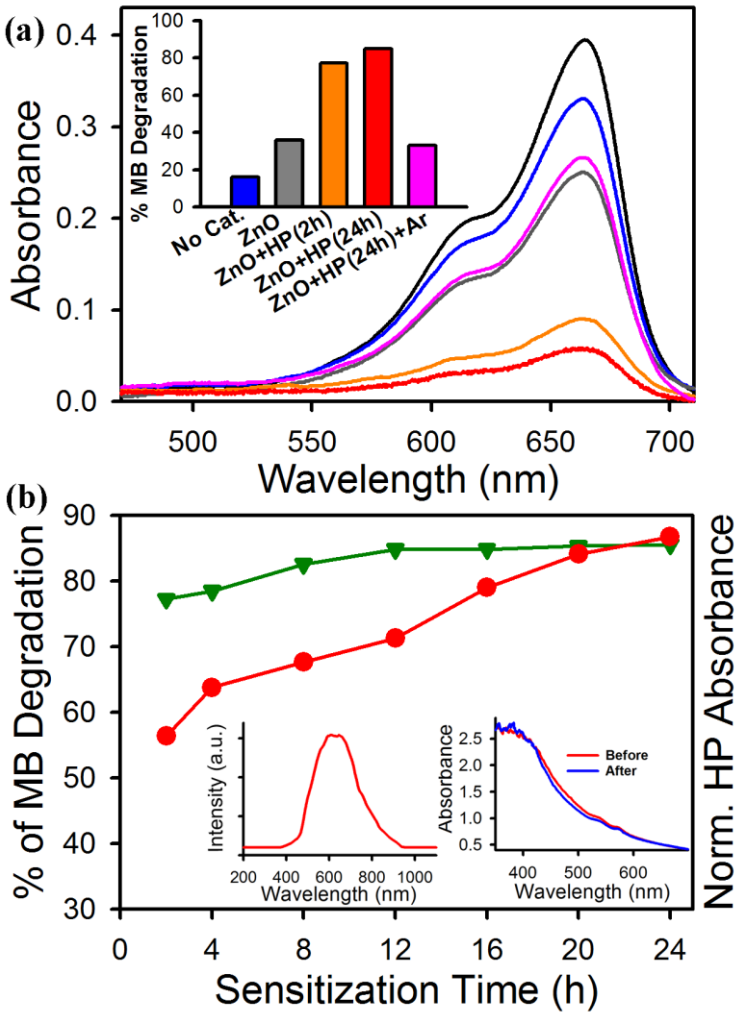

Figure 9.5. *a) UV-vis spectral changes of aqueous solution of MB in absence and the presence of ZnO, HP−ZnO LHNs, under visible-light irradiation. b) Dependence of photocatalytic activity on the dye-sensitization time. Inset (left) shows the optical response of our visible light source and inset (right) shows the absorbance of HP-sensitized (24 h) ZnO LHNs (on a quartz plate) before and after the photocatalysis process.*

extreme sensitization times, indicating the decolorization of MB during photoassisted reaction. The histogram (inset) clearly shows that degradation efficiency markedly enhanced in the presence of HP−ZnO LHNs, and it is also dependent on the HP sensitization time and reaches to ~85% after 24 h of HP sensitization.

In order to confirm that the HP−ZnO induced VLP process occurs *via* the formation of reactive oxygen species (ROS), we performed MB photodegradation in Argon (Ar) atmosphere. Under deaerated conditions, a suppression of O_2^{-}• radical production occurs and the reducing action of CB electrons is decreased, because of the inhibition of the degradation efficiency of HP−ZnO LHNs (24 h) from 85 to 33%. In this respect, Sun and Xu had used TiO_2-aluminum phthalocyanine nanohybrids to degrade water pollutant 4-cholorophenol where the catalyst capacity toward O_2 adsorption in aqueous solution was found to be a predominant factor [32]. For further understanding the effect of dye-sensitization time on VLP activity, a number of HP−ZnO substrates were prepared with different sensitization periods of 2, 4, 8, 12, 16, 20 and 24 h. Figure 9.5b shows that the absorption of HP−ZnO LHNs is quite expectedly increased with increasing sensitization times, and the catalytic activity also increased due to the higher adsorption of sensitizing dye on ZnO surface which was found to be saturated after 12 h of sensitization time and remain constant thereafter. It is worth noting that the increment of HP concentration must lower the possibility of MB to attach to ZnO surface that would lead to a deterioration of degradation efficiency for increasing HP sensitization time. However, the reverse output again reveals that the bleaching process is followed by ROS formation that are generated at the ZnO surface and subsequently transported to the MB layer. Therefore, the remote bleaching is not a simple reduction of MB to its leuco form at the surface of ZnO; rather MB is probably oxygenated or decomposed. This sort of remote bleaching of MB in the gas phase is well-speculated in the literature [49-50]. In addition, we have verified the photostability of HP−ZnO LHNs by measuring the absorbance of HP−ZnO film (on a quartz plate) prior to and after the completion of photocatalysis reaction. As shown in the inset of Figure 9.5b, after passing 2 mL aqueous solution of MB through the flow-device and 30 min of continuous light irradiation, it was found that a negligible amount of HP leached out from the quartz plate.

9.2.1.7. Water Contact Angle Measurements on HP−ZnO LHNs: The spreading of water on solid substrates is usually quantified through the contact angle, which positively characterizes the hydrophilicity and determines the biocompatibility of the materials [51]. The contact angle measurements were done on HP−ZnO films fabricated on a glass plate, under 0.5 sun and normal room-light intensity (0.2 sun). As shown in Figure 9.6, initially

HP−ZnO film shows a water contact angle of 129.1^{o} which gradually reduces with increasing time of irradiation. After 10 min of experimental time-window, it is found that

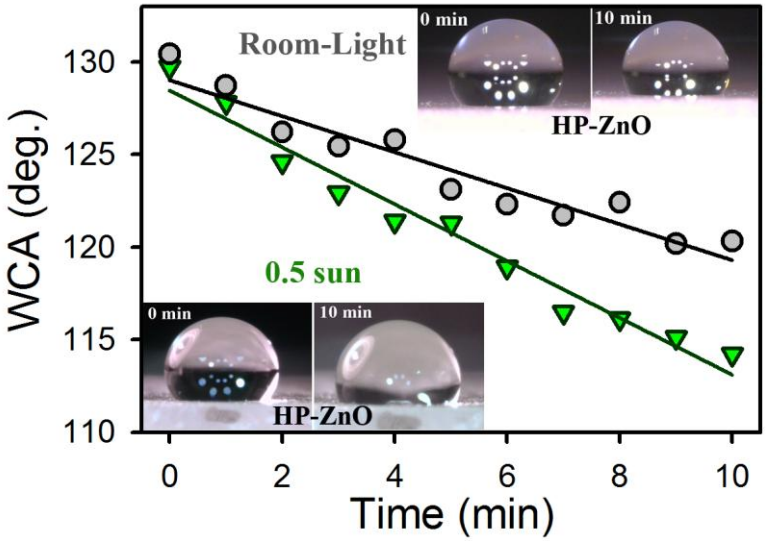

Figure 9.6. *Water contact-angle measurements on HP−ZnO modified substrates under the illumination of 0.5 sun and normal room light. Insets show their respective photographs.*

HP−ZnO becomes more hydrophilic when irradiated under 0.5 sun illumination, compared to normal room-light. This suggests that the electron−hole pair generation occurs at a much faster rate when higher intensity light incidents on the HP−ZnO surface. Upon illumination, HP will inject electrons to the ZnO conduction band which may get trapped in the surface defect states (mainly oxygen vacancy centers) if there is no external force to sweep these electrons out. As a consequence, the surface trapped electrons will build up a hydrophilic surface until an equilibrium state of release is reached. Therefore, higher light intensity would facilitate the photocatalysis of a water contaminant in LHNs. The insets show their corresponding photographs.

9.2.1.8. Optimized DSSC Performance: Photoelectrochemical measurements [52-53] were performed in a standard two-compartment cell, in acetonitrile containing 0.5 M LiI and 0.01 M I_2 as redox electrolyte and FTO/ZnO/HP as working electrode, while Pt/FTO was the counter electrode. Shown in Scheme 9.1 is the energy level alignment of ZnO NRs and porphyrin dyes, to demonstrate the electron transfer pathway in the photocurrent system. Previous studies have estimated that the CB and VB of the ZnO NRs are located at

−4.2 and −7.6 eV [9], and the LUMO and HOMO of phorphyrin dyes are located at −2.75 and −4.75 eV [54-55]. Upon visible-light irradiation, the electrons in HP molecules are

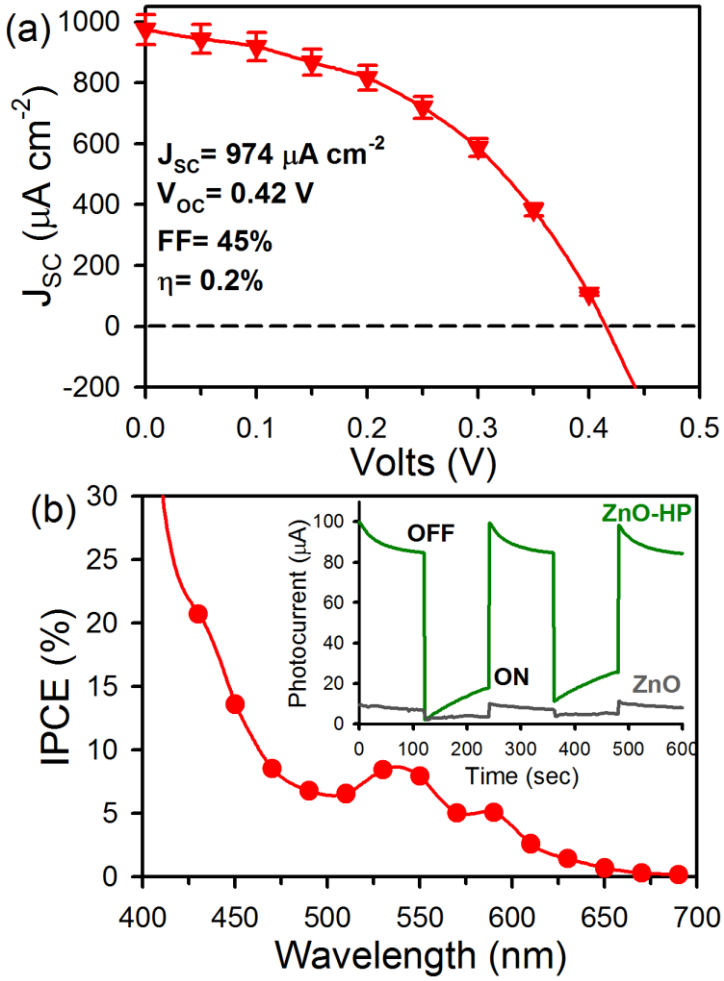

Figure 9.7. *a) Photocurrent−voltage (J−V) characteristics and b) incident photon-to-current conversion efficiency (IPCE) spectra for HP-sensitized ZnO NR-based DSSCs. Inset shows photocurrent responses of ZnO NRs (gray) and HP−ZnO LHN (green) modified FTO electrode under the bias voltage of 2.5 V. The photocurrent was measured across the thickness of the films with 25 mW cm^{-2} incident power from a halogen light source.*

injected to the CB of ZnO and consequently transported to the FTO plates, leading to a photocurrent. The photocurrent density−voltage (*J*−*V*) curves of the devices measured under AM 1.5 irradiation (100 mW cm^{-2}) are shown in Figure 9.7a, and the detailed photovoltaic parameters are summarized in Table 9.2. The short-circuit photocurrent density (J_{SC}), open-circuit photovoltage (V_{OC}), and *FF* of a HP-sensitized cell with the

iodine-based electrolyte are ~974±48 μA cm^{-2}, 0.42±0.02 V, and 45±0.6 %, respectively, with an overall conversion efficiency, η of 0.20±0.02 %. Note that a well-

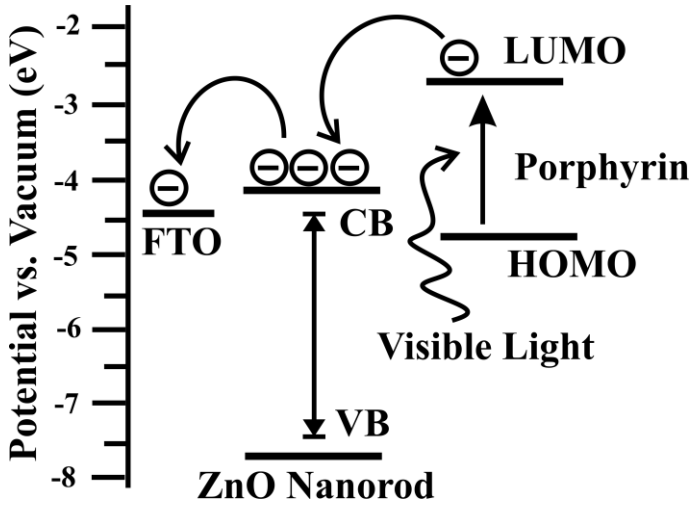

Scheme 9.1. *Schematic energy level diagram and electron-transfer path from porphyrin dyes to ZnO.*

recognized ruthenium-based solar cell dye N719 provides η of 0.13±0.01 under the same experimental conditions, which is comparable with HP−ZnO based DSSCs [53].

The incident photon-to-current conversion efficiency (IPCE) for HP-sensitized DSSCs is shown in Figure 9.7b. The IPCE, defined as the number of electrons collected per incident photon, was evaluated from short-circuit photocurrent (J_{SC}) measurements at different wavelengths (λ), and the IPCE was calculated using equation 2.31. The IPCE spectra are found to closely resembled the characteristic absorbance spectra of HP (Figure 9.2a), which exhibit peaks near 530 and 580 nm because of the Q bands, and reaches a maximum value of ~30% at the Soret region (~400 nm), signifying that the HP sensitizers on the photoanode surface are indeed responsible for photocurrent generation. In this respect, a recent study employed a noncovalent double-decker binding strategy to construct functional supramolecular single-wall carbon nanotubes-zinc porphyrin hybrids where a maximum of 12% IPCE has been achieved without any modification of porphyrin side-chains [56].

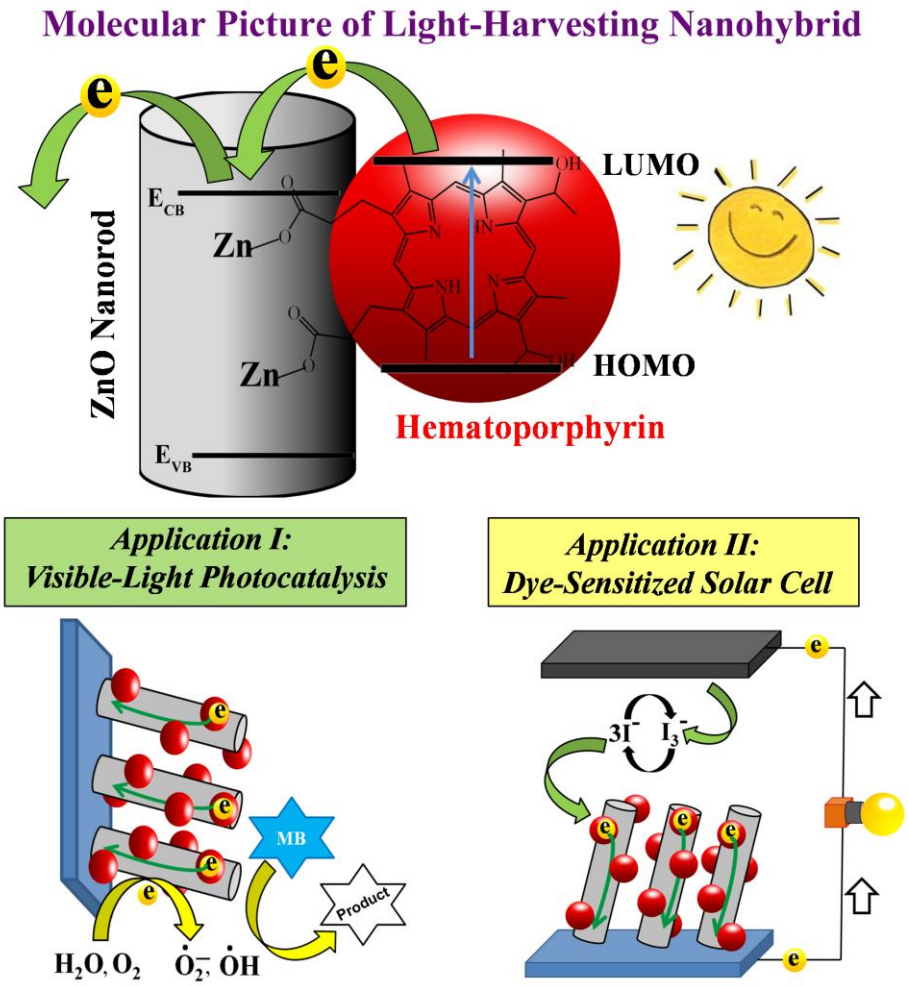

Scheme 9.2. *Schematic representation of a model light-harvesting nanohybrid (LHN) depicting covalently functionalized ZnO NRs with sensitizing dye, Hematoporphyrin (HP). The scheme illustrates the typical absorption process for visible-light in the LHNs: light is absorbed by the sensitizing dye HP, transferring an electron into the conduction band of ZnO. The trapped electron in ZnO is exploiting dual vital applications of using HP−ZnO nanohybrid as a model light-harvesting material: (I) visible-light photocatalysis and (II) dye-sensitized solar cells.*

Table 9.2. Device performance[b] of the HP-sensitized DSSCs.

Device	V_{OC} (V)	J_{SC} (μA/cm^2)	*FF* (%)	η (%)
HP−ZnO	0.42±0.02	974±48	45±0.6	0.20±0.02
N719−ZnO (control)	0.69±0.05	620±33	30±0.5	0.13±0.01

[b]*short-circuit photocurrent densities (J_{SC}/cm^2), open-circuit voltage (V_{OC}), fill factor (FF), and efficiency (η). The control experiment with N719 dye-sensitized system is provided from another report [53].*

The photoconductivity measurements [52-53, 57] (as discussed in section 3.1.13) of bare ZnO and HP-modified ZnO thin films are also performed in order to better understand the photocurrent response of the nanohybrids. Inset of Figure 9.7b shows the photocurrent response for the ZnO NR and HP−ZnO thin films, where an improved photocurrent was observed for the HP-modified ZnO thin film (~100 μA) under illuminated condition compared to the bare ZnO NR thin film (~10 μA).

9.3. Conclusion:

In conclusion, hematoporphyrin (HP) has been conjugated onto covalently functionalized ZnO NRs, forming electron donor−acceptor HP−ZnO nanohybrid, which is being established as a potential light-harvesting materials, as represented in Scheme 9.2. The new hybrid nanomaterial has been methodically characterized with the aid of standard microscopic and optical techniques. The FTIR and Raman scattering studies confirm the formation of HP−ZnO nanohybrid through the monodentate binding of ZnO and carboxylic groups of HP rather than simply physical adsorption. Steady-state and picosecond-resolved fluorescence measurements reveal efficient quenching of HP fluorescence in the HP−ZnO nanohybrid, suggesting that photoinduced charge transfer takes place from LUMO of HP to the CB of ZnO. Utilizing this phenomenon, a new dye-sensitized system, incorporating HP on ZnO, is realized for the photodegradation of aqueous organic pollutants under visible-light irradiation. Finally, a photoelectrochemical cell is constructed based on HP sensitization onto nanostructured ZnO at FTO plates. The FTO/ZnO/HP electrode revealed prompt, stable and reproducible photocurrent and photovoltage, with IPCE values as large as 30%, without the application of bias voltage. The present work demonstrates the exciting potential of porphyrins as light-harvesting green dyes that can simultaneously be used in visible-light photocatalysis and photovoltaics.

References

[1] C.Y. Chen, M. Wang, J.Y. Li, N. Pootrakulchote, L. Alibabaei, C. Ngoc-le, J.D. Decoppet, J.H. Tsai, C. Grätzel, C.G. Wu, S.M. Zakeeruddin, M. Grätzel, Highly Efficient Light-Harvesting Ruthenium Sensitizer for Thin-Film Dye-Sensitized Solar Cells, *ACS Nano* 3 (2009) 3103.

[2] M.K. Nazeeruddin, C. Klein, P. Liska, M. Grätzel, Synthesis of Novel Ruthenium Sensitizers and Their Application in Dye-Sensitized Solar Cells, *Coord. Chem. Rev.* 249 (2005) 1460.

[3] C. Ku, J. Wu, Electron Transport Properties in ZnO Nanowire Array/Nanoparticle Composite Dye-Sensitized Solar Cells, *Appl. Phys. Lett.* 91 (2007) 093117.

[4] Z. Wanga, H. Kawauchib, T. Kashimab, H. Arakawa, Significant Influence of TiO_2 Photoelectrode Morphology on the Energy Conversion Efficiency of N719 Dye-Sensitized Solar Cell, *Coord. Chem. Rev.* 248 (2004) 1381.

[5] C.L. Wang, C.M. Lan, S.H. Hong, Y.F. Wang, T.Y. Pan, C.W. Chang, H.H. Kuo, M.Y. Kuo, E.W.G. Diau, C.Y. Lin, Enveloping Porphyrins for Efficient Dye-Sensitized Solar Cells, *Energy Environ. Sci.* 5 (2012) 6933.

[6] S.L. Wu, H.P. Lu, H.T. Yu, S.H. Chuang, C.L. Chiu, C.W. Lee, E.W.G. Diau, C.Y. Yeh, Design and Characterization of Porphyrin Sensitizers with a Push-Pull Framework for Highly Efficient Dye-Sensitized Solar Cells, *Energy Environ. Sci.* 3 (2010) 949.

[7] C.W. Lee, H.P. Lu, C.M. Lan, Y.L. Huang, Y.R. Liang, W.N. Yen, Y.C. Liu, Y.S. Lin, E.W.G. Diau, C.Y. Yeh, Novel Zinc Porphyrin Sensitizers for Dye-Sensitized Solar Cells: Synthesis and Spectral, Electrochemical, and Photovoltaic Properties, *Chem. Eur. J.* 15 (2009) 1403.

[8] C.M. Drain, A. Varotto, I. Radivojevic, Self-Organized Porphyrinic Materials, *Chem. Rev.* 109 (2009) 1630.

[9] W. Tu, J. Lei, P. Wang, H. Ju, Photoelectrochemistry of Free-Base-Porphyrin-Functionalized Zinc Oxide Nanoparticles and Their Applications in Biosensing, *Chem. Eur. J.* 17 (2011) 9440.

[10] Y. Liu, Y. Zhang, S. Wang, C. Pope, W. Chen, Optical Behaviors of ZnO-Porphyrin Conjugates and their Potential Applications for Cancer Treatment, *Appl. Phys. Lett.* 92 (2008) 143901.

[11] M. Shrestha, L. Si, C.W. Chang, H. He, A. Sykes, C.Y. Lin, E.W.G. Diau, Dual Functionality of BODIPY Chromophore in Porphyrin-Sensitized Nanocrystalline Solar Cells, *J. Phys. Chem. C* 116 (2012) 10451.

[12] W.M. Campbell, K.W. Jolley, P. Wagner, K. Wagner, P.J. Walsh, K.C. Gordon, L. Schmidt-Mende, M.K. Nazeeruddin, Q. Wang, M. Grätzel, D.L. Officer, Highly Efficient Porphyrin Sensitizers for Dye-Sensitized Solar Cells, *J. Phys. Chem. C* 111 (2007) 11760.

[13] Q. Wang, W.M. Campbell, E.E. Bonfantani, K.W. Jolley, D.L. Officer, P.J. Walsh, K. Gordon, R. Humphry-Baker, M.K. Nazeeruddin, M. Gratzel, Efficient Light Harvesting by Using Green Zn-Porphyrin-Sensitized Nanocrystalline TiO_2 Films, *J. Phys. Chem. B* 109 (2005) 15397.

[14] H. Saarenpaa, E. Sariola-Leikas, A.P. Perros, J.M. Kontio, A. Efimov, H. Hayashi, H. Lipsanen, H. Imahori, H. Lemmetyinen, N.V. Tkachenko, Self-Assembled Porphyrins on Modified Zinc Oxide Nanorods: Development of Model Systems for Inorganic−Organic Semiconductor Interface Studies, *J. Phys. Chem. C* 116 (2012) 2336.

[15] Y. Xu, Z. Liu, X. Zhang, Y. Wang, J. Tian, Y. Huang, Y. Ma, X. Zhang, Y. Chen, A Graphene Hybrid Material Covalently Functionalized with Porphyrin: Synthesis and Optical Limiting Property, *Adv. Mater.* 21 (2009) 1275.

[16] G. Pagona, G.E. Zervaki, A.S.D. Sandanayaka, O. Ito, G. Charalambidis, T. Hasobe, A.G. Coutsolelos, N. Tagmatarchis, Carbon Nanohorn−Porphyrin Dimer Hybrid Material for Enhancing Light-Energy Conversion, *J. Phys. Chem. C* 116 (2012) 9439.

[17] X. Gong, T. Milic, C. Xu, J.D. Batteas, C.M. Drain, Preparation and Characterization of Porphyrin Nanoparticles, *J. Am. Chem. Soc.* 124 (2002) 14290.

[18] S.A. Abdul, J.B. Cui, Graphene-Enriched P3HT and Porphyrin-Modified ZnO Nanowire Arrays for Hybrid Solar Cell Applications, *J. Phys. Chem. C* 116 (2012) 9433.

[19] N.K. Subbaiyan, E. Maligaspe, F. D'Souza, Near Unity Photon-to-Electron Conversion Efficiency of Photoelectrochemical Cells Built on Cationic Water-Soluble Porphyrins Electrostatically Decorated onto Thin-Film Nanocrystalline SnO_2 Surface, *ACS Appl. Mater. Interfaces.* 3 (2011) 2368.

[20] J.R. Stromberg, A. Marton, H.L. Kee, C. Kirmaier, J.R. Diers, C. Muthiah, M. Taniguchi, J.S. Lindsey, D.F. Bocian, G.J. Meyer, D. Holten, Examination of Tethered Porphyrin, Chlorin, and Bacteriochlorin Molecules in Mesoporous Metal-Oxide Solar Cells, *J. Phys. Chem. C* 111 (2007) 15464.

[21] A. Yella, H.W. Lee, H.N. Tsao, C. Yi, A.K. Chandiran, M.K. Nazeeruddin, W.G.E. Diau, C.Y. Yeh, S.M. Zakeeruddin, M. Grätzel, Porphyrin-Sensitized Solar Cells with Cobalt (II/III)–Based Redox Electrolyte Exceed 12 Percent Efficiency, *Science* 334 (2011) 629.

[22] L. Zhao, L. Hu, X. Fang, Growth and Device Application of CdSe Nanostructures, *Adv. Funct. Mater.* 22 (2012) 1551.

[23] C.C. Chen, X.Z. Li, W.H. Ma, J.C. Zhao, H. Hidaka, N. Serpone, Effect of Transition Metal Ions on the TiO_2-Assisted Photodegradation of Dyes under Visible Irradiation: A Probe for the Interfacial Electron Transfer Process and Reaction Mechanism, *J. Phys. Chem. B* 106 (2002) 318.

[24] R. Asahi, T. Morikawa, T. Ohwaki, K. Aoki, Y. Taga, Visible-Light Photocatalysis in Nitrogen-Doped Titanium Oxides, *Science* 293 (2001) 269.

[25] N. Lu, X. Quan, J. Li, S. Chen, H. Yu, G. Chen, Fabrication of Boron-Doped TiO_2 Nanotube Aarray Electrode and Investigation of its Photoelectrochemical Capability, *J. Phys. Chem. C* 111 (2007) 11836.

[26] X.Z. Li, F.B. Li, Study of Au/Au^{3+}-TiO_2 Photocatalysts Toward Visible Photooxidation for Water and Wastewater Treatment, *Environ. Sci. Technol.* 35 (2001) 2381.

[27] Z. Zhang, W. Wang, L. Wang, S. Sun, Enhancement of Visible-Light Photocatalysis by Coupling with Narrow-Band-Gap Semiconductor: A Case Study on Bi_2S_3/Bi_2WO_6, *ACS Appl. Mater. Interfaces* 4 (2012) 593.

[28] J. Jiang, X. Zhang, P. Sun, L. Zhang, ZnO/BiOI Heterostructures: Photoinduced Charge-Transfer Property and Enhanced Visible-Light Photocatalytic Activity, *J. Phys. Chem. C* 115 (2011) 20555.

[29] G.S. Li, D.Q. Zhang, J.C. Yu, A New Visible-Light Photocatalyst: CdS Quantum Dots Embedded Mesoporous TiO_2, *Environ. Sci. Technol.* 43 (2009) 7079.

[30] H. Zhang, R.L. Zong, J.C. Zhao, Y.F. Zhu, Dramatic Visible Photocatalytic Degradation Performances due to Synergetic Effect of TiO_2 with PANI, *Environ. Sci. Technol.* 42 (2008) 3803.

[31] W. Zhao, Y. Sun, F.N. Castellano, Visible-Light Induced Water Detoxification Catalyzed by Pt II Dye Sensitized Titania, *J. Am. Chem. Soc.* 130 (2008) 12566.

[32] Q. Sun, Y. Xu, Sensitization of TiO_2 with Aluminum Phthalocyanine: Factors Influencing the Efficiency for Chlorophenol Degradation in Water under Visible Light, *J. Phys. Chem. C* 113 (2009) 12387.

[33] E. Bae, W. Choi, Highly Enhanced Photoreductive Degradation of Perchlorinated Compounds on Dye-Sensitized Metal/TiO_2 under Visible Light, *Environ. Sci. Technol.* 37 (2003) 147.

[34] S. Sarkar, A. Makhal, T. Bora, K. Lakshman, A. Singha, J. Dutta, S.K. Pal, Hematoporphyrin−ZnO Nanohybrids: Twin Applications in Efficient Visible-Light Photocatalysis and Dye-Sensitized Solar Cells, *ACS Appl. Mater. Interfaces* 4 (2012) 7027.

[35] B. Liu, H.C. Zeng, Hydrothermal Synthesis of ZnO Nanorods in the Diameter Regime of 50 nm, *J. Am. Chem. Soc.* 125 (2003) 4430.

[36] R.C. Srivastava, V.D. Anand, W.R. Carper, A Fluorescence Study of Hematoporphyrin, *Appl. Spectroscopy* 27 (1973) 444.

[37] P. Castillero, J.R. Sanchez-Valencia, M. Cano, J.M. Pedrosa, J. Roales, A. Barranco, A.R. Gonzalez-Elipe, Active and Optically Transparent Tetracationic Porphyrin/TiO_2 Composite Thin Films, *ACS Appl. Mater. Interfaces* 2 (2010) 712.

[38] T. Hasobe, K. Saito, P.V. Kamat, V. Troiani, H. Qui, N. Solladie, K.S. Kim, J.K. Park, D. Kim, F. D'Souza, S. Fukuzumi, Organic Solar Cells. Supramolecular Composites of Porphyrins and Fullerenes Organized by Polypeptide Structures as Light Harvesters, *J. Mater. Chem.* 17 (2007) 4160.

[39] H.M. Cheng, W.F. Hsieh, Electron Transfer Properties of Organic Dye-Sensitized Solar Cells based on Indoline Sensitizers with ZnO Nanoparticles, *Nanotechnology* 21 (2010) 485202.

[40] Y.X. Weng, L. Li, Y. Liu, L. Wang, G.Z. Yang, Surface-Binding forms of Carboxylic Groups on Nanoparticulate TiO_2 Surface Studied by the Interface-Sensitive Transient Triplet-State Molecular Probe, *J. Phys. Chem. B* 107 (2003) 4356.

[41] S.W. Boettcher, M.H. Bartl, J.G. Hu, G.D. Stucky, Structural Analysis of Hybrid Titania-based Mesostructured Composites, *J. Am. Chem. Soc.* 127 (2005) 9721.

[42] G.B. Deacon, R.J. Phillips, Relationships between the Carbon-Oxygen Stretching Frequencies of Carboxylato Complexes and the type of Carboxylate Coordination, *Coord. Chem. Rev.* 33 (1980) 227.

[43] D. Zhao, C. Chen, Y. Wang, W. Ma, J. Zhao, T. Rajh, L. Zang, Enhanced Photocatalytic Degradation of Dye Pollutants under Visible Irradiation on Al(III)-Modified TiO_2: Structure, Interaction, and Interfacial Electron Transfer, *Environ. Sci. Technol.* 42 (2008) 308.

[44] Y. Zhang, H. Jia, R. Wang, C. Chen, X. Luo, D. Yu, C. Lee, Low-Temperature Growth and Raman Scattering Study of Vertically Aligned ZnO Nanowires on Si Substrate, *Appl. Phys. Lett.* 83 (2003) 4631.

[45] P. Jiang, J.J. Zhou, H.F. Fang, C.Y. Wang, Z.L. Wang, S.S. Xie, Hierarchical Shelled ZnO Structures Made of Bunched Nanowire Arrays, *Adv. Funct. Mater.* 17 (2007) 1303.

[46] H.C. Liang, X.Z. Li, Visible-Induced Photocatalytic Reactivity of Polymer-Sensitized Titania Nanotube Films, *Appl. Catal. B* 86 (2009) 8.

[47] D.S. Wang, J. Zhang, Q.Z. Luo, X.Y. Li, Y.D. Duan, J. An, Characterization and Photocatalytic Activity of Poly(3-hexylthiophene)-Modified TiO_2 for Degradation of Methyl Orange under Visible Light, *J. Hazard. Mater.* 169 (2009) 546.

[48] C. Chen, W. Zhao, J. Li, J. Zhao, H. Hidaka, N. Serpone, Formation and Identification of Intermediates in the Visible-Light-Assisted Photodegradation of Sulforhodamine-B Dye in Aqueous TiO_2 Dispersion, *Environ. Sci. Technol.* 36 (2002) 3604.

[49] T. Tatsuma, S.I. Tachibana, T. Miwa, D.A. Tryk, A. Fujishima, Remote Bleaching of Methylene Blue by UV-Irradiated TiO_2 in the Gas Phase, *J. Phys. Chem. B* 103 (1999) 8033.

[50] T. Tatsuma, S. Tachibana, A. Fujishima, Remote Oxidation of Organic Compounds by UV-Irradiated TiO_2 via the Gas Phase, *J. Phys. Chem. B* 105 (2001) 6987.

[51] Y. Liu, Z. Lin, W. Lin, K.S. Moon, C.P. Wong, Reversible Superhydrophobic−Superhydrophilic Transition of ZnO Nanorod/Epoxy Composite Films, *ACS Appl. Mater. Interfaces* 4 (2012) 3959.

[52] S. Sarkar, A. Makhal, T. Bora, S. Baruah, J. Dutta, S.K. Pal, Photoselective Excited State Dynamics in ZnO-Au Nanocomposites and their Implications in Photocatalysis and Dye-Sensitized Solar Cells, *Phys. Chem. Chem. Phys.* 13 (2011) 12488.

[53] S. Sarkar, A. Makhal, K. Lakshman, T. Bora, J. Dutta, S.K. Pal, "Dual-Sensitization" via Electron and Energy Harvesting in CdTe Quantum Dots Decorated ZnO Nanorod-based Dye-Sensitized Solar Cells, *J. Phys. Chem. C* 116 (2012) 14248.

[54] D. Liu, W. Wu, Y. Qiu, S. Yang, S. Xiao, Q.Q. Wang, L. Ding, J. Wang, Surface Functionalization of ZnO Nanotetrapods with Photoactive and Electroactive Organic Monolayers, *Langmuir* 24 (2008) 5052.

[55] H.L. Kee, C. Kirmaier, Q. Tang, J.R. Diers, C. Muthiah, M. Taniguchi, J.K. Laha, M. Ptaszek, J.S. Lindsey, D.F. Bocian, D. Holten, Effects of Substituents on Synthetic Analogs of Chlorophylls. Part 2: Redox Properties, Optical Spectra and Electronic Structure, *Photochem. Photobiol.* 83 (2007) 1125.

[56] A.S.D. Sandanayaka, N.K. Subbaiyan, S.K. Das, R. Chitta, E. Maligaspe, T. Hasobe, O. Ito, F. D'Souza, Diameter-Sorted SWCNT–Porphyrin and SWCNT-Phthalocyanine Conjugates for Light-Energy Harvesting, *Chem. Phys. Chem.* 12 (2011) 2266.

[57] L. Hu, J. Yan, M. Liao, H. Xiang, X. Gong, L. Zhang, X. Fang, An Optimized Ultraviolet-A Light Photodetector with Wide-Range Photoresponse Based on ZnS/ZnO Biaxial Nanobelt, *Adv. Mater.* 24 (2012) 2305.

List of Publications

(Peer-Reviewed Journals)

1.* S. Banerjee, S. Sarkar, K. Lakhsman, J. Dutta and S. K. Pal
"UVA Radiation Induced Ultrafast Electron Transfer from a Food Carcinogen Benzo[a]Pyrene to Organic Molecules, Biological Macromolecules and Inorganic Nanostructures", *J. Phys. Chem. B* 117 (2013) 3726–3737.

2. S. Sarkar, A. Makhal, T. Bora, K. Lakhsman, A. Singha, J. Dutta and S. K. Pal
"Hematoporphyrin−ZnO Nanohybrids: Twin Applications in Efficient Visible-Light Photocatalysis and Dye-Sensitized Solar Cells", *ACS Appl. Mater. Interfaces*, 4 (2012) 7027−7035.

3. S. Sarkar, A. Makhal, K. Lakshman, T. Bora, J. Dutta and S. K. Pal
"Dual-Sensitization" *via* Electron and Energy Harvesting in CdTe Quantum Dots Decorated ZnO Nanorod-Based Dye-Sensitized Solar Cells, *J. Phys. Chem. C*, 116 (2012) 14248−14256.

4. S. Sarkar, A. Makhal, S. Baruah, M. Mahmood, J. Dutta and S. K. Pal
"Nanoparticle−Sensitized Photodegradation of Bilirubin and Potential Therapeutic Application", *J. Phys. Chem. C* 116 (2012) 9608−9615 (Nature-India Highlighted).

5. S. Sarkar$^{\neq}$, A. Makhal$^{\neq}$ and S. K. Pal ($^{\neq}$contributed equally)
"Protein-Mediated Synthesis of Nanosized Mn-doped ZnS: A Multifunctional, UV-Durable Bio-Nanocomposite", *Inorg. Chem.* 51 (2012) 10203−10210.

6. S. Sarkar[≠], A. Makhal[≠], S. K. Pal, H. Yan, D. Wulferding, F. Cetin and P. Lemmens ([≠]contributed equally)
Ultrafast Excited State Deactivation of Doped Porous Anodic Alumina Membranes, *Nanotechnology*, 23 (2012) 305705.

7. S. Sarkar, A. Makhal, T. Bora, S. Baruah, J. Dutta and S. K. Pal
"Photoselective Excited State Dynamics in ZnO−Au Nanocomposites and Their Implications in Photocatalysis and Dye-Sensitized Solar Cells", *Phys. Chem. Chem. Phys.* 13 (2011) 12488−12496 (Hot Article).

8. T. Bora, H. H. Kyaw, S. Sarkar, S. K. Pal and J. Dutta
"Highly Efficient ZnO−Au Schottky Barrier Dye-Sensitized Solar Cells: Role of Gold Nanoparticles on the Charge Transfer Process" *Beilstein J. Nanotechnol.* 2 (2011) 681−690.

9.* A. Makhal, S. Sarkar, T. Bora, S. Baruah, J. Dutta, A. K. Raychaudhuri and S. K. Pal
"Role of Resonance Energy Transfer in Light Harvesting of Zinc Oxide-Based Dye-Sensitized Solar Cells", *J. Phys. Chem. C* 114 (2010) 10390−10395.

10.* A. Makhal, S. Sarkar, T. Bora, S. Baruah, J. Dutta, A. K. Raychaudhuri and S. K. Pal
"Dynamics of Light Harvesting in ZnO Nanoparticles", *Nanotechnology* 21 (2010) 265703.

(Book Chapters)

1. S. Sarkar, A. Makhal and S. K. Pal
   "Ultrafast Spectroscopy and Technological Application of Light Harvesting Nanomaterials", (Book Chapter) in "NANOTECHNOLOGY" Edited by J. N. Govil, STUDIUM PRESS LLC, USA, 2012, Chapter 6, Entitled "Electronics and Photovoltaics".

2.* A. Giri, N. Goswami, S. Sarkar and S. K. Pal
   "Bio-Nanomaterials: Understanding Key Biophysics and their Applications", (Book Chapter) in "NANOTECHNOLOGY" Edited by J. N. Govil, STUDIUM PRESS LLC, USA, 2013, Volume 11, Chapter 13, Entitled "Biomaterials".

(Patents Filed)

1*. Waste Blood-Based Solar Cell for Low-Cost Renewable Energy.
   Indian Pat. Appl. (2011), 980/KOL/2011 dated 25th July 2011.

2*. Method and System of Enhanced Degradation of Bilirubin Involving Zinc Oxide (ZnO) Nanoparticles.
   Indian Pat. Appl. (2011), 964/KOL/2011 dated 20th July 2011.

* Not included in the thesis.